Universidade de Lisboa

Faculdade de Ciências

Departamento de Física

Numerical modelling in Transcranial Magnetic Stimulation

Ricardo Nuno Braço Forte Salvador

Doutoramento em Engenharia Biomédica e Biofísica

2009

Universidade de Lisboa

Faculdade de Ciências

Departamento de Física

Numerical modelling in Transcranial Magnetic Stimulation

Ricardo Nuno Braço Forte Salvador

Thesis supervised by Prof. Doutor Pedro Cavaleiro Miranda

Doutoramento em Engenharia Biomédica e Biofísica

2009

Aos meus pais e avós, sem o apoio dos quais não haveria tese.
Em memória do meu bisavô Mário e da minha tia Rosa.

CONTENTS

PHYSICAL QUANTITIES V

SYMBOLS AND ABBREVIATIONS VII

ABSTRACT IX

RESUMO XI

ACKNOWLEDGMENTS XVII

1 INTRODUCTION ..... - 19 -

1.1 AIM OF THE WORK ..... - 19 -
1.2 OVERVIEW OF TRANSCRANIAL MAGNETIC STIMULATION ..... - 20 -
1.2.1 Basic principles and history ..... - 20 -
What is TMS? ..... - 20 -
History of brain stimulation with electromagnetic fields ..... - 22 -
1.2.2 The electric field induced in TMS ..... - 24 -
Two sources of the electric field ..... - 24 -
The quasistatic approximation ..... - 25 -
Numerical modelling of the electric field ..... - 27 -
1.2.3 Field-neuron interaction in TMS ..... - 30 -
Neuron's membrane properties ..... - 30 -
Subthreshold and suprathreshold membrane response ..... - 31 -
Cable model and Cable equation ..... - 34 -
Rattay activation function for TMS ..... - 36 -
1.2.4 Instrumentation ..... - 37 -
Magnetic stimulators and pulse waveform ..... - 37 -
Coil design and optimization ..... - 38 -
1.2.5 Applications ..... - 39 -
Different effects of TMS ..... - 39 -
Clinical applications ..... - 40 -
Pathophysiology of movement disorders ..... - 41 -
Therapeutic applications ..... - 41 -
Basic brain research ..... - 42 -
Animal studies ..... - 43 -
1.2.6 Safety ..... - 43 -
Induction of seizures ..... - 43 -
Other side effects ..... - 43 -
1.3 THEORETICAL OVERVIEW OF NUMERICAL METHODS ..... - 44 -
1.3.1 Calculation of the electric field: the finite element method ..... - 44 -
Introduction ..... - 44 -
The method of weighted residuals ..... - 45 -
The finite element mesh ..... - 47 -
Numerical methods for solving large linear systems ..... - 50 -
1.3.2 Numerical methods for neuronal modelling ..... - 52 -
Active compartmental models of neurons ..... - 52 -
Integration methods for the cable equation ..... - 54 -

2 TMS OF DEEPLY LOCATED BRAIN REGIONS ..... - 59 -

2.1 INTRODUCTION AND OBJECTIVES ..... - 59 -
Problems when stimulating deep brain regions ..... - 59 -
Coil design optimization ..... - 61 -
External materials ..... - 62 -
Objectives ..... - 63 -
Published work ..... - 64 -
2.2 SIMPLE COIL DESIGNS: LOOP 1 AND LOOP 2 ..... - 64 -
2.2.1 Methods ..... - 64 -
Head and coil models ..... - 64 -
High permeability core models ..... - 65 -
Numerical calculations of the electric field ..... - 67 -
Calculation of coil inductance ..... - 68 -
Field focality ..... - 70 -
2.2.2 Results ..... - 71 -

Coil inductance - 71 -
Primary component of the electric field - 71 -
Secondary component of the electric field - 74 -
Total electric field - 76 -
Field focality - 79 -
2.2.3 Discussion - 81 -
Field induced by the loop 1 and 2 coil - 81 -
Effects of the use of ferromagnetic cores - 82 -
Model limitations - 83 -
2.3 A REALISTIC COIL MODEL: THE H1 COIL - 84 -
2.3.1 Methods - 84 -
Head and coil models - 84 -
High permeability core models - 86 -
Numerical calculations of the electric field - 86 -
Calculation of coil inductance - 87 -
Field focality - 87 -
2.3.2 Results - 88 -
Coil inductance - 88 -
Electric field distribution - 89 -
Field decay - 93 -
Field focality - 95 -
2.3.3 Discussion - 96 -
Field induced by the H1 coil - 96 -
Effects of the use of ferromagnetic cores - 96 -
Model limitations and future work - 98 -

3 FIELD – SINGLE NEURON INTERACTION IN TMS OF THE HUMAN MOTOR CORTEX - 101 -

3.1 INTRODUCTION AND OBJECTIVES - 101 -
Mechanisms of neuronal activation on TMS - 101 -
The human motor cortex - 104 -
TMS of the motor cortex - 106 -
Objectives - 109 -
Published work - 110 -
3.2 IMPORTANCE OF TISSUE HETEROGENEITY ON NEURONAL ACTIVATION DURING TMS - 111 -
3.2.1 Methods - 111 -
Volume conductor model and electric field calculation - 111 -
Calculation of the neuronal response to the induced electric field - 112 -
3.2.2 Results - 114 -
Electric field along the axon - 114 -
Axon's response to the applied electric field - 114 -
3.2.3 Discussion - 116 -
Influence of tissue heterogeneities on the induced electric field - 116 -
Stimulation thresholds - 116 -
Significance - 117 -
3.3 MODELLING TMS OF THE HUMAN MOTOR CORTEX - 118 -
3.3.1 Methods - 118 -
Sulcus model - 118 -
Temporal waveform of the electric field - 120 -
Types of neurons modelled - 121 -
Electrophysiological and morphological properties of the modelled neurons - 122 -
Numerical solution of the discretized cable equation - 123 -
3.3.2 Results - 123 -
Electric field along neurons - 123 -
Activation sites and mechanisms - 127 -
Influence of pulse waveform and current direction on activation thresholds - 129 -
Effects of tissue heterogeneities on activation sites and thresholds - 132 -
3.3.3 Discussion - 132 -
Mechanisms of stimulation and site of activation - 132 -
Interpretation of experimental results - 134 -
Model limitations and future work - 136 -

4 TMS OF SMALL ANIMALS - 139 -

4.1 INTRODUCTION AND OBJECTIVES - 139 -
Limitations of animal studies using rTMS - 139 -

Importance of coil size / brain size ratio - 140 -
Field focality - 141 -
Objectives - 142 -
Published work - 142 -
4.2 METHODS - 142 -
Mouse model - 142 -
Coil geometry and orientation - 143 -
Electric field calculation - 145 -
Assessment of coil performance - 146 -
4.3 RESULTS - 146 -
Distribution of the primary electric field - 146 -
Distribution of the total electric field - 147 -
Field's magnitude and decay along test lines - 150 -
Field's focality - 152 -
4.4 DISCUSSION - 155 -
Cause of the low induced electric field - 155 -
Performance of the different coil orientations - 157 -
Model limitations and future work - 158 -

5 CONCLUSIONS - 159 -

5.1 SUMMARY OF MAIN FINDINGS - 159 -
TMS of deeply located brain regions - 159 -
Field-single neuron interaction in TMS of the human motor cortex - 160 -
TMS of small animals - 161 -
5.2 LIMITATIONS OF THESE THEORETICAL MODELS - 162 -
Coil geometry - 162 -
Volume conductor geometry - 163 -
Dielectric properties of tissues - 164 -
Electrophysiological and morphological properties of neurons - 164 -
5.3 THE FUTURE OF NUMERICAL MODELLING IN TMS - 164 -

APPENDICES 167

A QUASISTATIC APPROXIMATION - 169 -

A.1 FORMAL DEFINITION OF THE QUASISTATIC APPROXIMATIONS - 169 -
A.2 GENERAL FORM OF THE EQUATIONS - 170 -
A.3 QUASISTATIC FORM OF THE EQUATIONS - 171 -

B VALIDATION OF NUMERICAL CALCULATIONS IN COMSOL - 173 -

B.1 COIL INDUCTANCE - 173 -
B.1.1 Introduction - 173 -
Inductance of circular loops - 173 -
Inductance of toroids - 174 -
B.1.2 Results - 174 -
Inductance of circular loops: influence of the radius of the coil - 174 -
Inductance of circular loops: influence of the radius of the wire - 178 -
Inductance of toroids - 178 -
B.1.3 Conclusions - 180 -

C ELECTROPHYSIOLOGICAL AND MORPHOLOGICAL PROPERTIES OF THE MODELLED NEURONS - 181 -

C.1 DISCRETIZED CABLE EQUATION - 181 -
C.2 AXON MODEL USED IN TISSUE HETEROGENEITY STUDY - 181 -
C.3 NEURON MODELS USED IN MOTOR CORTEX STUDY - 184 -

D VALIDATION OF NUMERICAL METHODS USED TO SOLVE THE DISCRETIZED CABLE EQUATION - 189 -

D.1 IMPLEMENTATION OF THE ALGORITHM IN MATLAB - 189 -
D.2 VALIDATION OF THE METHOD IMPLEMENTED IN MATLAB - 192 -
D.2.1 Introduction - 192 -
Comparison with NEURON - 192 -
D.2.2 Methods - 192 -
Specification of the model - 192 -
Implementation of the model in MatLab - 194 -

Implementation of the model in NEURON ..... - 195 -
D.2.3 Results ..... *- 196 -*
Comparison of stimulation thresholds ..... - 196 -
Comparison of the response of the transmembrane potential ..... - 199 -
Convergence rates ..... - 201 -
D.2.4 Conclusion ..... *- 202 -*

REFERENCES ..... - 203 -

Physical quantities

μ_0 : Magnetic permeability of free space ($4\pi \times 10^{-7}\, H/m$)

μ_r : Relative magnetic permeability of a medium

μ : Magnetic permeability of a medium ($\mu = \mu_0 \mu_r$, [μ]=*H/m*)

ε_0 : Electric permittivity of free space ($8.854 \times 10^{-12}\, F/m$)

ε_r : Relative electric permittivity of a medium

ε : Electric permittivity of a medium ($\varepsilon = \varepsilon_0 \varepsilon_r$, [ε]=*F/m*)

σ : Electric conductivity of a medium ([σ] = S/m)

ρ : Charge density ([ρ] = C / m^3)

f : Frequency ([f] = *Hz*)

w : Angular frequency ($w = 2\pi f$, [w]=*rad/s*)

L : Inductance ([L] = *H*)

C : Capacitance ([C] = *F*)

R : Resistance ([R] = Ω)

I : Current ([I] = *A*)

$\vec{E}$: Electric field ($[\vec{E}] = V/m$)

$\vec{D}$: Electric displacement field ($[\vec{D}] = C/m^2$)

$\vec{B}$: Magnetic field ($[\vec{B}] = T$)

$\vec{H}$: Magnetizing field ($[\vec{H}] = A/m$)

$\vec{J}$: Current density ($[\vec{J}] = A/m^2$)

ϕ : Scalar potential ($[\phi] = V$)

$\vec{A}$: Magnetic vector potential ($[\vec{A}] = T \cdot m$)

Symbols and abbreviations

AcPt: Action potential

aTES: Anodal Transcranial electric stimulation

CSF: Cerebrospinal fluid

CT: X-ray computed tomography

CTN: Corticospinal tract neuron

DLPFC: Dorsolateral prefrontal cortex

DV: Dorso-ventral

EEG: Electroencephalography

EMG: Electromyography

FEM: Finite element method

fMRI: Functional magnetic resonance imaging

GM: Grey matter

GMRES: Generalized minimum residual method

HPR: Half power region

LM: Latero-medial

LTD: Long term depression

LTP: Long term potentiation

M1: Primary motor cortex

MEP: Motor evoked potential

MRI: Magnetic resonance imaging

MSO: Maximum stimulator's output

PA/AP: Posterior-anterior / Anterior-posterior

PET: Positron emission tomography

PTN: Pyramidal tract neuron

RL/LR: Right to left / Left to right

RMT: Resting motor threshold

rTMS: Repetitive transcranial magnetic stimulation

SI /IS: Superior-inferior / Inferior-superior

TMS: Transcranial magnetic stimulation

WM: White matter

Abstract

In this work powerful numerical methods were used to study several problems that still remain unsolved in TMS.

The first problem that was studied is related to the difficulties that arise when stimulating sub-cortical deep regions with TMS, due to the fact that the induced field rapidly decays and loses focality with depth. This study's approach to overcome this difficulty was to combine ferromagnetic cores with a coil designed to induce an electric field that decays slowly. The efficacy of this approach was tested by using the FEM to calculate the field induced by this coil / core design in a realistically shaped head model. The results show that the core might make this coil even more suited for deep brain stimulation.

The second problem that was tackled is related to the lack of knowledge about the dominant mechanisms through which the induced electric field excites neurons in TMS. In this work the electric field along lines, representing trajectories of actual cortical neurons, was calculated using the FEM. The neurons were embedded in a realistically shaped sulcus model, with a figure-8 coil placed above the model. The electric field was then incorporated into the cable equation. The solution of the latter allowed the determination of the site and threshold of activation of the neurons. The results highlight the importance of axonal terminations and bends and tissue heterogeneities on stimulation of neurons.

The third problem that was studied concerns TMS of small animals and the lack of knowledge about the optimal geometry, size and orientation of the used coils. This was studied by using the FEM to calculate the electric field induced in a realistically shaped mouse model by several commercially available coils. The results showed that the smaller coils induced fields with higher magnitude, better focality, and smaller decay than the bigger coils.

These results highlight the importance of numerical modelling in TMS, either in coil design, determination of basic neurophysiologic mechanisms or optimization of experimental procedures.

Keywords: Transcranial magnetic stimulation (TMS); Finite element method (FEM); Numerical modelling; Neuronal modelling; Volume conductor modelling.

Resumo

A estimulação magnética transcraniana (TMS, do inglês *Transcranial magnetic stimulation*) é uma técnica de estimulação neuronal não-invasiva cujo princípio de funcionamento se baseia na lei de Faraday. Esta última estabelece que um campo magnético variável no tempo induz um campo eléctrico. Em TMS, o campo magnético é criado pela descarga rápida de uma elevada corrente através de uma bobina localizada próximo da zona que se pretende estimular. Por sua vez este campo induz um campo eléctrico, como estabelecido pela lei de Faraday. O campo eléctrico induzido em TMS coloca as cargas presentes nos meios intra e extracelular em movimento coerente o que, sob certas condições, provoca alterações no potencial de membrana dos neurónios afectados pelo estímulo, o que pode levar à geração de potenciais de acção. Dependendo da zona afectada pelo estímulo, a TMS pode dar origem a respostas fisiológicas diferentes, como contracções musculares no caso de estimulação do córtex motor. Têm também sido propostas várias possíveis aplicações terapêuticas desta forma de estimulação.

Desde a primeira aplicação com sucesso de TMS para estimular o córtex motor, atribuída a Anthony T. Barker em 1985, tem-se assistido a uma melhoria substancial do conhecimento acerca dos mecanismos físicos e fisiológicos subjacentes à técnica. Aliado a isso tem-se verificado uma optimização a nível de instrumentação, tanto no desenho dos estimuladores magnéticos como das bobinas de estimulação. No entanto, ainda subsistem limitações inerentes à TMS que permanecem por resolver, tanto a nível de instrumentação como a nível da compreensão dos mecanismos de funcionamento da técnica. O principal objectivo deste trabalho foi aplicar ferramentas de modelação numérica ao estudo de três problemas em aberto em TMS.

O primeiro problema que foi considerado relaciona-se com a estimulação de estruturas cerebrais sub-corticais localizadas profundamente. A estimulação destas estruturas tem-se tornado uma das áreas de investigação mais activas em TMS, uma vez que vários estudos apontam o seu papel nos mecanismos que medeiam a motivação e a recompensa, bem como nos mecanismos associados à depressão. No entanto, até à data, a TMS tem uma grande dificuldade em estimular regiões cerebrais profundas. A causa desta dificuldade prende-se com o facto da magnitude do campo induzido pelas bobinas tipicamente usadas, bobina circular e bobina em forma de oito, decair rapidamente com

a distância à bobina. Além disso, o campo tem também tendência a perder focalidade em regiões mais profundas, o que dificulta a estimulação precisa de uma dada região alvo. Nos últimos anos, os esforços têm-se focado no desenvolvimento de bobinas especialmente desenhadas para induzirem um campo que decai lentamente em profundidade. Um exemplo deste tipo de bobinas são as bobinas H, cujo formato faz com que estas induzam um campo que decai muito mais lentamente do que o induzido pelas bobinas usuais, mas à custa da focalidade do campo. Outros estudos têm apontado as vantagens da utilização de núcleos ferromagnéticos como forma de aumentar a magnitude do campo eléctrico e melhorar a sua focalidade. Estes núcleos, no entanto, têm até agora sido unicamente aplicados a bobinas com formatos tradicionais. Neste trabalho usou-se o método dos elementos finitos para estudar os efeitos da inclusão de núcleos ferromagnéticos numa das bobinas H, mais precisamente a bobina H1. Esta última foi desenhada para estimular estruturas localizadas sobre o hemisfério esquerdo em regiões pré-frontais dorso-laterais e ventro-laterais, com os neurónios orientados na direcção posterior-anterior, e estruturas localizadas em regiões pré-frontais mediais e orbitofrontais, com os neurónios alinhados preferencialmente ao longo da direcção lateral-medial. Numa primeira parte do trabalho foi criado um modelo da bobina H1, colocada sobre um modelo homogéneo e isotrópico de uma cabeça com um formato realista. Na segunda parte do trabalho usou-se o método dos elementos finitos para calcular o campo eléctrico induzido pela bobina H1 sobre o modelo realista da cabeça em três casos diferentes: bobina sem núcleos ferromagnéticos, bobina com um núcleo sobre o hemisfério esquerdo e bobina com um núcleo sobre a região frontal da cabeça. Em geral, a presença dos núcleos ferromagnéticos contribuiu para um aumento da magnitude da componente do campo eléctrico predominante na zona mais próxima do núcleo: posterior-anterior, no núcleo lateral, e lateral-medial, no núcleo frontal. Os núcleos também causaram um decréscimo do decaimento do campo ao longo do eixo superior-inferior. Contudo, o decaimento ao longo de outras direcções – direcção lateral-medial para o núcleo lateral e direcção anterior-posterior para o núcleo frontal – aumentou. Quanto à focalidade, a presença do núcleo frontal levou a uma diminuição da área estimulada, enquanto que o núcleo lateral aumentou a mesma. Os resultados sugerem que a presença dos núcleos pode melhorar algumas das propriedades do campo induzido pela bobina H1, tornando-a mais optimizada para estimulação de regiões localizadas profundamente. No entanto, face aos diferentes efeitos das duas posições

testadas para o núcleo, o posicionamento ideal terá sempre que levar em consideração a posição da região que se pretende estimular.

O segundo problema que foi estudado neste trabalho está relacionado com a falta de conhecimento acerca dos mecanismos precisos de interacção entre o campo eléctrico induzido em TMS e os neurónios. Estudos *in vivo* e *in vitro* têm ajudado a clarificar muitos dos possíveis mecanismos através dos quais o campo eléctrico estimula os neurónios. Regra geral esses estudos confirmam os resultados da teoria do cabo clássica que mostra que os neurónios são despolarizados (ficam com excesso intracelular de carga positiva) nas zonas onde é negativo o gradiente, ao longo do neurónio, da componente do campo induzido, na direcção do neurónio. Esses estudos também confirmam os resultados teóricos de que é possível obter estimulação mesmo em zonas onde o campo induzido é constante, desde que o neurónio termine ou dobre acentuadamente aí. Estes estudos, no entanto, não ajudam muito a clarificar os mecanismos dominantes no cérebro visto que, aí, os neurónios têm geometrias muito complexas e, como tal, existem muitos mecanismos possíveis de estimulação. Para tornar a situação ainda mais complexa, os resultados da estimulação dependem também da presença de heterogeneidades no meio condutor, que podem provocar variações muito rápidas no campo eléctrico ao longo dos neurónios, da orientação da bobina e da forma de onda do pulso de estimulação. Para ajudar a clarificar esta situação, neste trabalho criaram-se modelos diferentes de meios condutores que incluíam linhas representando as trajectórias aproximadas de neurónios. Em seguida, usou-se o método dos elementos finitos para calcular o campo eléctrico induzido ao longo desses neurónios por uma bobina em forma de oito. O campo eléctrico foi posteriormente usado na resolução de uma versão discretizada da equação do cabo, usando métodos numéricos apropriados. Num primeiro estudo, o volume condutor usado consistia apenas num paralelepípedo dividido em duas metades com condutividades eléctricas diferentes. O neurónio modelado nesse caso atravessava a interface de separação entre os dois meios e, como tal, o campo eléctrico ao longo do neurónio apresentava uma descontinuidade na zona da interface, devido à acumulação de carga que aí ocorre. Essa descontinuidade foi suficiente para estimular o neurónio com intensidades de estimulação dentro dos limites de funcionamento dos estimuladores magnéticos actuais. Num segundo estudo, construiu-se um modelo simplificado do sulco central e modelaram-se neurónios nesse modelo de sulco que se pensam serem relevantes para estimulação do córtex motor: neurónios piramidais do tracto cortico-espinhal,

interneurónios corticais e neurónios piramidais de associação. Os resultados mostraram que os neurónios modelados foram estimulados preferencialmente nas terminações axonais (interneurónios corticais) e nas dobras axonais (neurónios do tracto cortico-espinhal). Contrariamente ao sugerido no modelo inicial, a estimulação nunca ocorreu na zona onde os neurónios atravessaram a interface entre a matéria cinzenta e a matéria branca. No entanto, a descontinuidade do campo provocada por essa interface influenciou o limiar de estimulação. Nestes estudos o efeito da forma de onda do campo eléctrico induzido foi também contabilizado, sendo que os pulsos bifásicos conseguiram, regra geral, estimular os neurónios com limiares mais baixos do que os pulsos monofásicos. Estes resultados são consistentes com alguns resultados experimentais obtidos em estimulação do córtex motor em humanos e são úteis na previsão dos tipos de neurónios que são recrutados.

Por fim, o terceiro problema a ser considerado relacionou-se com a estimulação de pequenos animais recorrendo à TMS. Estudos envolvendo pequenos animais, especialmente roedores, têm sido usados para determinar os mecanismos neurofisiológicos da estimulação magnética. No entanto, estes resultados não podem ser imediatamente extrapolados para humanos, visto que os diferentes rácios entre o tamanho da bobina e o tamanho da cabeça levam a que os efeitos da estimulação sejam substancialmente diferentes. Outra dificuldade é a falta de consenso acerca da geometria, tamanho e orientação ideais para as bobinas usadas nestes estudos. Para clarificar esta situação, neste estudo usou-se o método dos elementos finitos para criar um modelo homogéneo e isotrópico de um rato com uma geometria realista. Em seguida calculou-se o campo eléctrico induzido por várias bobinas, baseadas em modelos comerciais, com diferentes geometrias, tamanhos e orientações. Os resultados mostraram que o campo resultante da acumulação de carga na interface entre a pele do rato e o ar diminuiu substancialmente o campo induzido pela bobina, além de aumentar o decréscimo em profundidade do campo. No que toca à focalidade do campo, analisada numa superfície representando o cérebro, esta melhorou muito devido ao campo causado pela acumulação de carga. Em termos da magnitude do campo induzido e do decaimento deste, as bobinas mais pequenas mostraram ser mais eficientes que as bobinas maiores. Estes resultados ajudam a prever procedimentos experimentais mais adequados para a estimulação de pequenos animais.

Os resultados obtidos nos três estudos efectuados mostram que técnicas de modelação numérica, como o método dos elementos finitos ou métodos de modelação de

neurónios, podem desempenhar um importante papel na optimização da instrumentação associada à TMS, no estudo dos mecanismos de interacção entre o campo e os neurónios e na optimização de procedimentos experimentais. O futuro da modelação numérica em TMS estará, então, assegurado e permitirá o desenvolvimento futuro da técnica, tanto no que toca a aplicações actuais como no que toca a possíveis aplicações futuras.

Palavras-chave: Estimulação magnética transcraniana (TMS, do inglês Transcranial magnetic stimulation); Método dos elementos finitos (FEM, do inglês Finite element method); Modelação numérica; Modelação neuronal; Modelação do volume condutor.

Acknowledgments

Believe it or not, but it is not easy to write a PhD thesis! It is essentially an individual work, in the sense that only one person is actually writing it, but it simply isn't possible without help from many other people. In this tiny space (only two pages) I will try to thank all the people that together made a huge contribution to this thesis.

My first words of acknowledgement go to my supervisor, Pedro Miranda, for all the support that he gave me in the last five years. He was the first to introduce me to the topic of magnetic stimulation and to the finite element method and to a number of fascinating topics that I will thoroughly discuss in the next 200 pages (give or take). More importantly than that, my supervisor is a person with whom it's very easy to get along with, which made working with him all this years a true pleasure. I would also like to thank him for the patience he had in reading work after work time after time...

I would also like to thank professor Eduardo Ducla-Soares, for it was him that first introduced me to the fascinating topic of Biophysics and Biomedical Engineering and guided my early studies in these fields. He also introduced me to IBEB and kept encouraging me through all this work.

Part with this work was developed in collaboration with Abraham Zangen and Yiftach Roth. I would like to thank their support and the availability for discussion that they showed. Another part of this work was developed in collaboration with Peter Basser, to who I would also like to thank for the speed he always demonstrated in answering our e-mails.

I must also thank my fellow colleagues, Paula and Sofia, who, together with me, walked this hard path. Sofia, like me, worked in modelling this amazing technique that is TMS, while Paula studied a vastly inferior and underpowered technique (tDCS or something like that…). However, they both deserve my most sincere acknowledgements for, if it weren't for them, this journey would've been a very lonely one. Curiously we all finished our thesis at about the same time, much to the dismay of our supervisor who had to read and review three thesis.

Working in IBEB has also been a fantastic experience. I say this not because of the building itself (although there's nothing wrong with it) and certainly not because of the surroundings (IBEB is close to an awfully looking football stadium), but because of the people that work there: Beatriz (for all the patience she had with me), Nuno Matela and

Nuno Oliveira (with whom I had some important football discussions), Sandra (who gave me some useful tips about writing my thesis), Susana and Mónica (whose devotion to work served as an inspiration to me), Mai Lu (who I bothered with countless questions about Chinese history), Abeye (who endured along with me the harsh trial of a vegetarian meal), Pedro Almeida (who encouraged me in a time when I was feeling down), Alexandre Andrade (with whom I had some interesting political discussions) and countless others. These people created a calming and relaxing environment that increased my productivity at least two-fold.

I also thank my closest friends who helped me take my mind out of research: Marco (my PIC burning buddy from my dark times at IST), Rodolfo, Sandro and Jorge (my fellow Tropical Sardines and some of the worst poker players the world has ever seen…) and Fábio (with whom I discussed important manga topics).

Por fim eu gostaria de agradecer à minha família. Foram os seus membros que me continuaram a empurrar para a frente, apoiando-me nos tempos difíceis. É claro que os meus pais foram quem mais me apoiou, dando-me apoio incondicional e acreditando sempre em mim em alturas em que nem eu acreditava... Não posso exprimir por palavras o quão importante o seu apoio foi para mim.

Vale-de-Marmelos, October 5th, 2009

Ricardo Nuno Bruno Forte Salvador

This work was funded by the Portuguese Foundation for Science of Technology under grant nº SFRH/BD/23537/2005. I would like to offer my sincere acknowledgments to FCT for this support. Without it, I and countless other students wouldn't have an opportunity to take our PhD courses.

1 Introduction

In this initial chapter the main objectives of this work will be presented. Additionally this chapter will also present a brief theoretical overview of transcranial magnetic stimulation (TMS) as well as of the most important numerical techniques used in this work.

1.1 Aim of the work

Since the first reported successful stimulation of a human subject with TMS (Barker and Jalinous, 1985), the number of applications of this technique has increased greatly. Nowadays, it is used in several cognitive studies and it is being tested for the treatment and diagnosis of a variety of diseases. Our understanding of the basic physical principles of this technique and of its physiological effects has also greatly evolved since the early days, which allowed for several optimizations, both in the instrumentation and in the experimental procedures. Despite this, there are still some problems regarding the application of TMS that remain unsolved and there is a lack of knowledge about some of the mechanisms through which it works.

One of the problems is the fact that TMS struggles to achieve stimulation of sub-cortical deep brain structures, because the field induced by the coils used nowadays rapidly decays and loses focality with increasing distance from the coil. This has become an active research topic in TMS, especially since the appearance of several recent studies that seem to indicate that stimulation of some deep structures may play a role in the study of reward and motivation mechanisms, as well as on the treatment of drug resistant depressions.

Another area that is still not well understood concerns the activation of neurons in TMS. Several possible stimulation mechanisms have been thoroughly studied, but the

dominant mechanisms for each type of neuron in the brain that is affected by a TMS pulse is still not well known. This impairs our understanding of the results obtained when stimulating some areas of the brain such as the motor cortex.

Finally, there is a lack of knowledge regarding the effects of TMS on small animals, such as mice. This stems from the fact that these animals have very different head sizes and geometries when compared to humans. Therefore, for the same size, geometry and orientation of the coil, the field induced in a human head can be very different from the field induced in the head of a small animal. This diminishes the usefulness of studies conducted in these animals, given that the results cannot be promptly extrapolated to humans.

It was this work's objective to study the three topics described above to try to increase the overall knowledge about the mechanisms through which TMS operates and to overcome some of its problems. To do so powerful numerical techniques were used to model the field induced during TMS and its effect on accurate models of neurons. The topics previously mentioned are discussed individually in three chapters of this thesis. Each chapter contains a detailed review of what is known about the topic it concerns, a description of the methods used to study the problem, and a summary of the main results that were obtained.

In the remainder of this chapter, a brief overview of TMS and of the numerical techniques used in this work will be presented. The objective of this brief introduction is to familiarize the reader with some important concepts that will become necessary in the following chapters.

1.2 Overview of transcranial magnetic stimulation

1.2.1 Basic principles and history

What is TMS?

TMS is a non-invasive brain stimulation technique that achieves stimulation by the rapid surge of a high current pulse through a coil located near the region of the brain to

be stimulated. According to Biot-Savart's law, the time-varying current flowing in the coil gives rise to a time-varying magnetic field[1]:

$$\vec{B}(\vec{r},t) = \frac{\mu_0}{4\pi} I(t) \oint_C \frac{d\vec{l} \times (\vec{r} - \vec{r}')}{\left|\vec{r} - \vec{r}'\right|^3} \qquad \textbf{1.2.1.1}$$

where μ_0 represents the magnetic permeability of free space, I the current that flows in the coil, $\vec{r}$ is the position vector of the point where the field is being calculated and $\vec{r}'$ is the position vector of the current point of integration along the coil. The integral is performed along the coil, in the direction of the current. With the magnetic stimulators used nowadays, the current in the coil can reach a value of more than 5 kA, giving rise to strong magnetic fields ranging from 1 - 4 T. The duration of the current and of the magnetic field is, however, very short, lasting less than 1 ms (Jalinous, 1998).

The time-varying magnetic field induces an electric field. This principle is known as Faraday's law of induction, and can be expressed mathematically by one of Maxwell's equations (Jackson, 1999):

$$\vec{\nabla} \times \vec{E} = -\frac{\partial \vec{B}}{\partial t} \qquad \textbf{1.2.1.2}$$

The electric field induced in TMS is very intense (typically 100 V/m in the brain, (Roth et al., 1991b)) and has the same duration as the magnetic field (less than 1 ms, (Jalinous, 1998)).

Even though the magnetic field gives its name to TMS, it is the induced electric field that leads to neuronal stimulation, by forcing the free charges in the intra and extracellular media of neurons into coherent motion, which may cause some of these neurons to become depolarized (excess of positive charge on the intracellular side of the membrane). If the depolarization reaches a given threshold the neurons can fire action potentials, which propagate to other neurons synaptically.

The TMS pulse can generate a number of different physiological responses according to the brain area over which the coil is placed over. One area often studied is the hand area of the motor cortex, the stimulation of which gives rise to contralateral hand muscle movements. However, TMS can also exert a temporary reversible disruptive effect on brain activity over a target area, which is called a "virtual lesion". One example of such a "virtual lesion" is the inhibition of perception of a given visual

[1] It is usually considered that $\vec{B}$ represents the magnetic flux density and not the magnetic field. The latter usually refers to $\vec{H}$. Throughout this work, however, the magnetic field will always be represented by $\vec{B}$, given that $\vec{B}$ is the most fundamental quantity (Jackson, 1999).

stimulus by a TMS pulse applied over the occipital cortex. It should not be inferred from these results that the effects of a TMS pulse are restricted to the stimulation site. Instead, studies that combine TMS with neuroimaging techniques such as functional magnetic resonance imaging (fMRI) (Bohning et al., 1998) or positron emission tomography (PET) (Paus et al., 1997), show that the effect propagates into connected and functionally coupled areas, including sub-cortical brain regions.

History of brain stimulation with electromagnetic fields

The history of TMS cannot be dissociated with the history of electromagnetism or bioelectric phenomena. The first reports (4000 B. C.) of bioelectric events come from ancient Egypt, and describe the catfish that, if caught by a fishermen's net would generate electric shocks forcing the fishermen to release the entire catch. Much later (47 A. C.), the roman philosopher Scribonius Largus recommended the use of another electric fish, the torpedo fish, as a cure for headaches and arthritis. Despite these early observations, it was not until the late eighteenth century, with the works of Galvani, that the subject of bioelectricity started to develop as a quantitative subject. Galvani discovered that when touching with a charged scalpel on the exposed femoral nerve of a dissected frog, violent contractions were elicited at the frog's leg.

It was also around the late eighteenth century that the topic of electrostatics and magnetism underwent substantial development with the experiments of Cavendish (from 1771 to 1773) and Coulomb (published in 1785). In 1819, Oersted discovered that current flowing in a wire deflected a magnetic compass, and later, in 1831, Faraday noticed that when moving a coil through a stationary magnet, a current was induced in the coil, thus establishing that a changing magnetic field induced an electric field.

The first documented experiment of electrical brain stimulation was made in 1874 by Dr. Robert Bartholow, who injected current through two electrodes placed over the exposed dura of a patient. He discovered that current injection elicited contralateral limb movements.

Magnetic stimulation started developing as a subject in the late nineteenth century (1896), with the works of Jaques d'Arsonval who reported flickering visual sensations in a subject whose head was placed within a strong time-varying magnetic field. He called these visual sensations 'magnetophosphenes'. Unaware of d'Arsonval's work, Beer published in 1902 a paper also describing the induction of these

'magnetophosphenes' with a time-varying magnetic field. Soon after several researchers started to study the topic of 'magnetophosphenes' (see Figure 1.2.1.1 a), but it was not until 1946 with the work's of Walsh and Barlow, that the site of stimulation was identified as the retina and not the occipital cortex.

Stimulation of nerves with time-varying magnetic fields was demonstrated for the first time by Kolin et al. in 1959, using a frog's sciatic nerve. Later, in 1965, Bickford et al. were able to twitch skeletal muscles in intact rabbits, frogs and human subjects. In 1985, Barker and co-workers, working at the University of Sheffield, demonstrated a magnetic stimulator that was capable of achieving stimulation of the motor cortex of human subjects (Figure 1.2.1.1 b). They placed an excitation coil on the scalp over the motor cortex and recorded twitch muscle action potentials from the contralateral abductor digitii minimi using skin surface electrodes. From this first application of TMS, the potential clinical interest of this technique has continued to grow. This has leaded the Sheffield's group to introduce the technique to a number of manufacturers. TMS stimulators (Figure 1.2.1.1 c and d) are now commercialized worldwide by several companies, like Magstim (http://www.magstim.com), Magventure (http://www.magventure.com/) or Nexstim (http://www.nexstim.com/).

Figure 1.2.1.1: (a) One of the first devices used to investigate the induction of 'magnetophosphenes' by Silvanus P. Thompson in 1910; (b) The first magnetic stimulator developed by the Sheffield's group, attached to a circular coil; (c) and (d) Modern-day magnetic stimulators: Masgtim 200 stimulator and Magstim Rapid stimulator, respectively. Both stimulators are attached to a figure-8 coil (figures a and b taken from **http://www.scholarpedia.org**; figure c and d taken from **http://www.magstim.com**).

1.2.2 The electric field induced in TMS

Two sources of the electric field

As was already explained before, the time-varying current flowing through the coil gives rise to a time-varying magnetic field that, according to Faraday's law, induces an electric field. As the electric field is the one that leads to stimulation of neurons, it is important to determine the spatial and temporal variation of this field. To do so, it is convenient at this point to introduce the magnetic vector potential ($\vec{A}$), which relates to the magnetic field according to the expression:

$$\vec{B} = \vec{\nabla} \times \vec{A} \qquad \textbf{1.2.2.1}$$

Substituting 1.2.2.1 into Faraday's law (1.2.1.2) the following expression is obtained:

$$\vec{\nabla} \times \left(\vec{E} + \frac{\partial \vec{A}}{\partial t} \right) = 0$$

Because the curl of the gradient of a scalar function is zero (Jackson, 1999), the quantity within the curl in the previous expression can be written as a gradient of some scalar potential: $-\vec{\nabla}\phi$. Rearranging terms the following expression is obtained for the total electric field induced in the brain during TMS:

$$\vec{E} = -\frac{\partial \vec{A}}{\partial t} - \vec{\nabla}\phi \qquad \textbf{1.2.2.2}$$

Equation 1.2.2.2 expresses the electric field in terms of a magnetic vector potential and a scalar potential. Most importantly it shows that the electric field induced by TMS is the sum of a primary component ($-\partial\vec{A}/\partial t$) and a secondary component ($-\vec{\nabla}\phi$). Each of these components can be given a physical meaning.

The primary component is the field that would be induced by the coil in a uniform isotropic medium such as air, if no conductive medium (head) was present. Under a set of approximations valid for the frequency range used in TMS, this field component depends only on the geometry of the coil and on the temporal waveform of the current's time derivative.

The secondary component of the field results from charge accumulation at the boundaries that separate media with different electrical conductivities (e.g. the scalp / air interface or the white matter / grey matter interface). In order to understand why

charge accumulates at these interfaces consider that, at the latter, the normal component of the current density ($\vec{J}$) must be continuous (Jackson, 1999):

$$(\vec{J}_1 - \vec{J}_2).\vec{n} = 0 \qquad \textbf{1.2.2.3}$$

Recalling that for a conductive medium such as the brain, the current density is given by $\vec{J} = \sigma\vec{E}$, and that the primary component of the field is continuous across the interface (this field component depends only on the geometry of the coil), it is easily concluded that the only way to respect 1.2.2.3 is that charge accumulates at the interface. This charge accumulation will increase the electric field at the medium with lower electrical conductivity and decrease it at the medium with higher electrical conductivity. This is illustrated in Figure 1.2.2.1. It should also be noted that charge accumulation only occurs if the primary electric field has some component perpendicular to the interface. This can be inferred from 1.2.2.3, which only involves the normal component of the current density and, thus, of the electric field.

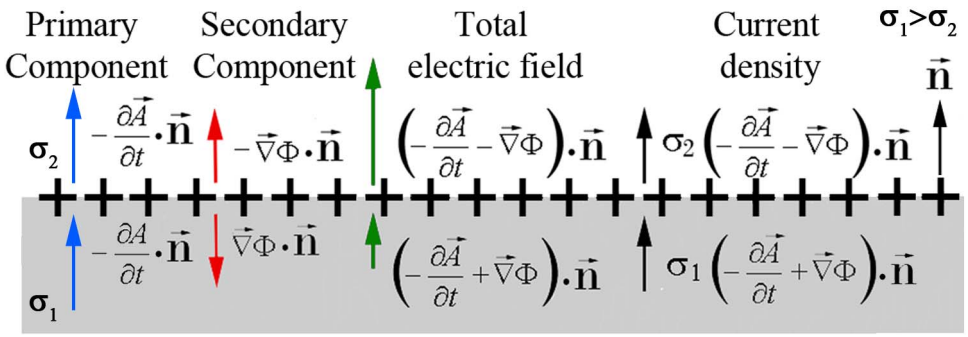

Figure 1.2.2.1: Charge accumulation at the interface between two media with different electrical conductivities: σ_1 for the grey medium (bottom half) and σ_2 for the white medium (top half). The size of the arrows is proportional to the value of the field's component normal to the interface. The primary field (blue arrow) is continuous across the interface, whereas the secondary field (red arrow) increases the electric field in the medium with smaller conductivity and decreases it in the medium with higher conductivity. As a consequence, the total electric field (green arrow) is discontinuous across the interface, but the normal component of the current density (black arrow) is continuous. In this particular example $\sigma_1 > \sigma_2$; if $\sigma_1 < \sigma_2$ charge accumulation at this interface would be negative.

The quasistatic approximation

From the previous discussion it follows that finding a solution for the total electric field induced in the brain during TMS is equivalent to finding a solution for both the scalar and magnetic vector potentials. This task is simplified by applying the quasistatic approximation (Plonsey and Heppner, 1967; Roth et al., 1991a; Heller and van

Hulsteyn, 1992), which is valid for the range of frequencies of TMS pulses, from DC to 10 kHz according to (Miranda et al., 2003), and for typical dielectric properties of brain tissues at those frequencies: σ = 1 S/m and ε_r = 10^4 (ε = 8.85×10^{-8} F/m) (Roth et al., 1991a).

The quasistatic approximation is actually a set of three approximations. The first approximation concerns propagations effects, which take into account the time required for changes in the source of a field (coil or charge in the tissue) to propagate to any other field point. In TMS, these propagation effects can be neglected if the wavelength of the electromagnetic field is much higher than the dimensions of the human head. Considering a value of 10 kHz for the frequency of a TMS pulse, the wavelength of the field in the brain, $\lambda = 1/\left(f\sqrt{\mu\varepsilon}\right)$, is of 300 m, a value much higher than any dimensions associated with the human body, which clearly demonstrates the validity of this approximation.

The second approximation consists in ignoring the capacitive effects of the brain tissue, considering the tissue essentially conductive. Under this approximation, the time that it takes for charge to accumulate at the boundaries between tissues with different conductivities is negligible. To check the validity of this approximation, Gauss's law ($\vec{\nabla}\cdot\vec{E} = \rho/\varepsilon$) can be combined together with the Continuity equation ($\vec{\nabla}\cdot\vec{J} = -\partial\rho/\partial t$) to show that, inside any tissue the charge density (ρ) decays exponentially with a time constant ε / σ. The ratio between this time constant and the duration of the stimulating pulse gives a measure of the validity of this approximation: if the ratio is small, charge accumulates at a much faster rate than the frequency of the stimulating pulse. Using the same values as before for the frequency and dielectric properties of brain tissues, the ratio between the two time constants is of the order of 10^{-3}, which proves that this approximation is valid.

The third and last approximation is to neglect skin-depth, i.e. the distance that fields can penetrate into tissues. In TMS, the externally applied magnetic field induces currents in brain tissues, which in turn induce their own magnetic field. These two sources of magnetic field tend to oppose each other, which causes the external field to decay as it penetrates into tissue. The distance along the tissue at which the field has already decayed to about *1/e* of the field at the surface is called skin-depth (Cheng, 1989) and is given by $1/\sqrt{\pi f\sigma\mu}$. Using the values already introduced, the skin-depth

for the field induced in TMS is of 5 m, which again proves the validity of this approximation.

Under the quasistatic approximation, finding solutions for the scalar and magnetic potentials reduces to solving Laplace's and Poisson's equations (Cheng, 1989) for the scalar and vector potential, respectively (see Appendix A for a detailed proof):

$$\nabla^2 \phi = 0 \qquad \textbf{1.2.2.4}$$

$$\nabla^2 \vec{A} = -\mu_0 \vec{J}_{coil} \qquad \textbf{1.2.2.5}$$

where $\vec{J}_{coil}$ refers to the current density in the stimulating coil. Equations 1.2.2.4 and 1.2.2.5 must be solved using the appropriate boundary conditions given by 1.2.2.3 and using the fact that the scalar potential must be continuous at the interfaces that separate media with different conductivities.

Laplace equation (1.2.2.4) is only valid for a homogeneous and isotropic medium. This is clearly not the case for the human head, because it contains several different kinds of tissues with different dielectric properties and because brain tissues also have anisotropic properties (Miranda et al., 2003). It is possible to generalize 1.2.2.4 so that it takes into account tissue anisotropy and heterogeneity (Miranda et al., 2003):

$$-\vec{\nabla} \cdot \left(\underline{\underline{\sigma}} \frac{\partial \vec{A}}{\partial t} \right) - \vec{\nabla} \cdot \left(\underline{\underline{\sigma}} \vec{\nabla} \phi \right) = 0 \qquad \textbf{1.2.2.6}$$

where $\underline{\underline{\sigma}}$ represents the electrical conductivity tensor.

Numerical modelling of the electric field

The spatial distribution of the primary component of the electric field can be determined by solving 1.2.2.5 and requires knowledge about the geometry of the coil. It is possible to show (Cheng, 1989) that a general solution of 1.2.2.5 is given by:

$$\vec{A}(\vec{r},t) = \frac{\mu_0}{4\pi} \int_{V'} \frac{\vec{J}_{coil}(\vec{r}',t)}{|\vec{r} - \vec{r}'|} dv' \qquad \textbf{1.2.2.7}$$

where the integration is performed along the coil's volume.

One way to calculate 1.2.2.7 is to represent each wire of the coil by a line (zero cross section) carrying a current *I* (Tofts, 1990; Grandori and Ravazzani, 1991; Roth et al., 1991a; Roth et al., 1991b; Miranda et al., 2003). Assuming this simplification, the volume integral in 1.2.2.7 reduces to a line integral around the coil:

$$\vec{A}(\vec{r},t) = \frac{\mu_0 I(t)}{4\pi} \int_{Coil} \frac{d\vec{l}}{|\vec{r} - \vec{r}'|} \qquad \textbf{1.2.2.8}$$

Equation 1.2.2.8 has been solved analytically for a circular loop, using elliptic integrals (Cheng, 1989; Jackson, 1999). This model is very useful because it can be applied to all coil geometries that are composed of circular loops. One important example of the latter is the figure-8 coil, which consists of two circular loops located side-by-side and carrying currents flowing in opposite directions (Ueno et al., 1988). Another method to calculate $\vec{A}$ that has been proposed (Roth et al., 1991a) is to approximate the coil by a polygon and sum the vector potential induced by each side of the polygon. It should be mentioned, however, that approximating the wire by a line causes errors in the calculation of the vector potential especially in superficial regions close to the coil (Salinas et al., 2007). More complex models take into account the complete three dimensional geometry of the coil, by dividing each wire into several filamentary loops and solving 1.2.2.8 for each of those loops.

Once the spatial distribution of the vector potential is known, the primary component of the electric field can be found by finding the negative first temporal derivative of 1.2.2.8. As the only term in 1.2.2.8 that has a temporal dependency is *I(t)* it can easily be deduced that the primary component of the electric field is proportional to the first temporal derivative of the current on the coil. This also applies to the secondary component of the electric field, because the magnitude of the latter is proportional to the magnitude of the primary component. The temporal waveform of the electric field induced in TMS will be discussed in more detail in the 'Instrumentation' section.

Figure 1.2.2.2 shows the norm of primary component (calculated using a theoretical expression, (Cheng, 1989; Jackson, 1999)) of the field for two coils traditionally used in TMS: the circular coil (a) and the figure-8 coil (b). The field is stronger under the coil windings and drops to zero in the centre of the loops and for regions far away from the coil. For the circular coil, the field only has an azimuthal component, whereas for the figure-8 coil, the field under the intersection of both sets of loops is oriented almost completely in the *y* direction. Under the figure-8 intersection, the field's magnitude is maximum and almost double of the field's magnitude under the circular coil.

Regarding the secondary component of the field, determining its spatial distribution requires solving Laplace's equation for the scalar potential, 1.2.2.4. Unlike the calculation of the primary component of the field, which only requires knowledge about

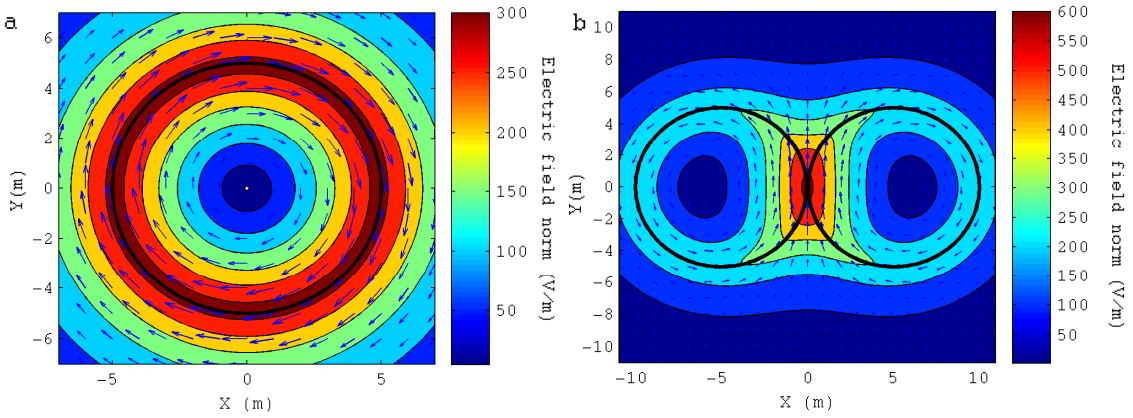

Figure 1.2.2.2**:** Norm of the primary component of the electric field induced by a circular coil (a) and by a figure-8 coil (b). The direction of the field is indicated by blue arrows. The coils are centred in the *xoy* plane and the figures show the field for a plane 1 cm below the coil. The circular coil has a radius of 5 cm and 9 loops. The figure-8 coil is composed of two circular coils with similar properties to the one in (a). The coils are located side-by-side, separated by a gap of 1 mm. The field's values were obtained for a fixed current's rate of change of 100 A/μs.

the geometry and orientation of the coil, for the calculation of the secondary component information about the geometry of the head and the dielectric properties of its different tissue types is also needed.

Initial studies performed with simple geometries (Tofts, 1990; Roth et al., 1991b; Eaton, 1992; Esselle and Stuchly, 1994) have all shown that the secondary component of the field greatly changes the total electric field. This is due to the fact that the secondary field reduces to zero the components of the total electric field perpendicular to the scalp's surface (Roth et al., 1991b). The secondary field also affects, however, other components of the total field and increases its decay. This secondary component of the field is, therefore, of crucial importance when optimizing coils to stimulate deep brain regions, as will be discussed in more detail in Chapter 2.

More recently, the advent of faster computers and powerful numerical methods, such as the finite element method (FEM), has enabled the use of more realistic head models (Starzynski et al., 2002; Wagner et al., 2004; Chen and Mogul, 2009) and the investigation of the effects of tissue anisotropy and heterogeneity on the electric field (Miranda et al., 2003; De Lucia et al., 2007).

1.2.3 Field-neuron interaction in TMS

Neuron's membrane properties

TMS stimulates neurons due to the force that the induced electric field exerts on the electric charges present both in the intra and extracellular medium. To understand why the charge movement leads to neuronal activation, it is necessary first to understand the basic properties of the neuron's membrane.

Neurons are very specialized cells of the nervous system. They are able to generate and propagate electrical signals, termed action potentials (AcPts). Patterns of these AcPts encode information within the nervous system. A neuron consists of a cell body or soma from which specialized processes called neurites arise (Figure 1.2.3.1). One of these processes is the axon, which usually conveys information away from the soma. The other processes are the dendrites, which transmit information to the soma. Axons have specialized endings, axon terminations, which come in close contact with regions of other neurons at synapses, where information is passed from one neuron to others. The axons of many neurons are covered by a myelin sheath except at regularly spaced gaps called Ranvier nodes. The myelin acts as an insulator and significantly increases the propagation speed of AcPts.

The ability of neurons to generate, propagate and transmit electrical signals is due to their highly specialized cell membrane. The latter contains ionic channels, which are transmembrane proteins that act as macromolecular pores in the cell membrane. These channels make the membrane permeable to ions that exist both in the intra and extracellular media, most significantly sodium (Na^+), potassium (K^+) and chloride (Cl^-) ions. At rest, the concentrations of these ions in the intra and extracellular media differ, the concentration of Na^+ ions being higher in the extracellular medium and that of K^+ ions being higher in the intracellular medium. Because the neurons' membrane is permeable to these ions, they tend to flow through it pushed by the concentration gradient. This diffusion of ions causes charges of opposite sign to accumulate in the outer and inner membrane's surface, which creates an electric field that influences the ionic charges diffusing through the membrane. If the cell membrane was permeable to only one ion, the voltage difference between the intra and extracellular cell membrane (transmembrane potential) would be such as to create an electric field that would oppose the diffusional forces. The membrane's voltage at which equilibrium is attained is called

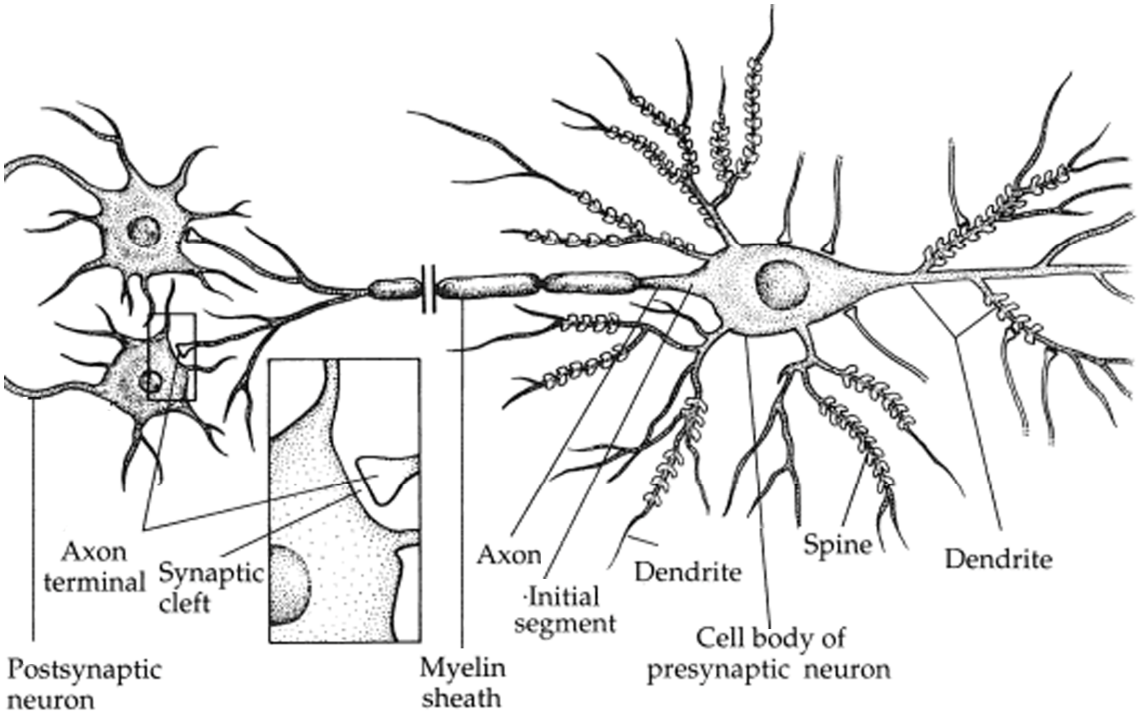

Figure 1.2.3.1: Schematic drawing of a neuron. This neuron receives input from several synapses at the cellular body and dendrites and establishes synapses with other neurons (postsynaptic neurons). The neuron has one axon and several dendrites. The unmyelinated first portion of the axon immediately after the cell body is called the initial segment. The dendrites have spines, which increase their synaptic area. (Adapted from (Martin, 1996)).

the Nernst potential. The values of the Nernst potential for each ionic specie differ from neuron to neuron, but they are usually of the order of -88 mV, for K^+ ion, and +61 mV, for the Na^+ ion (Malmivuo and Plonsey, 1995). A similar phenomenon happens in the cellular membrane of neurons, for which the resting transmembrane potential varies from neuron to neuron between -40 mV and -100 mV (Hille, 1992).

In addition to containing these ionic channels, the lipid bilayer of cellular membranes separates the internal and external conducting solutions by a thin insulating gap, thus acting as a capacitor.

Subthreshold and suprathreshold membrane response

When current is injected into a neuron, either artificially via intracellular electrodes or as a response to a signal from another neuron, some of it spreads intracellularly to other areas of the neuron, and some of it flows through the membrane. The membrane's current is the sum of two contributions: a capacitive term and an ionic term. The first one refers to charge that accumulates on both sides of the cellular membrane and charge

up the membrane's capacitor, whereas the second term refers to the current that goes through the membrane's ionic channels.

Early experiments have shown that depending on the magnitude of the injected current two different responses can be observed for the transmembrane potential. If the magnitude is below a given threshold, a subthreshold response is elicited, as shown in Figure 1.2.3.2. In this regime, the membrane acts as a parallel RC circuit, with the transmembrane potential initially increasing (depolarizing current pulse) / decreasing (hyperpolarizing current pulse) exponentially with time, reaching a given plateau and then, after the current stops being injected, decreasing also exponentially. This is a linear response, because the maximum value reached by the transmembrane potential has a linear relation with the magnitude of the injected current. In this regime, the ionic channels in the membrane can be modelled as resistors with a constant conductance.

When the magnitude of a depolarizing current pulse is equal to or greater than a given threshold, a suprathreshold membrane response - action potential - is elicited (Figure 1.2.3.3). AcPts are rapid membrane responses that maintain a constant waveform and magnitude and that propagate without attenuation along the axon, contrary to what happens in the linear response, which decays spatially with distance from the site of current injection. The mechanisms behind the generation and propagation of AcPts were studied for the first time in the squid's giant axon, but have been shown to apply to numerous other species and types of neurons. When the membrane depolarization reaches a given threshold, voltage gated sodium channels are activated, greatly increasing the permeability of the neuron to sodium ions, which enter the neuron pushed by the concentration gradient. This rapid sodium inflow accounts for the initial upstroke of the AcPt. Soon afterwards, the sodium channels start to become inactive thus decreasing the membrane's permeability to this ion again and preventing the transmembrane potential from increasing further. Moreover, voltage gated potassium channels reach full activation after the sodium channels do. This leads to an outflow of potassium ions, which repolarises the transmembrane potential to baseline. The sodium current that enters the axon in the initial phase of the AcPt depolarizes adjacent axonal areas thus initiating the process there, which explains why AcPts propagate along a neuron. From the above description, it can be deduced that in order to account for suprathreshold responses, the ionic channels cannot be modelled as linear resistors. Instead, in this case, the conductance of the channels must be modelled by non-linear

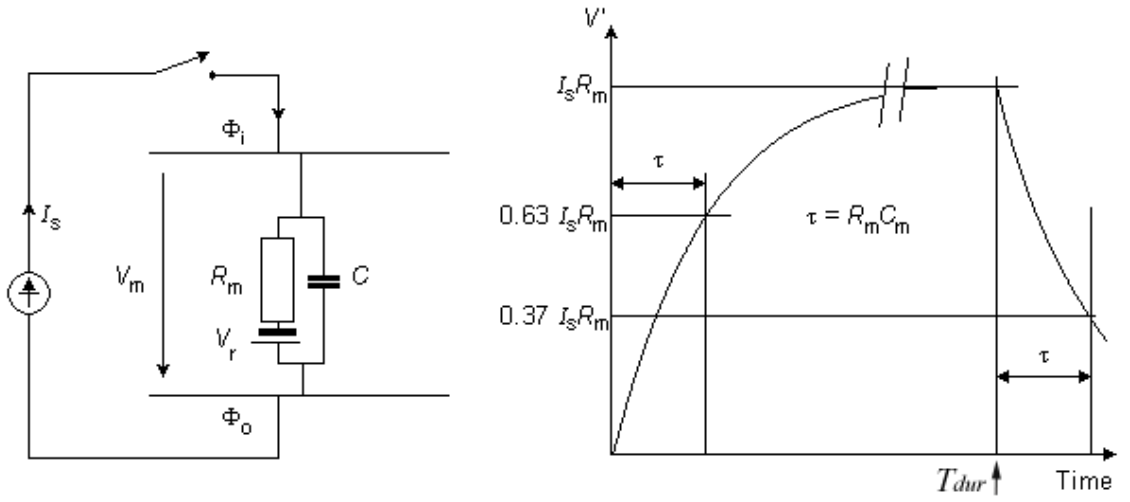

Figure 1.2.3.2: Passive response of a neuron's membrane. The figure in the left shows the electrical circuit equivalent to the membrane. *C* is the membrane's capacitance and R_m its ionic resistivity. The figure in the right shows the membrane's response to a square current pulse of magnitude I_s and duration T_{dur}. The transmembrane's potential initially increases exponentially with a time constant R_mC, reaches a constant value proportional to the injected current and then starts to decay exponentially after the current stops being injected. (Adapted from (Malmivuo and Plonsey, 1995)).

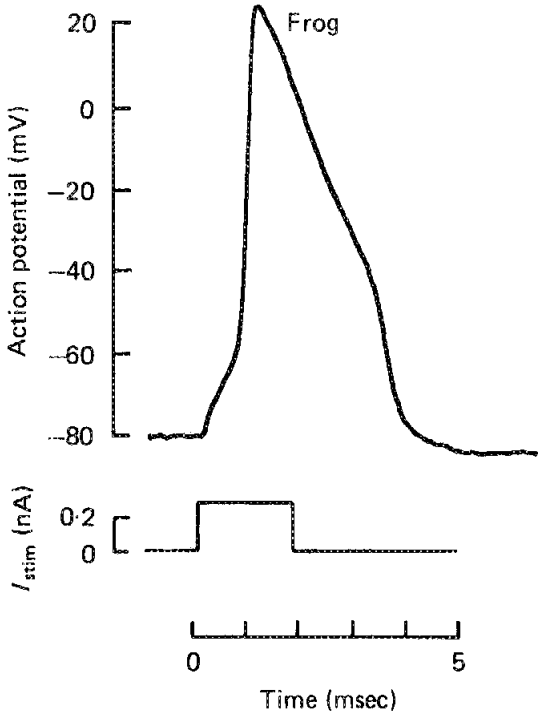

Figure 1.2.3.3: Action potential recorded in a Ranvier node of a frog's sciatic nerve at 14 ºC. The AcPt was elicited as a response to the square current stimulus shown below (Adapted from (Chiu et al., 1979)).

functions of the transmembrane potential.

Cable model and Cable equation

As was said before, the field induced in TMS influences the transmembrane potential. It is possible to quantify this interaction by assuming some simplifications, which will now be discussed. The first simplification is to consider that the neuron can be represented as a linear cylinder, representing the axon. This is not strictly necessary, for it is possible to extend this model to include the cellular body, dendrite, axon hillock and initial segment. Also, it is not necessary for the cylinder to be linear, as fibre tapering, bending and branching can all be taken into account. Other underlying simplifications of this model are (Roth and Basser, 1990): *(i)* to assume that the intracellular potential is only a function of the distance along the axon; *(ii)* to model the axoplasm as an Ohmic linear conductor with conductance G_a and *(iii)* to neglect the extracellular potential produced by the fibre's own activity. The latter have been shown to be good approximations and are very often used in the literature (Roth and Basser, 1990; Basser and Roth, 1991; Nagarajan et al., 1993).

Under the simplifications assumed before and considering the membrane properties discussed in the previous sections, the axon can be represented as the linear network shown in Figure 1.2.3.4. The latter representation assumes that the membrane has been divided into smaller sections and that the membrane properties within those sections remain constant. In the case of myelinated axons, which is considered here, each Ranvier node is represented by one section and the myelinated internodes are divided into several sections, depending on the spatial resolution required. In this model, the circuit representing the membrane at the myelinated internodes only accounts for linear responses (parallel RC circuit), whereas in the circuit that represents the membrane at Ranvier nodes active responses are taken into account by modelling voltage gated sodium and potassium channels.

In the model constructed thus far, the axial current between point x and $x+\Delta x$ of the discretized axon can be written as:

$$I_i(x+\Delta x) = G_a(V(x) - V(x+\Delta x)) + G_a \int_x^{x+\Delta x} E_x(s)ds \qquad \textbf{1.2.3.1}$$

where V represents the transmembrane potential.

In this expression, the first term on the right follows from Ohm's law and the second

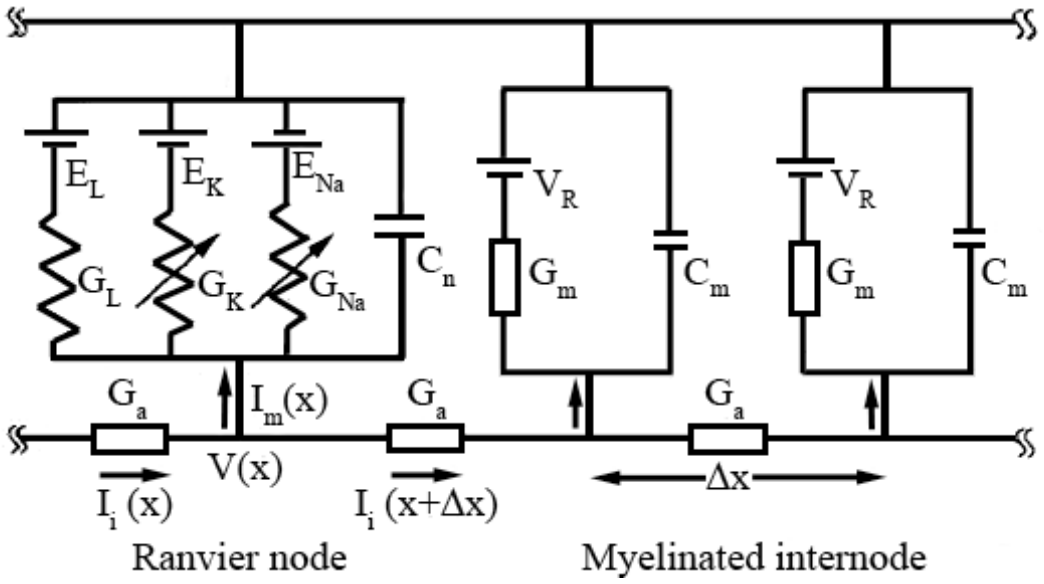

Figure 1.2.3.4: Electrical network representation of a myelinated nerve fibre. I_i represents the intracellular axial current, I_m the membrane current, Δx the length of the space step and G_a the total conductance of the intracellular medium. The membrane is represented by a capacitor (C_n and C_m, represent the total membrane capacitance at the Ranvier nodes and myelinated internodes, respectively) in parallel with several resistors, representing the ionic channels. The latter can have a constant conductance G_m in the myelinated internode sections or conductances that vary with the membrane's potential (G_K, G_{Na}) in Ranvier nodes. At the myelinated internodes, the battery in series with the resistors (V_R) represents the membrane resting potential. At the Ranvier node, the batteries represent the Nernst potential of sodium (E_{Na}), potassium (E_K) and leakage (E_L) currents.

term accounts for the effect of the field induced in TMS in the direction of the axon (E_x). The difference between the axial current that goes out of a given node and the current that goes into that node must be equal to the current that goes through the membrane, which is the sum of a capacitive component and an ionic current component:

$$I_m(x) = C_m \frac{dV(x)}{dt} + I_{ionic}(x) \qquad \textbf{1.2.3.2}$$

Hence, equating 1.2.3.2 to the difference between $I_i(x+\Delta x)$ and $I_i(x)$, given by 1.2.3.1, the following expression can be obtained (Nagarajan et al., 1993):

$$C_m \frac{dV(x)}{dt} + I_{ionic}(x) = G_a(V(x-\Delta x) - 2V(x) + V(x+\Delta x)) - G_a\left(\int_x^{x+\Delta x} E_x(s)ds - \int_{x-\Delta x}^{x} E_x(s)ds\right) \qquad \textbf{1.2.3.3}$$

The cable equation (1.2.3.3) is actually a set of equations, one for each point of the discretized axon. Finding its solution requires knowledge about the total applied electric field, $\vec{E}$, and about the membrane properties. In the case of suprathreshold membrane

models, this set of equations must be solved together with a set of equations that describe the behaviour of voltage gated ionic channels. Later on in this chapter several numerical algorithms suitable to solve these equations will be discussed.

In the case where only subthreshold membrane phenomena is of interest, taking the limit of 1.2.3.3 when $\Delta x \to 0$ yields the following alternative version of the cable equation (Roth and Basser, 1990):

$$\tau \frac{\partial V'}{\partial t} + V' - \lambda^2 \frac{\partial^2 V'}{\partial x^2} = -\lambda^2 \frac{\partial E_x}{\partial x} \qquad \textbf{1.2.3.4}$$

where V' is equal to the membrane's potential minus the membrane's resting potential and λ and τ are the space and time constants, respectively. It is possible to show (Malmivuo and Plonsey, 1995) that the space and time constants are a measure of the spatial and temporal decay of the polarization caused by a given subthreshold stimulus.

Rattay activation function for TMS

If the neuron is initially at rest, no ionic current flows through its membrane and the transmembrane potential remains constant along it. Therefore, the cable equation reduces to:

$$C_m \frac{dV(x)}{dt} = -G_a \left(\int_{x}^{x+\Delta x} E_x(s)ds - \int_{x-\Delta x}^{x} E_x(s)ds \right) \qquad \textbf{1.2.3.5}$$

From the last equation it can be seen that if the term on the right hand side is positive, then the membrane will become depolarized by the electric field. On the other hand, if the same term is negative, then the membrane will become hyperpolarized. Given its ability to predict the polarization produced by the electric field, the right hand side of equation 1.2.3.5 is known as the activation function (Rattay, 1986).

A more traditional way to write the activation function takes advantage of the approximate form of the cable equation 1.2.3.4 (Roth and Basser, 1990; Nagarajan et al., 1993):

$$S = -\lambda^2 \frac{\partial E_x}{\partial x} \qquad \textbf{1.2.3.6}$$

The activation function shows that the neuron's membrane will become depolarized by a TMS induced field when the spatial derivative of E_x in the direction of the neuron is negative. However, as will be discussed further in Chapter 3, membrane polarizations can be induced even in regions where the field is homogeneous, provided that the

neuron follows curved trajectories, bends or terminates abruptly. The latter enable stimulation of neurons at thresholds much lower than those required for stimulation by the gradient of the electric field induced by the coil.

1.2.4 Instrumentation

Magnetic stimulators and pulse waveform

Magnetic stimulators are devices capable of discharging a high current pulse through a coil in a short period of time. A simplified design of a magnetic stimulator is shown in Figure 1.2.4.1. The capacitor is charged by a DC high power supply (voltage V_C) and then its energy is discharged into the stimulating coil (inductance L). The resistance R represents the equivalent resistance of the capacitor, inductor and switches.

The resultant current waveform is usually a damped sine wave. The damping is caused by the resistance so, depending on its value, two different types of current waveforms can be created: monophasic (overdamped) waveforms and biphasic (underdamped) waveforms (Figure 1.2.4.2 a). Monophasic stimulators usually require an additional resistance in the circuit, in order to increase damping. The fact that more energy is dissipated in monophasic pulses than in biphasic pulses makes the latter more suitable for protocols where multiple stimulating pulses are applied in quick succession (repetitive transcranial magnetic stimulation, rTMS).

The terms monophasic and biphasic apply to the current in the coil but, in TMS, the induced electric field is proportional to the time derivative of the current in the coil. The waveform of *dI/dt* for monophasic pulses usually consists on an initial positive phase of high magnitude followed by a negative phase with much smaller magnitude (see Figure 1.2.4.2 b, full line). For biphasic pulses, *dI/dt* has three different phases with decreasing magnitudes and alternating polarities (Figure 1.2.4.2 b, dashed line). However, the magnitude of the peaks is not as heavily damped as for the monophasic pulses.

For all types of waveforms, the initial phase of the stimulating pulse (duration of the first phase of *dI/dt*) lasts for $t_p=T/4$, where $T \approx 2\pi\sqrt{LC}$ is the circuit's resonant period (Peterchev et al., 2008). Typical values of T range from 50 μs to 100 μs. The maximum magnitude of the current's time derivative - stimulator output - is given by V_C / L. Nowadays stimulators can achieve outputs of more than 100 A/μs.

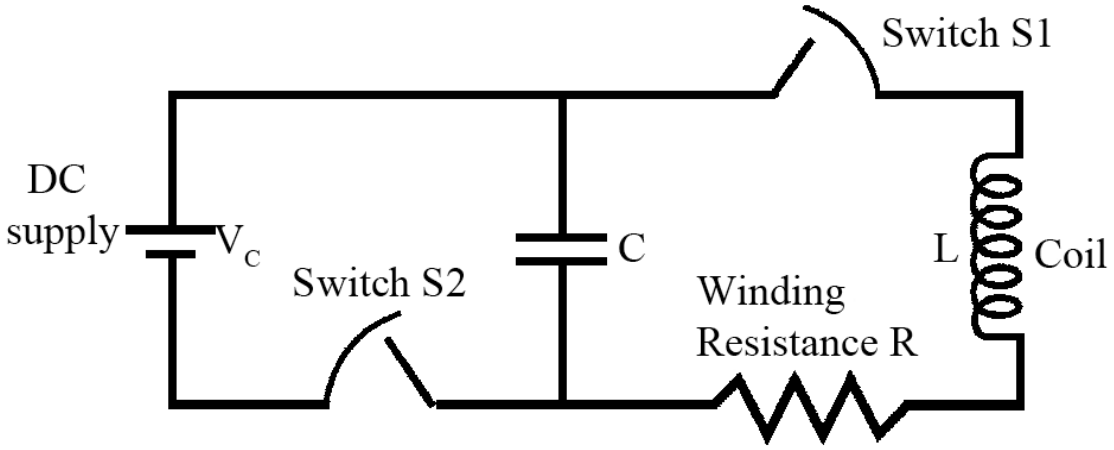

Figure 1.2.4.1: Simplified magnetic stimulator design. The DC power supply (V_C) charges a bank of capacitors (C), which then discharges through the coil L. The total resistance of the windings, capacitor and switches is represented by R. The switch $S1$ is in fact a thyristor, capable of switching a large current in a short period of time. (Adapted from (Davey and Epstein, 2000)).

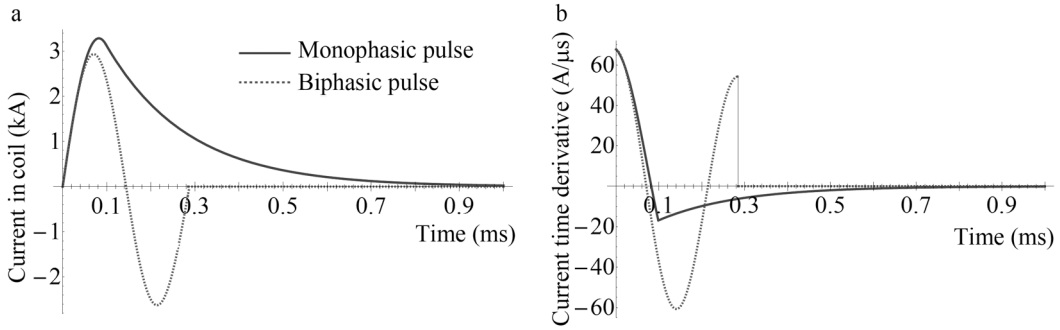

Figure 1.2.4.2: Coil current waveforms (a) and their time derivatives (b) for monophasic and biphasic pulses. The terms monophasic and biphasic refer to the current waveform. The current time derivative is biphasic, for the monophasic current pulse, and triphasic, for the biphasic current pulse. The waveforms shown correspond to a capacitor's charging voltage of 1107 V and a coil inductance of 16.35 μH, which yields a maximum value of 67 A/μs for the current's time derivative.

Coil design and optimization

Coils used in TMS must be carefully designed so that they are able to stimulate a target brain region without posing safety risks to both the subject and the technician handling it, and without damaging the magnetic stimulator they are plugged into. Unfortunately, no perfect coils exist and the design of an efficient coil for TMS is a complex process requiring several tradeoffs between coil design parameters.

In order to efficiently stimulate a target brain region, coils must induce a sufficiently high electric field in a target brain region. Additionally, the field must be localized

enough, so that only the target regions are affected by the stimulus, and must not decay significantly with depth, thus allowing for deeply located brain regions to be stimulated without inducing high fields at superficial regions. This will be discussed in more detail in Chapter 2, when discussing coil optimization for stimulation of deeply located brain regions.

Coils should also be efficient, in a sense that they should allow for stimulation without requiring very high currents flowing through it. A very high current will increase substantially the temperature of the coil (Ruohonen et al., 1997) a situation which is especially problematic in rTMS. Coil heating poses safety risks to the subjects, as the coil is in close contact with the scalp. To solve this, many coil manufacturers provide their coils with cooling mechanisms (Ruohonen et al., 1997). Another problem that arises from excessively high currents is the fact the they increase the magnetic forces in the coil, which tend to deform the latter (Cohen and Cuffin, 1991).

Finally, another important parameter of a coil is its inductance. If a coil has a very small inductance (typically under 10 μH) it cannot be directly plugged into a magnetic stimulator, as it can damage it. However, coils with very high inductances are not appropriate as well, given that they induce lower electric fields than coils with smaller inductances.

1.2.5 Applications

Different effects of TMS

The first application of TMS (Barker and Jalinous, 1985) was to stimulate the motor cortex of a healthy human subject. Nowadays, motor cortex stimulation studies continue to be one of the most common applications of TMS. The TMS pulse activates pyramidal neurons from the corticospinal tract, which synapse into motor neurons at the spinal cord. Motor neuron activation leads to a muscular contraction, which can be measured as an electrical signal by small needle electrodes inserted into the skin or by surface electrodes, a technique called electromyography (EMG) (Mills, 2005). The electrical signal recorded by EMG is called a motor evoked potential (MEP). It is of interest in many applications to measure parameters related to these MEPs, especially the threshold (intensity of the TMS stimulus needed to generate an MEP in a target muscle) and duration of the silent period (a pause in the ongoing EMG activity produced by TMS). Another measurement that is useful is the corticomotor conduction time, the time

that it takes the signal to propagate from the motor cortex to the motor neuron in the spinal cord. In Chapter 3 a thorough discussion about the mechanisms of MEP generation in TMS of the motor cortex will be presented.

Other experiments use paired-pulse paradigms to stimulate the motor cortex. In these experiments, two TMS pulses are applied, separated by a time delay of 1 – 200 ms (Di Lazzaro et al., 2008). The initial pulse is called the conditioning stimulus, whereas the second pulse is called the test stimulus. The outcome depends on the intensities of both stimuli and on the interval between them, ranging from a suppression of the MEP to an increase on the size of the MEP.

Developments in the design of magnetic stimulators have enabled the application of many stimuli at frequencies ranging from 1 Hz to 50 Hz: repetitive transcranial magnetic stimulation (rTMS). The range of applications of rTMS has increased greatly over the years, given that it can produce powerful effects that outlast the period of stimulation. One of these effects is that slow frequency rTMS (frequencies between 0.2 and 1 Hz) will cause a decrease in brain excitability, whereas high frequency rTMS (frequencies of 5 Hz or faster) will increase brain excitability[2]. These effects provide the basis to many of the therapeutic applications of rTMS as will be discussed further below.

Another useful property of either single pulse TMS and rTMS is their ability to temporarily disrupt the normal behaviour of a given cortical area, thus creating a 'virtual brain lesion' (Pascual-Leone et al., 2000). This enables investigators to establish the causal role and the timing of the contribution of a given cortical area to the behaviour or response under investigation.

Clinical applications

One important application of TMS is the diagnosis and assessment of the severity of multiple sclerosis using measures of the corticomotor conduction time. The latter is increased in multiple sclerosis due to the demyelinization of neurons in the corticospinal tract, which slows down propagation speed of nerve signals.

[2] In TMS, the stimulation threshold is used as a measure of brain excitability: a low threshold corresponds to a high excitability and vice-versa.

The chances of recovery after stroke can also be evaluated using TMS. In fact, it has been shown that when a patient is paralysed, the presence of a MEP indicates good chances of recovery, whereas the absence of a MEP indicates poor chances.

Another clinical application stems from the ability of rTMS to produce 'virtual lesions'. This has lead to the appearance of studies that test rTMS as an alternative to the Wada test when determining the cerebral dominance for language functions prior to surgery (Abou-Khalil, 2007). However rTMS is not as reliable as the Wada test.

Pathophysiology of movement disorders

TMS plays a major role in the study of the pathophysiology of many movement disorders, such as Parkinson's disease, corticobasal degeneration, Huntington's chorea, ataxias, among several others (for a complete review see (Cantello, 2002)). These pathologies induce changes in the characteristics of MEPs and on the results of paired-pulse paradigms. As there are some models for the mechanisms behind MEPs and the results of paired-pulse TMS, the abnormal results obtained with the disorders can be linked to specific problems in the central nervous system. This is useful to suggest possible courses of treatment.

Therapeutic applications

The major therapeutic applications of rTMS are in psychiatric disorders, especially major depression. The main target for stimulation in depression is the dorsolateral prefrontal cortex (DLPFC), because it is thought to be a part of a network of brain regions that regulates mood. This network includes other areas such as the prefrontal, cingulate, parietal and temporal cortical regions as well as parts of the striatum, thalamus and hypothalamus, but many of these are not accessible to TMS because the field it induces decays rapidly with increasing depth (Wassermann and Lisanby, 2001). Studies with high- and low-frequency rTMS over the DLPFC have revealed that rTMS does indeed have some anti-depressant effects, but that the latter depend highly on patient variables such as age and response to medication (Hallett, 2007). Up to date information about the optimal parameters for rTMS in depression (coil type and orientation, frequency of stimulation, intensity, duration of treatment) is still lacking. Improving the ability of coils to stimulate deeper structures in the brain may improve these results. This is the main motivation for Chapter 2 of this work, which deals with the optimization of coils to stimulate deep brain regions in TMS.

Another important application of rTMS is the treatment of patients with movement disorders such as Parkinson's disease (following the observation that rapid rate rTMS can speed up reaction times in these patients) and dystonia (low frequency rTMS can increase the level of intracortical inhibition lacking in these patients). These results, however, remain controversial, as it is often difficult to replicate results from important studies (Cantello, 2002).

Other more recent applications are to patients recovering from stroke, where high-frequency rTMS is applied to increase brain plasticity in the injured area of the brain, and to patients with epilepsy, where low-frequency rTMS might reduce the excessive brain activity in the epileptic area.

Basic brain research

The ability of TMS and rTMS to induce temporary 'virtual brain lesions' has been used in a series of studies where the performance of a subject in a given task is assessed both before and after disruption of activity by TMS / rTMS. If the disruption of the activity of the brain's area is accomplished with single pulse TMS, information about the timing at which the contribution of the disrupted area is important in a given task can be obtained. This is feasible due to the short duration of a TMS pulse, which results in a high temporal resolution ranging from 5 – 10 ms (Sack, 2006). In recent years, TMS induced virtual lesions have been used to investigate higher perceptual and cognitive abilities related to a variety of cortical areas. Examples of these include investigations into the role of parietal cortex in spatial attention and working memory; the role of the inferior frontal cortex in semantic and phonological word processing tasks; the role of motor and premotor areas during the anticipation of forces associated with object lifting, among several others (see (Pascual-Leone et al., 2000; Sack, 2006) for reviews).

The studies involving 'virtual lesions' must be interpreted with care though, given that multiple brain areas can be activated due to focal TMS / rTMS activation or due to the functional reorganization of the brain to compensate for the virtual lesion. To overcome these limitations, TMS has been combined with functional brain imaging techniques, such as electroencephalography (EEG) (Virtanen et al., 1999), PET (Paus et al., 1997) and fMRI (Bohning et al., 1998). These combinations have some technical difficulties,

due essentially to the high magnetic field induced during TMS. This requires that technical modifications be performed in the devices.

Animal studies

All the first initial studies involving TMS were done in humans. However, as many results were not well understood, the number of investigations in small animals, especially rodents, increased over the years. One of the major objective of these studies is to investigate the mechanism through which rTMS influences the brain, and thus provide a basis to understand many of its putative therapeutic effects. These studies have shown that rTMS has some striking effects on brain excitability, neurotransmitter systems and gene regulation in neurons (see (Lisanby and Belmaker, 2000) for a review). However, these results cannot be immediately extrapolated to humans, due to differences in coil size to head size ratio. This strongly diminishes the field induced in the heads of small animals (Weissman et al., 1992) and leads to a loss of focality of the induced field, which might result in a proportional bigger area of the brain to be excited in the small animal's head as compared to humans. This is the topic of Chapter 4 of this work, where these limitations will be discussed in more detail.

1.2.6 Safety

Induction of seizures

TMS is usually regarded as a safe technique, with not many reported cases of side-effects. By far, the most important adverse effect reported in TMS studies is the induction of epileptic seizures. This is more likely to occur when using high-frequency rTMS. The patients however, recovered well after the seizure, with no physical sequels. There have been also some reports of syncope (loss of consciousness). To prevent seizure induction in rTMS experiments safety guidelines have been developed, which suggest maximum frequency of stimulation as a function stimuli intensity (Wassermann, 1998).

Other side effects

One important safety parameter in TMS is coil temperature, given that the latter is located close to the subject's scalp. This limits the intensity and frequency of

application of the TMS pulse. Active cooling mechanisms applied to the coil diminish this problem.

Other studies also report a transient increase in auditory threshold after application of single-pulse TMS and rTMS (Pascual-Leone et al., 1993). This results from the intense, but brief, sound produced by the mechanical deformation of the stimulating coil. To prevent damage, foam earplugs are usually employed in single-pulse TMS and rTMS experiments.

Another well documented side-effect is the uncomfortable sensation (sometimes pain) felt by subjects due to stimulation of muscles and nerves near the stimulation coil. This sensation tends to increase with stimulation intensity.

Finally, care should be taken regarding the effects of the intense but brief magnetic field induced during TMS. Although the magnetic field by itself is thought to have no adverse effects, it can disrupt the electrical circuitry of devices such as pacemakers. Subjects with implanted metal devices should also not be stimulated by TMS, unless the magnetic and electric properties of the implanted metal are well known.

1.3 Theoretical overview of numerical methods

1.3.1 Calculation of the electric field: the finite element method

Introduction

The finite element method (FEM) is a powerful numerical technique for solving differential equations that describe a physical problem. In this work particularly, this method allowed for the calculation of the electric field induced by an arbitrarily shaped coil in a conductive medium.

Following (Zienkiewicz and Taylor, 2000), the FEM can be defined as a method to solve a continuum problem such that *(i)* the continuum is divided into several elements that are described by a number of parameters, and *(ii)* the solution of the complete system can be given by the assembly of its elements, which follows a standard set of rules. This last property makes the FEM amenable to computer implementation which in part explains the reason for its success.

From a formal point of view it will be considered that the problem to be solved can be described by a set of differential equations of the form:

$$\mathbf{A(u)} = \mathbf{0} \qquad \textbf{1.3.1.1}$$

where ***A*** is a column vector that contains all the differential equations that describe a given problem and **u** is the unknown scalar or vector function that satisfies the equations. The problem described by 1.3.1.1 is defined in a certain domain Ω, a volume or area, and on the boundaries of that domain, Γ, boundary conditions must be imposed in order to solve the problem. These are given by a new set of equations:

$$\mathbf{B(u)} = \mathbf{0} \qquad \textbf{1.3.1.2}$$

In the FEM, an approximate solution, $\hat{\mathbf{u}}$, for 1.3.1.1 is sought in the form of:

$$\mathbf{u} \approx \hat{\mathbf{u}} = \sum_{i=1}^{n} \mathbf{N}_i \mathbf{a}_i = \mathbf{Na} \qquad \textbf{1.3.1.3}$$

where $\mathbf{N_i}$ are known shape functions and $\mathbf{a_i}$ are parameters, most of which are unknown.

As will be discussed in more detail below, the discretization 1.3.1.3 allows casting the differential equations 1.3.1.1 as an equivalent system of linear equations of the form:

$$\mathbf{Ka} = \mathbf{f} \qquad \textbf{1.3.1.4}$$

where **K** is a matrix often referred to as the element stiffness matrix and **f** is a column vector, which is usually called the force vector. Inverting **K** makes it possible to find the parameters **a**, which yield an approximate solution ($\hat{\mathbf{u}}$) of the differential equation. The number of elements in the column vector **a** is the number of degrees of freedom of the problem, i.e. the number of parameters that must be determined in order to obtain the solution.

The method of weighted residuals

There are two FEM formulations: the method of weighted residuals and the method of determination of a variational functional. Here, only the first formulation will be introduced, given that it is the approach implemented in the FEM software package used in this work. In this formulation differential equations 1.3.1.1 and 1.3.1.2 are expressed in an equivalent integral form:

$$\int_{\Omega} \mathbf{v}^{\mathbf{T}} \mathbf{A(u)} d\Omega + \int_{\Gamma} \bar{\mathbf{v}}^{\mathbf{T}} \mathbf{B(u)} d\Gamma = \mathbf{0}, \forall_{\mathrm{v},\bar{\mathrm{v}}} \qquad \textbf{1.3.1.5}$$

that can be shown to be equivalent to equations 1.3.1.1 and 1.3.1.2. The variables $\mathbf{v}$ and $\bar{\mathbf{v}}$ are column vectors of arbitrary weighting functions defined in the domain of the problem. The only restriction imposed on the weighting functions is that they are bounded. Regarding the functions **u** it is additionally required that, if *n* is the maximum

order of the derivatives occurring in **A**, their *n-1* derivatives are continuous. This imposition is required so that the integral 1.3.1.5 yields a finite value.

It is often possible to perform integration by parts on 1.3.1.5 obtaining an alternative form of the equations:

$$\int_{\Omega} \mathbf{C(v)}^{\mathrm{T}} \mathbf{D(u)} d\Omega + \int_{\Gamma} \mathbf{E}(\overline{\mathbf{v}})^{\mathrm{T}} \mathbf{F(u)} d\Gamma = \mathbf{0}\,, \forall_{\mathrm{v},\overline{\mathrm{v}}} \qquad \textbf{1.3.1.6}$$

The operators **C**, **D**, **E** and **F** contain lower order derivatives than those occurring in 1.3.1.5 and, therefore, the integral form 1.3.1.6 is less restrictive, admitting functions **u** that have lower order continuous derivatives than required by 1.3.1.5. This is why equation 1.3.1.6 is called the weak form of equations 1.3.1.1 and 1.3.1.2.

In the method of weighted residuals, the weighting functions are written as:

$$\mathbf{v} = \sum_{\mathbf{j}=1}^{\mathbf{n}} \mathbf{w}_{\mathbf{j}} \delta \mathbf{a}_{\mathbf{j}} \quad \overline{\mathbf{v}} = \sum_{\mathbf{j}=1}^{\mathbf{n}} \overline{\mathbf{w}}_{\mathbf{j}} \delta \mathbf{a}_{\mathbf{j}} \qquad \textbf{1.3.1.7}$$

where $\delta\mathbf{a_j}$ are unknown parameters and $\mathbf{w_j}$ and $\overline{\mathbf{w}}_{\mathbf{j}}$ are known functions.

Inserting 1.3.1.7 into 1.3.1.5 the following expression is obtained:

$$\delta \mathbf{a}_{\mathbf{j}} \left[\int_{\Omega} \mathbf{w}_{\mathbf{j}}{}^{\mathrm{T}} \mathbf{A(Na)} d\Omega + \int_{\Gamma} \overline{\mathbf{w}}_{\mathbf{j}}{}^{\mathrm{T}} \mathbf{B(Na)} d\Gamma \right] = \mathbf{0}$$

where 1.3.1.3 has already been used to approximate **u**. Since the $\delta\mathbf{a_j}$ are arbitrary, the last expression yields the following set of equations to determine $\mathbf{a}_{\mathrm{i}}$:

$$\int_{\Omega} \mathbf{w}_{\mathbf{j}}{}^{\mathrm{T}} \mathbf{A(Na)} d\Omega + \int_{\Gamma} \overline{\mathbf{w}}_{\mathbf{j}}{}^{\mathrm{T}} \mathbf{B(Na)} d\Gamma = \mathbf{0},\ j = 1,...\mathrm{n} \qquad \textbf{1.3.1.8}$$

The weak form equivalent of 1.3.1.8 is given by:

$$\int_{\Omega} \mathbf{C}(\mathbf{w}_{\mathbf{j}})^{\mathrm{T}} \mathbf{D(Na)} d\Omega + \int_{\Gamma} \mathbf{E}(\overline{\mathbf{w}}_{\mathbf{j}})^{\mathrm{T}} \mathbf{F(Na)} d\Gamma = \mathbf{0}\,,\ j = 1,...,\mathrm{n} \qquad \textbf{1.3.1.9}$$

The name weighted residuals comes from the fact that **A(Na)** represents the residual of approximating **u** by 1.3.1.3, and therefore 1.3.1.8 is just the weighted integral of the residuals.

According to the choice of the functions $\mathbf{w_j}$ and $\overline{\mathbf{w}}_{\mathbf{j}}$, there are several different kinds of weighted residual methods. One commonly used is the Galerkin method, for which the weighting functions, $\mathbf{w_j}$ and $\overline{\mathbf{w}}_{\mathbf{j}}$, are the same as the shape functions, $\mathbf{N}_{\mathrm{j}}$.

In most cases, the operators **C**, **D**, **E** and **F** are linear operators, which means that 1.3.1.9 can be expressed as a linear system of equations of the form 1.3.1.4. The

Galerkin method often leads to a symmetric **K** matrix, which as a number of computational advantages, although this is not always the case.

The finite element mesh

One of the most useful features of the FEM is that the shape functions $\mathbf{N_i}$ are only defined locally for a subpart of the domain, which is called a finite element. The finite elements cover the entire domain of the problem, forming the finite element's mesh (see Figure 1.3.1.1). The advantage of defining these functions locally is that the integral 1.3.1.9 can be rewritten as:

$$\sum_{e=1}^{m}\left(\int_{\Omega^e}\mathbf{C}(\mathbf{N_j})^{\mathbf{T}}\mathbf{D}(\mathbf{Na})d\Omega+\int_{\Gamma^e}\mathbf{E}(\mathbf{N_j})^{\mathbf{T}}\mathbf{F}(\mathbf{Na})d\Gamma\right)=\mathbf{0}\,,\ j=1,...,\mathrm{n} \qquad \textbf{1.3.1.10}$$

where Ω^e is the domain of each element, Γ^e its part of the boundary and *m* is the total number of elements in the mesh. The integral form 1.3.1.10 allows building the matrix **K** from simpler matrices $\mathbf{k^e}$, a process known as assembly.

Within each finite element, the approximate solution $\hat{\mathbf{u}}$ can be given by an expansion similar to 1.3.1.3:

$$\mathbf{u}\approx\hat{\mathbf{u}}=\sum_{\mathbf{i=1}}^{\mathbf{n}}\mathbf{N_i}\mathbf{a_i}^{\mathbf{e}}=\mathbf{Na^e} \qquad \textbf{1.3.1.11}$$

where the superscript **e** indicates that the values $\mathbf{a^e}$ vary from element to element, and n is the number of nodes of each element. For linear elements, the latter correspond to the vertices of the element, but for higher order elements additional nodes are considered. The shape functions in the previous expansion must be chosen in such a way that, as the mesh is refined (the number of elements is increased) the approximate Galerkin solution converges to the exact solution. This requires that these functions obey a set of criteria (for a detailed discussion see (Hughes, 2000; Zienkiewicz and Taylor, 2000)).

One example of elements for which the convergence criteria hold, under certain circumstances, is the isoparametric element. To define these, an arbitrary quadrilateral element in $\Re^2$, illustrated in Figure 1.3.1.2, is considered. If the element is not too distorted (i.e. if the angles between the edges are less than 180º) it is possible to find a linear coordinate mapping from Ω^e, the element's domain in $\Re^2$, to a parent domain, □, in a space with coordinates $\boldsymbol{\xi}=(\xi,\eta)$ where the element can be represented by a biunit side square (also shown in Figure 1.3.1.2). For these elements, this mapping can

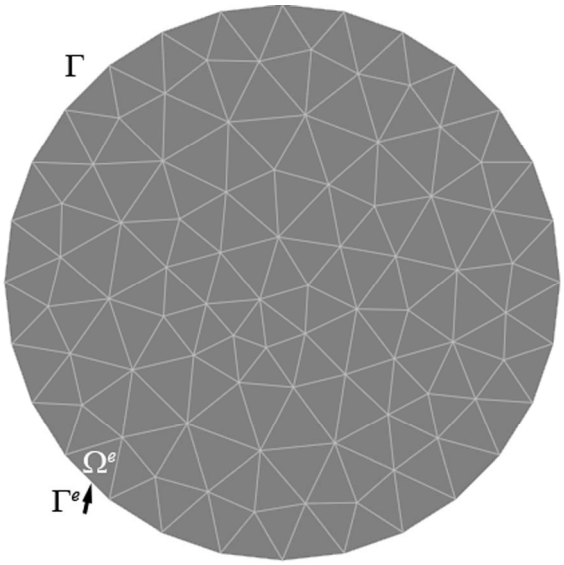

Figure 1.3.1.1: Finite element mesh of a unit circle in 2D. The mesh comprises triangular elements with domain Ω^e, which cover the entire circle.

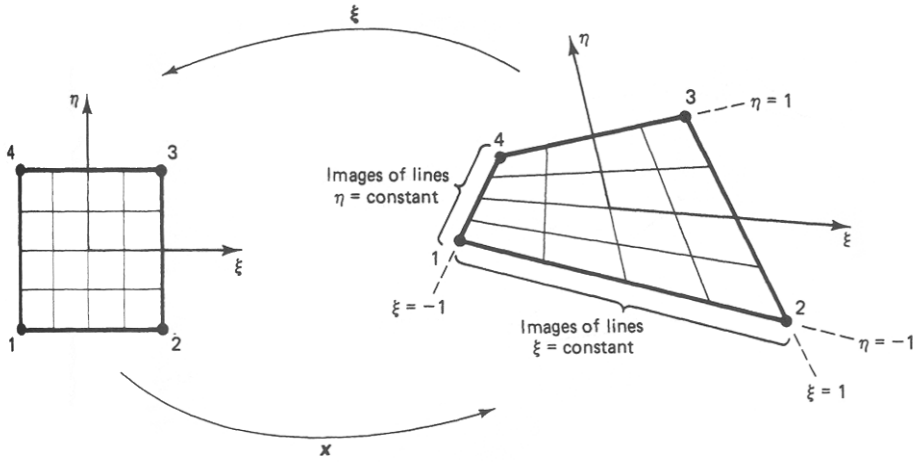

Figure 1.3.1.2: Mapping of an arbitrary 2D quadrilateral element (in the right) to the parent domain (shown in the left). In the parent domain, the element is represented as a biunit square. (Figure taken from (Hughes, 2000)).

be expressed as a linear combination of functions N_i, which can be used as shape functions in the expansion of the approximate solution in the finite element:

$$\hat{u}(\xi) = \sum_{a=1}^{4} N_a(\boldsymbol{\xi}) d_a^{\mathbf{e}} \qquad \textbf{1.3.1.12}$$

where it has been assumed, for simplicity, that u is a scalar function. For these linear elements, there is one shape function for each node (vertice) of the element. These functions are illustrated in Figure 1.3.1.3 for the case of the quadrilateral element.

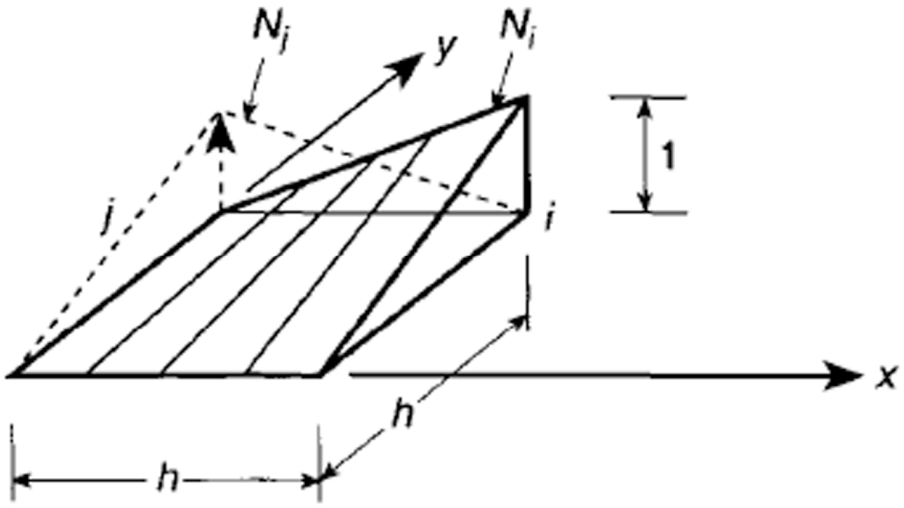

Figure 1.3.1.3: Linear interpolation functions for a square element in 2D. Each element node, *i*, is associated with one interpolation function, N_i, which has a unitary value at that node and is zero at all the other nodes. (Figure taken from (Zienkiewicz and Taylor, 2000)).

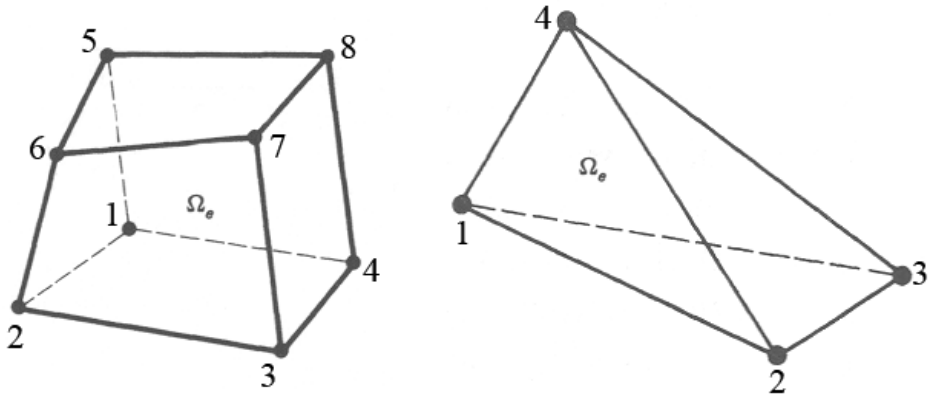

Figure 1.3.1.4: Linear hexahedron (left image) and tetrahedron (right image). The tetrahedron results from coalescing nodes in the hexahedron element. (Adapted from (Hughes, 2000)).

Coalescing nodes 3 and 4 of the biunit side square in ξ- space makes it possible to obtain triangular elements. These considerations can be generalized to 3D space, thus obtaining linear hexahedral elements and linear tetrahedral elements (see Figure 1.3.1.4). The latter are often used because of their ability to adapt to complex geometries.

The discussion until now has focused only on linear elements. However, it is possible to obtain higher order elements. These often provide a better approximation to the solution of the problem at the cost of an increased computational effort. For higher order elements, nodes are located not only on the vertices of elements, but also on their

edges and faces. For these elements, the shape functions can be calculated by multiplying Lagrange polynomials (Hughes, 2000), which is why these elements are also called Lagrange elements. The additional computational effort that these elements carry comes from the fact that the greater number of nodes in each element increases the degrees of freedom of the problem and, therefore, the size of the stiffness matrix **K**.

Another important family of finite elements, especially in electromagnetic applications, is that of the vector elements (also called curl elements). The need for this type of elements in electromagnetics stems from the fact that the boundary conditions for $\vec{E}$ or $\vec{H}$, i.e. that the tangential component of the field be continuous between media with different electric / magnetic properties (Jackson, 1999), are not naturally taken into account by the elements discussed thus far (Silvester and Ferrari, 1996). The vector elements solve this problem by attributing degrees of freedom to the edges of the elements. For tetrahedron elements, for instance, a vector trial function can be given by a linear combination of six edge element interpolation functions, $\boldsymbol{\tau}_{\mathbf{m}}$, which correspond to each of the six edges of the tetrahedron:

$$\hat{\mathbf{u}}(\xi) = \sum_{a=1}^{6} \boldsymbol{\tau}_{\mathbf{a}}(\xi) d_a^{\,\mathrm{e}} \qquad \textbf{1.3.1.13}$$

One common type of vector elements is the Nedelec-Bossavit edge elements family (Silvester and Ferrari, 1996), for which the edge element interpolation functions in the previous expansion are defined in such a way so that they are perpendicular to all edges of the element, except the one they represent. A graphical representation of these vector interpolation functions for the case of a 2D triangular element is shown in Figure 1.3.1.5. With this type of elements, the tangential components of the vector field are continuous across element boundaries. Another key aspect of these elements is that they can be used, in the same mesh, together with scalar Lagrange elements. This way, scalar elements can be used to describe a scalar variable (such as the scalar potential in TMS field calculations) and, at the same time, vector elements can be used to describe a vector variable (such as the magnetic vector potential).

Numerical methods for solving large linear systems

The FEM, especially in 3D modelling, often gives rise to a large system of linear equations in the form of 1.3.1.4. Direct methods for solving that set of equations are based on the factorization of the matrix **K** into easily invertible matrices. These methods

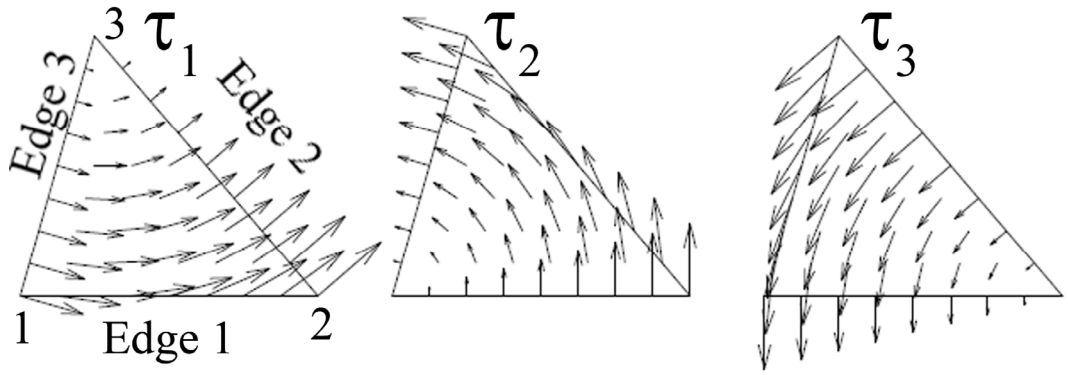

Figure 1.3.1.5: Linear vector interpolation functions for a triangular element in 2D. Each edge of the element (edge *i*), is associated with a vector function ($\boldsymbol{\tau}_i$). These vector functions only have a tangential component in the edge associated with each one of them. (Adapted from (Jacobsson, 2007)).

are very robust but they tend to require an amount of computational resources which scales poorly with the problem size. Other type of solvers, iterative solves, require less storage and fewer operations than direct methods, making them the only viable solution for very large systems.

Iterative system solvers successively approximate the solution, **a**, based on an initial guess, $\mathbf{a}^{(0)}$. For a stationary iterative method, this can be expressed as:

$$\mathbf{a}^{k+1} = \mathbf{T}\mathbf{a}^{k} + \mathbf{c}\,,\ k = 0,1,... \qquad \textbf{1.3.1.14}$$

where the *k*-iteration approximation of the solution, $\mathbf{a}^{k}$ is called the iterate, **T** is the iteration matrix and **c** is a vector. These methods are called stationary because the matrix **T** and the vector **c** are fixed. There are also nonstationary iterative methods, for which the computations involve information that changes at each iteration. Many of the latter methods are also called Krylov subspace methods. A detailed description of these methods is outside the scope of this work and can be found elsewhere (Barrett et al., 1993). One particularly relevant example of such a method is the generalized minimum residual (GMRES) method, which can be applied to any nonsymmetric linear system. The GMRES method needs an increasing amount of physical memory as the number of iterations grows. Therefore, a restart iteration, *m*, must be provided. When the iterations reach the number *m* the process restarts. These are called GMRES(m) methods and their convergence depends critically on the value chosen for *m*.

For iterative methods to converge, it is often required to precondition the system, which means transforming the original system into another system more amenable to being solved iteratively. A preconditioner is the matrix that does this transformation. One common set of preconditioning methods are the incomplete factorization methods

(also called incomplete LU methods). In these methods the preconditioner is given by $\mathbf{M} = \overline{\mathbf{L}}\,\overline{\mathbf{U}}$ where $\overline{\mathbf{L}}$ and $\overline{\mathbf{U}}$ are, respectively, lower and upper triangular matrices that are approximations of the LU factorization of the matrix **K**. The fact that approximate versions of **L** and **U** are used instead of the accurate LU decomposition, comes from the fact that usually the **L** and **U** matrices are less sparse than **K**, which makes them less suitable for numerical implementation. In incomplete LU, this problem is avoided by defining a relative drop-tolerance parameter, τ, which is used as a dropping criterion for inserting new elements in the matrices $\overline{\mathbf{L}}$ and $\overline{\mathbf{U}}$ (for details see, for instance, (Benzi, 2002)). The choice of the value for the drop-tolerance is essential for the convergence of this method: if the value is too small, convergence is fast but the method is not very memory efficient; if the value is too large many of the matrix elements are rejected, which reduces memory requirements but results in slower convergence.

An additional family of methods that will be discussed here are the geometric multigrid solvers / preconditioners. The multigrid algorithm uses one or several auxiliary coarser finite element meshes. Then, by performing some computations on the coarser meshes, fewer operations are needed to find the solution in the finer mesh. This iterative method is both fast and memory efficient (see (Comsol, 2008) for a more detailed overview of this methods).

1.3.2 Numerical methods for neuronal modelling

Active compartmental models of neurons

As was discussed above, the interaction between the electric field induced in TMS and the transmembrane potential is given, under some approximations, by the cable equation 1.2.3.3, which is reproduced here for the sake of convenience:

$$C_m \frac{dV(x)}{dt} + I_{ionic}(x) = G_a(V(x-\Delta x) - 2V(x) + V(x+\Delta x)) - G_a\left(\int_x^{x+\Delta x} E_x(s)ds - \int_{x-\Delta x}^{x} E_x(s)ds\right).$$

Intrinsic to this form of the cable equation is a spatial discretization of the neuron, where each portion of the membrane is given appropriate electrophysiological properties. One important parameter is the ionic current term, I_{ionic} which describes the current that goes through the membrane ionic channels. As was also discussed before,

there are two types of models used to describe this current: passive models and active models.

In the so-called passive models, the relation between the ionic current and the transmembrane potential is linear and can thus be represented by the following expression:

$$I_{ionic}(x) = \pi \Delta x d_i g_L (V(x) - V_r) \qquad \textbf{1.3.2.1}$$

where d_i is the section's diameter, Δx its length, g_L is the constant membrane conductance per unit area and V_r is the membrane's resting potential.

Active models for the ionic current describe more complex behaviour, such as the generation and propagation of actions potentials. Hence, the expression for I_{ionic} is far more complicated than 1.3.2.1. There are several mathematical descriptions available in the literature for this current, each based on electrophysiological studies performed with different neurons and different species, e.g. (Hodgkin et al., 1952; Frankenhaeuser and Huxley, 1964; Chiu et al., 1979). Here only one model will be discussed, which was also used in this work, c.f. Chapter 3. This model is based on human sensory fibres data (Wesselink et al., 1999). For this model, the expression for the ionic current term is given by:

$$\begin{aligned} I_{ionic}(x) = \pi d_i \Delta x [& g_{Na} m^3 h (V(x) - E_{Na}) + g_K n^4 (V(x) - E_K) \\ & + g_L (V(x) - E_L)] \end{aligned} \qquad \textbf{1.3.2.2}$$

where the terms inside the square brackets represent sodium, potassium and leakage current terms. The parameters g_{Na} and g_K are the maximum value of the membrane's conductance (per unit area) to sodium and potassium ions, respectively. The functions m, h and n are dimensionless variables which describe the behaviour of voltage gated sodium (m and h) and potassium (n) channels. The latter can be obtained by solving the following set of ordinary differential equations:

$$\begin{aligned} \frac{dm}{dt} &= \alpha_m (1 - m) - \beta_m m \\ \frac{dh}{dt} &= \alpha_h (1 - h) - \beta_h h \\ \frac{dn}{dt} &= \alpha_n (1 - n) - \beta_n n \end{aligned} \qquad \textbf{1.3.2.3}$$

The functions α and β in 1.3.2.3 depend on the transmembrane potential (see (Wesselink et al., 1999) for details).

Finding the temporal variation of the transmembrane potential for each compartment of the discretized neuron requires that *n* equations of the form of 1.2.3.3, one for each compartment, be solved. For active compartments 1.2.3.3 is coupled with equations 1.3.2.3. This requires that efficient numerical algorithms are employed for the solution (integration) of this coupled system of differential equations.

Integration methods for the cable equation

Integration methods for the cable equation all assume some kind of temporal discretization, which allows for the calculation of the transmembrane potential and the dimensionless gating variables (*m*, *h* and *n*) from a set of initial values. In most cases, it is assumed that the membrane is initially at rest (Roth and Basser, 1990), i.e.,

$$\begin{aligned} &V(x) = V_r \\ &\frac{dm}{dt} = \frac{dh}{dt} = \frac{dn}{dt} = 0, \quad t = 0 \end{aligned} \qquad \textbf{1.3.2.4}$$

The most obvious way to integrate the cable equation is to use the value of the ionic current at a previous time step to calculate the transmembrane potential at the new time step. This procedure, known as the forward Euler method, discretizes the cable equation in the following way (Mascagni, 1998):

$$\begin{aligned} C_m \frac{V^{t+1}(x) - V^t(x)}{\Delta t} + {I_{ionic}}^t(x) = G_a(V^t(x-\Delta x) - 2V^t(x) \\ + V^t(x+\Delta x)) - G_a\left(\int_x^{x+\Delta x} {E_x}^t(s)ds - \int_{x-\Delta x}^{x} {E_x}^t(s)ds\right) \end{aligned} \qquad \textbf{1.3.2.5}$$

where Δt is the temporal grid step and the upper index $t+1$ indicates that the variable is to be evaluated at time $t+\Delta t$, where t is the current time of integration. Equations 1.3.2.3 can be discretized in a similar manner:

$$\frac{\theta^{t+1}(x) - \theta^t(x)}{\Delta t} = \alpha_\theta(V^t(x))(1 - \theta^t(x)) - \beta_\theta(V^t(x))\theta^t(x). \qquad \textbf{1.3.2.6}$$

where θ represents any of the dimensionless gating variables. This method is very straight forward and easy to implement computationally, however it has been shown to be numerically unstable and inaccurate (Hines and Carnevale, 1997).

The forward Euler is known as an explicit method, because the calculation of the transmembrane potential at each time step only requires knowledge about the ionic current at the previous time step. There are also implicit methods, for which the solution of the potential at each time step requires knowledge about the ionic current at both the

new time step and the previous one. This methods are somewhat harder to implement computationally but are often more stable and accurate.

One example of such implicit methods is the backward Euler method. In this method, the discretization is such that the ionic current term on the left-hand side of 1.3.2.5 and all the terms on the right-hand side of 1.3.2.5 and 1.3.2.6 are evaluated at step *t+1* and not *t*. This set of equations is usually solved using an iterative procedure, known as Picard's iteration (Mascagni, 1998). This iterative method first estimates the solution to the transmembrane potential at the time step *t+1* by solving 1.3.2.5, as usually done in the forward Euler method. This estimate is then used in the backward Euler equivalent to equation 1.3.2.6, which yields estimates for the dimensionless variables *m*, *h* and *n* at the time step *t+1*. The updated values of *m*, *h* and *n* are then used to recalculate the transmembrane potential. This method continues until the values obtained for the transmembrane potential, and the dimensionless variables converges within a given tolerance value. This method has been shown to converge, provided that the temporal step is small enough. However it has also been shown to be inaccurate, i.e., the error due to the temporal discretization reduces slowly with decreasing temporal time step.

Another implicit method that is as stable as the backward Euler's method and more accurate is the Crank-Nicolson's method. In this method, the cable equation is discretized in the following way:

$$
\begin{aligned}
C_m \frac{V^{t+1}(x)-V^{t}(x)}{\Delta t} + \frac{I_{ionic}{}^{t}(x) + I_{ionic}{}^{t+1}(x)}{2} = \\
\frac{G_a}{2}\left(V^{t}(x-\Delta x) - 2V^{t}(x) + V^{t}(x+\Delta x)\right) \\
+ \frac{G_a}{2}\left(V^{t+1}(x-\Delta x) - 2V^{t+1}(x) + V^{t+1}(x+\Delta x)\right) \\
- \frac{G_a}{2}\left(\int_{x}^{x+\Delta x} E_x{}^{t}(s)ds - \int_{x-\Delta x}^{x} E_x{}^{t}(s)ds \right) \\
- \frac{G_a}{2}\left(\int_{x}^{x+\Delta x} E_x{}^{t+1}(s)ds - \int_{x-\Delta x}^{x} E_x{}^{t+1}(s)ds \right)
\end{aligned}
\qquad \textbf{1.3.2.7}
$$

From the previous equation it can be seen that the Crank Nicolson method simply averages the ionic current term and the axial current term (right hand side of the cable equation) at time steps *t* and *t+1*. This approach, however, has the downside that the solution for the ionic current term at the time step *t+1* requires knowledge about the transmembrane potential at the same time step, which is unknown. To solve this problem several iterative approaches have been employed which successfully

approximate the term $I_{ionic,n}^{t+1}$ until 1.3.2.7 is fulfilled (see (Cooley and Dodge, 1966) for a corrector-predictor approach to this problem). Another alternative approach has been devised (Hines, 1984) which avoids iteration of the non-linear equations. This is accomplished by staggering two temporal grids: one used to calculate the transmembrane potential and another one used to calculate *m*, *h* and *n*. The two time grids are shown in Figure 1.3.2.1. It is possible to show that, maintaining the same accuracy as in 1.3.2.7, the parameters of interest can be evaluated at the staggered grid using:

$$\begin{aligned} V^{t+\Delta t/2}(x) &= \frac{V^{t}(x)+V^{t+\Delta t}(x)}{2} \\ I_{ionic}{}^{t+\Delta t/2}(x) &= \frac{I_{ionic}{}^{t}(x)+I_{ionic}{}^{t+\Delta t}(x)}{2} \end{aligned} \qquad \textbf{1.3.2.8}$$

This expansion can be used in 1.3.2.7 yielding the following discretized version of the cable equation:

$$\begin{aligned} 2C_m\frac{V^{t+\Delta t/2}(x)-V^{t}(x)}{\Delta t}+I_{ionic}{}^{t+\Delta t/2}(x) &= \frac{G_a}{2}(V^{t+\Delta t/2}(x-\Delta x) \\ &-2V^{t+\Delta t/2}(x)+V^{t+\Delta t/2}(x+\Delta x)) \\ &-\frac{G_a}{2}\left(\int_{x}^{x+\Delta x}E_x{}^{t+\Delta t/2}(s)ds-\int_{x-\Delta x}^{x}E_x{}^{t+\Delta t/2}(s)ds\right) \end{aligned} \qquad \textbf{1.3.2.9}$$

The previous expression requires that the term $I_{ionic}{}^{t+\Delta t/2}$ be found, which only requires knowledge about the values of *m*, *h* and *n* at the staggered grid. The latter can be found using an appropriate discretization of the equations 1.3.2.3:

$$\begin{aligned} \frac{\theta^{t+\Delta t/2}(x)-\theta^{t-\Delta t/2}(x)}{\Delta t} &= \alpha_\theta(V^{t}(x)) \\ &-(\alpha_\theta(V^{t}(x))+\beta_\theta(V^{t}(x)))\frac{\theta^{t+\Delta t/2}(x)+\theta^{t-\Delta t/2}(x)}{2} \end{aligned} \qquad \textbf{1.3.2.10}$$

The previous expression can be used to calculate the term $I_{ionic}{}^{t+\Delta t/2}$ from the values of $m^{t+\Delta t/2}$, $h^{t+\Delta t/2}$ and $n^{t+\Delta t/2}$. The ionic current term is then used in equation 1.3.2.9 allowing for the calculation of the transmembrane potential at the staggered time grid, $V^{t+\Delta t/2}(x)$. Finally, the latter value is then substituted into 1.3.2.8 allowing for the calculation of $V^{t+\Delta t}(x)$. This method produces a $o(\Delta t^2)$ solution avoiding iteration of the equations (Hines and Carnevale, 1997).

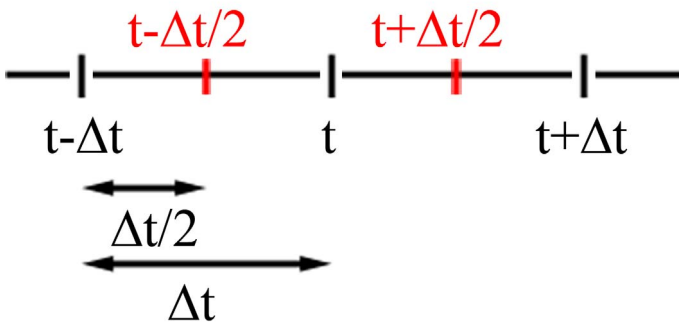

Figure 1.3.2.1: Staggered time grid used to solve the cable equation when discretized using Crank-Nicolson's method. The black markers indicate the main time grid, where the values of the transmembrane potential are meant to be determined. The red markers show the staggered grid, which is used to calculate the dimensionless variables *m*, *h* and *n*.

2 TMS of deeply located brain regions

TMS struggles to achieve stimulation of deeply located brain regions because the electric field induced by most coils decays rapidly and loses focality with increasing distance from the coil. In this chapter the effects of combining ferromagnetic cores with coils specifically designed to induce a field that decays slowly with depth are described. The cores increase the magnitude and focality of the field and decrease its decay with depth along certain directions, depending on the position of the core. These results suggest that the ferromagnetic cores make these coils more suitable for stimulation of deep brain regions.

2.1 Introduction and objectives

Problems when stimulating deep brain regions

As was discussed in the introductory chapter, TMS is a well established tool that allows for non-invasive stimulation of the brain. The effectiveness of TMS has been demonstrated when it is applied to stimulate cortical regions, most notably the motor cortex (Rothwell, 1997). More recently, interest in stimulating deeper sub-cortical structures has arisen, but the effectiveness of TMS in stimulating a given region drastically decreases with distance between the stimulating coil and the region to be stimulated. There are two causes for the decrease in efficiency when stimulating deep regions with TMS. The first one is the rapid decay with depth of the magnitude of the induced electric field, and the second one is the loss of focality of the field.

The rapid decay of the magnitude of the induced electric field is a well known feature of the conventionally used TMS coils, i.e. the circular and figure-8 coils, and it has been demonstrated by several numerical studies. Roth et al., for instance, (Roth et al., 1991b)

have shown that the magnitude of the field induced by a circular coil, with one of its sides placed over the vertex of a three-layered spherical head model, decreases approximately 50 % between the scalp's surface and the brain's surface, which corresponds to a distance of only 1.2 cm in their model (see Figure 2.1.1). To make matters worse, for any coil configuration, the field's maximum will always occur at the surface of the scalp (Heller and van Hulsteyn, 1992). Therefore, increasing the stimulator's output will increase the field both at the target region and at the scalp's surface. A very high electric field at the scalp can cause pain to the patient, associated with stimulation of nerves and muscles in the scalp. The only way to optimize stimulation of deep regions with TMS is, therefore, to decrease the decay of the field, i.e., to increase the ratio between the field at the target region and the field at the surface of the scalp.

The focality of the induced electric field is another important parameter in TMS, given that the spatial extension of the electric field is one of the factors that determine the structures that are stimulated. The field induced by many TMS coils has a large spatial extension and, therefore, poor focality (Hsu and Durand, 2001; Kim et al., 2006a). This situation is aggravated for regions further away from the coil, given that the spatial extent of the field increases.

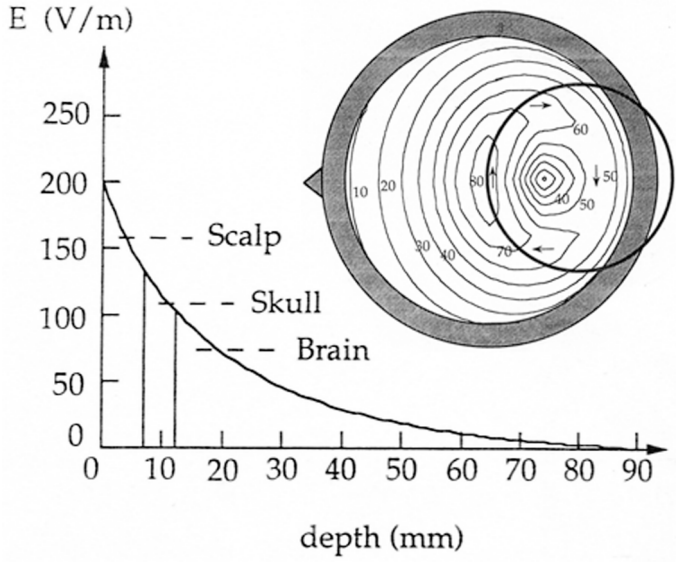

Figure 2.1.1: Decay of the magnitude of the electric field induced by a circular coil located over a three-layered spherical head model. The position of the coil with respect to the head is shown in the figure's inset. The coil has 8 turns and a 5 cm radius. The field values are for a stimulator output of 100 A/μs (Adapted from (Roth et al., 1991b)).

Coil design optimization

Many studies have shown that specific coil designs may improve some of the problems with conventional coils. One example of such a coil design, optimized to induce a field that decays slowly with depth, was introduced by Roth et al. (Roth et al., 2002). In that study three reasons are pointed out as the cause of the rapid decay of the induced field. The first reason is the spatial concentration of coil wires, which leads to a faster decay-rate of the field that they induce. In an optimized coil, the wires that induce field in the direction of interest should be scattered over the target region, thus leading to a deeper penetration of the induced field. The second reason is the proximity of return paths, i.e. wires carrying a current that induces a field in a direction opposite to the direction of stimulation. These wires should be placed away from the target region, given that the field that they induce reduces the field over the target region and contributes to a faster decay with depth. The third reason is the secondary field, which is created by the accumulation of charge at boundaries separating media with different electrical conductivities (c.f. Chapter 1, page 24 / 25). As was stated before, the secondary field significantly reduces the total electric field and contributes to its faster spatial decay. The most important contribution for this field is the charge that accumulates at the scalp/air interface. Charge accumulation at any boundary only occurs if the primary field has a non-zero component perpendicular to the boundary. Given that the primary field has a direction parallel to the wire that induces it, only coil wires perpendicular to the scalp lead to charge accumulation at the scalp/air interface. Therefore, these elements must be carefully located away from the target region as well. These three reasons led to design constraints that were used to build coils, termed H coils (Roth et al., 2002; Zangen et al., 2005; Roth et al., 2007) that induce a field that decays slowly with depth. There are several alternative designs for the H coils, as shown in Figure 2.1.2. One of these H coil designs, termed the H1 coil, will be thoroughly described later on. The ability of such coils to activate the motor cortex when placed at large distances above the scalp was shown to be better than that of standard coils (Zangen et al., 2005) and the safety and cognitive effects of these coils have been demonstrated in humans (Levkovitz et al., 2007). However, the focality of the H coils is not optimal, due to their large size, which leads to a wide spatial distribution of the induced field.

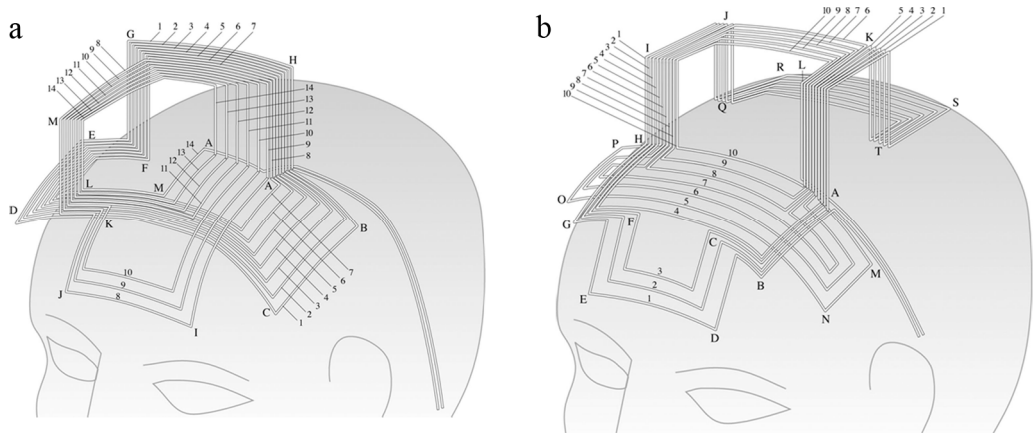

Figure 2.1.2: Geometry of H1 (a) and H2 (b) coils. The coils have the same design principles but were designed to stimulate different target regions: left prefrontal cortex for the H1 coil and medial orbitofrontal cortex for the H2 coil. (Adapted from (Roth et al., 2007)).

To improve the focality of the induced field, several alternative coil designs have also been proposed. One early design was the so-called slinky coil (Ren et al., 1995; Zimmermann and Simpson, 1996). The slinky coils, shown in Figure 2.1.3 a, can be thought as solenoids with N turns stretched into a semicircle, in such a way that the several turns are joined at a common point. Under the point where the turns are joined the induced field reaches its maximum and is very focal. However, given the high concentration of radial elements in that region, the field's decay increases. Another proposed design is the 3D differential coil (Hsu and Durand, 2001), which is shown in Figure 2.1.3 b. This coil uses coils placed perpendicularly to the plane containing a figure-8 coil to increase its focality. However, as happened with the slinky coil, the extra radial components affect the field's decay. Decreasing the size of the stimulation coil also contributes to a better focality however, as discussed before, that leads to several technical difficulties in building the coil due to increased mechanical stress and coil heating.

External materials

Another way of improving the characteristics of coils for deep brain stimulation is to use materials with special properties, such as ferromagnetic cores, copper sheets or mu-metal sheets.

Ferromagnetic cores are made from a material with a high magnetic permeability. When positioned close to a coil, they increase the magnetic field ($\vec{B}$) induced by the coil by a factor proportional to their relative magnetic permeability μ_r. Therefore

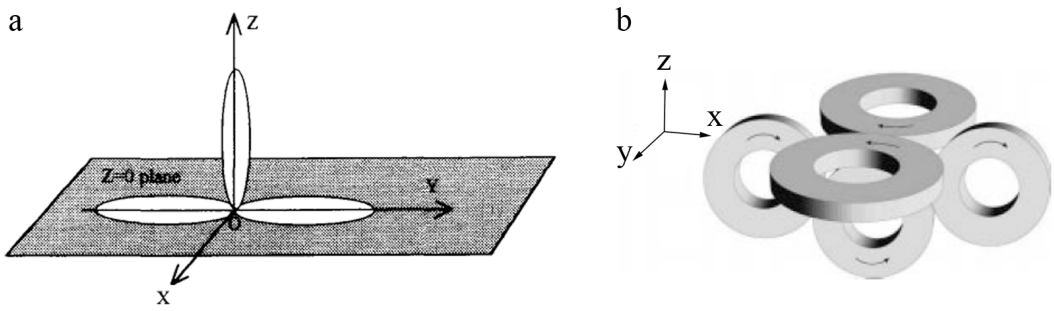

Figure 2.1.3: Schematic drawings of two coils designed to improve the field's focality: a slinky coil with three turns (a) and the 3D differential coil (b). (Adapted from (Ren et al., 1995) and (Hsu and Durand, 2001)).

ferromagnetic cores have been proposed to increase the magnitude of the electric field induced by the coils and to lessen its decay (Carbunaru and Durand, 2001; Epstein and Davey, 2002; Han et al., 2003).

Whereas the majority of studies have focused on the use of ferromagnetic cores, some groups have studied the effects of other materials. Copper sheets, for instance, have been considered as a possible way to improve the coil focality (Kim et al., 2006a), given that the high electrical conductivity of copper can effectively shield a given area from electric fields. However, the copper sheet decreases the magnitude of the field (Davey and Riehl, 2006; Kim et al., 2006a) and induces Joule heating (Davey and Riehl, 2006), making it unsuitable for application in studies involving humans. It has also been suggested to use mu-metal sheets to shield the electric and magnetic fields induced by return paths (Roth et al., 2002). Mu-metal is a material with very high electrical conductivity and permeability and, therefore, can effectively shield from electromagnetic fields.

Objectives

As was said before, many of the studies involving external materials study ferromagnetic cores and point them out as a possible way to make coil's more suitable for deep brain stimulation. However, until now, these studies all focused on combining ferromagnetic cores with conventional coil designs. In this work the advantages of combining these cores with the H coils were studied, to further improve their ability to stimulate deep brain regions. Given the complex geometry of the H coils, some preliminary investigations on simpler coils were initially performed. These simpler coils, termed loop 1 and loop 2, share many design principles with the more complex H

coils and, as such, provided a good starting point. Additionally this work was also extended to a more complex coil, termed the H1 coil, that was designed to stimulate deep dorsolateral and ventrolateral prefrontal cortical regions, with a preference for the left hemisphere and for neurons oriented in the PA direction, as well as more medial prefrontal and orbitofrontal cortices with preference for neurons oriented in the lateral-medial direction.

Published work

The work that is described in the following two sections originated one publication in an international peer-reviewed journal and a publication in a conference proceedings:

P1: Salvador R, Miranda PC, Roth Y, Zangen A High permeability cores to optimize the stimulation of deeply located brain regions using transcranial magnetic stimulation. Phys Med Biol 2009;54:3113-28.

Proc1: Salvador R, Miranda PC, Roth Y, Zangen A. High-permeability core coils for transcranial magnetic stimulation of deep brain regions. 29th Annual Conference of the Engineering in Medicine and Biology Society. Lyon, 2007:6653-6.

This proceeding's paper was presented orally at the 29th Annual IEEE EMBS conference.

2.2 Simple coil designs: loop 1 and loop 2

2.2.1 Methods

Head and coil models

The coil used in this part of the study is shown in Figure 2.2.1.1, placed over a spherical head model. The coil consists of two loops, termed loop 1 and loop 2, specially designed to induce a field that decays slowly with depth. The coil induces a strong field in the posterior-anterior (PA) direction (*x* axis in Figure 2.2.1.1) over the left hemisphere, due to wires 1 and 2, as well as in the right-left (RL) direction (*y* axis in Figure 2.2.1.1) over the head's front, due to wires 3 and 4. In order to decrease the

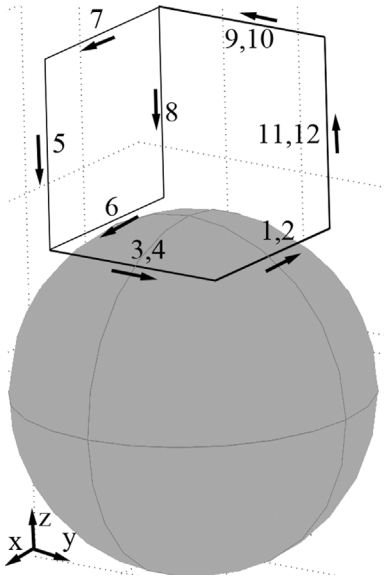

Figure 2.2.1.1: Loop 1 and 2 coil placed over a spherically shaped homogeneous head model. The coil comprises two loops. Loop 1 includes all odd numbered wires, whereas loop 2 includes all even numbered wires. All wires have a length of 10 cm. The arrows indicate the direction of the current in the coil in the positive going phase of the current stimulus. The spherical head model has a radius of 9.2 cm and is centred in the origin of the coordinate system used. In this model, the *x* axis points in the posterior-anterior (PA) direction, the *y* axis in the right-left (RL) direction and the *z* axis in the inferior-superior (IS) direction.

spatial decay of the induced field, wires predominantly radial to the head's surface (wires 5, 8, 11 and 12) are placed away from the target regions. Furthermore, the return paths are also located away from these regions, either away from the scalp (wires 7, 9 and 10) or close to it (wire 6). All wires have a length of 10 cm.

The head model used consisted in a spherical homogeneous and isotropic medium, with a radius of 9.2 cm, a model that has been used as an approximate representation of the human head in previous studies (Rush and Driscoll, 1968). The head was modelled with an electrical conductivity of 0.33 S/m and a relative dielectric permittivity of 10^4. These values are representative of the human brain tissue at the frequencies typically involved in TMS (<10 kHz) (Gabriel et al., 1996b; Goncalves et al., 2003).

High permeability core models

In this work, specially designed ferromagnetic cores were placed over loop 1 and 2, as shown in Figure 2.2.1.2. The c-shaped cores were created from cylinders, cut in such a way that the inner surface of the core follows the outer surface of the head model. The cores have a thickness of 9.5 cm and an angular opening of approximately 115º (angle

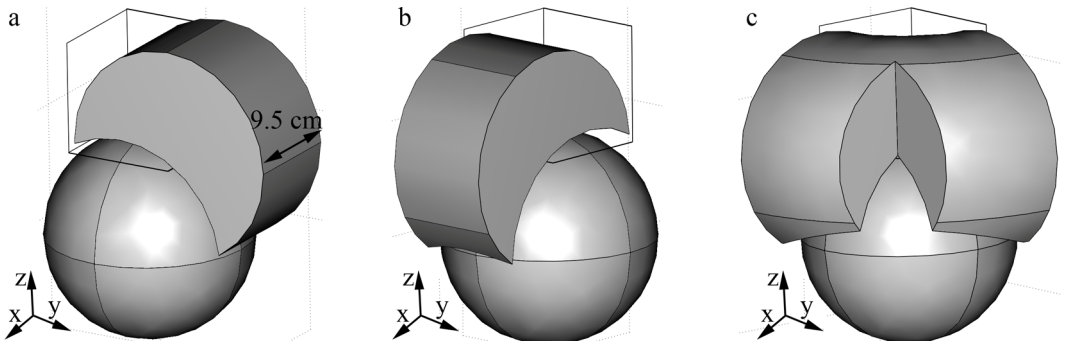

Figure 2.2.1.2: C-shaped ferromagnetic cores placed over the loop 1 and 2 coil. Three different models were created: (a) a lateral core model, where the core is placed over the left hemisphere; (b) a frontal core model, where the core is placed over the head's front; (c) a dual-core model, with a core that covers both the left hemisphere as well as the head's front.

between the two edges of the core). The distance between the inner surface of the core and the surface of the head is of 1.8 cm.

In order to test the effects of core position, three different core orientations were tested. In one model, shown in Figure 2.2.1.2 a, the core is placed over the left hemisphere, approximately centred over wires 1 and 2. In another model (Figure 2.2.1.2 b), the core is placed over the head's front, centred over wires 3 and 4. Finally, in a third model the core is designed to cover both the left hemisphere and the head's front (see Figure 2.2.1.2 c).

Creating an accurate model for the cores is a complex task, partly because the ferromagnetic cores used in TMS applications are laminated (Epstein and Davey, 2002). The purpose of this lamination is to reduce eddy currents losses; the thinner the laminations, the more pronounced the effect is. For such cores, the conductivity in a direction parallel to the laminations is much higher than the conductivity in a perpendicular direction (Silva et al., 1995). For the relative magnetic permeability, something similar happens, although the difference between the values in the parallel and perpendicular directions is much smaller (Silva et al., 1995). For this particular coil design, the core laminations should be perpendicular to the x or y axis, depending on whether the lateral or frontal cores are considered. This will strongly decrease the conductivity perpendicularly to the laminations, thereby decreasing the eddy current loss in the core induced by wires 1-2 (lateral core) and 3-4 (frontal core). In order to reduce computational needs, the cores were modelled as homogeneous and isotropic materials with a bulk electrical conductivity of 1 S/m (modelling the conductivity in directions perpendicular to the laminations) and a bulk magnetic permeability of $10^4 \mu_0$

(modelling the permeability in directions parallel to the laminations). This is a first approximation of the effects of the core on the field induced in the region of the head that is close to it: for the wires located near the core, the laminations will effectively reduce the conductivity while not changing much the magnetic permeability. The effects of these cores on the field induced by wires with different orientations relative to the direction of the laminations is not correctly accounted for by these homogeneous and isotropic core models. An example of this is the effect of the lateral core on the field induced by wires 3-4, or the effect of the frontal core on the field induced by wires 1-2. However, given the distance between these wires and the cores, this should only introduce second-order corrections to the calculated induced field.

Another simplification in this model is the fact that the cores are considered linear materials obeying the constitutive relation $\vec{B} = \mu\vec{H}$ where the magnetic permeability, μ, is a scalar. This linearity assumption should be valid for materials with high saturation magnetic fields (e.g. supermendur or ferrite cores). Furthermore, as noted by Epstein and Davey (Epstein and Davey, 2002), some degree of saturation can be tolerated as the electric field's maximum occurs when the rate of change of the current is maximum, whereas the magnetic field's maximum occurs when the current in the coil reaches its maximum value.

Numerical calculations of the electric field

All field calculations were performed using the finite element method, as implemented by the commercially available program Comsol 3.3a (www.comsol.com). This program includes an electromagnetics package for calculating the total electric field induced in a conducting medium by an arbitrary current distribution placed outside it. It solves for the magnetic vector ($\vec{A}$) and electric scalar (ϕ) potentials at each node of the mesh and the total electric field is then determined according to expression 1.2.2.2:

$$\vec{E} = -\frac{\partial \vec{A}}{\partial t} - \vec{\nabla}\phi$$

In order to find a solution for the potentials at each node point, the package solves the following set of partial differential equations:

$$\vec{\nabla} \times \vec{\nabla} \times (\mu^{-1}\vec{A}) + (jw\sigma - w^2\varepsilon)\vec{A} + (\sigma + jw\varepsilon)\vec{\nabla}\phi = 0 \qquad \textbf{2.2.1.1}$$

$$\vec{\nabla} \cdot \left[(jw\sigma - w^2\varepsilon)\vec{A} + (\sigma + jw\varepsilon)\vec{\nabla}\phi\right] = 0 \qquad \textbf{2.2.1.2}$$

where all fields are assumed to have a time-harmonic variation with angular frequency *w*. In the previous expressions, σ represents the electrical conductivity tensor. Equation 2.2.1.1 is obtained by substituting 1.2.2.2 and the constitutive relations, $\vec{B} = \mu\vec{H}$ and $\vec{D} = \varepsilon\vec{E}$, into Ampere's law, $\vec{\nabla} \times \vec{H} = \vec{J} + \partial\vec{D}/\partial t$. Expression 2.2.1.2 is the continuity equation, obtained by taking the divergence of 2.2.1.1.

At first, it may seem strange that neither of equations 2.2.1.1 and 2.2.1.2 include the external current density term, $\vec{J}_{coil}$, as shown in Poisson's equation for the vector potential, 1.2.2.4. This is related to the way the coil is modelled in Comsol: to reduce computational needs, the coil wires are approximated by lines where the maximum value of the total current, I_0, is specified (this is shown in Figure 2.2.1.1). The term $\vec{J}_{coil}$ would appear as a source term in the right hand side of 2.2.1.1 if the coil wires were represented in a realistic way. No additional term would appear in 2.2.1.2 given that the divergence of $\vec{J}_{coil}$ is zero.

Equations 2.2.1.1 and 2.2.1.2 do not take advantage of the quasistatic approximation. However, it is possible to show that they reduce to Poisson's and Laplace's equations (1.2.2.5 and 1.2.2.4), respectively if the quasistatic approximations are taken into account (see Appendix A).

For all models used, the finite element mesh comprised between 50000 and 200000 tetrahedral elements, depending on the complexity of the model. The mesh contained Lagrange linear elements for the scalar potential and vector linear elements for the vector potential. Due to the large number of degrees of freedom in the models, an iterative solver was chosen (GMRES), which demanded the use of a preconditioner (Incomplete LU). Models with ferromagnetic cores did not converge using the drop tolerance value set by default in Comsol (0.01). This problem was solved by decreasing the drop tolerance to 10^{-5}, which significantly increased the computation time of the preconditioning but led to a fast convergence of the iterative solver. All models took less than 30 minutes to solve, on a computer with two dual core Xeon 5160 processors clocked at 3 GHz and 16 GB of RAM.

Calculation of coil inductance

As discussed previously (see page 28 of Chapter 1) the total electric field induced during TMS is proportional to the time derivative of the current in the coil. In this study

the electric field was analysed at the time point when it was highest. Thus it was important to ensure that the maximum time derivative of the current in the numerical simulations was the same as the one provided by actual stimulators. It was mentioned previously that a magnetic stimulator can provide a maximum current time derivative that depends on both the inductance of the coil (L) and the charging voltage of the capacitors (V_C), according to the expression $dI/dt = V_C / L$. The finite element program used, however, assumes that the current in the coil has a sinusoidal variation in time with a frequency, f, and a peak value I_0. From this, it can be seen that the maximum current time derivative during the simulation is given by $dI/dt = 2\pi f I_0$. Combining the two previous expressions, the following expression is obtained for the peak current value to be used in the numerical simulations:

$$I_0 = \frac{1}{2\pi f}\frac{V_C}{L} \qquad \textbf{2.2.1.3}$$

The frequency value to be used in the previous expression was estimated to be 5 kHz, a value in between the typical range of frequencies of most TMS pulses (DC to 10 kHz according to (Miranda et al., 2003)). The charging voltage, V_C, was set to 100 V, which is much smaller than the values typically used (the Magstim Rapid Stimulator, for instance, can output a maximum of about 1980 V). This small value was chosen because the coil used in this study contains fewer loops (2 loops) than those of most commercially available coils (9 to 18 loops). Therefore, this coil has a smaller inductance and, if the same charging values were used, that would result in very high values for dI/dt. The low value used for V_C ensured that the values of dI/dt obtained remained close to the values usually used. Finally, the current peak value also depends on the inductance of the coil, which had to be determined first.

Calculation of the coil's inductance required the construction of a new coil, similar to the previous model of the loop 1 and 2 coil but with a wire radius of 1.35 mm (see Figure 2.2.1.3). That specific value for the wire radius was chosen because it is the same as that of the wire used to build the H coils. One of the wires of the coil was cut so that different boundary conditions could be imposed at each end. One end was grounded, whereas at the other end, a uniform current density of 1 Am^{-2} was specified. This allowed for the calculation of the impedance of the coil, $Z = R + jwL$, where R is the coil's resistance. Taking the imaginary part of the impedance and dividing it by the angular frequency, yielded an estimate of the coil's inductance. Once the inductance for

the different coil/core configurations was known, expression 2.2.1.3 provided the current peak value used in the field calculations, for a fixed capacitor's charging voltage.

In order to validate the results obtained with Comsol, it was used to calculate inductances of coil / core models for which a theoretical expression for the inductance is known.

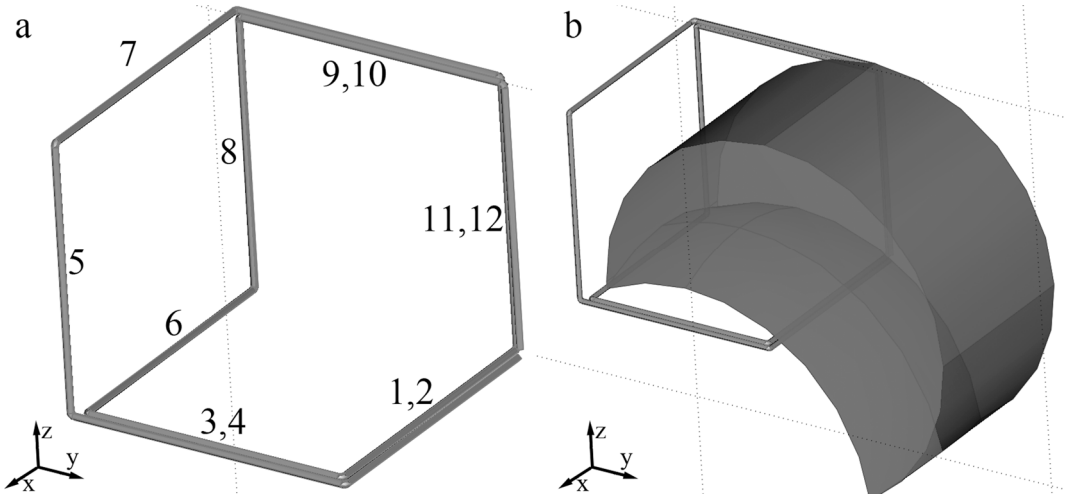

Figure 2.2.1.3: Coil model used in inductance calculations (a). The coil wire was modelled with a circular cross-section with radius 1.35 mm. The wires have approximately the same dimensions as those in the model used to calculate the electric field. The core placed over this coil model is represented in (b).

Field focality

To assess the field's focality, the solution along several concentric spheres located inside the head model, with radii ranging from 3 cm to 9 cm, was calculated. For each sphere, the area of the half power region (HPR) was considered. The latter is defined as the region where (Carbunaru and Durand, 2001):

$$\left\|\vec{E}\right\| \geq \frac{\left\|\vec{E}\right\|_{Max}}{\sqrt{2}} \qquad \textbf{2.2.1.4}$$

where $\left\|\vec{E}\right\|$ represents the electric field's norm and $\left\|\vec{E}\right\|_{Max}$ represents the field's norm maximum value over that surface. It has been shown that the HPR provides an appropriate measure of the excitation region of a coil (Hsu and Durand, 2001). In order to obtain a more accurate value of the HPR, the mesh on the surface of each ellipsoid was refined by reducing the maximum element size.

2.2.2 Results

Coil inductance

The inductance values for the loop 1 and 2 coil, calculated at a frequency of 5 kHz, are shown in Table 2.2.1. The increase in the coil's inductance was about the same for both the left and the dual core (the core that covers both the left hemisphere and the head's front) configurations, approximately 62%. The validation studies presented in Appendix B, indicate that the numerical results deviate from the approximate theoretical expression by less than 4 %.

Using these inductance values in expression 2.2.1.3, the values for the peak current shown in the table, for a capacitor's charging voltage of 100 V, were obtained. The maximum value of the current's time derivative, which is a measure of the stimulus intensity, is also presented in this table.

Table 2.2.1: Inductance, peak current and current time derivative for the different loop 1 and 2 coil / core configurations.

Model	Inductance (μH)	Current (kA)	dI/dt (A μs^{-1})
No core	1.3	2.4	75
Lateral core	2.1	1.5	47
Frontal core	1.9	1.7	52
Dual (frontal and lateral) core	2.1	1.5	47

Primary component of the electric field

The primary component of the field induced by the loop 1 and 2 coil without the presence of ferromagnetic cores is shown in Figure 2.2.2.1 for an axial slice located at z = 5 cm, approximately 3 cm below the plane containing wires 1, 2, 3, 4 and 6 (see Figure 2.2.1.1). As shown in the figure, the field was maximum over the left hemisphere, in the PA direction (x axis), and over the head's front, in the LR direction (direction opposite to the y axis). The field over the left hemisphere was induced mainly

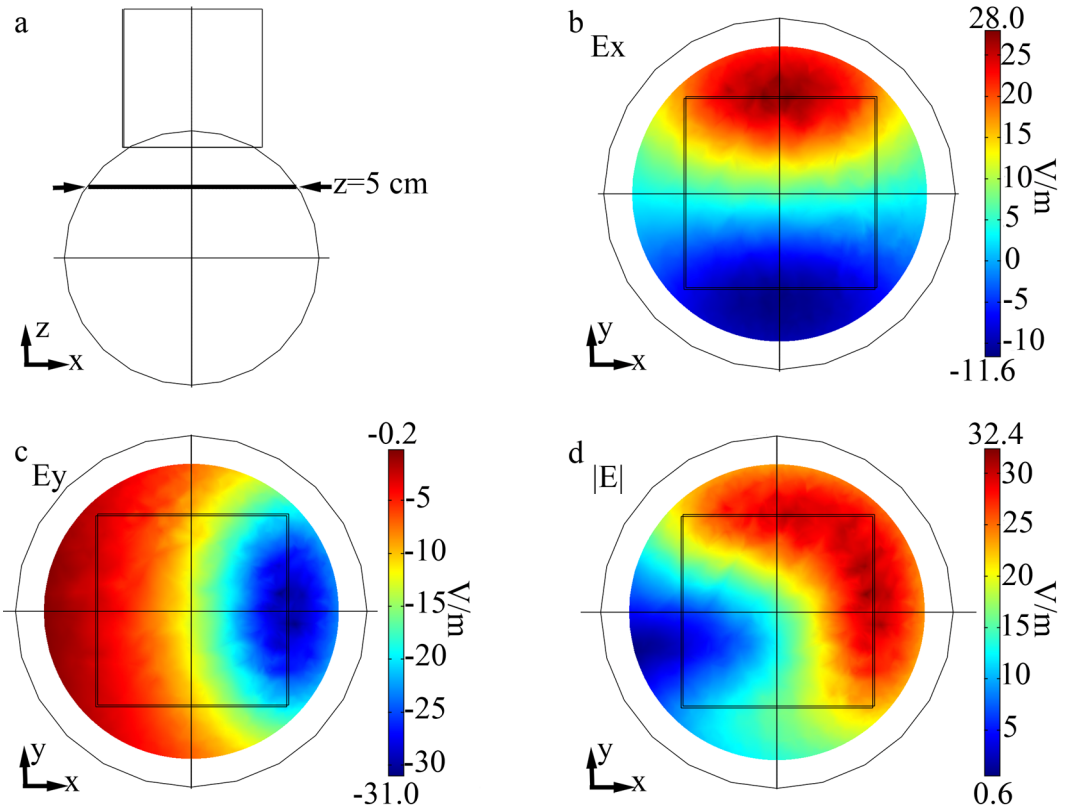

Figure 2.2.2.1: Primary component of the field induced by loop 1 and 2 without a core. (a) Lateral view of the head model (view from the right hemisphere). The arrows indicate the position of the axial slice located at z = 5 cm, 3 cm below the plane containing wires 1, 2, 3, 4 and 6 of the coil; (b) x component (PA direction) of the primary electric field; (c) y component (RL direction) of the total electric field. The negative values of this component of the field indicate that the field points in the LR direction; (d) Norm of the primary component of the electric field.

by wires 1 and 2 of the coil, whereas the field over the head's front was induced by wires 3 and 4. Over the right hemisphere and at the back of the head, the field was weaker because some of the coil wires at those regions were located away from the scalp (wires 7, 9 and 10 in Figure 2.2.1.1).

The presence of the cores had two main effects. The first effect was to increase the primary component of the field along the direction that was dominant at the region of the head closer to the core. Hence, over the left hemisphere, the lateral core increased the primary electric field along the PA direction by as much as 181 % of the value without the core (Figure 2.2.2.2 a), whereas over the head's front the frontal core increased the primary field along the LR direction by as much as 176 % of the value without the core (Figure 2.2.2.2 d). The second effect of the core was to decrease the magnitude of the field along other directions, albeit much less than it increased the field

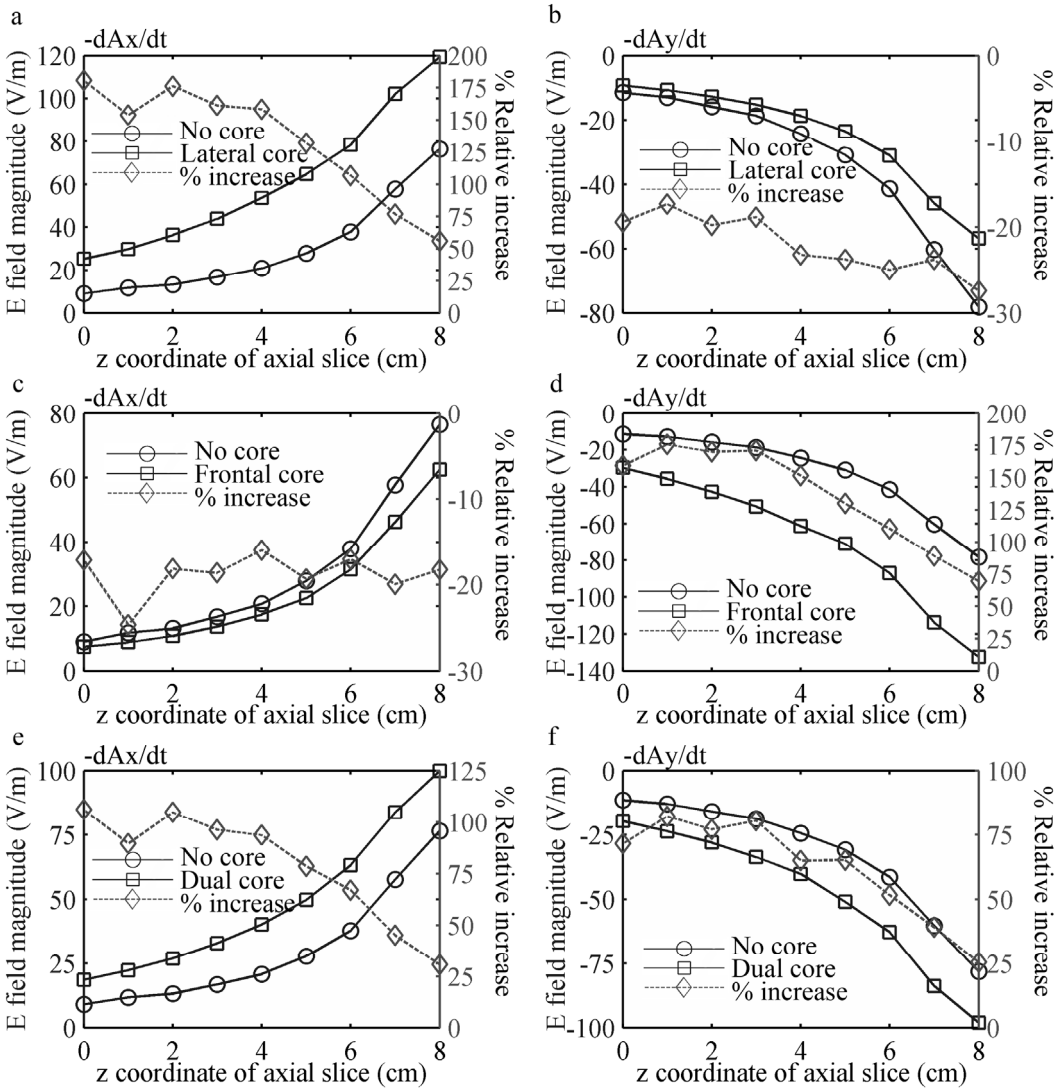

Figure 2.2.2.2: Maximum value of the primary component of the field induced by loop 1 and 2 for several axial slices (slice z = 0 cm coincides with the sphere's equatorial plane, and z = 8 cm is the position of the coil wires that are closest to the head). (a) value of the field in the PA direction (x component) over the left hemisphere, for both the model with the lateral core and the model without it; (b) same as (a) but now for the field in the RL direction (y axis) over the head's front; (c) /(d) same as (a)/(b), respectively, but now for the model with the frontal core; (e)/(f) same as (a)/(b), respectively but now for the model with the dual core configuration.

at the regions close to it. The lateral core, for instance, decreased the field induced along the LR direction over the head's front by as much as 27 % of the value without the core (Figure 2.2.2.2 b). Similarly, the frontal core decreased the field induced over the left hemisphere in the PA direction, by as much as 25 % of the value without the core (Figure 2.2.2.2 c).

The dual-core configuration combined the effects of the two previously mentioned models causing a field increase slightly smaller than that observed in the other two

models (see Figure 2.2.2.2 e and f): 106 % increase of the field in the PA direction over the left hemisphere, and 81 % increase of the field in the LR direction over the head's front.

A characteristic common to all core models tested here is the fact that the field's relative increase tended to increase for the axial slices further away from the coil's wires.

Secondary component of the electric field

The scalar potential, ϕ, for the model without cores, shown in Figure 2.2.2.3 a, was maximum under the radial wires 11, 12 and 5, indicating that under the radial components high charge accumulation occurred, as expected. The secondary component of the field is also shown in the figure. Over the left hemisphere, the field due to charge accumulation was positive along the AP direction, and its values ranged from 27 % to 55 % of the value of the primary field along the PA direction. Over the head's front, the secondary field was positive along the RL direction, and its values ranged from 7 % to 41 % of the value of the primary field along the LR direction. Therefore, the secondary field tended to oppose the primary field over both the left hemisphere and the head's front.

The presence of the lateral core over the left hemisphere changed the spatial distribution of the scalar potential by shifting its maximum, which was located under wire 5 in the model without core, more to the head's front (compare Figure 2.2.2.3 b with Figure 2.2.2.3 a). Furthermore, the value of the scalar potential increased: the maximum increased about 2.5 times, whereas the absolute value of the minimum increased about 2 times. This was a direct consequence of the increase in the primary component of the field along the PA direction caused by the lateral core. Due to the change in the spatial distribution of the scalar potential, the decrease of the total electric field over the left hemisphere in the PA direction, due to the secondary field, was much more pronounced in this model than it was in the model without the core: the secondary field ranged from 53 % to 93 % of the value of the primary field.

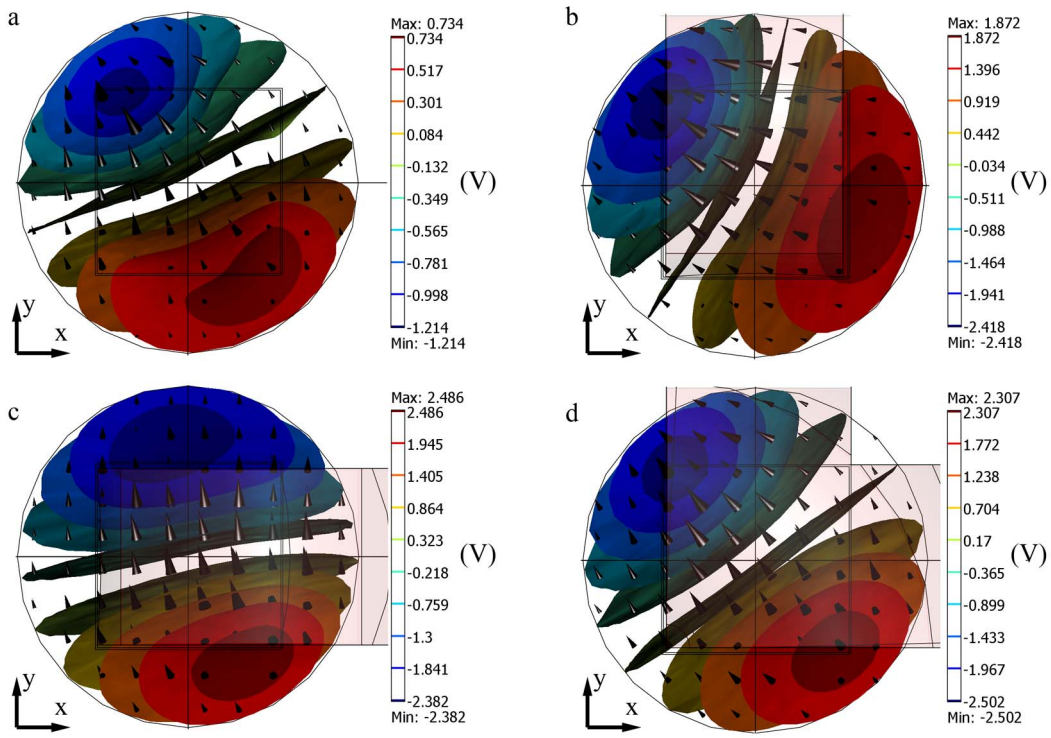

Figure 2.2.2.3: Spatial distribution of the scalar potential (isocontours) and of the secondary field (arrows) for the different models considered. (a) loop 1 and 2 without any core; (b) model with lateral core over the left hemisphere; (c) model with the frontal core; (d) model with the dual core. The shaded areas represent the areas covered by the core.

The frontal core also changed the spatial distribution of the scalar potential, by shifting the maximum over the right hemisphere to a more lateral position (see Figure 2.2.2.3 c), and it increased its value as well. In this model, this change caused the secondary field to oppose the primary field over the head's front along the LR direction much more strongly than it did in the model without the core: the secondary field ranged from 53 % to 95 % of the value of the primary field over the head's front.

In the dual-core model, as with the other two core models, there was a strong increase of the magnitude of the scalar potential. However, contrary to what happened before, the spatial distribution of the scalar potential did not change much as compared to the model without any core (see Figure 2.2.2.3 d). Therefore, in this model, the secondary field opposed the primary component of the field as it did in the model without the core, only now the magnitude of this secondary component was much higher: the secondary field ranged from 45 % to 83 % of the value of the primary field over the left hemisphere along the PA direction, and 48 % to 88 % over the head's front along the LR direction.

Total electric field

The total electric field induced by the loop 1 and 2 coil without cores is shown in Figure 2.2.2.4 e, i and m for a slice located at z = 5 cm. As was the case with the primary component of the field (see Figure 2.2.2.1), the total field was maximum over the left hemisphere, along the PA direction, and over the head's front, along the LR direction. Due to the secondary field, however, the values of the field at those two regions were smaller than those observed for the primary field (compare Figure 2.2.2.4 e and i with Figure 2.2.2.1 b and c). Also due to charge accumulation, there was an increase of the field over the right hemisphere, along the AP direction, and at the back of the head, along the RL direction.

As was reported for the primary component of the field, the main effect of the lateral core was to increase the total electric field over the left hemisphere along the PA direction (compare Figure 2.2.2.4 e/m with f/n), and to decrease the total field over the head's front along the LR direction (compare Figure 2.2.2.4 i/m with j/n). The only exception occurred for the field over the axial slices located at z = 0 cm and z = 1 cm where, in presence of the core, the field along the PA direction over the left hemisphere decreased (Figure 2.2.2.5 a), and the field in the LR direction over the head's front increased (Figure 2.2.2.5 b). For all the other slices the increase of the field in the PA direction was much smaller than that reported for the primary component (compare Figure 2.2.2.5 a with Figure 2.2.2.2 a), reaching a maximum relative increase of only 21 % (slice z= 4 cm) of the value without the core, as opposed to the 181 % increase reported for the primary component. This was caused by the increase in the secondary component of the field that tended to oppose the primary field. Regarding the field decrease in the LR direction, it was also slightly smaller than that reported for the primary component (maximum decrease of 21 % as opposed to a 27 % maximum decrease for the primary component) and it varied much more along the different axial slices (compare Figure 2.2.2.5 b with Figure 2.2.2.2 b).

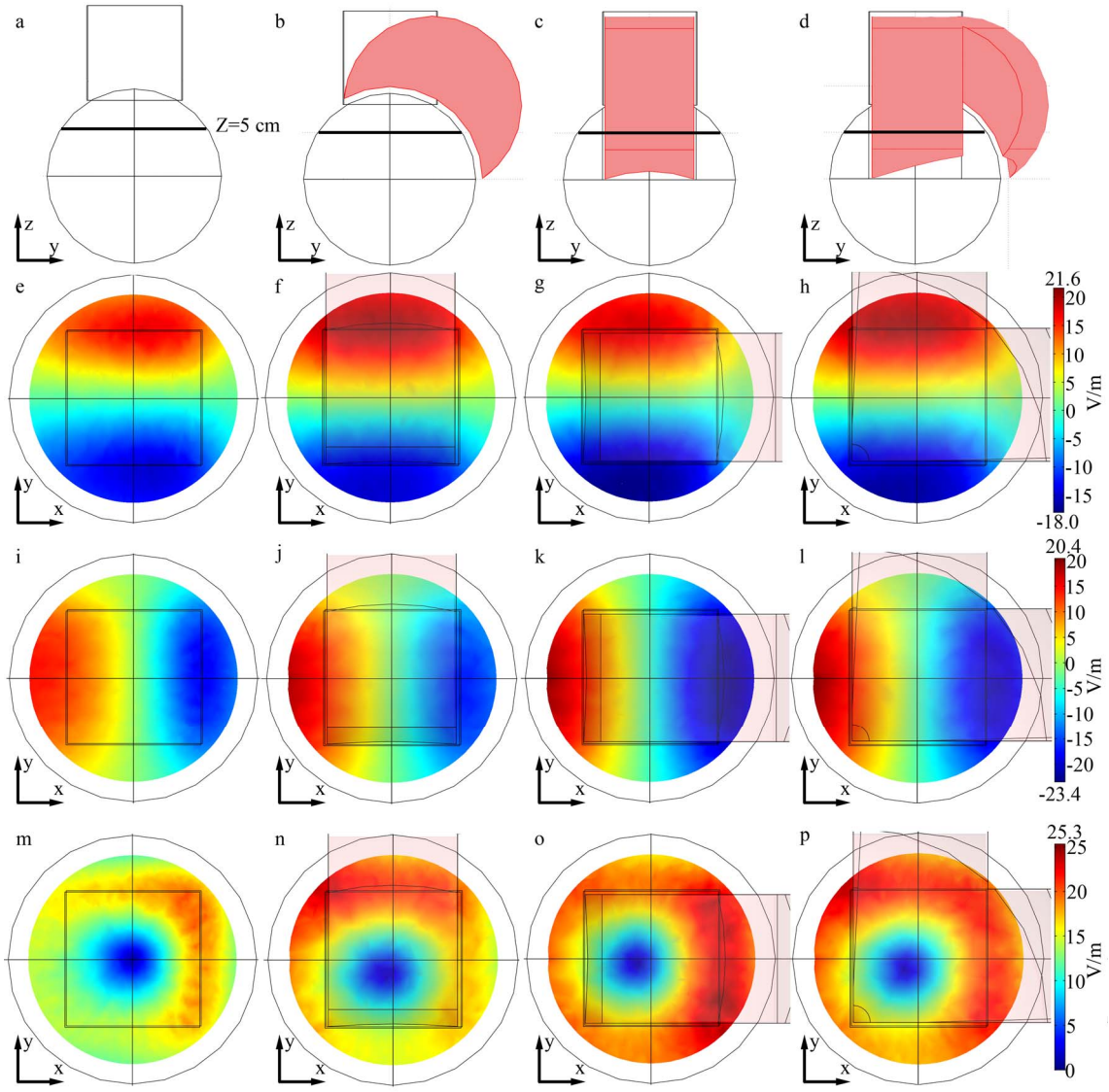

Figure 2.2.2.4: Total electric field induced in all the different coil / core configurations. Each column corresponds to a different model: the first column in the left (a, e, i and m) represents the model without any core, the second column (b, f, j and n) the model with the lateral core, the third column (c, g, k and o) the model with the frontal core, and the last column (d, h, l and p) the model with the dual core. Within each column, the first line indicates the position of the axial slice (located at z = 5 cm), the second line shows the spatial distribution of the x component of the total electric field, the third line the y component of the field, and the last line the electric field's norm. The colourbar that appears at the end of each line is common to all the slices in that line. The shaded areas in some models represent the position of the cores.

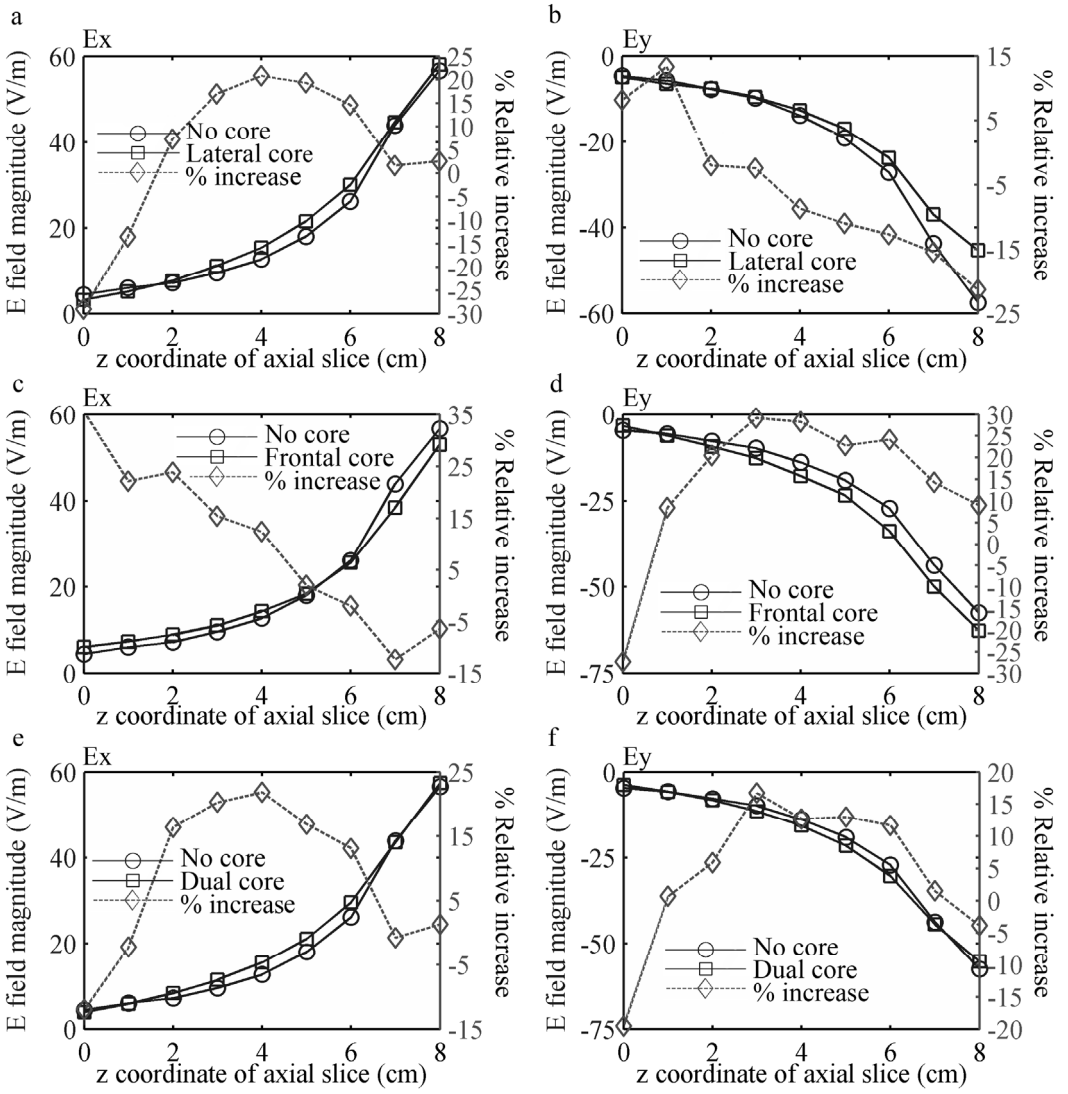

Figure 2.2.2.5: Maximum value of the total electric field induced by loop 1 and 2 for several axial slices (slice z = 0 cm coincides with the sphere's equatorial plane, and z = 8 cm is the position of the coil wires that are closest to the head). (a) value of the field in the PA direction (x component) over the left hemisphere, for both the model with the lateral core and the model without it; (b) same as (a) but now for the field in the RL direction (y axis) over the head's front; (c)/(d) same as (a)/(b), respectively, but now for the model with the frontal core; (e)/(f) same as (a)/(b), respectively but now for the model with the dual core configuration.

As was also reported for the primary component of the field, the relative total field increase due to the lateral core was more pronounced for the middle axial slices (between z = 2 cm and z = 6 cm) than for the top axial slice (z = 8 cm). That resulted in a slight decrease of the field's decay along the axial slices, because the maximum value of the field still occurred in the upper axial slice.

The results obtained for the frontal core were slightly different than those obtained for the lateral core. This core increased the total electric field over the head's front and

along the LR direction (compare Figure 2.2.2.4 i/m and k/o), consistently with what was observed when analysing the primary field. The relative increase was much smaller for the total field (maximum of 29 % in Figure 2.2.2.5 d) than for the primary field (maximum of 159 %). However, contrary to what was previously observed for the primary field, this core tended to increase the total field along the PA direction over the left hemisphere in most of the axial slices considered (the only exceptions were the slices located between z = 8 cm and z = 6 cm). This relative increase became higher for the deeper axial slices, reaching a maximum of 36 % of the value without the core (see Figure 2.2.2.5 c). Despite this, it should be noted that even with this increase the dominant component of the field in this model occurred along the LR direction over the head's front (see Figure 2.2.2.4 o). As was also reported for the lateral core, the relative increase of the total field in the LR direction over the head's front was higher for the slices located between z = 2 cm and z = 7 cm than for the top slice (z = 8 cm), which resulted in a slight decrease of the field's decay.

The dual core combined the effects of the two previously mentioned cores, by increasing both the total field in the PA direction over the left hemisphere, and the field in the LR direction over the head's front (see Figure 2.2.2.4 h, l and p). As reported for the primary field, this increase was slightly smaller that that reported for each core applied individually, reaching only 22 % for the field over the left hemisphere (Figure 2.2.2.5 e) and 17 % for the field over the head's front (Figure 2.2.2.5 f). As before, the presence of this core also lead to a slight decrease in the field decay along most axial slices.

Field focality

The HPR in each of the spherical surfaces used to study the focality of the electric field is shown in Figure 2.2.2.6 for all the models considered thus far. The values plotted in the figure represent a normalized HPR, obtained by dividing the HPR by the total area of each sphere.

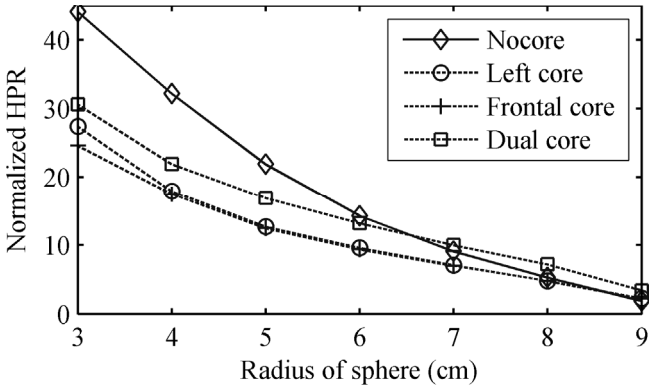

Figure 2.2.2.6: Normalized HPR values for each coil / core model as a function of the radius of each of the spherical surfaces used to calculate the focality. The normalized HPR were obtained by dividing the HPR for each model by the total area of each spherical surface.

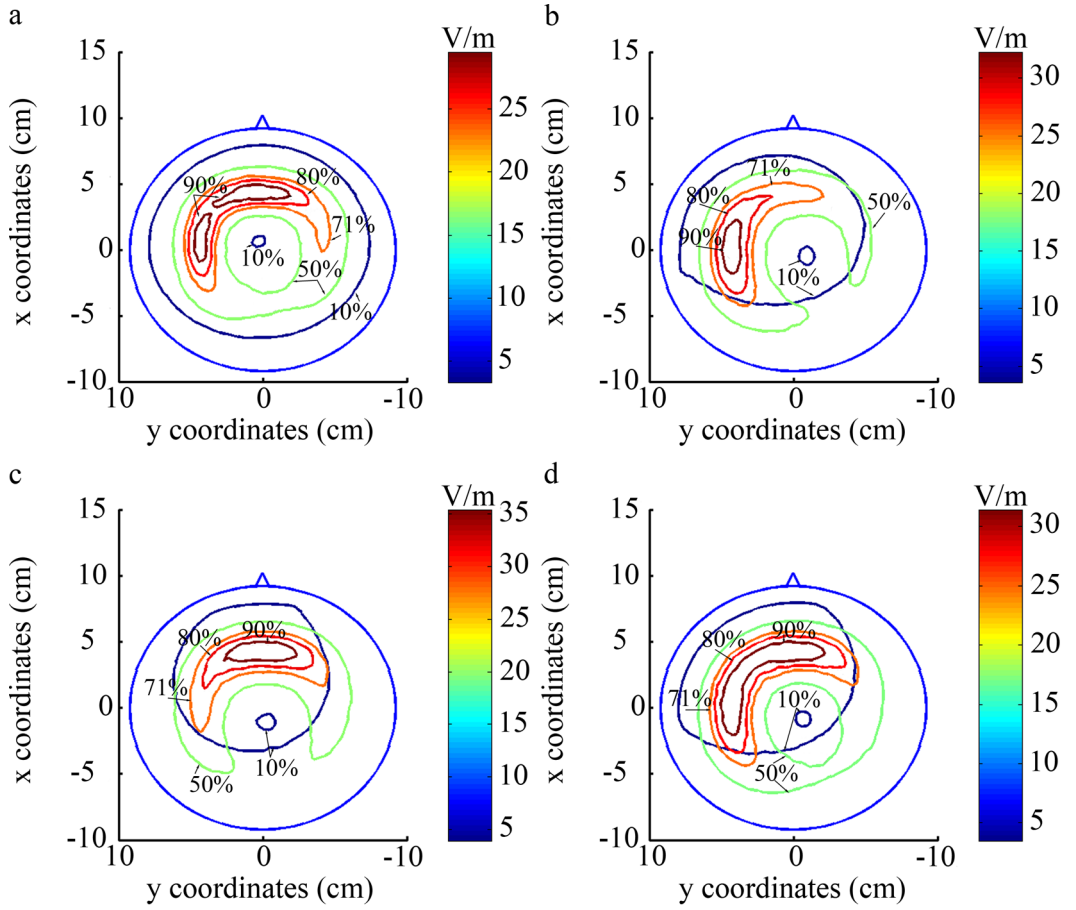

Figure 2.2.2.7: Contour plots of the total electric field over a spherical surface with a radius of 8 cm. (a) model without any core; (b) model with the lateral core; (c) model with the frontal core; (d) model with the dual core. The HPR is encompassed by contour 71 % (orange). The contours are shown in a spherical surface and so they appear to intersect in this top view, but that never happens.

As shown in Figure 2.2.2.6, the normalized HPR in the model without the cores tended to increase as spheres further away from the surface of the head model were considered.

An isocontour plot of the norm of the electric field induced in this model is shown in Figure 2.2.2.7 a, for a spherical surface located 1.2 cm away from the head's surface. In the figure it can be seen that the HPR, which corresponds to the isocontour where the field's norm is approximately 71 % of its maximum value, covered both the left hemisphere and the head's front. This is an expected result, since the electric field was maximum at those regions.

The presence of the lateral core increased the normalized HPR in the surface of the sphere with a 9 cm radius, and decreased it in the remaining spherical surfaces. The decrease of the normalized HPR was a consequence of the selective increase on the total field over the left hemisphere caused by the presence of the core. That increase shifted the HPR towards the left hemisphere as can be seen in Figure 2.2.2.7 b which tended to decrease the area of the HPR. This focality increase became more pronounced for smaller spheres.

The frontal core affected the normalized HPR in a manner similar to the frontal core: the core increased the HPR for the most superficial sphere and decreased it for all the other spheres (Figure 2.2.2.6). In this model the core shifted the HPR to the head's front (Figure 2.2.2.7 c). The shift was caused by the selective increase of the field over the head's front promoted by the frontal core.

The dual core model had a different effect on the normalized HPR, increasing it for the spheres with radius 9 cm, 8 cm and 7 cm, and decreasing it for the remaining spheres (Figure 2.2.2.6). This decrease, however, was never as pronounced as those observed with the other core models. The dual core model increased the field over both the left hemisphere and the head's front, therefore not shifting the HPR area as was seen in the previous cases (Figure 2.2.2.7 d).

2.2.3 Discussion

Field induced by the loop 1 and 2 coil

The loop 1 and 2 coil induced a strong electric field over two main regions: the left hemisphere, along the PA direction, and the head's front, along the LR direction. The magnitude of the field over those two regions was similar and, therefore, the HPR covered those two regions. This is a disadvantage in terms of focality, given that this way the coil is likely to stimulate two target neuronal populations at the same time:

neurons over the left hemisphere and mostly aligned with the PA direction and neurons at the head's front, mostly aligned with the LR direction.

Effects of the use of ferromagnetic cores

The most obvious effect of the association of ferromagnetic cores with the loop 1 and 2 coil was to make one of the two previously mentioned field directions dominant over the other. This way, the lateral core shifted the dominant component of the field towards the left hemisphere, along the PA direction. On the other hand, the frontal core shifted the dominant component of the field towards the head's front, along the LR direction.

Associated with the change in the field's distribution promoted by the cores, there was also an increase on the magnitude of the total electric field. This magnitude increase was, however, much smaller that that observed for the primary component of the field. The main factor that limited the increase of the field's magnitude due to the presence of the core was the strong increase of the secondary field along the direction opposite to the direction of the primary field that was more affected by the core. Therefore, in the model with the lateral core, the strong increase of the primary component of the field over the left hemisphere along the PA direction was balanced out by a strong increase of the secondary field along the AP direction. Likewise, in the model with the frontal core, the same happened but now for the field along the LR direction over the head's front. These results again prove the importance of the secondary field in the calculation of the total electric field induced in TMS.

Another effect of the presence of the cores was the high inductance increase with respect to the model without the cores. Coil inductance is an important parameter in TMS because, as it was already discussed, the maximum value of the current's time derivative is inversely proportional to the inductance. This way, for the same capacitor's charging voltage, a coil with a large inductance will yield a smaller current's time derivative than a coil with a small inductance. As the total electric field is proportional to the current's time derivative, if the increase in inductance due to the core was too high, that would mean that a very high voltage would be needed to reach a strong electric field. Therefore, in realistic coil designs, the inductance increase due to the presence of the core needs to be monitored so that the coil / core apparatus can be plugged into a magnetic stimulator.

Finally, the field's focality was also improved by the core. The lateral and frontal core models shifted the HPR towards the left hemisphere and the head's front, respectively, therefore decreasing its value. The dual core also diminished the HPR area, except for the outer spherical surfaces (radii ranging from 7 cm to 9 cm), where the HPR slightly increased. The HPR shift observed in the models with the lateral and frontal cores also means that, for those models, there was only one dominant region where the field's magnitude was maximum. Therefore, contrary to what happened in the model without cores and in the model with the dual core, the model with the lateral core targeted preferably neurons located over the left hemisphere and oriented along the PA direction, whereas the model with the frontal core targeted preferably neurons located over the head's front and oriented along the LR direction.

Model limitations

The results presented thus far indicate that ferromagnetic cores, when associated with the loop 1 and 2 coil, increase the magnitude of the induced field and its focality. Therefore, these coil / core models might be useful in applications where the target region is located deeply in the brain. However, this work has some limitations that may affect the results.

The first limitation is related to the spherical head model used in the study. While this model is a good first approximation of the local geometry of the head, a more detailed model should include a realistic representation of the head. This gains even more importance since the results presented here highlight the importance of the secondary field, which strongly depends on the geometry of the model representing the head.

Another limitation of this work is associated with the very simple coil model used. The coil has some characteristics common to the H1 coil, but the latter has a much more complex design having multiple wires, with different lengths, spread over the scalp. A more detailed study must include a realistic representation of the coil.

These limitations were addressed in the work reported in the following section. That work generalized the previous study by combining high permeability cores with an accurate model of the H1 coil placed over a realistically shaped homogeneous head model.

2.3 A realistic coil model: the H1 coil

2.3.1 Methods

Head and coil models

The coil used in this work is shown in Figure 2.3.1.1, placed over a realistically shaped homogeneous head model. This coil model is an accurate representation of the H1 coil (Roth et al., 2007) in terms of the position, orientation and length of its wire segments. The coil has 14 wires spread over the left hemisphere (elements AP 1–14 in Figure 2.3.1.1, carrying current flowing in the AP direction), which induce an electric field in the PA direction. The return paths for these elements are placed over the right hemisphere (elements PA 1–14), some close to the scalp (PA 1–6) and others away from it (PA 7–14). The wires placed over the front of the head (elements RL 1–14) induce an electric field in the LR direction (y axis). The return paths of these wires (LR 1–14) are located in the back of the head and away from its surface. Elements IS 1–14 and SI 1–14 induce a field parallel to the z axis (SI direction). The wires close to the scalp follow approximately the curvature of the head model and therefore induce a field with a negligible normal component.

The head model used was built from MRI images of the same head-shaped phantom used to measure the field induced by the H1 coil in a previous study (Roth et al., 2007). The model, shown in Figure 2.3.1.1, was divided into two sections with different dielectric properties: an upper section, with a height of 11 cm, representing the average brain size along the SI axis (Roth et al., 2007) and a lower section representing air. As in the previous study, the upper section was modelled as a homogeneous and isotropic medium, with an electrical conductivity of 0.33 S/m and a relative electrical permittivity of 10^4. The lower section was modelled with an electrical conductivity of 0 S/m and a relative electrical permittivity of 1. The horizontal cut dividing the two sections is perceptible in Figure 2.3.1.1, at the level of the nasion.

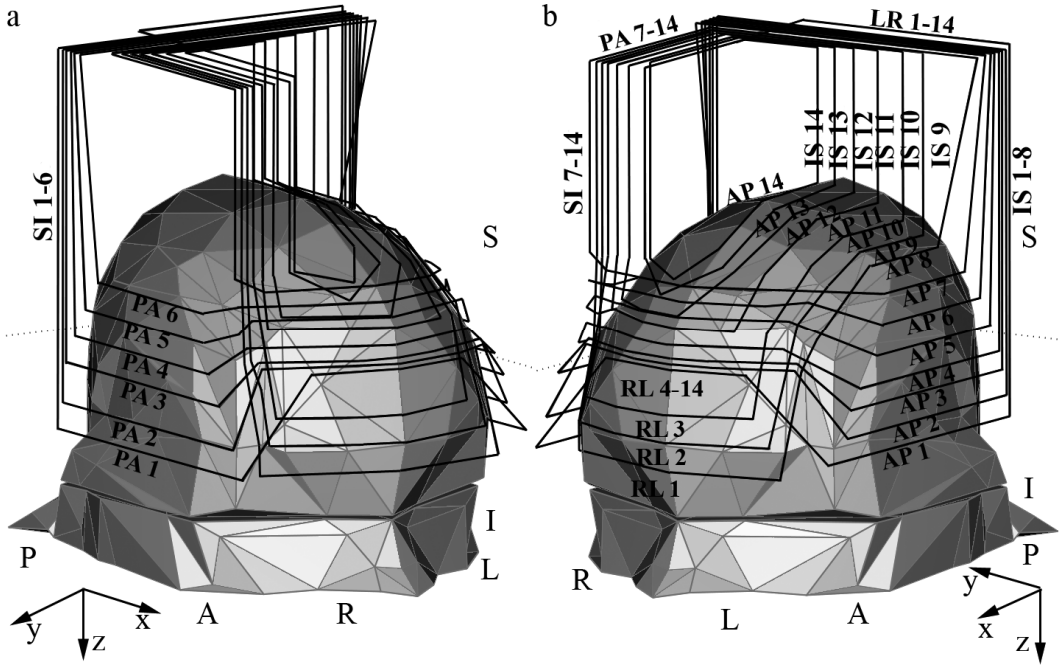

Figure 2.3.1.1: A model of the H1 coil placed over a realistically shaped homogeneous head model. (a) right hemisphere view; (b) left hemisphere view. The wire names indicate the current direction in the wires in the positive going phase of the stimulus: PA: posterior–anterior (*x* axis); LR: left–right (*y* axis); SI: superior–inferior (*z* axis). The vertex of the head model is located at $z = 0$ cm, and the horizontal cut, which separates both regions of the model, is located at $z = 11$ cm.

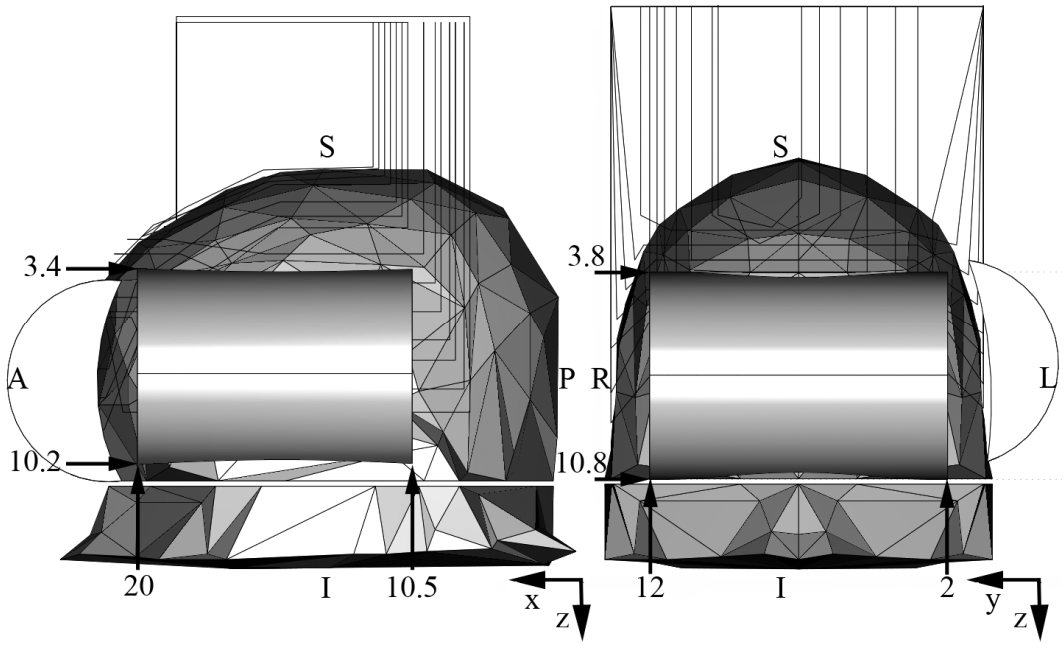

Figure 2.3.1.2: Cores placed over the head and coil model. The figure on the left shows a view from the left hemisphere, whereas the figure on the right shows a frontal view of the model. The arrows indicate the coordinates (in cm) of the cores' upper/lower and anterior/posterior boundaries. The models used in the calculations contained only one core: either the frontal core or the lateral one.

High permeability core models

In this work, specially designed ferromagnetic cores were placed over the H1 coil, as shown in Figure 2.3.1.2. The cores were created from cylinders 7 cm in diameter, cut in such a way that their inner surfaces follow approximately the curvature of the head in that region. Because the effect of the core depends on its placement, two different models were created: one with the core placed over the left hemisphere and another one with the core placed over the front of the head. These two positions were chosen because they correspond to the two regions targeted for stimulation by the H1 coil, as stated previously. The frontal core has a length of 10 cm whereas the left core is slightly shorter (9.5 cm). The left core's upper end is placed near wire AP 6 (Figure 2.3.1.2) and its lower end is located 1.8 cm below wire AP 1. The frontal core's upper end is located near wire RL 8 (the RL wire that connects with wire AP 12) and its lower end is located 1.8 cm below wire RL 1.

The previous discussion about core laminations also applies to this model of the cores. Here, again, the cores were modelled with a bulk electrical conductivity of 1 S/m and a bulk relative magnetic permeability of 10^4.

Numerical calculations of the electric field

All field calculations were performed using the same finite element package used in the previous study. The only difference between the two works results from the increased complexity of the geometry of the H1 coil and of the realistic head model as compared to the previous model, which only contained the loop 1 and 2 coil and a spherical head model. Due to the increased complexity of the geometry, the finite element's mesh of these models had many more elements than the mesh of the previous ones, which made it impossible to use the same preconditioner due to memory limitations. Hence, in this work a more memory efficient preconditioner was used: the Geometric Multigrid. As was previously mentioned, this preconditioner requires two meshes: a coarser initial mesh and a finer mesh. The solution is obtained in the finer mesh, which comprised about 10^6 elements for all the models solved. Using this preconditioner combined with the GMRES solver, all models took about 4 h to solve on a computer with two dual core Xeon 1560 processors clocked at 3 GHz and 16 GB of RAM.

The surface triangulation representing the head model in all the images does not represent the finite element's boundary mesh; it is only a result of the method used to reconstruct the geometry from the phantom MRI images.

Calculation of coil inductance

As was discussed previously for the loop 1 and 2 coil, in order to determine a realistic peak value for the current flowing in the H1 coil it is necessary to determine the frequency of the pulse, the capacitor's charging voltage and the coil's inductance. The first two parameters depend on the stimulator to which the coil is connected. In all the studies found in the literature that use the H1 coil, it is connected to the Magstim Rapid stimulator (Levkovitz et al., 2007; Roth et al., 2007). Figure 2.3.1.3 a shows the approximate waveform (*dI/dt*) of this stimulator, whereas Figure 2.3.1.3 b shows the energy spectral density of the waveform (absolute value of the waveform's Fourier transform). Based on Figure 2.3.1.3 b a value of 3.5 kHz was chosen for the frequency, because this is the frequency value that yields maximum energy. Regarding the capacitor's charging voltage, it was set to approximately 46 % of the maximum output of the Magstim Rapid stimulator (V_{CMax}= 1980 V). This value has already been used in another study performed with the H1 coil (Roth et al., 2007) and can actually induce activation of the motor cortex in most subjects (Levkovitz et al., 2007). Regarding the calculation of the coil's inductance, it was performed using a model of the H1 coil in which the wires are not represented by lines but, instead, they have a circular cross section with a radius of 1.35 mm (Figure 2.3.1.4). Once the frequency, voltage and inductance were calculated, equation 2.2.1.3 was used to calculate the peak value of the current flowing in the coil.

Field focality

To assess the field's focality in this model, the solution along several concentric ellipsoids located inside the head model was calculated. The centre and semi-axis of the ellipsoids were chosen so that they would adapt to the curvature and dimensions of the head model. For each elliptic surface, the HPR was calculated according to expression 2.2.1.4. In order to obtain accurate results for HPR, the mesh on the surface of each ellipsoid was refined by reducing the maximum element size.

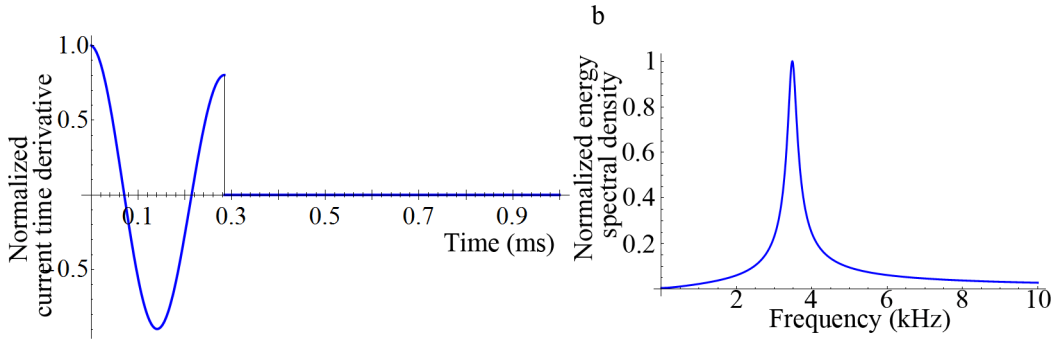

Figure 2.3.1.3: Frequency that yields maximum energy spectral density of the pulse's waveform. (a) Nomalized waveform output of the Magstim Rapid stimulator; (b) Normalized energy spectral density of the pulse's waveform. The peak value is reached at a frequency of 3.5 kHz.

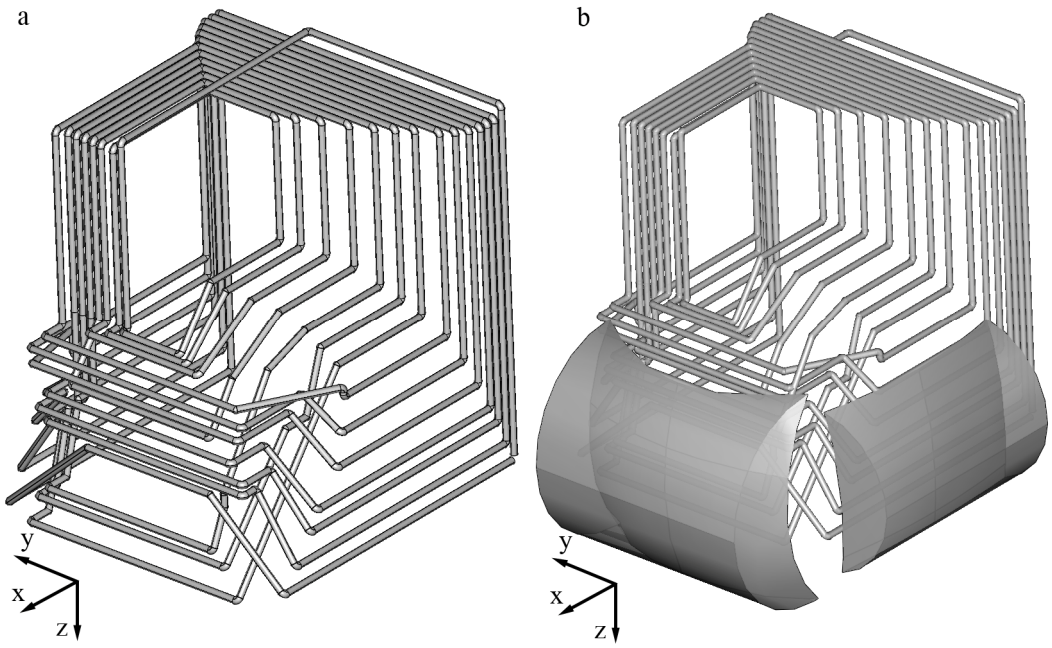

Figure 2.3.1.4: Model of the H1 coil used in inductance calculations (a). The coil wire was modelled with a circular cross-section with radius 1.35 mm. The wires have approximately the same lengths as those in the model used to calculate the electric field. The cores placed over this coil model are represented in (b). As in Figure 2.3.1.2, both cores are represented at the same time in (b) but, in the calculations, only one was used each time.

2.3.2 Results

Coil inductance

The inductance values for the H1 coil, calculated at a frequency of 3.5 kHz, are shown in Table 2.3.1. The increase in the coil's inductance was about the same for either the left or the frontal core configurations, approximately 3%. The validation

studies indicate that the numerical results deviate from the approximate theoretical expression by less than 4%.

Using these inductance values in expression 2.2.1.3, the values for the peak current shown in the table, for a capacitor's charging voltage of 900 V, were obtained. The maximum value of the current's time derivative, which is a measure of the stimulus intensity, is also presented in this table.

Table 2.3.1: Inductance, peak current and peak current time derivative for the different H1 coil / core configurations.

Model	Inductance (μH)	Current (kA)	dI/dt (A μs^{-1})
No core	22.24	1.84	40.5
Lateral core	22.84	1.79	39.4
Frontal core	22.88	1.79	39.3

Electric field distribution

The H1 coil without the core induced a strong x component of the field in both the PA and AP directions over the left and right hemispheres, respectively. This is illustrated in Figure 2.3.2.1 b for a slice located 6.3 cm below the head's vertex. Considering all slices, the maximum field value was 118 V/m over the left hemisphere and -113 V/m over the right hemisphere. The coil also induced a strong field in the LR direction over the front of the head (see Figure 2.3.2.1 c) with an overall maximum field value of 146 V/m, all slices considered. Regarding the x component of the field, in the top axial slices (up to roughly the z coordinate of wire AP 6, z< 3.9 cm), the field was more intense over the left hemisphere than over the right one. For lower axial slices, the field intensity was approximately the same over both hemispheres, except for the lowest slices (z> 8.3 cm) where the field was clearly more intense over the right hemisphere. Near the front of the head, the y component of the field was more intense than the x component, except in the higher axial slices (up to the position of wire AP 7, z< 2.8 cm). The z component of the field was always smaller than the x and y components, although not completely negligible. In the top axial slices, the maximum value of this component reached 52% (at slice z = 1.3 cm) of the field's norm maximum. However, as lower axial slices were considered, this value decreased, reaching 21% at the lowest axial slice (at z = 9.3 cm). Hence, particularly for the lower axial slices, the electric

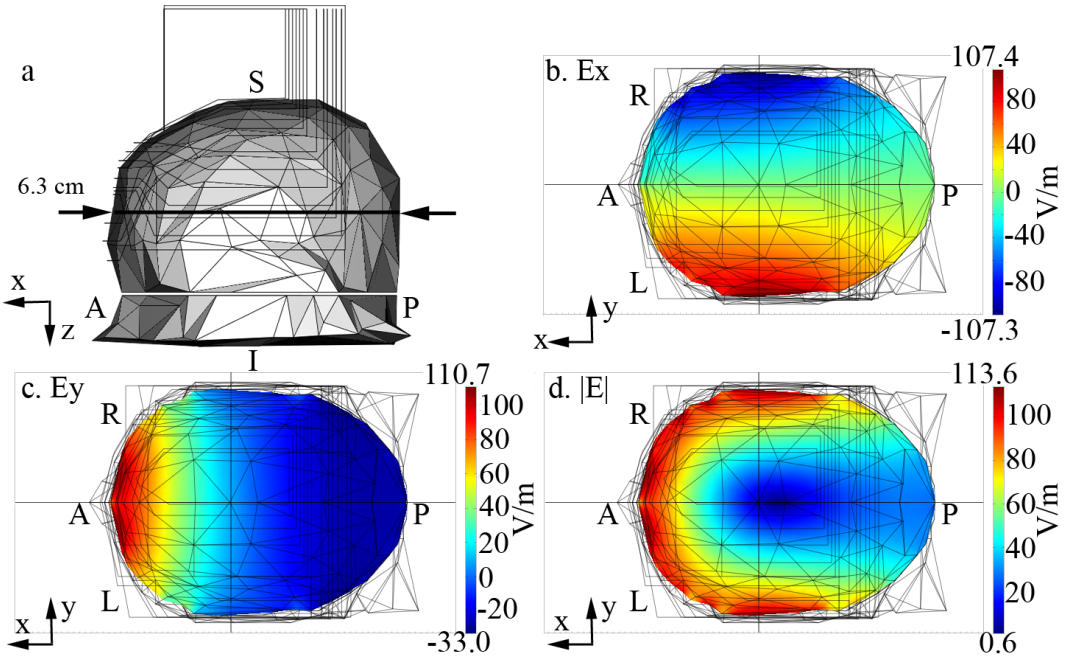

Figure 2.3.2.1: Electric field induced by the H1 coil without a core. (a) Lateral view of the head model (left hemisphere). The arrows indicate the position of the axial slice located 6.3 cm below the head's vertex; (b) *x* component (PA direction) of the total electric field; (c) *y* component (LR direction) of the total electric field; (d) total electric field's norm.

field's norm was mainly determined by the *x* and *y* components of the field, being stronger over the front of the head and over the left and right hemispheres (Figure 2.3.2.1 d).

The placement of the core over the left hemisphere increased the *x* component of the electric field under the core but did not change significantly the field over the right hemisphere. This is illustrated in Figure 2.3.1.2 d and f, which show the *x* component of the field with and without the core, respectively, for a slice located at z= 6.3 cm. For the sake of clarity, negative values of the electric field have been omitted in Figure 2.3.1.2. This allowed for a better visualization of the effects of the cores on the region of interest by making full use of the available colour scale. For axial slices lower than 1 cm below the core's upper edge (z> 4.4 cm, as shown in Figure 2.3.1.2), the *x* component of the field increased by as much as 25% of its maximum value without the core, as shown in Figure 2.3.2.3 a. For slices located above this mark (z< 4.4 cm), the field decreased slightly, by between 1% and 15% of the values without the core. The core did not affect significantly the field's *y* component over the front of the head. This is illustrated in Figure 2.3.1.2 h and j, which show the field's norm with and without the core, respectively, for the slice located at z = 6.3 cm. As can be seen, the field's norm

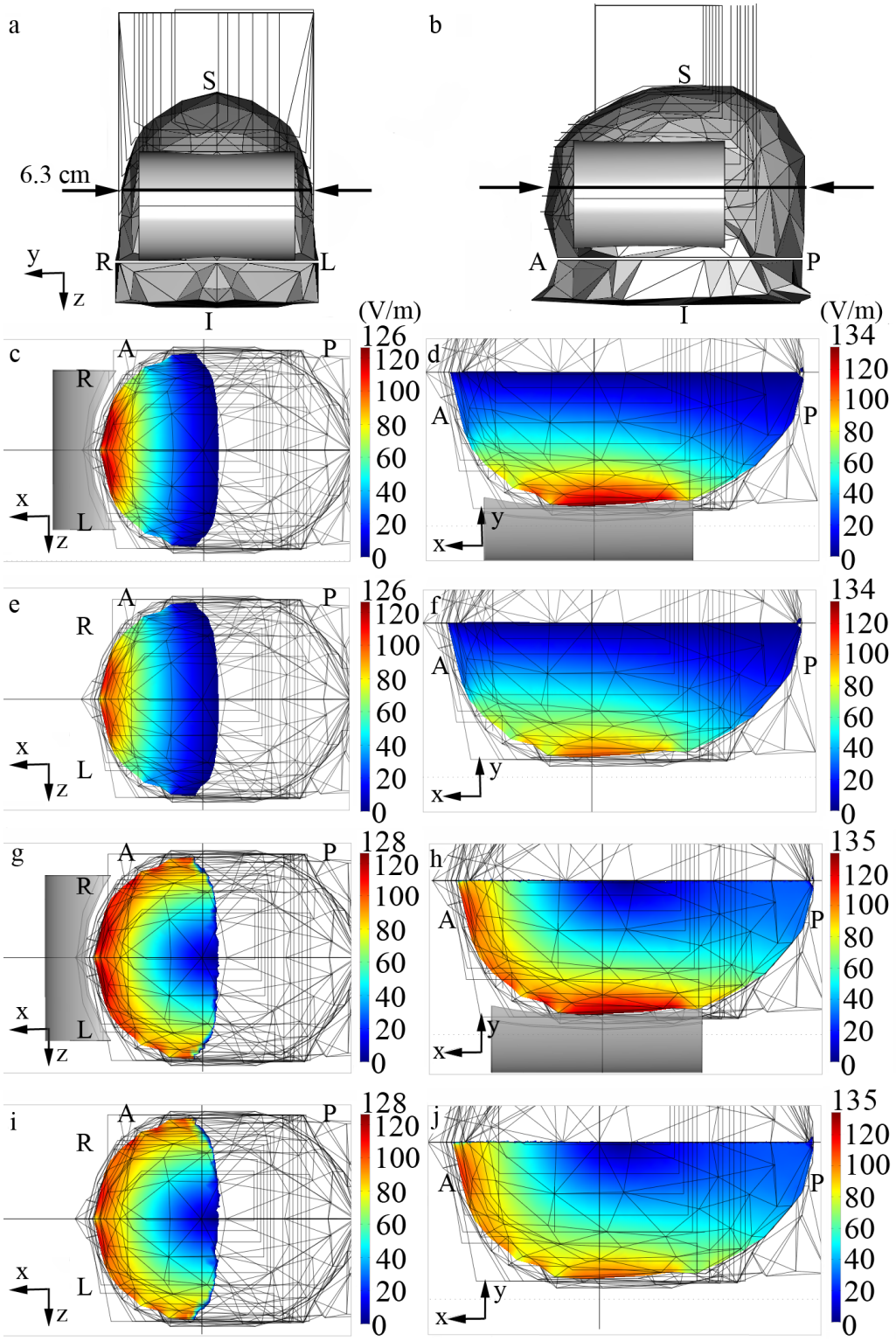

Figure 2.3.2.2: Total electric field induced in a slice located 6.3 cm below the head's vertex; (a) and (b) indicate the position of the axial slice with respect to the frontal and lateral cores, respectively; (c) and (e) show the field in the LR direction (*y* axis) and over the front of the head, with and without the frontal core, respectively; (g) and (i) show the field's norm for the two previous cases; (d) and (f) show the *x* component of the induced field in the PA direction and over the left hemisphere, for the model with and without the lateral core, respectively; (h) and (j) show the field's norm for the two previous cases.

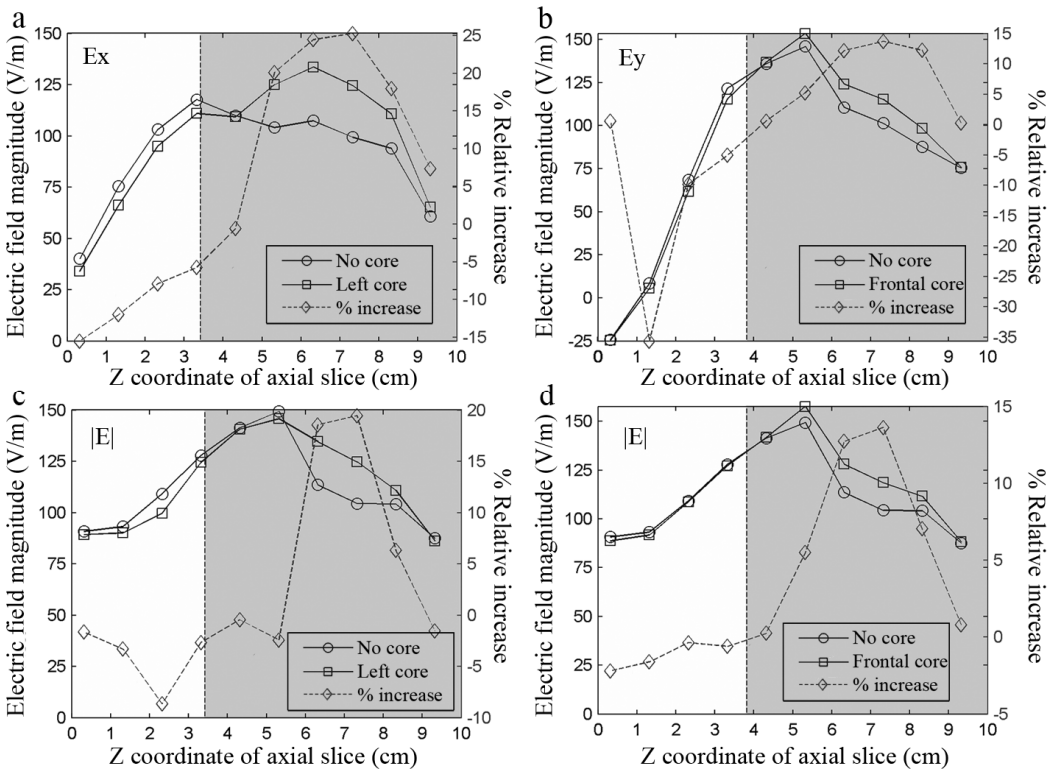

Figure 2.3.2.3: Maximum value of the electric field for several axial slices (z = 0 cm corresponds to the head's vertex); (a) displays the value of the field in the PA direction (x component), over the left hemisphere, for both the model with the lateral core and the model without it; (b) shows the field in the LR direction (y component), over the front of the head for the model with the frontal core and for the model without it; (c) and (d) show the maximum value of the field's norm for the lateral and frontal cores, respectively. The shaded area represents the slices covered by the core. The core's upper edge is located approximately at z = 3.4 cm in (a) and (c) and at z = 3.8 cm in (b) and (d).

increased over the left hemisphere, due to an increase of its x component, but not over the front of the head. The increase of the maximum value of the field's norm over some axial slices was usually lower than the increase of the maximum value of the field's x component over the left hemisphere (e.g. slices z = 5.3 cm and z = 8.3 cm in Figure 2.3.2.3 c). That happened because the maximum value of the field's norm at those slices was mostly determined by the y component of the field over the front of the head.

The frontal core had a similar effect to the core over the left hemisphere; only now it was the y component of the field over the front of the head that was affected (compare Figure 2.3.1.2 c and e). In this configuration, the core tended to slightly decrease the field in the slices located above it (except for the upper slice, where the core slightly increased the field) and tended to increase the field in all other slices, as can be seen in Figure 2.3.2.3 b. Again, the maximum increase (14% of the field without the core)

occurred for the slices located near the middle of the core (z = 6.3 cm to z = 8.3 cm). This core configuration did not change significantly the x component of the field over either the right or left hemisphere (less than 1.3% for the slice depicted in Figure 2.3.1.2), as can be seen by comparing Figure 2.3.1.2 g and i, which show that the most significant difference observed in the field's norm was over the front of the head. The y component of the field in the back of the head was not affected significantly (2.3% for the same slice). Contrary to what happened for the model with the lateral core, the increase of the field's norm due to the presence of the lateral core was about the same as the increase of the y component of the field over the front of the head (compare Figure 2.3.2.3 b and d), as the latter was usually the dominant component for the axial slices located under the core.

The increase in the primary component of the field ($-\partial\vec{A}/\partial t$) due to the presence of the core was always greater than the increase in the total electric field. For the core placed over the left hemisphere, the maximum increase in the primary field's component (in the PA direction) was 46% of the value without the core, to be compared to a 25% maximum increase in the total electric field. The frontal core had a maximum increase of 29% in the primary component of the field (LR direction) and only a 14% maximum increase in the total field. This effect was due to the increase in the secondary component of the field ($-\vec{\nabla}\phi$ component) as a result of the presence of the cores. This secondary source of the field tended to oppose the primary source thereby decreasing the total electric field.

Calculations were also conducted to determine the effects of charge accumulation in the boundary that divides the head model at the level of the nasion (z = 11 cm). The results indicated that the presence of the boundary only slightly changed the overall field distribution, this effect being greater closer to the boundary. For a plane located at z = 6.3 cm, for instance, the maximum difference between the field's norm was less than 1% of the values obtained in the model without the boundary. For a plane located 1 mm above the boundary, this value increased to 4.4%.

Field decay

As was seen previously, the relative increase in the field's magnitude caused by the presence of the core was higher for the lower axial slices than for the upper ones. Consequently, the field's decay along SI lines was reduced. This effect applied to both

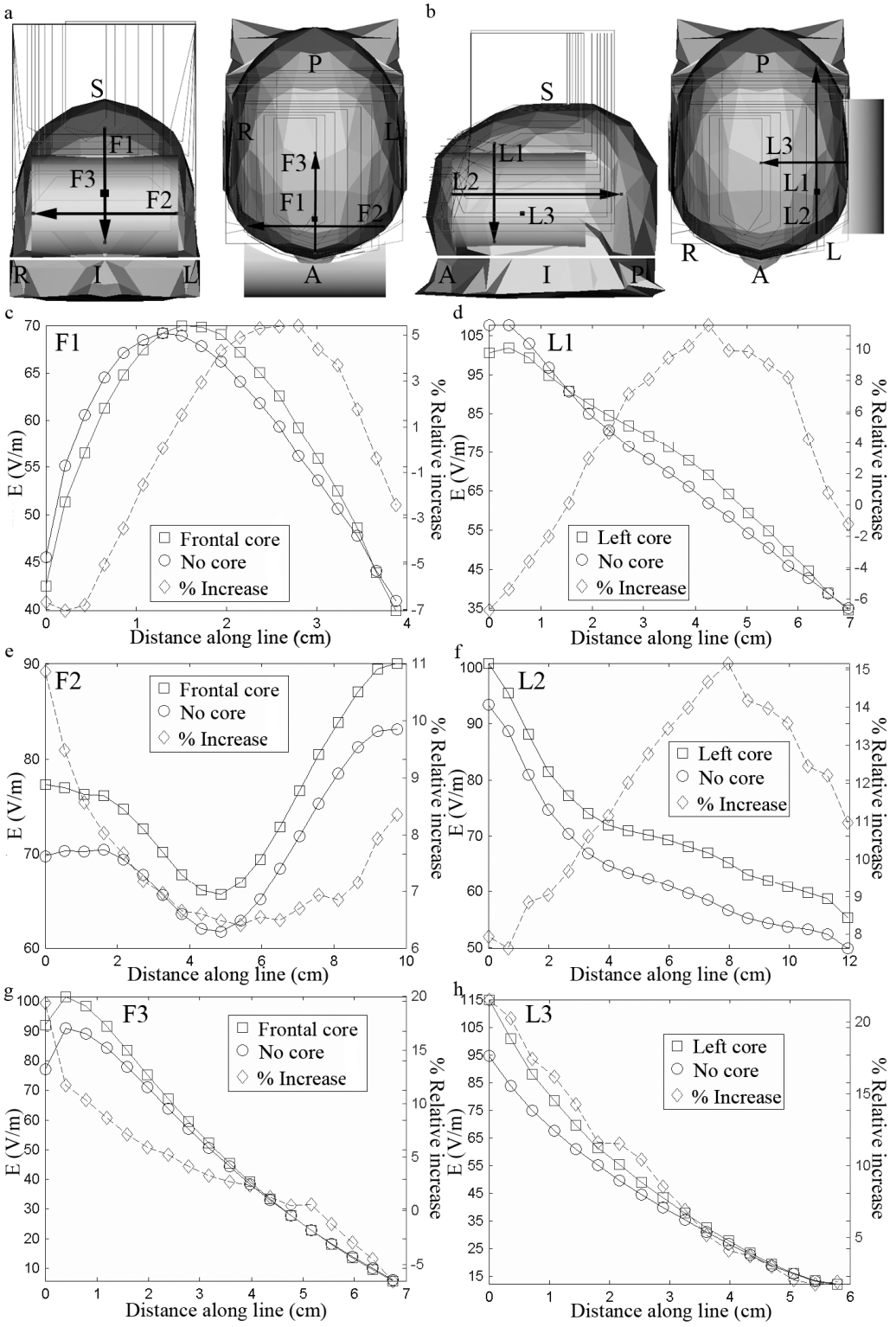

Figure 2.3.2.4: Effects of the two core configurations on the electric field norm along six test lines, shown in (a) and (b). The effects of the frontal core were investigated along lines F1–F3 (shown in (a)), whereas the effects of the lateral core were investigated along lines L1–L3 (shown in (b)). The plots on the left column show the field along lines F1–F3. The field along lines L1–L3 is shown by the plots on the right column. Lines L1 and L2 are located at a maximum distance of 2.1 cm from the scalp on the left, whereas lines F1 and F2 are located at maximum distances of 2.35 cm and 2.3 cm, respectively, from the scalp on the forehead.

core configurations used and is illustrated in Figure 2.3.2.4 c (frontal core) and d (lateral core) for lines F1 and L1, the positions of which are indicated in Figure 2.3.2.4 a and b. Along line L1, the field increased by as much as 12%, whereas along line F1 it increased by as much as 6%.

The effect of the core on the field's decay along AP lines varied according to the position of the core. If the core was placed over the front of the head, the decay along these lines tended to become faster. This was caused by the fact that, with this core, the field's relative increase was high near the front of the head and diminished as more posterior regions of the head were considered. This is shown by line F3 (Figure 2.3.2.4 a) for which the field increase reached 19% close to the core but only 3% at a distance of 3 cm from it (Figure 2.3.2.4 g). For the left core, however, the decay of the field along PA lines, located in the left hemisphere, tended to decrease. This can be seen by analysing the effect of the core along line L2 (Figure 2.3.2.4 b). The plot in Figure 2.3.2.4 f shows that the core increased the field for all points along the line. However, as this increase was higher for more posterior regions of the line, the field's decay slightly decreased (maximum decrease of 4%).

The field's decay along LR lines also depended on the core's placement. For these lines, the decay increased when the core was placed over the left hemisphere as the field's relative increase tended to diminish for points further away from the left hemisphere. This is illustrated by line L3 (Figure 2.3.2.4 b), for which the field increase due to the core dropped from 22% near the core to 7% about 3 cm from it (Figure 2.3.2.4 h). When the core was placed over the front of the head, the field's decay was not significantly changed. This effect is illustrated in Figure 2.3.2.4 e for line F2. Along this line, the field's relative increase was approximately constant (ranging from 6% to 7%) for almost all points, except for the beginning and endpoints, where it rose by as much as 11%.

Field focality

The calculated HPR areas are shown in Table 2.3.2, together with the total area of each of the four concentric ellipsoids used to study the focality. The core over the left hemisphere tended to decrease the field's focality, particularly for the larger ellipsoids, which are closer to the core: the increase in HPR area for the smallest ellipsoid was of only 2%, whereas it reached 20.3% for the largest ellipsoid. The frontal core, however, had the opposite effect, increasing the field's focality. Again, the effect was more

pronounced for the larger ellipsoids than for the smaller ones: the HPR decreased by 15.3% for the larger ellipsoid and by 9.3% for the smaller ones.

Table 2.3.2: Focality for several core-coil configurations as measured by the area of the HPR for the field's norm. The HPR values were calculated from the modelled total electric field data.

Ellipsoid's area (cm^2)	H1 without core (cm^2)	H1 with core over the left hemisphere (cm^2)	H1 with core over the front of the head (cm^2)
438.0	64.2	77.2	54.3
301.4	80.0	84.6	68.6
189.8	59.6	61.6	53.3
103.2	35.9	36.6	32.5

2.3.3 Discussion

Field induced by the H1 coil

The results shown for the total electric field inside the head model induced by the H1 coil without the core agree well with experimental results published previously (Roth et al., 2007) for the same coil. In particular, there is a general agreement in the spatial distribution of the field. Both sets of results show a high magnitude for the field in the PA direction over the left hemisphere and for the field in the latero–medial (LM) direction over the prefrontal and orbitofrontal cortices. Furthermore, the calculated coil's inductance is very similar to the one measured for the H1 coil: 22 μH. The coil modelled in this work is, therefore, a good approximation of the real H1 coil that is being used in several clinical trials today.

Effects of the use of ferromagnetic cores

Regarding the effect of the core on the induced electric field's magnitude, it was found that the core increased it for the axial slices located near the core and decreased it for the axial slices located above the core. The increase in the field's magnitude predicted in this study is not as high as the ones reported in other studies using high permeability cores. For example, Epstein and Davey (Epstein and Davey, 2002) reported a 100% increase at a distance of 2 cm from the coil; this is due to the fact that for conventional

coils (circular, figure-8) it is easy to wind the coil wires tightly around the core. The open design of the H1 coil reduces the coupling of the magnetic flux produced by the current in the coil into the core. This low coupling also explains why the core did not increase the inductance of the coil significantly (always less than 3%). Even if the inductance increase were high, it could be kept within the operating range by reducing the number of coil windings. Some studies indicate that the field induced with the core is still stronger than the field without the core when the inductance is kept constant using this approach (Epstein and Davey, 2002).

The maximum increase in the field's magnitude varied with core configuration, being higher for the lateral core (25%) than for the frontal core (14%). This effect was probably due to differences between core design and wire configuration under the core, which may have lead to a more efficient coupling between the wires and the core over the left hemisphere.

The core located over the left hemisphere increased the field in that region but it did not change significantly the field induced over the right hemisphere. This lead to an increase in the asymmetry of the field, which under threshold stimulation parameters would make the coil much more selective for stimulating regions in the left hemisphere. The H1 coil was already designed with that intent (Roth et al., 2007); however, the core significantly improved this tendency.

The fact that the core increased the field's magnitude for the lower axial slices (the ones located nearer the core) and decreased it for the slices located above the core is important, causing a slower decay of the field along SI (z axis) lines. This allows for a more efficient stimulation of neural structures located deeply along this axis, without increasing the field induced in regions located above the cores. The effect of the cores on the field's decay along LR and AP lines depended on core position. These effects can be understood by noting that the cores increased the magnitude of the dominant component of the field near the region they were placed over. Hence, over the left hemisphere, the increase was higher in more posterior regions of this hemisphere because there the wires were placed closer to the core whereas near the front of the head the wires bended away from the core. This explains why the decay in AP lines decreased in the presence of the lateral core. Also, because the effect of the core tended to decrease with distance from it, the decay in the LM direction increased. Over the front of the head, the wires were all at about the same distance from the frontal core,

which explains why the core did not change significantly the field's decay along LR lines but increased the decay along the AP direction.

The cores also affected the focality of the field. While the core placed over the left hemisphere increased the HPR, therefore decreasing the field's focality, the frontal core decreased the HPR, hence improving the field's focality. This was caused by the fact that without the core, the field induced by the coil in the lateral–medial direction over the prefrontal and orbitofrontal cortices was stronger than the field induced in the PA direction over the left hemisphere. The core over the left hemisphere increased the latter component of the field causing the HPR to cover not only the front of the head but also the left hemisphere, which explains the decrease in focality. The frontal core, however, shifted the HPR even more to the front of the head, by making the LM component of the field larger. This focality increase that occurred when the core was placed over the front of the head might be important in applications where one of the regions of interest is located in the vicinity of the orbitofrontal cortex.

Model limitations and future work

One of this work's limitations is that the head model used, while having the gross geometric shape of a human scalp, did not take into account tissue heterogeneity and anisotropy, which have been shown to significantly alter the field distribution in TMS (Miranda et al., 2003; De Lucia et al., 2007). The usage of a more realistic head model that takes these two factors into account will prove useful in the exact prediction of the effects of the field induced by these coil/core model but should not change much the conclusions reported here regarding the effects of the ferromagnetic cores on the field induced by the H1 coil. These depend mainly on charge accumulation at the scalp/air interface, which is well approximated by the homogenous and isotropic head model used in this work.

Because the cores affected the electric field more in the area underneath them, it is possible that stimulation with these coils might activate some muscles and nerves in the scalp, causing pain to the patient. This effect might be reduced by placing the cores further away from these areas or by reducing the stimulator's output. Determination of the ideal placement of the cores as well as of stimulator's output can only be obtained via experimental trials.

Finally, it should be pointed out that similar core designs may also be applied to the H2 coil (Roth et al., 2007) or other H coils. The present results also do not exclude the possibility that other coil designs may be more appropriate for integration with high permeability cores. Simultaneous optimization of coil and core design may lead to further improvement in the stimulation of deep brain regions.

3 Field – single neuron interaction in TMS of the human motor cortex

There are several possible mechanisms through which the electric field induced during TMS can stimulate neurons. *In vivo* and *in vitro* studies have provided useful insights on the dominating stimulation mechanisms in peripheral nerve stimulation but those results cannot be immediately extrapolated to brain stimulation, because neurons in the brain have more complex geometries and establish several interconnections with other neurons. In this chapter the FEM method is used to determine the electric field induced along models of neurons during TMS. This extracellular field distribution is then incorporated into the cable equation. The solution of this equation yields the spatial and temporal variation of the transmembrane potential for the neurons modelled. The results obtained highlight the importance of tissue heterogeneity and some geometric features of neurons, mainly bends and terminations, on activation of neurons in the motor cortex.

3.1 Introduction and objectives

Mechanisms of neuronal activation on TMS

In Chapter 1 it was stated that the steady-state polarization induced by the electric field applied along the axis of a straight neuron can be predicted by the activation function, which for the case of TMS can be written as:

$$S = -\lambda^2 \frac{\partial E_x}{\partial x}$$

where E_x represents the electric field along the axis of the neuron.

The activation function predicts that a long, straight and homogeneous neuron will become depolarized at the peak negative-going spatial derivative of the induced field measured along the nerve (see Figure 3.1.1), a site referred to as the 'virtual cathode'. At the positive-going peaks of the field's derivative, the 'virtual anodes', hyperpolarization occurs. *In vivo* and *in vitro* studies have confirmed these stimulation sites for peripheral nerve magnetic stimulation (Nilsson et al., 1992; Maccabee et al., 1993).

Neuronal excitation does not require, however, that the electric field has a spatial variation. Effective field gradients along the neuron can be generated even in presence of a locally uniform field, provided that the neuron bends or terminates in the field (Reilly, 1989), as is shown in Figure 3.1.2. Several *in vitro* and simulation studies have shown that stimulation at bends and terminations can be achieved at thresholds proportional to the peak electric field along the neuron at that site (Amassian et al., 1992; Maccabee et al., 1993; Nagarajan et al., 1993; Maccabee et al., 1998). In the case of fibre bends, the threshold is also dependent on the angle of the bend: shaper bends originate a greater effective gradient that leads to a greater depolarization (Roth, 1994). In the peripheral nervous system, bends and terminations are thought to have little influence on stimulation, given that those neurons are long and follow almost straight trajectories. Neurons in the brain, on the other hand, are short, which causes the electric field along them to be almost constant, and often bend (Maccabee et al., 1993). Hence stimulation of neurons in the brain is thought to occur at lowest thresholds in the regions where the total electric field is maximum, and not where it has a higher spatial variation.

Another factor that can significantly affect neuronal activation is the presence of inhomogeneities in the media surrounding the neurons. One early study investigated the effects of neuroforamina in nerve root magnetic stimulation (Maccabee et al., 1991). The authors found that when the induced field was predominantly perpendicular to the spinal cord, the presence of the non-conducting neuroforamina increased its magnitude and spatial derivative, thus facilitating the stimulation of nerve roots. Another study focused on the effects of muscle and fat inhomogeneity in peripheral magnetic stimulation of the median nerve in the elbow (Kobayashi et al., 1997). In that study it was shown that the charge accumulation occurring at the muscle-fat interface significantly distorted the primary field induced by the coil. The secondary field changed the field's spatial derivative along the neuron, leading to the appearance of

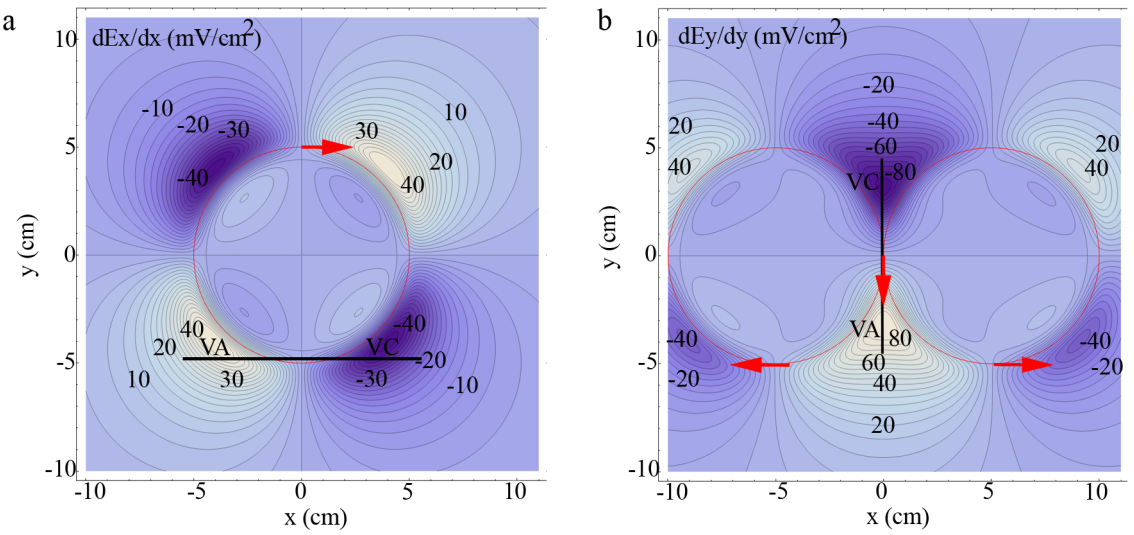

Figure 3.1.1: Contour plots of the gradient of the electric field induced by a circular coil (a) and a figure-8 coil (b). The thick black lines indicate the position of neurons placed underneath the coils. The coils are represented by the red circles and the direction of the current in the coil in the positive-going phase of the stimulus pulse is indicated by the red arrows. For the neuron indicated in (a), the peak negative value o *dEx/dx* is the point of maximum depolarization (virtual cathode, VC) and the peak positive value is where maximum hyperpolarization occurs (virtual anode, VA). In (b) the same explanation holds, but now considering the value of *dEy/dy*, given that the neuron is aligned with the *y* axis in that figure. Each coil contains only one turn. The circular loops comprising the circular coil and the figure-8 coil have the same dimensions: 5 cm radius. The values shown are for a stimulator output of 67.7 A/μs.

virtual cathodes at the nerve even in coil orientations that induced a field predominantly perpendicular to the nerve. Tissue heterogeneities have also been proposed to be very important in stimulation of neurons in the brain. These neurons often cross the interfaces that separate media with different electrical conductivities, as is the case of the WM-GM interface. Thus, the field along these neurons is discontinuous at the interface. The jump in the component of the electric field normal to the interface can be quantified according to the following expression (Miranda et al., 2003):

$$\Delta E_n = -2\left(\frac{\sigma_1 - \sigma_2}{\sigma_1 + \sigma_2}\right)\frac{\partial \vec{A}}{\partial t}\cdot\vec{n} \qquad \textbf{3.1.1}$$

where σ_1/σ_2 is the electrical conductivity of the media before / after the interface, as determined by the direction of the electric field, and $-\partial\vec{A}/\partial t\cdot\vec{n}$ is normal component of the primary electric field at the interface. This field jump may lead to a substantial polarization of the membrane potential (Liu and Ueno, 2000; Miranda et al., 2003).

For a given neuron, any of the aforementioned stimulation mechanisms can be the

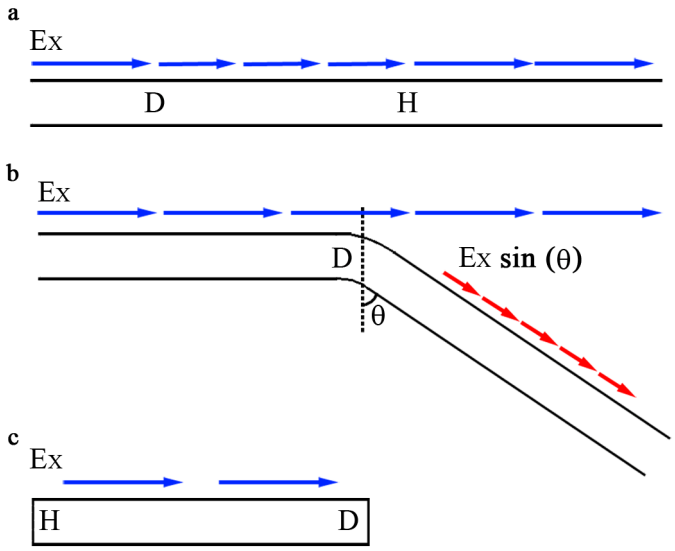

Figure 3.1.2: Possible stimulation mechanisms of a neuron. The blue arrows indicate the induced field at the region where the neuron is located. The size of the arrows is proportional to the magnitude of the field along the neuron. (a) Field along the neuron has a spatial variation. The neuron's membrane becomes depolarized when the variation is negative and hyperpolarized when it is negative; (b) Neuron bends in a region where the field is homogeneous. The first half of the neuron is aligned with the induced field, but along the second half the field is smaller (red arrow). Therefore, at the region of the bend a depolarization occurs; (c) Small neuron is located in a region where the field along it is homogeneous. The neuron's membrane is depolarized at one termination (the one towards which the field is directed to) and hyperpolarized at the other. (Illustration based on (Ruohonen, 1998))

dominant one, depending on several factors such as the geometry of the neuron, the properties and geometry of the media surrounding the neuron, the orientation of the coil or the direction of current in the coil. The only way to determine the influence of all these factors is through numerical modelling.

The human motor cortex

The lack of knowledge about the dominant stimulation mechanisms for each type of neuron in the brain makes it difficult to interpret the results obtained when stimulating certain regions of the brain with TMS. Perhaps the best example of such is the stimulation of the motor cortex with TMS.

The primary motor cortex (M1) is one of the many cortical and sub-cortical areas involved in the control of voluntary movement (Brodal, 1998). It is located in the caudal part of the precentral gyrus, extending from the lateral sulcus to the medial part of the cerebral hemisphere (see Figure 3.1.3 a). Fibres in M1 project to interneurons and motor-neurons on the contralateral side of the spinal cord. Thus it plays a key role in the

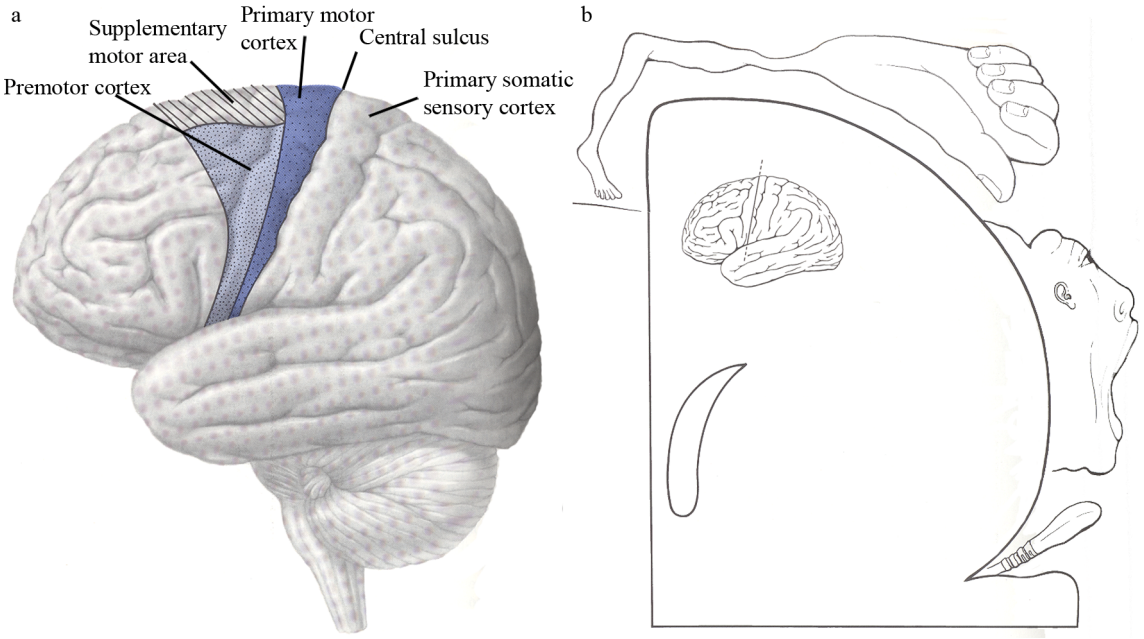

Figure 3.1.3: Schematic representation of the human motor cortex. (a) shows the location of the main cortical areas involved in the control of voluntary movement, as well as of the primary somatic sensory cortex. (b) shows a schematic view of a coronal section passing through the central sulcus, as shown in the inset. The figure shows the areas of the human body controlled by each part of the M1 and it shows the somatotopic organization of the motor cortex. (Figures adapted from (Martin, 1996)).

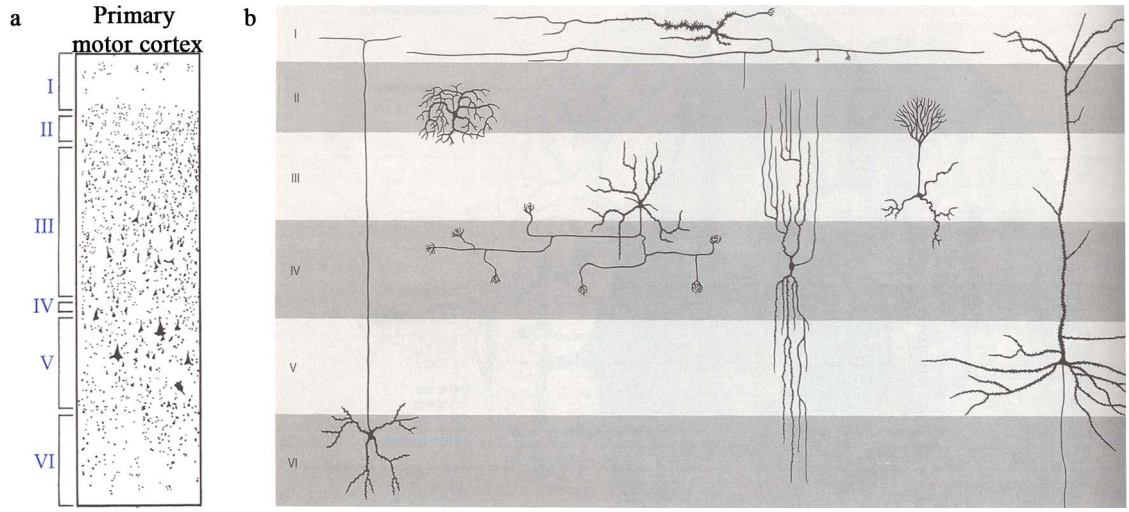

Figure 3.1.4: Laminar organization of the human motor cortex. (a) shows the cytoarchitectonic organization of the primary motor cortex, as viewed from Nissl-stained sections. Layers II and IV are virtually absent, whereas layer V contains the large somas of pyramidal cells. (b) shows a representation of the most common types of cortical neurons. Starting from the left, the first six neurons represent cortical interneurons, whereas the last neuron represents a pyramidal cell. For the pyramidal cell, the soma is contained in layer V, the apical dendrite rises perpendicularly towards layer I and the axon exits the GM. (Figure (a) adapted from (Martin, 1996); figure (b) adapted from (Standring, 2004)).

execution of voluntary movement. The mapping of the different muscles in the body into M1 follows a somatotopic organization, with adjacent body parts being represented in adjacent sites in the cortex, as shown in Figure 3.1.3 b.

From a cytoarquitectonic perspective, M1 is, like other cortical areas, organized horizontally into layers (see Figure 3.1.4 a) and vertically into columns ~300 μm wide separated by cell-sparse regions 100 μm wide (Mountcastle, 1997). The layers are numbered from I to VI, I being the most superficial layer and VI the deepest one. In the motor cortex however, layer IV is very underdeveloped and layers III and VI are larger than in other cortical areas (Martin, 1996). The two previous layers are enlarged because they contain the somas of very large cells, termed pyramidal neurons. Pyramidal neurons in layer V send their axons through the WM as part of the pyramidal tract and are thus called pyramidal tract neurons (PTNs). The latter contains two sets of neurons: the corticospinal tract neurons (CTNs), which project directly to the spinal cord, and the corticobulbar tract fibres, which project to the brain stem. Pyramidal neurons in layer III send their axons primarily to other areas of the cortex, thus providing long range communication between different cortical areas. These neurons are called pyramidal association fibres. The non-pyramidal cells in the cortex are interneurons, cells with axons that do not reach the WM (Figure 3.1.4 b). Some of these interneurons have an axon which courses vertically across the cortical layers, either towards the cortical surface or the WM; other interneurons have axons that project horizontally (Brodal, 1998). These interneurons provide short-range intracortical communication between cortical columns.

TMS of the motor cortex

Before the discovery that TMS could stimulate the motor cortex (Barker and Jalinous, 1985), other forms of stimulation using electrodes were used to that effect. One example of such a study used electrodes to stimulate the exposed motor cortical surface of cats and monkeys, and then recorded evoked activity in the pyramidal tract (Patton and Amassian, 1954). The results showed that the stimulating current pulse evoked a short latency wave complex followed by a series of low voltage inflections. The authors termed the first wave a D (Direct)-wave because, due to its latency, it was thought to result from direct stimulation of the PTNs emanating from the motor cortex. The inflections following the D-wave were termed I (Indirect)-waves. Because the latter had

a longer latency than the D-wave and disappeared when the cortex was damaged, I-waves were thought to result from transsynaptic activation of PTNs via cortical interneurons. Later studies in humans using anodal transcranial electric stimulation (aTES), where one electrode (the anode) is placed approximately over the motor cortex and the other electrode (cathode) is placed above the head's vertex, showed that at threshold intensity, a D-wave was evoked, followed by I-waves as the intensity of stimulation rose (Figure 3.1.5, top waveform) (Di Lazzaro et al., 1998).

TMS of the motor cortex has also been shown to elicit D- and I-waves, although the patterns of recruitment of these waves differ from what is observed with electrical stimulation (Day et al., 1989). Furthermore, the results obtained with TMS vary substantially with the geometry of the coil that is used, the orientation of the predominant component of the induced electric field, the stimulus waveform (monophasic or biphasic) and the intensity of stimulation. One common setup that has been shown to evoke motor responses at lowest thresholds, employs a figure-8 coil with its central section placed approximately perpendicular to the central sulcus, close to the representation of the hand-area in the motor cortex. With this orientation, the main component of the induced electric field is perpendicular to the central sulcus, either in the AP or PA direction. With a monophasic current pulse, the effects of this form of stimulation depend essentially on the direction of the induced field during the first phase of the *dI/dt* pulse. If the induced field during this phase points in the PA direction, at threshold intensity, descending corticospinal volleys recorded from the cervical epidural space show a series of volleys with latencies 1-1.4 ms longer than the D-wave evoked by aTES (Di Lazzaro et al., 1998). As stimulus intensity grows, the volleys increase in size and are followed by other volleys, as shown in the third line of Figure 3.1.5. Due to its latencies, these waves are termed I-waves and are numbered by order of recruitment. The interpeak interval between I-waves is 1.5 ms, which corresponds to a discharge frequency of 600 Hz (Di Lazzaro et al., 2008). At higher stimulus intensities, a D-wave is evoked that as the same latency as the D-wave evoked by aTES (Kaneko et al., 1996; Nakamura et al., 1996; Di Lazzaro et al., 1998; Di Lazzaro et al., 2001). On the other hand, if the field during the first phase of a monophasic *dI/dt* pulse points in the AP direction, late I-waves (I_3-waves, shown in Figure 3.1.5, fourth line) are generated at lowest threshold (Sakai et al., 1997). However this is not always the case, as in other studies early I-wave generation as well as D-wave generation have been reported, although these waves had a slightly longer latency than the I- and D-waves recorded

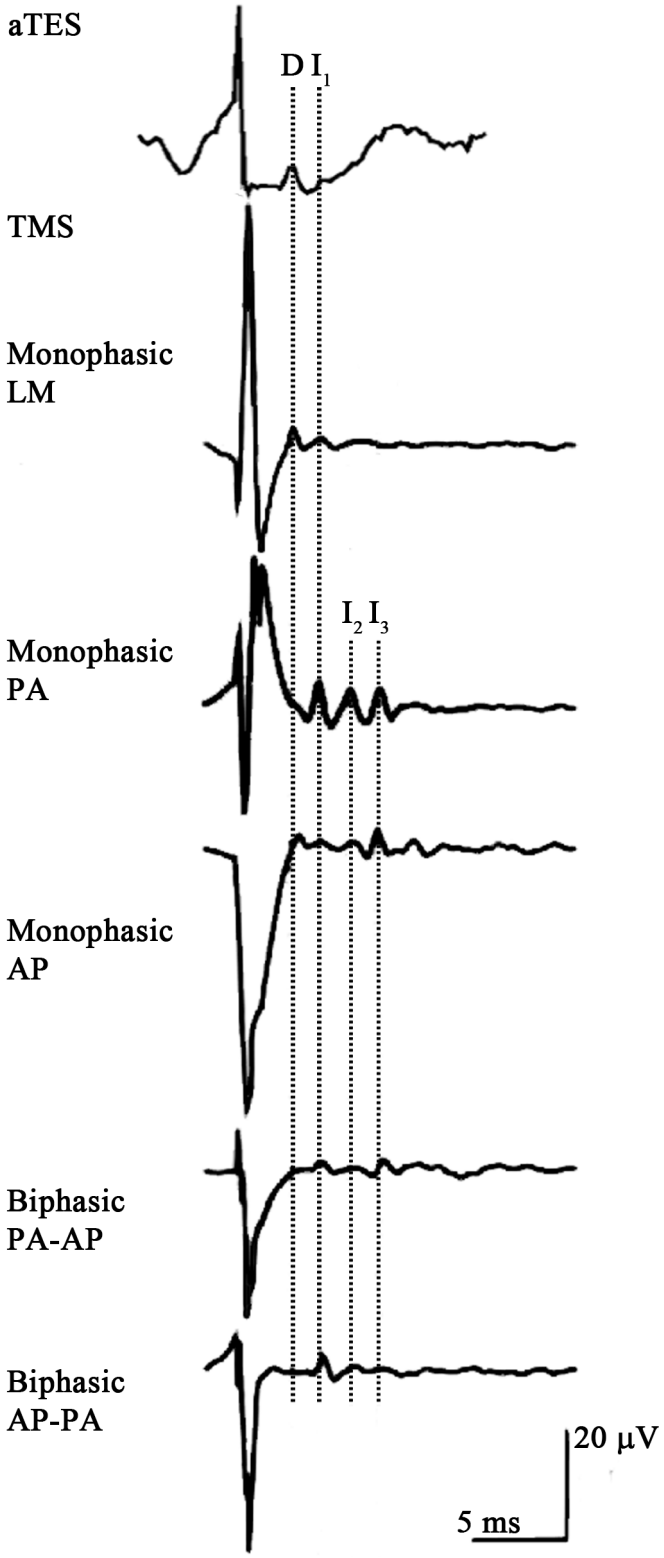

Figure 3.1.5: Typical D- and I-wave responses obtained from aTES and TMS with different orientations of the induced electric field. The waveforms shown are descending volleys recorded from the cervical epidural space. (Figures adapted from (Di Lazzaro et al., 1998) and (Di Lazzaro et al., 2008)).

after PA stimulation (Di Lazzaro et al., 2001). Regarding stimulation with biphasic pulses, the results are less consistent between subjects, even in the same study (Di Lazzaro et al., 2008). Biphasic stimulation when the electric field during the first phase points in the PA direction (often called biphasic PA-AP stimulation) yields several possible outcomes (Di Lazzaro et al., 2001): either an I_1-wave, a delayed I_1-wave followed, at higher stimulation intensities, by a delayed D-wave (latency difference of 0.3 ms between these waves and those elicited by PA stimulation), or an I_3-wave. Biphasic AP-PA stimulation, on the other hand, evokes a pattern of waves similar to that evoked by PA stimulation (Di Lazzaro et al., 2001). At threshold, this form of stimulation evoked I_1-waves with a latency 0.3 ms later than the I_1-waves evoked after PA stimulation (see Figure 3.1.5, last line). In some subjects a D-wave was also evoked at high stimulation intensities.

Another common setup uses a figure-8 coil but now oriented with its central section in the LM direction. Monophasic stimulation with this coil orientation has been shown to evoke, at threshold, D-waves with the same latency as the ones evoked by aTES followed by I_1-waves (Werhahn et al., 1994; Di Lazzaro et al., 1998; Di Lazzaro et al., 2001; Di Lazzaro et al., 2004b), as shown in the second line of Figure 3.1.5. As the intensity of the stimulating pulse increases, further I-waves appear.

Using a circular coil centred over the head's vertex, instead of the more common figure-8 coil, D-waves are preferentially elicited, although they tend to have a latency higher than those evoked after LM stimulation or aTES (Burke et al., 1993; Di Lazzaro et al., 2002). In other subjects, an I_1-wave was evoked instead of the D-wave.

Objectives

The first objective of this work was to test the hypothesis that tissue heterogeneities are possible sites for stimulation of neurons in TMS, and to quantify its importance as compared to other stimulation mechanisms. To do so, a model was created with a neuron that crossed an interface between two media with different electrical conductivities. The total electric field along this neuron was then calculated with the FEM, and it was then used in the solution of the cable equation. This way, the response of the modelled neuron to the field was calculated and the polarization induced at the interface was then compared to the polarizations induced at the neuronal terminations. The second objective of this work was to determine the stimulation mechanisms that rule activation of several types of neurons present in the human motor cortex. In order

to do so, an idealized model of the central sulcus was created, and the total electric field induced by a figure-8 coil placed over it was calculated using the FEM (Silva et al., 2008). The electric field was then used to determine the response of compartmental models of neurons. The results shed light on the dominant stimulation mechanisms of TMS of the motor cortex and are shown to be consistent with several of the experimental observations summarized above.

Published work

The work described in the following two sections originated one publication in an international peer-reviewed journal and one publication in conference proceedings.

P1: Miranda PC, Correia L, Salvador R, Basser PJ Tissue heterogeneity as a mechanism for localized neural stimulation by applied electric fields. Phys Med Biol 2007;52:5603-17.

Proc1: Salvador R, Silva S, Basser PJ, Miranda PC. A simulation study of the mechanisms that govern direct activation of pyramidal tract neurons in Transcranial Magnetic Stimulation. In: Kakigi R, Yokosawa K, Kuriki S editors. 16th International Conference on Biomagnetism. Sapporo: Hokkaido University Press, 2008:269-271.

Proceeding's paper, **Proc1**, was also presented in a poster session at the Biomag 2008 International Conference on Biomagnetism.

The work was also presented in a poster session at the 3rd International Conference on Transcranial Magnetic and Direct Current Stimulation, with the title 'A simulation study of the mechanisms that govern direct activation of neurons in the motor cortex by transcranial magnetic stimulation', Salvador R, Silva S, Basser PJ, Miranda PC.

A paper has been submitted to an international peer reviewed journal and is currently under consideration:

Salvador R, Silva S, Basser PJ, Miranda PC. Determining which mechanisms lead to activation in the motor cortex: a modeling study of transcranial magnetic stimulation using realistic stimulus waveforms and sulcal geometry.

3.2 Importance of tissue heterogeneity on neuronal activation during TMS

3.2.1 Methods

Volume conductor model and electric field calculation

In order to assess the importance of tissue heterogeneities in neuronal activation during TMS, a model was created similar to the one suggested by Liu et al. (Liu and Ueno, 2000). The model, shown in Figure 3.2.1.1, consisted in a rectangular hexahedron with dimensions (x, y, z) = 60 cm × 40 cm × 5 cm divided in half. One half of the hexahedron was modelled with an electrical conductivity similar to that of the grey matter at low frequencies, 0.333 S/m according to (Haueisen et al., 1997), whereas the other half was modelled with an a conductivity value similar to that of the white matter, 0.143 S/m also according to (Haueisen et al., 1997).

The model contained, above the hexahedron, a figure-8 coil oriented in such a way that its central section was perpendicular to the interface, i.e. aligned with the x axis. The coil was based on a commercially available model provided by Magstim: the Magstim Double 70 mm coil. Based on descriptions of the coil available on other works (Thielscher and Kammer, 2002; Thielscher and Kammer, 2004), the model of this coil contained two circular wings with 9 turns each. Each turn was represented in Comsol by a circular line with a radius given by the following expression: $r_i = 26.5 + 2.125\times (i\text{-}1)$ mm, i = 1 to 9.

Also contained in the model was a line parallel to the x axis, thus crossing the interface perpendicular to it. The line had a length of 6 cm and represented an idealized neuronal trajectory with 3 cm in each medium. This line was placed 3 cm below the plane containing the coil.

The model was created in Comsol using the same quasistatics package that has already been described in detail in Chapter 2 (see page 67/68). In this particular model, the mesh along the line representing the neuron was refined by decreasing the size of the mesh elements along it. The resulting finite element mesh contained 86833 tetrahedral elements. As in the models described in Chapter 2, Lagrange linear elements were used for the scalar potential (ϕ) and vector linear elements for the vector potential ($\vec{A}$). The model was solved using the GMRES iterative solver together with the Incomplete LU preconditioner. Contrary to the models described in Chapter 2, the drop tolerance set

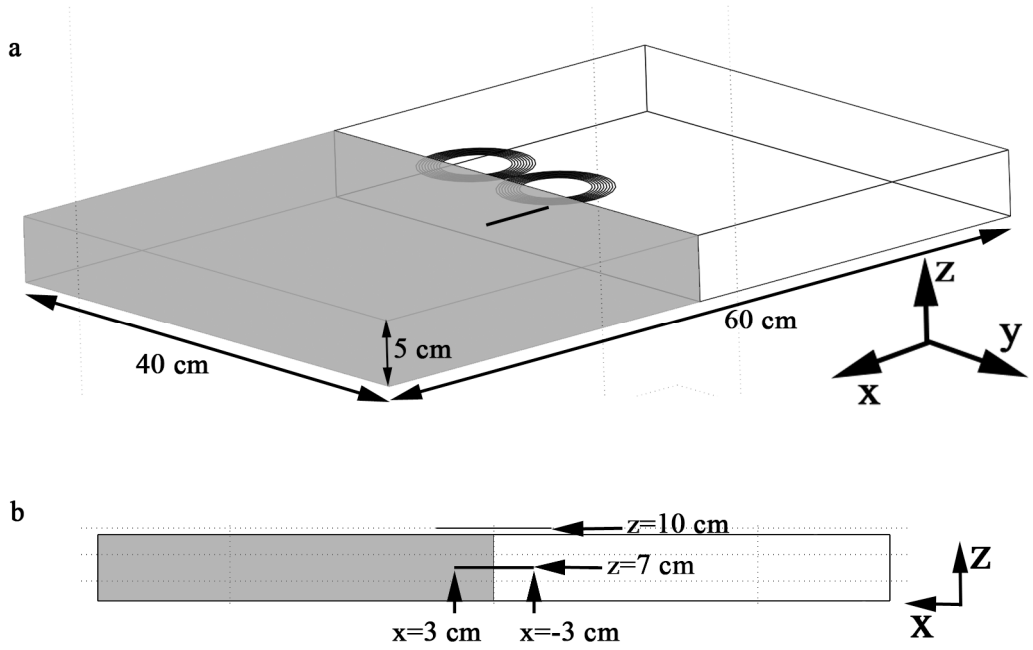

Figure 3.2.1.1: Two different views of the geometric model used to determine the influence of tissue heterogeneities on neuronal activation. The model dimensions are indicated in (a) and the dimensions of the line representing the neuron in (b). The line is placed 3 cm below the plane that contains the figure-8 coil. The half of the model coloured in grey represents the GM (σ = 0.333 S/m), whereas the other half represents the WM (σ = 0.143 S/m).

by default in Comsol proved to be sufficient for the solution to converge.

Calculation of the neuronal response to the induced electric field

The electric field calculated in Comsol was used to calculate the neuronal response of an axon, which was represented in the model by the line. This model of neuron did not include many of the sections usually represented in accurate neuron models, such as the initial segment, axon hillock, soma or dendrite. This simplified model was used given that it is usually the axon of neurons that crosses interfaces in the brain. One example of such is the axon of pyramidal neurons in the motor cortex, which crosses the GM-WM interface.

The morphological and electrophysiological properties of the modelled axon are described in detail in Appendix C. In summary, the axon contains myelinated sections, representing internodes, where the membrane is modelled as a passive RC circuit (see (Basser, 2004) for a complete description), and active Ranvier nodes. The properties of the membrane at the Ranvier nodes were based on the description of myelinated motor and sensory neurons of rabbits (Chiu et al., 1979; Werhahn et al., 1994). The external

diameter of the axon (including the myelin sheath) was of 10 μm, which corresponds to medium calibre pyramidal fibres according to Lassek (Lassek, 1942).

The properties of the axon model were used to solve a discretized version of the cable equation, 1.2.3.3. At each termination of the axon, sealed-end boundary conditions were implemented (Nagarajan et al., 1993), which guaranteed that charge could accumulate at each end. The resulting set of equations was solved using the backward Euler's method combined with Picard's iterative procedure with a tolerance of 10^{-6}. All algorithms were implemented in MatLab 7.1 (R14) SP3 (www.mathworks.com).

Finding a solution of the cable equation also required knowledge about the total electric field along the axon. The electric field was calculated in Comsol using the model described above. The field at 200 points equally distributed along the line representing the axon was then exported to MatLab and fitted using fifth order polynomial functions and Heaviside functions. The latter were required to model the field's discontinuity at the interface.

Another factor that greatly influences the neuronal response is the temporal variation of the electric field. As was mentioned in the previous chapter, Comsol assumes a harmonic variation of the current and of the fields with time. However, this is not an accurate description of the waveform of the electric field induced in TMS (see Chapter 1, page 38). In order to solve this problem, the spatial distribution of the electric field along the line was exported from Comsol at the time instant when it was maximum. In MatLab, the field was normalized by dividing it by the maximum value of the current's time derivative in Comsol: $2\pi f I_0$, where f is the frequency (5 kHz in this model) and I_0 the maximum value of the current flowing in the coil (3184 A). This normalized field was then multiplied by waveforms whose amplitude and time course were similar to the ones provided by a commercially available magnetic stimulator: the Magstim 200 stimulator (www.magstim.com). This stimulator outputs a waveform identical to the one shown in Figure 1.2.4.2 b (full line). The threshold values presented in the 'Results' section will be given either as the value of dI/dt provided by the stimulator, or as a percentage of the maximum stimulator's output (MSO). As previously discussed, for a magnetic stimulator this value is given by V_C/L, where V_C is the capacitor's charging voltage and L is the coil's inductance. For the Magstim 200 stimulator, $V_{C\,Max}$= 2800 V (Kammer et al., 2001) and for this coil L=16.35 μH (Magstim, 2005), which yields 171 A/μs for the value of dI/dt_{Max} at the maximum stimulator's output (MSO).

3.2.2 Results

Electric field along the axon

The electric field along the line representing the axon is shown in Figure 3.2.2.1. The field in the homogeneous model, where both media have the same electrical conductivities, is stronger directly under the coil's centre, where it reaches a maximum of 100.4 V/m. In the heterogeneous model the field is discontinuous at the interface between the two media. In the medium with smallest electrical conductivity, the WM, the field is stronger than the field in the homogeneous model; in the medium with highest conductivity, the GM, the field is always weaker than the field in the homogeneous model. At the interface, the field's jump reaches - 79.5 V/m, a value that is in good agreement with that predicted using expression 3.1.1, -80.2 V/m. At the axon's right termination, in the GM, the field reaches a value of 52.4 V/m.

Axon's response to the applied electric field

The field's discontinuity at the interface was capable of eliciting AcPts within operating range of the Magstim 200 magnetic stimulator. This is shown in Figure 3.2.2.2 for a stimulator's output of 61 A/μs. Another place where AcPt generation occurs is the right termination of the axon in the GM. These two AcPts collide in the GM and stop propagating. The AcPt generated at the interface continues to propagate through the WM. At the left termination of the axon, a strong hyperpolarization occurs during the first phase of the stimulating pulse, followed by a weaker depolarization during the second phase.

The maximum value reached by the membrane's potential at the interface and at the right termination as a function of stimulator's intensity is shown in Figure 3.2.2.3. The plot shows that for low stimulation intensities, the membrane's potential varies linearly with stimulator's output (subthreshold membrane phenomena). As the intensity of stimulation increases, the membrane's response is no longer linear. The figure also shows that the membrane's potential at the termination rises faster with stimulation intensity than the potential at the interface. Thus, the threshold for AcPt generation at the interface (53.6 A/μs, i.e. 31.3 % of MSO) is higher than the threshold at the termination (43.0 A/μs, i.e. 25.1 % of MSO).

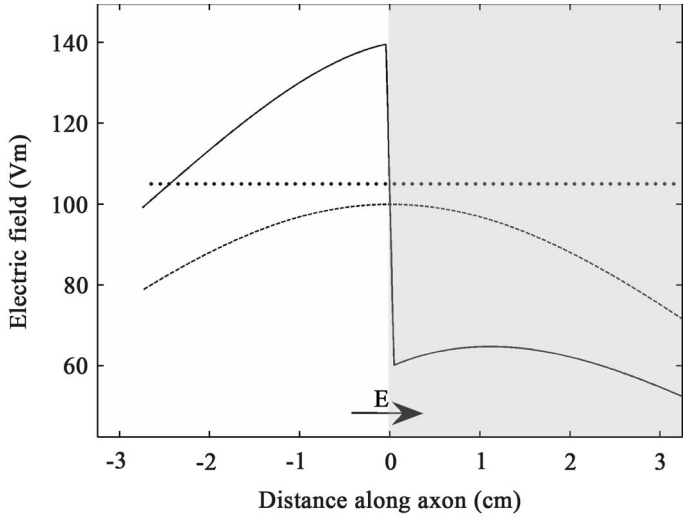

Figure 3.2.2.1: Electric field along the line that represents the axon. The dashed line represents the field in the homogeneous model (both media have the same conductivities), whereas the solid line represents the field in the heterogeneous case. The shaded portion of the plot represents the medium modelling the GM. The arrow indicates the direction of the electric field in the positive going phase of the stimulus waveform. These field values were obtained for a stimulator's output of 61 A/μs.

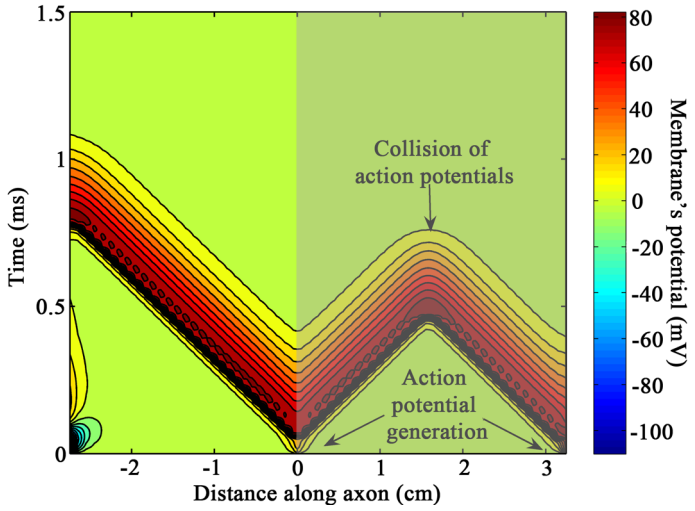

Figure 3.2.2.2: Contour plot of the membrane's potential as a function of distance along the axon and time for a stimulator's output of 61 A/μs. The 80 mV contour represents the maximum value of the membrane potential during the AcPt. The portion of the contour plot representing propagation in the GM (positive values for the 'Distance along the axon') is shown in dimmer colours.

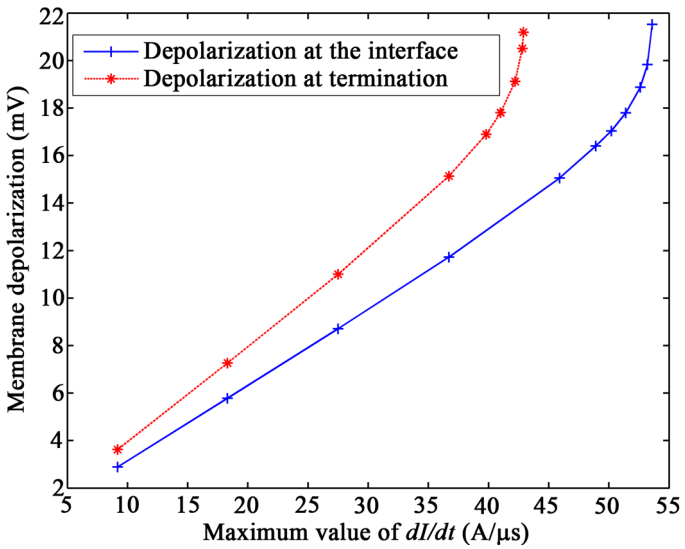

Figure 3.2.2.3: Membrane's depolarization as a function of stimulator's output. The red dots indicate the depolarization at the axon's termination in the GM, whereas the blue dots indicate the depolarization at the tissue's interface.

3.2.3 Discussion

Influence of tissue heterogeneities on the induced electric field

The presence of the tissue heterogeneity significantly affected the field induced by the coil, not only close to the interface but also at points far away from it. This is seen by the fact that, at 3 cm from the interface, the field in the heterogeneous model is still much different from the field in the homogeneous model. This shows that tissue heterogeneities do not influence neuronal activation only by creating a discontinuity on the field along the neurons. Instead, the effects of heterogeneities on the values of the field at the terminations can also significantly affect stimulation thresholds.

Stimulation thresholds

The results presented above indicate that the field's discontinuity, occurring at the interfaces between tissues with different electrical conductivities, can lead to the generation of AcPts. Furthermore, the thresholds for stimulation were well within the operating range of the Magstim 200 magnetic stimulator. This indicates that modelling tissue heterogeneities is essential in order to understand activation mechanisms in TMS.

In this particular model, the thresholds for AcPt generation due to charge accumulation at the axonal termination were, however, always smaller than the thresholds for AcPt generation at the interface. This result can be predicted by performing a steady-state

analysis of the cable equation. This analysis predicts that the depolarization at the axon's termination is proportional to λE_x (for $L >> \lambda$, where L is the neuron's length), where λ is the axon's space constant and E_x is the value of the field along the neuron at the termination (see (Roth, 1994) for more details). A similar analysis performed at the field's discontinuity at the interface yields that the polarization there is proportional to $-\lambda \Delta E_x / 2$, where ΔE_x is the jump of the electric field along the neuron at the interface (see (Plonsey and Barr, 2000)). Using the values for E_x and ΔE_x presented in the 'Results' section, the ratio between the polarization at the interface and the polarization at the axon's termination is 0.76. This value is in good agreement with the ratio of the thresholds for stimulation at the interface and at the termination: 0.80.

Significance

The results presented here indicate that the field jumps that occur at discontinuities in the electric conductivity at tissue interfaces can lead to significant membrane polarizations and thus influence the neuron's response. This stimulation mechanism is very important for neurons in the brain, as many of them often cross interfaces between tissues with different conductivities. One well known example are the pyramidal neurons, whose axons cross the WM-GM interface.

The importance of this stimulation mechanism, however, strongly depends on the geometry of the neuron. For instance, if the neuron has a trajectory predominantly perpendicular to the field induced by the coil, the fact that it crosses the interface will not lead to any significant changes in the field along it. In this case, the fact that the neuron crosses the interface will not lead to any significant membrane polarization. Furthermore, the fact that neurons often bend close to the interfaces may further complicate the prediction of which stimulation mechanism is more determinant in the stimulation of neurons in the brain during TMS.

This will be addressed in the second part of this chapter, which uses more realistic models for the neurons and the volume conductor in order to try to predict the dominant stimulation mechanisms of neurons in TMS of the motor cortex.

3.3 Modelling TMS of the human motor cortex

3.3.1 Methods

Sulcus model[1]

In the first part of this work, the electric field induced by a figure-8 coil in a model of the central sulcus was calculated along lines that represent the trajectories of several cortical neurons that have been described in the literature. A more detailed description of these neurons will be presented further ahead.

The model of the volume conductor that was used here is the same as the one used by S Silva et al. (Silva et al., 2008), and it is shown in Figure 3.3.1.1. This model contains a simplified straight central sulcus, with a maximum depth of 21 mm, and three different media representing the GM, WM and cerebrospinal fluid (CSF). These three media were modelled as homogeneous and isotropic media with electrical conductivities similar to those described in the literature for these tissues at the low frequencies (<10 kHz) of most TMS pulses: 1.79 S/m, 0.33 S/m and 0.15 S/m for the CSF, GM and WM, respectively (Robillard and Poussart, 1977; Gabriel et al., 1996b; Baumann et al., 1997; Haueisen et al., 1997). The layer representing the GM is modelled with a thickness of 3 mm, which represents the average cortical thickness in the M1 area.

The model also contains a figure-8 coil above the volume conductor, at a distance of 1 cm from the CSF / air interface and 3 cm from the GM / CSF interface. The coil is oriented in such a way that its central section is perpendicular to the sulcus. With this coil orientation the main component of the field is either in the PA or AP direction. The figure-8 coil is based on the same Magstim Double 70 mm coil described in the last section, because this coil is usually used in experimental protocols involving motor cortex stimulation.

[1] All the models and electric field calculations described in this part of the 'Methods' section were done by Sofia Silva. The interested reader can find more detailed information about this model on her PhD thesis.

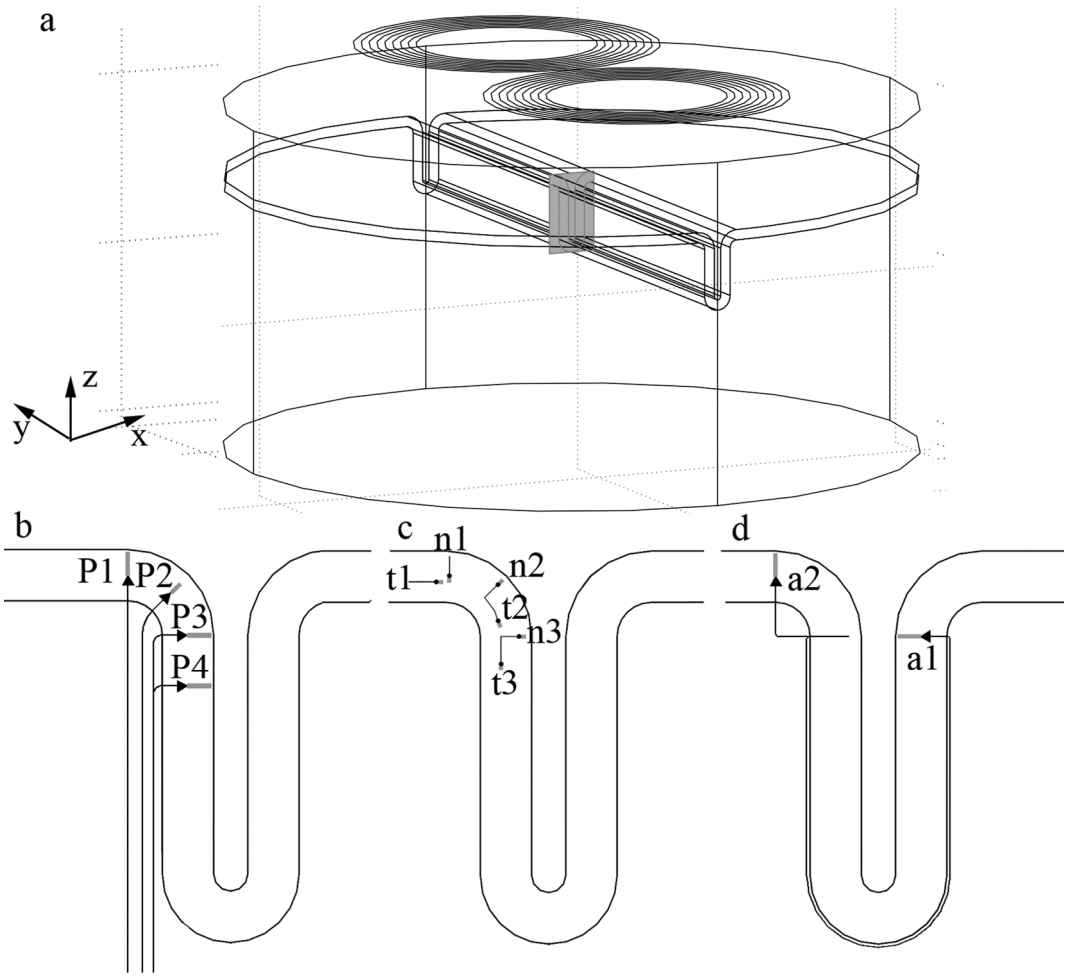

Figure 3.3.1.1: Volume conductor geometry used to model TMS of the human motor cortex. (a) Top view of the model, including the figure-8 coil and, directly under the central section of the coil, the plane that contains the modelled neurons. The plane is shown in light-grey; (b)/(c)/(d) representation of the modelled neurons. *P* neurons represent the PTNs; *t* and *n* neurons represent interneurons / axon collaterals with a predominant orientation either tangential or normal to the WM-GM interface, respectively; *a* neurons represent pyramidal association fibres projecting to the M1.

The model was built in Comsol 3.5 using the quasistatics package. As before, the mesh along the lines that represent the neurons was refined. The type of elements used and the choice for the solver were similar to the ones described in the previous work.

After the field was calculated, the component of the electric field tangent to the trajectory of each neuron, E_s, was exported from Comsol[2]. This field was then fitted using LabFit (http://www.angelfire.com/rnb/labfit/index.htm), ZunZun.com

[2] Up until know, the field along the neuron has been referred to as E_x. However, given that in this work E_x also represents the component of the field along the x axis, E_s is used instead.

(www.zunzun.com) or Microsoft EXCEL™. In order to determine the influence of the field due to charge accumulation at tissue boundaries, the component of $-\partial\vec{A}/\partial t$ tangent to the trajectory of each neuron, E_{sh}, was also calculated. The latter is a good approximation of the field that would be obtained in a homogeneous model of the sulcus (all tissues having the same electrical conductivity), provided that the charge accumulation at the model / air interface is negligible.

Temporal waveform of the electric field

In order to correctly model the temporal waveform of the field, E_s, exported from Comsol, a similar approach as the one described in the previous work was employed. In brief, E_s exported from Comsol was normalized by dividing it by the maximum value of *dI/dt* in Comsol. The field values were then multiplied by waveforms whose amplitudes and time courses are similar to the output of two commercial stimulators often use in experimental protocols: the Magstim 200 and the Magstim Rapid. The output of these stimulators is illustrated in Figure 1.2.4.2. The first stimulator outputs a monophasic current pulse, which results in a biphasic *dI/dt* pulse. The second stimulator outputs a biphasic current pulse, which results in a triphasic *dI/dt* pulse. Through the remainder of this work these two pulses will be referred to as either monophasic or biphasic, respectively, which applies only to the current's waveform. This is misleading, as the electric field induced in TMS is proportional to *dI/dt* and not to the current, however this convention will be followed here in accordance to common practice in the literature.

In addition to the waveform of the stimulus, the initial direction of the current in the coil was also varied. As a consequence, each neuron was tested with four different kinds of stimulating pulses that will be referred to as: monophasic AP, monophasic PA and biphasic AP-PA, biphasic PA-AP.

Like in the previous work, stimulation thresholds will be given either as the value of *dI/dt* provided by the stimulator or as a percentage of the MSO. As mentioned before, for the Magstim 200 stimulator connected to this coil dI/dt_{Max}=171 A/μs at MSO. The Magstim Rapid stimulator can be programmed to go up to dI/dt_{Max}=122 A/μs but, at that value, the stimulator's frontal panel indicates 120 % MSO[3].

[3] This information was provided by an anonymous reviewer.

Types of neurons modelled

In this work 12 different neurons were modelled, which are represented in Figure 3.3.1.1 b, c and d.

Neurons *P1-P4* represent large PTNs. The model for these neurons includes a large cell body located in layer V and a representation of the apical dendrite that terminates near layer I (Brodal, 1998; Standring, 2004). The model also includes a long axon that enters the WM perpendicularly to the GM-WM interface (Kammer et al., 2007), coursing through it in a direction parallel to the sulcus wall. Most of the axons of these neurons bend once they leave the GM in order to enter the internal capsule (Rothwell, 1997; Manola et al., 2005), a fact that is taken into account in this model.

Neurons *t1-t3* and *n1-n3* model interneurons that provide long-range intracortical connections within the motor cortex, via the GM (Brodal, 1998; Esser et al., 2005). Neurons of the first type (*t1-t3*) are oriented tangentially to the WM-GM interface, modelling intralayer connections. They have lengths of 2 mm (Esser et al., 2005) and are located in layer V. These may represent axon collaterals of pyramidal neurons or interneurons oriented predominantly tangentially to the cortical surface (Meyer, 1987; Brodal, 1998). Neurons *n1-n3* are oriented perpendicularly to the WM-GM interface and model interlayer connections between layers II/III and layer V (Esser et al., 2005), having an average length of 1.5 mm. These neurons may represent either PTN axon collaterals or interneurons with predominantly vertical orientation (Meyer, 1987). As was seen before, interneurons have geometries far more complex than those of the modelled neurons (see Figure 3.1.4 b). However, given that most of them align either tangentially or perpendicularly to the sulcus wall (Brodal, 1998; Fox et al., 2004; Standring, 2004), these two groups of cells ('*t*' and '*n*') are a good generalization of the possible orientations and positions of interneurons and axon collaterals in a sagittal section of the cortex.

Finally, neurons *a1* and *a2* model pyramidal association fibres. These neurons have their somas located in layer III of the cortical area of origin and project to pyramidal cells of the same layer (III) located in the primary motor cortex. Neuron *a1* projects from the primary somatosensory cortex (area 3b, in the posterior bank of the central sulcus) to area 4, in the anterior bank of the central sulcus. Neuron *a2* connects two areas of the motor cortex: the putative forelimb motor cortex on the precentral gyrus

(area 6) and the anterior bank of the central sulcus. The existence of these connections has been demonstrated in monkeys (Yamashita and Arikuni, 2001).

Every cell modelled in this work is contained in the vertical plane that separates the two wings of the coil, shown in light-grey in Figure 3.3.1.1 a.

Electrophysiological and morphological properties of the modelled neurons

The model of PTNs used in this work is based on a previous model proposed by Manola et al. (Manola et al., 2007) with a few changes. A full description of the properties of the modelled neurons is presented in Appendix C. In brief, the model contains active compartments (with sodium, potassium and leakage currents) that represent nodes of Ranvier, the initial segment and the axon hillock. The soma and apical dendritic tree were modelled by passive RC compartments, with a time constant of 10.3 ms and a space constant of 1.5 mm. The myelinated internodes were also modelled by passive RC compartments, but with properties different from the ones used to model the soma and dendrite (Tasaki, 1955).

Cortical interneurons and association fibres were modelled with the same membrane properties as the PTNs. It should be mentioned, however, that this is only a very rough approximation, especially for cortical interneurons (Tsugorka et al., 2007), for which the transmembrane potential is thought to behave differently from PTNs. In spite of that, and given that much is still unknown about the membrane properties of neocortical cells, the same model was used.

The different neurons modelled in this study have different morphological properties. The main differences are in the length of the apical dendritic tree (longer for pyramidal neurons than for cortical interneurons), and the size and shape of the soma (large flask shaped cell bodies for pyramidal cells and small cylinders for cortical interneurons). Also, the range of fibre diameters studied depended upon the type of neuron considered. For pyramidal cells, diameters varied between 6 μm and 20 μm, which corresponds to medium to large-sized pyramidal cells according to (Lassek, 1940). Cortical interneurons are thought to have smaller diameters, although accurate values are still largely unavailable (Manola et al., 2007). Here a range of fibre diameters between 3.5 μm and 6 μm was chosen, which corresponds to small to medium calibre pyramidal cells (Lassek, 1940).

Numerical solution of the discretized cable equation

The properties of each of the modelled neurons were used to solve a discretized version of the cable equation, 1.2.3.3. As was done in the work described in the previous section, at each termination of the neuron, sealed-end boundary conditions were implemented. However, unlike the last work, the resulting set of equations was solved by using a Crank Nicolson's method with a staggered time grid. This method is as reliable as the backward Euler's method, which was used in the work described in the last section, but is more accurate, as was discussed in Chapter 1 (see page 55). Furthermore, the use of a staggered grid approach prevented the need for an iterative procedure, which highly decreased computational time. All algorithms were implemented in MatLab 7.1 (R14) SP3 (www.mathworks.com), and they are described in more detail in Appendix D. A typical calculation took less than 1 minute to perform on a computer with a 2 GHz dual core processor and 2 Gb of RAM.

Several calculations were performed in order to test the accuracy of this algorithm, as is described in full detail in Appendix D. In these calculations the results obtained using the algorithm implemented in MatLab were compared with the results obtained using a well established software for the solution of compartmental neuron models: Neuron 6.0 (http://www.neuron.yale.edu/neuron/). The analysis of the results obtained using the two programs showed a good agreement between them, both in the stimulation thresholds and in the time and space variations of the transmembrane potential.

3.3.2 Results

Electric field along neurons

The effective electric field, E_s, along cortical interneurons is shown in Figure 3.3.2.1 for *t* neurons and in Figure 3.3.2.2 for *n* neurons. In those figures, negative values E_s indicate that the effective electric field is directed from dendrite to axon terminal, the opposite applying to positive values of E_s. The electric field along cortical interneurons was high for neurons parallel to the plane of the coil (*xoy* plane in Figure 3.3.1.1) and positioned close to it, and low for neurons not completely parallel to the same plane or located further away from the coil. This way, neuron *t1* had the highest value of E_s,

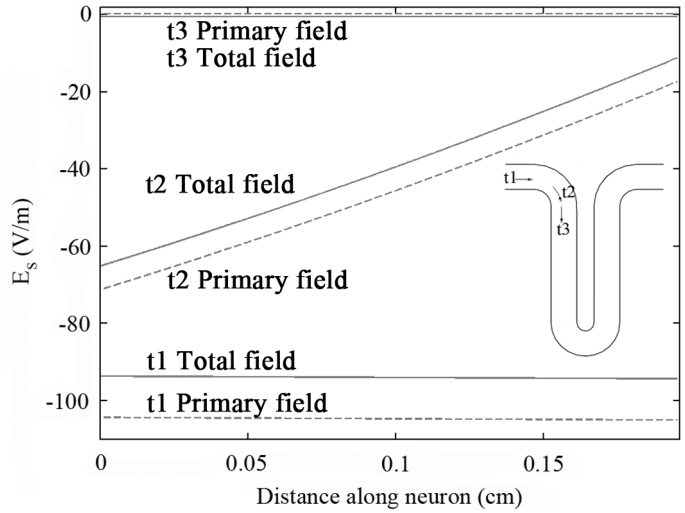

Figure 3.3.2.1: Spatial variation of E_s and E_{sh} for the cortical interneurons located tangentially to the GM-WM interface. The position of the neurons in the sulcus model is shown in the figure's inset. All field values were obtained for a stimulator's output of 67.7 A/μs. In the figure, distance is measured from the axon terminal towards the dendrite.

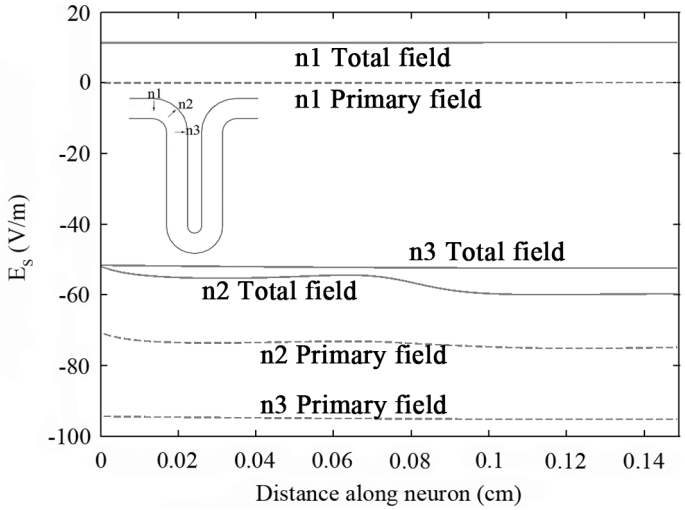

Figure 3.3.2.2: Spatial variation of E_s and E_{sh} for the cortical interneurons located perpendicularly to the GM-WM interface. The position of the neurons in the sulcus model is shown in the figure's inset. All field values were obtained for a stimulator's output of 67.7 A/μs. In the figure, distance is measured from the axon terminal towards the dendrite.

reaching -94 V/m for a stimulator's output of 67.7 A/μs[4]. Neurons *n1* and *t3*, on the other hand, are perpendicular to the plane of the coil and, as such, the effective electric

[4] This value of stimulator's output was chosen because it corresponds to the resting motor threshold (RMT) value identified by Kammer et al (2001) for monophasic PA stimulation with the Magstim 200 stimulator and a figure-8 coil similar to the one modelled in this study.

field along them was the lowest among all the modelled interneurons resulting only from charge accumulation at the boundaries. Neuron *n3*, located in the sulcus wall, is also aligned parallel to the coil but is located further away from it. Therefore E_s along it was smaller than along *t1*, with a maximum value of only -52 V/m for the same stimulator's output. Neurons *n2* and *t2* are not completely parallel to the coil's plane but are located very close to it. The effective electric field along these neurons had roughly the same magnitude as along neuron *n3*. Another important characteristic of E_s along *t* and *n* neurons was that it was almost constant (see Figure 3.3.2.1 and Figure 3.3.2.2). This happened because these neurons are very small and straight and are located relatively close to the centre of the coil. The only exception to this was neuron *t2*: due to the fact that this neuron curves away from the plane of the coil, there was a significant variation of E_s along it.

The homogeneous field E_{sh}, shown in Figure 3.3.2.1 and Figure 3.3.2.2 by the dashed lines, was always higher than E_s, which shows that the field due to charge accumulation reduces the component of the electric field along the neurons. This reduction was especially relevant for neurons lying perpendicular to the WM-GM interface (*n* neurons) for which the ratio between E_s and E_{sh} reached 1.8 (*n3*). For *t* neurons the reduction was smaller, with this ratio reaching a maximum value of only 1.1 for *t1*.

Contrary to the neurons mentioned above, the field along PTNs (Figure 3.3.2.3) and association fibres (Figure 3.3.2.4) varied considerably. One reason for this is that the axons of these neurons often bend sharply. Fibre bends gave rise to localized variations of the effective electric field due to a change in the orientation of the neurons relative to the coil. These effects are illustrated in Figure 3.3.2.3 b, c and d (arrow 2), for PTNs, and in Figure 3.3.2.4 a (arrows 2 and 6) and b (arrow 2), for association fibres. Another cause for the variability of E_s along these neurons is that they, unlike interneurons, often cross the WM-GM interface. Consistently to what was observed in the first part of this chapter, the field due to charge accumulation at this interface creates a discontinuity in E_s, which is shown in Figure 3.3.2.3 b, c and d (arrow 3) and in Figure 3.3.2.4 a (arrows 1 and 7) and b (arrow 1). Because charge accumulation depends on the existence of tissue heterogeneities, E_{sh} lacked these discontinuities (Figure 3.3.2.3 and Figure 3.3.2.4, dashed lines). Apart from these localized variations, E_s along the

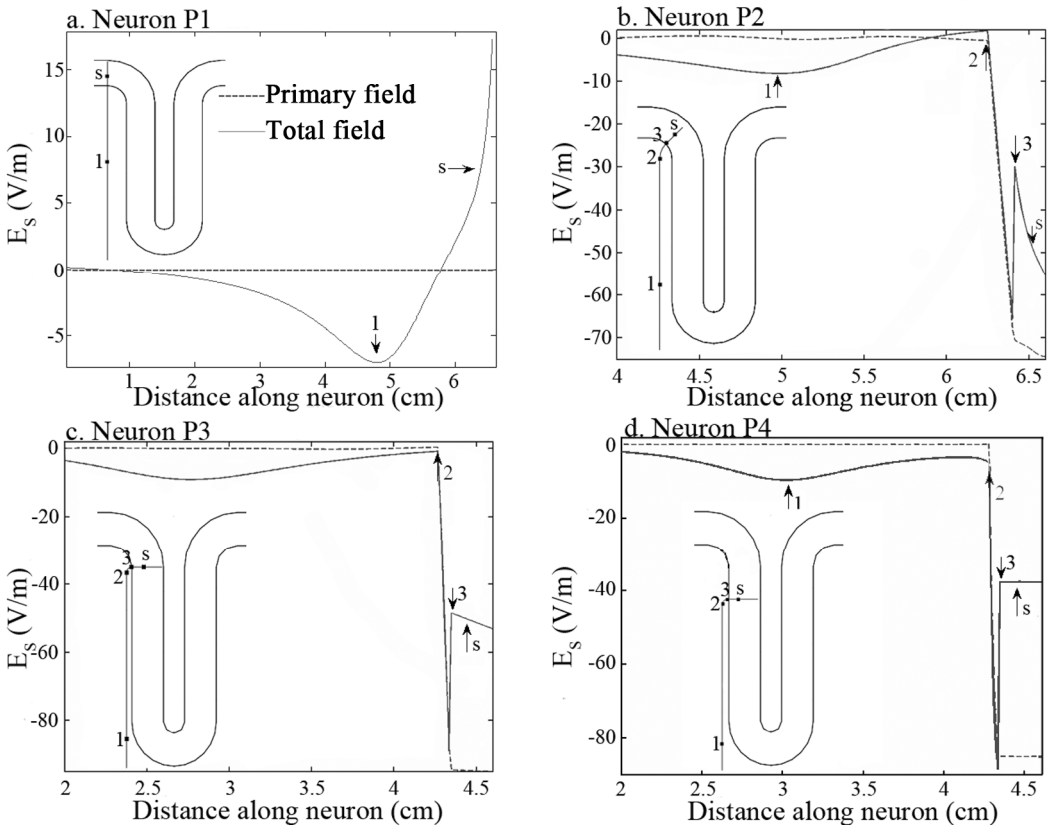

Figure 3.3.2.3: Spatial variation of E_s and E_{sh} for neurons *P1-P4* (a-d). The position of the neurons in the sulcus model is shown in the figures' insets. The arrows in the plots indicate the position of the most important features of the field (numbers) as well as the position of the soma (letter 's'). All field values were obtained for a stimulator's output of 67.7 A/μs. In the figure, distance is measured from the axon terminal towards the dendrite.

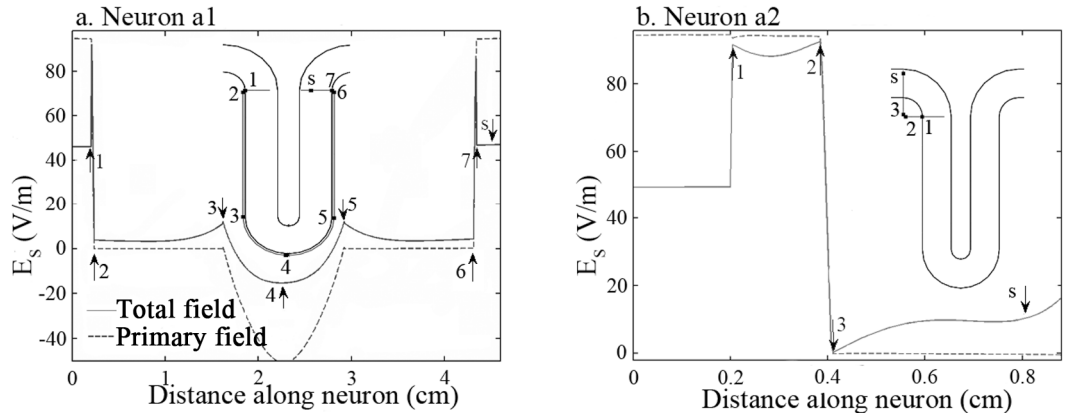

Figure 3.3.2.4: Spatial variation of E_s and E_{sh} for neurons *a1-a2* (a-b). The position of the neurons in the sulcus model is shown in the figures' insets. The arrows in the plots indicate the position of the most important features of the field (numbers) as well as the position of the soma (letter 's'). All field values were obtained for a stimulator's output of 67.7 A/μs. In the figure, distance is measured from the axon terminal towards the dendrite.

remaining sections of these neurons was relatively homogeneous, having high magnitudes if the section was aligned with the coil and close to it, and very low magnitudes when the section was perpendicular to the coil. An example of the latter is neuron *P1*, which is always perpendicular to the coil. The effective field along this neuron was very small, resulting only from charge accumulation at the interfaces.

Activation sites and mechanisms

For cortical interneurons, stimulation always occurred at their axonal terminations. This is shown in Figure 3.3.2.5 a, where the action potential is seen propagating antidromically from the axon termination towards the soma and dendrite. In this figure, the propagation seems to be instantaneous due to the small size of this neuron. However, the AcPtn propagates at a finite velocity of about 12.4 m s^{-1}. Stimulation at the dendritic end could never be achieved, because the polarization that occurred there had a faster spatial decay and a lower magnitude than at the axonal termination. This effect was not only restricted to interneurons, but also applied to all the neurons modelled in this work. Stimulation of interneurons was, therefore, more easily achieved when the electric field induced in the tissue was directed along the dendrite-axon axis (PA direction for the neurons depicted in Figure 3.3.1.1 c).

PTNs were always stimulated in the WM, in the region where they bend after leaving the GM (see Figure 3.3.2.5 b). This did not apply to neuron *P1*, which has no bends. When the electric field induced in the tissue was in the PA direction, the variation of E_s along the neuron (from axon to dendrite) due to the bend was negative, which caused a depolarization of the membrane. Therefore, stimulation occurred with lowest thresholds when the field was in the latter direction. The discontinuity in E_s that occurred at the WM-GM interface tended to induce a polarization that opposed the one induced at the fibre bend. In the case of the AP oriented electric field, the membrane was depolarized at the field discontinuity. However, because the hyperpolarization occurring at the nearby fibre bend had a higher magnitude, stimulation never occurred due to the "discontinuity mechanism".

The case of association fibres was less straightforward. Due to their complex trajectories, these neurons possessed several sites where high polarizations occurred, which lead to a competition among several stimulation mechanisms. Neuron *a1* (Figure 3.3.2.4 a) was stimulated at lower thresholds when the electric field was induced in the

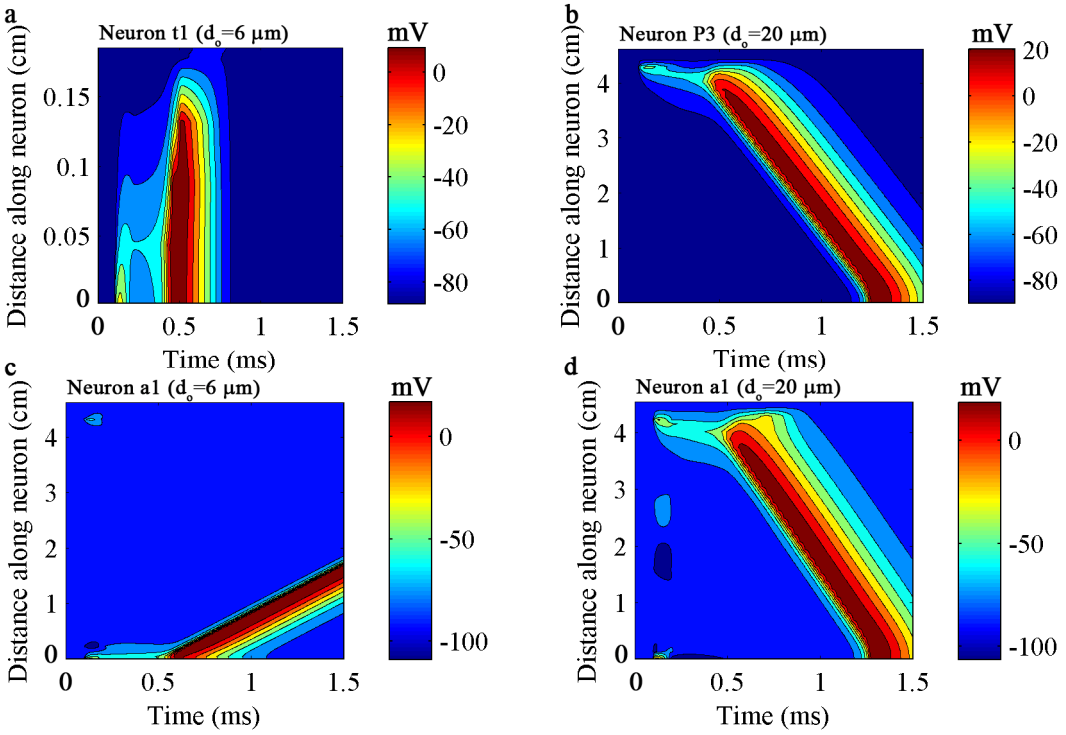

Figure 3.3.2.5: Contour plots of the transmembrane potential as a function of distance along the neuron and time, showing action potential generation and propagation. The contour at 20 mV indicates the maximum depolarization attained during an action potential. (a) Neuron *t1* with outer diameter of 6 µm; (b) Neuron *P3* with outer diameter of 20 µm; (c)-(d) Neuron *a1* with outer diameters of 6 µm and 20 µm, respectively. All plots were obtained for a monophasic current pulse. The direction of the field in the first phase of the stimulating pulse was chosen as the one that yielded lowest threshold of stimulation: PA for neurons *t1* and *P3* and AP for neuron *a1*. The amplitude of the current pulse was set to threshold.

AP direction. However, stimulation sites depended on the diameter of the neurons. For smaller neurons (diameters between 6 µm and 12 µm) stimulation occurred at the axonal termination in the motor cortex (see Figure 3.3.2.5 c). Larger neurons (14 µm to 20 µm) were stimulated more easily at the first fibre bend occurring after the neuron left the somatosensory cortex (arrows 6-7 in Figure 3.3.2.4 a), as is shown in Figure 3.3.2.5 d. This shift in activation site was due to the cancellation between the 1) depolarization induced at the fibre termination, in the motor cortex, and 2) the hyperpolarization induced at the last fibre bend, which occurs before entering the GM (arrows 1-2 in Figure 3.3.2.4 a). The rapid change in the electric field occurring at the bottom of the sulcus (arrows 3-5 in Figure 3.3.2.4 a) also influenced the transmembrane potential, although less than the other mechanisms (Figure 3.3.2.5 d). Regarding neuron *a2*, it was also stimulated more easily by an AP directed electric field, which induced charge accumulation at its axonal termination.

Influence of pulse waveform and current direction on activation thresholds

As stated previously, cortical interneurons and PTNs were stimulated more easily when the electric field was induced in the PA direction. This occurred at different phases of the TMS waveform, depending on its type (monophasic or biphasic) and on the initial direction of the current in the coil. For monophasic PA pulses stimulation occurred at the first phase of the waveform; whereas for monophasic AP pulses it only occurred in the second phase of the waveform. This is clearly illustrated in Figure 3.3.2.6 a and b for neuron *P3*. As the second phase is smaller than the first one, stimulation thresholds were much higher for AP than for PA pulses, by a factor of 2.7 to 2.8. This is less than the ratio between the peak values of the first and second phases, 4:1, a fact that can be attributed to the longer duration of the second phase, which will therefore induce a longer depolarization (compare the duration of the depolarizations observed in Figure 3.3.2.6 a and b). Stimulation of these neurons with biphasic pulses was more easily attained with AP-PA pulses, at the second phase of the waveform (see Figure 3.3.2.6 d) as this was the only phase to induce a PA directed field. Thresholds for stimulation with this waveform type were even lower than thresholds for stimulation with monophasic PA pulses even though the magnitude of the first phase of the monophasic PA pulse is greater than the magnitude of the second phase of the biphasic AP-PA pulse. The ratio between thresholds for AP-PA pulses and for PA pulses varied between 0.7 and 0.9. This again is related to the longer duration of the second phase of the biphasic pulse as compared to the first phase of the monophasic pulse. For biphasic PA-AP pulses, stimulation occurred due to the cumulative effect of the depolarizations induced by the first and third phases of the pulse waveform (see Figure 3.3.2.6 c). Contrary to what happened for AP-PA pulses, the thresholds for PA-AP pulses were about 1.1 times higher than those for monophasic PA pulses.

Since association fibres were most easily stimulated by AP directed electric fields, stimulation of these neurons occurred at waveform phases different from the ones where stimulation of the other modelled neurons occurred. Therefore, stimulation of association fibres with the lowest thresholds was always attained with biphasic PA-AP stimulation (at the second phase), followed by monophasic AP stimulation (at the first phase). Thresholds for biphasic AP-PA stimulation (third phase) were somewhat higher, and monophasic PA pulses (second phase) had the highest stimulation thresholds.

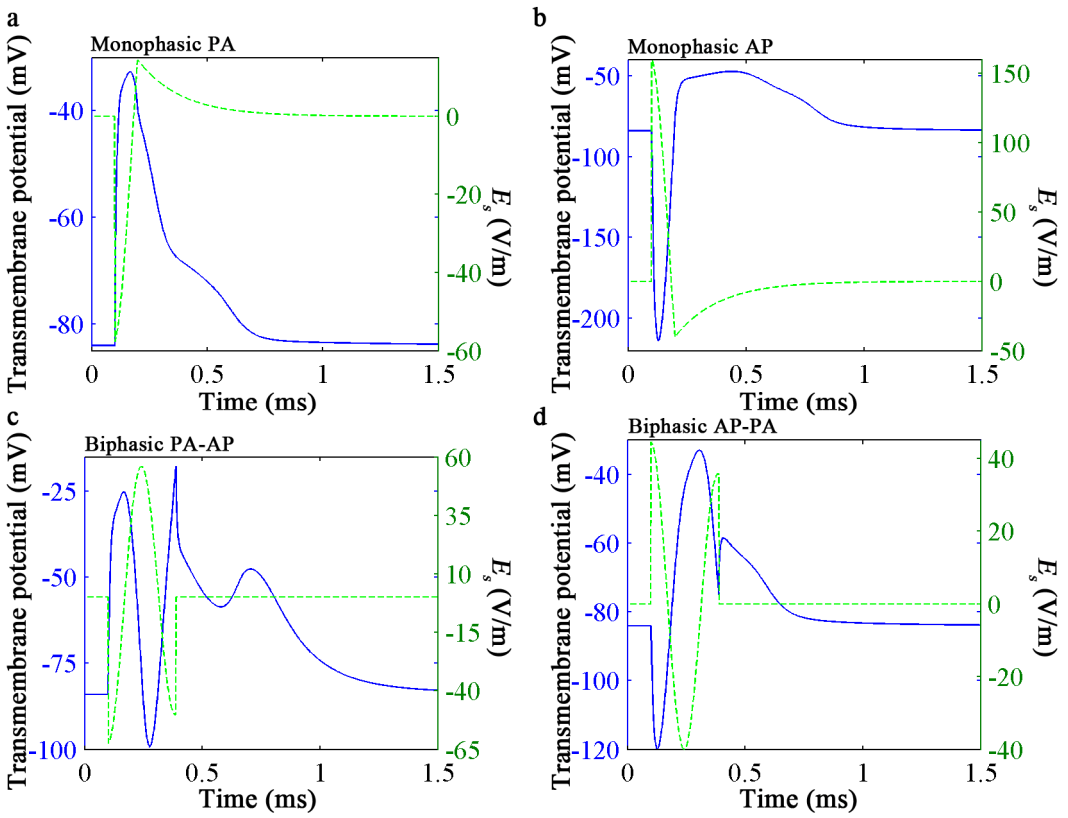

Figure 3.3.2.6: Temporal waveform of the transmembrane potential (blue line) and E_s (dashed green line) at the Ranvier node that corresponds to the activation site of neuron *P3*: (a) Waveforms for a monophasic PA pulse: (b) waveforms for a monophasic AP pulse; (c) waveforms for a biphasic PA-AP pulse; (d) waveforms for a biphasic AP-PA pulse. All plots were obtained at a stimulation intensity just below activation threshold.

Table 3.3.1 summarizes the results presented thus far. Neurons not represented in the table (neuron *P1*, *t2*, *t3* and *n1*) had very high stimulation thresholds and are not likely to be stimulated at all. The table shows that neuron *a2* (for $d_0 = 20$ μm) had the lowest threshold of all neurons in the model, followed closely by neuron *t1* (for $d_0 = 6$ μm) in the gyrus. Neurons *P2* and *P3* ($d_0 = 20$ μm) had similar stimulation thresholds, but higher than those of *a2* and *t1* neurons. Stimulation thresholds for neuron *P4* were, on average, 18% higher than those for *P3* (range: 13% - 26%). Neuron *a1* had a threshold slightly higher than those of *P2* and *P3* but lower than that of *P4*. Neurons *n2* and *n3* both had thresholds higher than those of neuron *P4*.

Table 3.3.1: Lowest stimulation thresholds for PTNs (*P2*, *P3, P4*), cortical interneurons (*t1*, *n2* and *n3*) and association fibers (*a1*, *a2*) as a function of waveform type. The table also shows the sites and mechanisms of activation and the phase of the waveform at which stimulation occurred.

Neuron	Pulse type		Lowest threshold		Stimulation		Phase of waveform[b]
			A/μs	% of MSO[a]	Site	Mechanism	
P2	Mono	PA	**97.7**	57%	Axonal bend in white matter	Charge accumulation at the bend	1st 2nd 2nd 3rd
		AP	**263.1**	154%			
	Bi	AP-PA	**73.4**	72%			
		PA-AP	**107.3**	106%			
P3	Mono	PA	**90.9**	53%			
		AP	**252.9**	148%			
	Bi	AP-PA	**70.7**	70%			
		PA-AP	**98.4**	97%			
P4	Mono	PA	**105.9**	62%			
		AP	**291.4**	170%			
	Bi	AP-PA	**81.5**	80%			
		PA-AP	**114.4**	113%			
t1	Mono	PA	**65.7**	38%	Axonal termination (grey matter)	Charge accumulation at axonal termination	
		AP	**162.6**	95%			
	Bi	AP-PA	**48.0**	47%			
		PA-AP	**72.7**	72%			
n2	Mono	PA	**116.7**	68%			
		AP	**289.8**	170%			
	Bi	AP-PA	**85.1**	84%			
		PA-AP	**127.5**	125%			
n3	Mono	PA	**127.9**	75%			
		AP	**318.1**	186%			
	Bi	AP-PA	**93.4**	92%			
		PA-AP	**139.7**	137%			
a1	Mono	PA	**171.7**	101%	Axonal termination[c] (grey matter, M1)	Charge accumulation at axonal termination	2nd 1st 3rd 2nd
		AP	**104.8**	61%			
	Bi	AP-PA	**106.7**	105%			
		PA-AP	**79.1**	78%			
a2	Mono	PA	**70.2**	41%			
		AP	**40.6**	24%			
	Bi	AP-PA	**41.6**	41%			
		PA-AP	**31.1**	31%			

a: All values above 100 % for the Magstim 200 stimulator, and 120 % for the Magstim Rapid stimulator are outside the range of values that the stimulator can provide.
b: Phase of pulse waveform for which stimulation occurred. Each row corresponds to the pulse types displayed in the second column.
c: For all pulse types, except monophasic PA, the threshold for activation at the bend after the fiber leaves the somato-sensory cortex was very similar to this one.

Effects of tissue heterogeneities on activation sites and thresholds

The influence of tissue heterogeneities on activation sites, as assessed by testing the neuron's response to E_{sh} instead of E_s, was negligible. However activation thresholds always increased, the magnitude of this increase varying from neuron to neuron.

Regarding cortical interneurons, thresholds for activation tended to increase proportionally to the decrease of the field along the neuron. For neuron *t1*, for instance, the ratio between thresholds for stimulation with field E_s and field E_{sh}, 1.1, was the same as the ratio between the magnitude of the two effective electric fields at the axonal termination (the site of AcPt generation for these neurons). This was also the case for neuron *n3* (ratio of 1.8), neuron *t2* (ratio of 1.1), and there was also a very good agreement between the two ratios for neurons *n2* (ratio of 1.3 between thresholds and 1.4 between the electric fields).

For the other neuron types, tissue heterogeneities also resulted in increased thresholds. Regarding pyramidal tract neurons, the ratio between thresholds was larger for neuron *P4* (about 1.9) than for neurons *P3* (about 1.7) and *P2* (about 1.4). Finally, for association fibers, the thresholds increased more for neuron *a1* (ratio of thresholds of about 2) than for neuron *a2* (ratios between 1.1 and 1.4).

3.3.3 Discussion

Mechanisms of stimulation and site of activation

The dominant mechanism leading to neuronal activation and the site where it occurred varied substantially among the modelled neurons. The neurons modelling PTNs (*P*) were excited in the white matter where they bent (neuron *P1* was an exception because it is perpendicular to the coil and follows a straight trajectory). The modelled cortical interneurons (*n* and *t*), on the other hand, were excited at their axonal terminations provided they were aligned with the main component of the field. Finally, pyramidal association fibres (*a*) were stimulated either at their axonal termination or at some sharp axonal bend. These results highlight the importance of fibre bends and axonal terminations in stimulation of motor cortical neurons, as has been previously suggested (see Chapter 3.1).

Apart from the two aforementioned stimulation mechanisms, another stimulation mechanism also influenced the activation thresholds. This can be seen by comparing the response of *P* neurons to homogeneous and heterogeneous effective electric fields. The

homogeneous effective field differs from the heterogeneous one essentially by the absence of the field discontinuity (arrow 3 in Figure 3.3.2.3 b-d). However, stimulation thresholds were smaller for the homogeneous model, indicating that the discontinuities in E_s diminished the effectiveness of stimulation at fibre bends, even though the latter remained the dominant stimulation mechanism. This effect strengthens the importance of modelling tissue heterogeneities, as was stressed in the previous study. It should be noted that the effects of tissue heterogeneities depend on the ratio between the conductivities at the interfaces between tissues. If this ratio differs significantly from the one that was modelled, the results reported here may vary.

The results obtained in this study also agree well with some of the predictions obtained by performing a steady-state analysis of the cable equation (Roth, 1994). As was discussed before, this analysis yields that the depolarization at fibre terminals is proportional to $\lambda E_{s\,term}$ for $L>>\lambda$, where L is the neuron's length, λ is the axon's space constant and $E_{s\ term}$ is the value of the field along the neuron at the termination. At neurons that bend sharply in a homogeneous field (a not completely accurate description for the *P* neurons used in this work, which do not bend sharply but instead have a small curvature), the same analysis shows that the depolarization is determined by the orientation of the two fibre branches in respect to the direction of the total electric field. For a fibre oriented like *P3*, the depolarization is proportional to $\lambda E_{s\,bend}/2$, where $E_{s\ bend}$ is the magnitude of the field along the segment of the neuron inside the GM at the bend. These results are consistent with the fact that the overall effectiveness of stimulation at axonal terminations was much greater than that of stimulation at fibre bends: the threshold for activation of cortical interneurons was smaller that that for stimulation of PTNs, even though the diameters of the former (maximum of 6 μm) were much smaller than those of the latter (maximum of 20 μm). The theoretical prediction that thresholds for stimulation by these mechanisms were proportional to the strength of E_s along the neuron was also confirmed in this study: the ratio between the homogeneous and the heterogeneous effective electric fields along cortical interneurons was equal to the ratio between activation thresholds for both the homogeneous and the heterogeneous models.

The present results do not exclude the possibility that other stimulation mechanisms may also lead to neuronal activation. Fibre branching, for instance, was not included in this model but it has been shown to lead to significant changes in membrane

polarization, combining the effects of fibre bends and non-uniformities (Roth, 1994). Modelling fibre branching may be relevant for cortical interneurons, given their highly ramified geometry (see Figure 3.1.4). In that case, action potential generation may not occur exclusively at the axonal terminations.

Interpretation of experimental results

The present results fit well with the experimental data obtained for monophasic PA stimulation with a figure-8 coil. With this form of stimulation, medium calibre cortical interneurons (diameter of 6 μm) oriented parallel to the WM-GM interface at the top of the gyrus (neuron *t1*) were stimulated at a threshold of 65.7 A/μs, a value that lies in the range of experimental values reported in the literature for I-wave generation: 43.5 – 67.1 A/μs (Di Lazzaro et al., 1998; Di Lazzaro et al., 2001; Kammer et al., 2001). At higher thresholds, 90.9 A/μs, direct stimulation of large PTNs located at the lip of the gyrus could be obtained. Once-again this value agrees well with the range of experimental values reported for the generation of D-waves: 82.1-91.2 A/μs (Di Lazzaro et al., 1998; Di Lazzaro et al., 2004a). In the literature, stimulation intensities are often given as the percentage of RMT (Kammer et al., 2001). Considering RMT to be the same as the threshold for stimulation of neuron *t1*, stimulation of large PTNs at the lip of the gyrus could only be achieved at 138 % RMT. Neuron *P4* could only be stimulated at a threshold of 161 % RMT, which is somewhat more than the usual range of stimulation intensities for D-wave generation (up to 150 % RMT). This way, direct stimulation of PTNs below 150 % RMT could only be achieved in this model up to a depth of 1.8 cm below the cortical surface (the position of the portion of the *P4* neuron inside the GM).

Cortical association fibres (*a2*) could also be stimulated with monophasic PA pulses at thresholds close to the ones obtained for stimulation of cortical interneurons: 70.2 A/μs for d_o=20 μm. However, given that these neurons do not project as far as PTNs do, it seems unlikely that they have such large diameters (Manola et al., 2007). Considering smaller diameters, the thresholds would increase to values between those of cortical interneurons and PTNs.

Regarding monophasic AP stimulation, these results indicated that the cortical interneurons modelled in this work could not be stimulated at thresholds achievable with the magnetic stimulators considered here. This was a direct consequence of i) the

specific orientation chosen for the horizontally aligned cortical interneurons in the model, i.e., dendrite posterior to axon, and ii) the difficulty in stimulating the apical dendrite, which likely resulted from the fact that the duration of the TMS pulse is much shorter than the membrane time constant. Reversing this orientation would cause thresholds for AP stimulation to be similar to ones obtained for PA stimulation. The distribution of orientations of horizontal interneurons is possibly isotropic, but no evidence could be found in the literature of the actual orientation pattern. Using the monophasic AP pulse, PTNs also could not be stimulated at thresholds within operating range of TMS devices; with this direction of the current, PTNs were strongly hyperpolarized at their bending site, during the first phase of the pulse waveform. In this case, depolarization only occurred during the second phase of the waveform, which has a much smaller magnitude. However, during AP stimulation, D-waves have been reported (Di Lazzaro et al., 2001). This could be a result of stimulation of PTNs from other cortical areas, like the somatosensory cortex or premotor and supplementary motor areas. PTNs from these areas, as opposed to what happened with PTNs emanating from M1, have their bends oriented in such a way that they are depolarized with an AP oriented field and hyperpolarized with PA oriented fields. Yet, stimulation of PTNs from the somatosensory cortex was shown not to elicit a motor response (Di Lazzaro et al., 2008). Moreover, such neurons are thought to have small diameters (in the 2-4 μm range; (McComas and Wilson, 1968)) and are therefore very difficult to stimulate, according to the results presented in this work. No similar information could be found for the fibres emanating from the premotor and supplementary motor areas and, therefore, they might be a possible source for D-wave generation with an AP oriented field.

An important difference between monophasic PA and AP stimulation is that the latter gives rise, preferentially, to longer latency I-waves (I_3-waves) (see Chapter 3.1, page 107). Several works have attributed this difference between PA and AP stimulation as a consequence of the latter stimulating a different population of neurons, other than cortical interneurons (Sakai et al., 1997; Di Lazzaro et al., 2004a). Esser et al. (Esser et al., 2005) have suggested that association fibres may be responsible for the different outcomes of AP and PA stimulation. There, the authors presented simulations that showed that stimulation of fibres projecting from the somatosensory cortex to the motor cortex, at the site where the fibres bend into the motor cortex, led to a wave with the same latency of an I_3-wave. The results presented in this work suggest that pyramidal

association fibres (neurons *a1* and *a2*) have thresholds for monophasic AP stimulation much smaller than those for PA stimulation. Stimulation of these neurons can only give rise to an I-wave, so this could be the possible source of the late I-waves observed under AP stimulation. Neuron *a2* is especially relevant, given that its thresholds – ranging between 111.8 A/μs and 40.6 A/μs for fibre diameters between 6 μm and 20 μm, respectively – are in good agreement with experimental measurements of thresholds for AP stimulation (values between 59.7 A/μs and 99 A/μs, (Di Lazzaro et al., 2001; Kammer et al., 2001)). Neuron *a1*, which represents the type of fibres identified by Esser et al. as giving rise to the late I-wave, had stimulation thresholds somewhat higher than those observed experimentally, with values between 104.8 A/μs and 137.9 A/μs. Still regarding Esser's work it should be noted that the present results do not support their hypothesis as to where stimulation occurs. The present work shows that an AP pulse would hyperpolarize association fibres projecting from the somatosensory cortex (*a1*) in the region where it bends into the motor cortex. Stimulation of these association fibres with AP pulses always occurred at the fibre terminal in layer III of the motor cortex.

Finally, biphasic pulses always stimulated neurons with the second or third phase of the waveform, depending on the type of neuron and initial direction of the current in the coil. For pyramidal tract neurons and cortical interneurons, activation with biphasic AP-PA pulses occurred during the second phase of the waveform (the only one that induced a PA directed electric field), at thresholds lower than those necessary for stimulation with monophasic PA pulses (in terms of the maximum value of the current's time derivative). The increased efficiency of the second phase predicted here is in good agreement with results reported by others (Maccabee et al., 1998; Kammer et al., 2001), who attribute it to the fact that the second phase of the waveform lasts twice as long as the first phase of a monophasic pulse, rendering it more effective.

Model limitations and future work

One of the main limitations of this work is that accurate experimental data describing the active membrane properties of cortical neurons are still unavailable. The model used in this work is based on data obtained from human myelinated sensory fibres (Wesselink et al., 1999), which may not be appropriate to describe the three kinds of neurons modelled in this work. Additionally, data regarding the diameters of the fibres

modelled here are still lacking, except for pyramidal tract neurons (Lassek, 1940). These two parameters may significantly affect the stimulation thresholds reported here. However, the dominant stimulation mechanisms for each type of neuron are probably less susceptible to changes in these parameters.

Another important limitation of this study lies in the assumption that the wall of the central sulcus follows a straight vertical trajectory. As shown in (Yousry et al., 1997) the sulcus instead follows a hook-shaped trajectory, curving to more anterior regions at deeper sites. Nevertheless, the upper region of the sulcal wall follows an almost straight trajectory. As activation of neurons occurs only in the more superficial regions of the sulcus, it is expected that the model yields a good prediction of the electric field induced at these superficial regions. A more important consequence of this hook-shaped trajectory is that PTNs leaving the M1 may not have such a sharp bend as that modelled in this work. If that is so the depolarization induced at the bend may not be dominant over other stimulation mechanisms such as that occurring at the WM-GM interface. This model is also not suitable for the study of LM stimulation, given that the results of the latter probably derive from the Ω shape of the hand-area of the motor cortex when seen in an axial plane (Yousry et al., 1997).

Despite these limitations, the modelling work described in this chapter is still very useful in predicting stimulation mechanisms in TMS of the human motor cortex, particularly in assessing the effects of different coil geometries, orientations, and current waveforms. Further refinements to this work may be achieved by using high-resolution human head models that include a detailed 3D description of the geometry of the cortical sheet (e.g. (Chen and Mogul, 2009)). Additionally, such a model could be improved by including simulations of synaptic connections between the several neurons represented (as was done by (Esser et al., 2005), but without performing electric field calculations). That would allow not only to investigate the mechanisms that determine stimulation of an individual neuron, but also to predict the response due to synaptic interactions between neurons in the network.

4 TMS of small animals

Despite the several putative therapeutic applications of rTMS, its effects are still largely unknown. Animal studies, most of which using rodents, have been used to study the possible mechanisms through which rTMS exerts its effects. However, the smaller head of rodents as compared to that of humans has been reported to lead to a decreased electric field as well as poor focality of stimulation. In this study the FEM is used to determine the distribution of the field induced by commercially available coils, with different geometries and sizes. Additionally, several different coil orientations were also considered, some based on actual orientations described in the literature. The results show that the small head size / coil size ratio lead to an increase on the secondary field due to charge accumulation that greatly reduces the total electric field. The secondary field, however, improves the focality of the electric field. These results are expected to help predict the optimal combination of coil geometry, size and orientation for stimulation of small animals.

4.1 Introduction and objectives

Limitations of animal studies using rTMS

The physiological mechanisms underlying many of the reported effects of rTMS still remain largely unknown. Over the last few years, animal studies, especially using rodents, have been used to study the effects of rTMS. Small animals such as these can be exposed to higher doses than humans, and histological analysis of brain slices can detect changes in neurotransmitter systems and regulation of early genes (Lisanby and Belmaker, 2000). Studies involving electrical stimulation of brain slices of rodents, which were subject to rTMS prior to their death, can also shed light on the effect of

rTMS on neurophysiological mechanisms that are thought to be responsible for the effects of rTMS on brain excitability: long term potentiation (LTP) and long term depression (LTD) (Ogiue-Ikeda et al., 2003; Ahmed and Wieraszko, 2006; Kim et al., 2006b). Furthermore, several animal models are also useful in the study of putative therapeutic applications of rTMS such as to the treatment of depression (Porsolt swim test, (Zyss et al., 1999)) and mania (amphetamine model of mania, (Shaldivin et al., 2001)).

Nonetheless there are some striking differences between small animal rTMS studies and human rTMS studies, which may limit the usefulness of the former. One of the first differences to be detected is the fact that it is much harder to achieve a motor response, via magnetic stimulation of the motor cortex, in small animals than in humans (Weissman et al., 1992; Liebetanz et al., 2003). This effect might result simply from a different cortical organization of the motor system in rodents as compared to humans. However other studies have also shown that it is much more difficult to induce seizures, via rTMS, in animals than in humans (Lisanby and Belmaker, 2000). Another difference between these studies lies in the fact that results obtained using animal studies are more robust than those observed in clinical trials (Lisanby and Belmaker, 2000).

Importance of coil size / brain size ratio

One possible explanation for the apparent difficulty in stimulating the motor cortex of small animals and in inducing seizures is related to the different ratio between the coil size and the head size in humans and animals. The importance of this factor was demonstrated for the first time by Weissman and co-workers (Weissman et al., 1992). They measured the electric field induced by several different coils inside spheres surrounded by insulating rubber layers, representing the skull, and filled with a saline solution. The results, replicated in Figure 4.1.1, indicated that the peak electric field inside the sphere was inversely proportional to the radius of the sphere. Therefore, in rodents, the total induced electric field is much smaller as compared to the field induced in a human head, which might explain the previous observations involving rTMS of small animals. Weissman et al. attributed the decrease in the field with the decrease of the radius of the head to the fact that a smaller head captures a smaller fraction of the total magnetic flux. This hypothesis will be discussed in more detail further ahead.

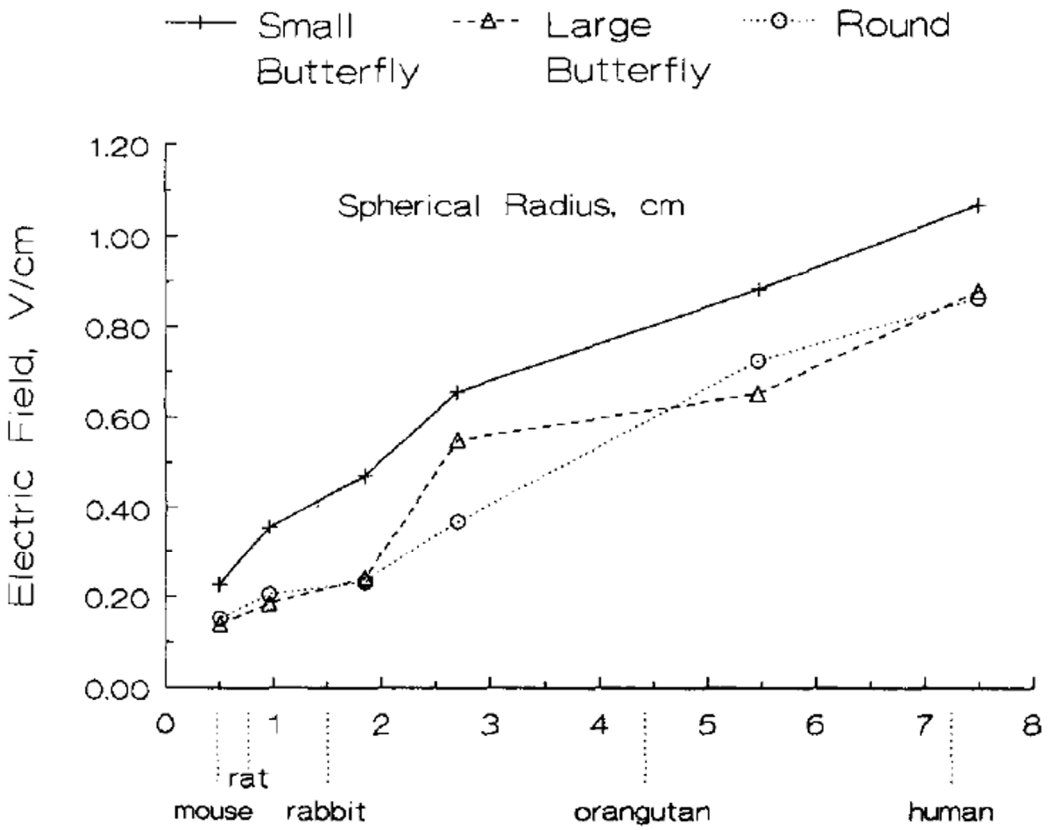

Figure 4.1.1: Peak electric fields induced by three different coils in 6 spherical head models of different sizes and filled with a saline solution. Representative brain volumes of 5 animal species are shown for direct comparison to their equivalent radii. (Figure taken from (Weissman et al., 1992)).

Field focality

Another important difference between rTMS of small animals and humans is the focality of the electric field. This is referred in virtually every study involving rTMS of small animals and it results from the intuitive notion that a coil bigger than the head will result in 'whole brain stimulation', as opposed to stimulation of human subjects that is thought to be more focal. This fact is thought to be responsible for the more robust effects of rTMS observed in small animals, and it has been suggested that less focal coils should be more suitable for human applications.

This is a well accepted property of rTMS of small animals but, up to date, studies quantifying the focality of the induced electric field are, to the best of our knowledge, still lacking.

Objectives

From what was described above, an accurate knowledge about the field's distribution is needed in order for the studies performed in small animals to be useful to the human case. Some studies do exist, in which the FEM is used to calculate the field distribution in a realistic model of a rat's head (Zheng et al., 2005), but these studies focus on a limited number of coil geometries and orientations. Furthermore, the effects of coil inductance on the output of the stimulator were not taken into account in those studies, and important parameters such as the focality of the field and its decay with depth were not discussed in detail.

It was this work's objective to determine the field induced in a realistic mouse model by coils with different geometries, sizes and orientations. The analysis focused on the magnitude of the total electric field, its focality and decay with increasing depth, and it took into account the inductance of the coils and how it affects stimulator output.

Published work

The work described in the following section originated one publication in a conference proceedings:

Proc 1: Salvador R and Miranda PC. Transcranial magnetic stimulation of small animals: a modelling study of the influence of coil geometry, size and orientation. 31st Annual Conference of the Engineering in Medicine and Biology Society. Minneapolis, 2009: 674: 7.

This proceeding's paper was presented in a poster session at the 31st Annual IEEE EMBS conference.

4.2 Methods

Mouse model

The model used in this study (see Figure 4.2.1) was based on a previously built finite-element mesh of a mouse (Dogdas et al., 2007), available online at: http://neuroimage.usc.edu/Digimouse.html. This mesh was built from co-registered X-

ray computed tomography (CT) and cryosection data of a normal nude mouse (weight 28 g). The surface mesh representing the skin was converted into an IGES file using Matlab (version 2008, www.mathworks.com) and 3Data Expert software (version 8.1, http://www.deskartes.com). The file was then read by Comsol 3.5 and converted into a solid. A similar procedure was applied to the outer surface of the brain which is also represented in the model. In order to reduce the finite element mesh complexity, only half of the mouse was meshed.

Despite the fact that the model includes the outer surface of the brain, the latter is not attributed different dielectric properties, and its only purpose is data visualization. The mouse is, therefore, modelled as a homogeneous and isotropic medium with an electrical conductivity of 0.33 S/m and a relative dielectric permittivity of 10^4, which are the same values as those used in the homogeneous head models used in the study about the effects of ferromagnetic cores (see Chapter 2).

Coil geometry and orientation

In this work two different circular coils and two different figure-8 coils, available from the Magstim Company, were modelled. The details of these coils are summarized in Table 4.2.1 and further information can be found in (Jalinous, 1998) and (Magstim, 2005).

The coils were oriented in different ways according to their geometry. Four different orientations were considered for the circular coils (see Figure 4.2.2 b, c, e and f) and two for the figure-8 coils (Figure 4.2.2 d and g). Regarding the circular coils, in two of the modelled orientations the coil is placed perpendicularly to the *xoy* plane (Figure 4.2.2 b, e), whereas in the other two orientations the coil is parallel to this plane (Figure 4.2.2 c, f). Furthermore, in some orientations (Figure 4.2.2 b, c) the coil's wires closest to the brain are aligned mainly with the PA direction (*y* axis) whereas in other orientations (Figure 4.2.2 e, f) the wires are aligned with the RL direction (*x* axis). The figure-8 coils are always placed parallel to the *xoy* plane, with its central section aligned either with the PA direction (Figure 4.2.2 d) or the RL direction (Figure 4.2.2 g). Because in these orientations the coil wires are aligned with one specific direction, they will be referred to as focal coil orientations.

For the circular coils, one additional orientation was modelled in which the field induced in the brain has no dominant component (see Figure 4.2.2 a). The latter will, therefore, be referred to as a non-focal orientation through the remainder of this work.

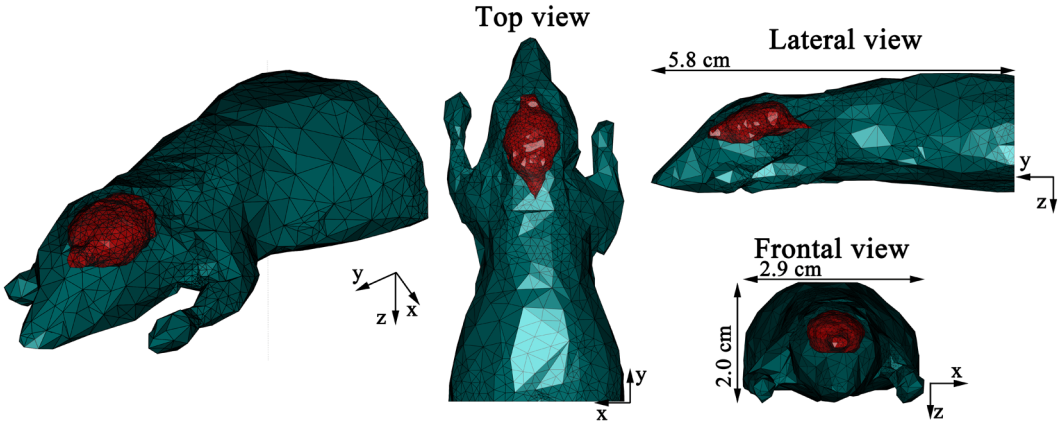

Figure 4.2.1: Finite element mesh of the mouse model used in this work. The red surface shown in the figure represents the mouse's brain. The *y* axis points in the PA direction, the *x* axis in the RL direction and the *z* axis in the dorsal-ventral (DV) direction.

Table 4.2.1: Properties of the coils used in this work.

Coil	Geometry	Inductance (μH)
Circular 50 mm	Inner diameter: 25 mm Outer diameter: 77 mm Windings: 18	13.5[a]
Circular 70 mm	Inner diameter: 40 mm Outer diameter: 77 mm Windings: 15	16.25
Figure-8 25 mm	Inner diameter: 18 (×2) mm Outer diameter: 42 (×2) mm Windings: 14	10.11[a]
Figure-8 70 mm	Inner diameter: 56 (×2) mm Outer diameter: 87 (×2) mm Windings: 9	16.35

a: These small coils need to be connected to a serial inductor when they are connected to the Magstim Rapid stimulator (Magstim, 2005). The serial inductor increases the inductance of the coils by 4.89 μH.

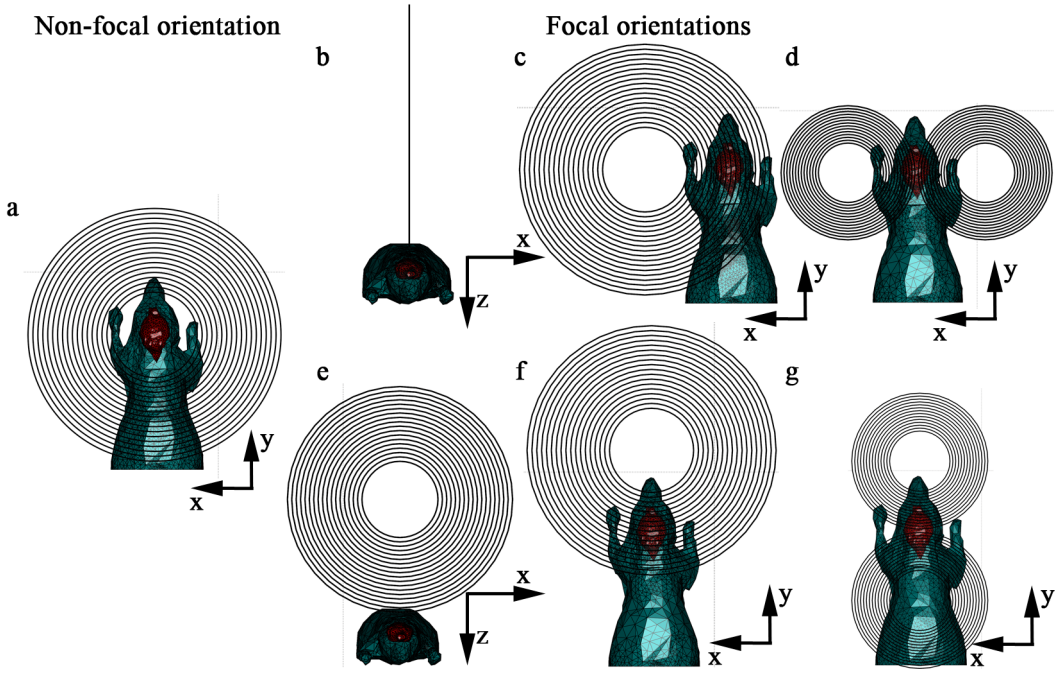

Figure 4.2.2: Multiple coil orientations used in this study: (a) non-focal orientation, consisting of a circular coil (50 mm coil in the figure) centred above the rat's head; (b), (c), (d) focal orientations with the wires closest to the brain aligned with the PA direction (*y* axis); (e), (f), (g) focal orientations with wires aligned with the RL axis (*x* axis).

The non-focal orientation as well as the two orientations considered for the figure-8 coils are usually used in several studies involving rTMS of rodents. The four remaining orientations considered for the circular coils are not usually described in the literature. However, they were considered because, like the orientations modelled for the figure-8 coils, they have their wires aligned with one predominant direction.

Electric field calculation

The total electric field induced in the tissue by the coils was calculated using the finite element method, as implemented by Comsol. The calculation used the same quasi-statics package as described in the previous chapters.

The values of the electric field displayed in the 'Results' section were obtained at the time instant when the field is maximum. As the total electric field induced in TMS is proportional to the time derivative of the current in the coil, it is important to guarantee that realistic values for this parameter are used. As was seen before, for magnetic stimulators the maximum value of the current time derivative depends on the charging voltage of the capacitors (V_C) and on the inductance of the coil (L) according to the expression $dI/dt|_{Max} = V_C/L$. The values for the inductance of the coils modelled here

are shown in Table 4.2.1. In this study the modelled stimulator was based on the Magstim Rapid (Magstim, 2006) model, because it is more suitable for rTMS applications. For this device the MSO, i.e. 100 % on the front panel, corresponds to V_C = 1650 V. However it can be programmed to go up to 120 % MSO (V_C = 1980 V, (Kammer et al., 2001)).

After adaptive meshing, the finite element mesh of the models comprised between 0.5 to 1.5 million tetrahedral first order elements, and took about 3 hours to solve on a computer with two dual core processors (Intel Xeon 5160) clocked at 3 GHz and 16 Gb of RAM memory.

Assessment of coil performance

For each coil orientation, the magnitude, decay and focality of the induced electric field were calculated. The magnitude and decay of the field were analyzed by considering lines that start at the maximum of the field at the brain's surface and end at a central point inside the brain. The focality was analyzed by determining the HPR (Carbunaru and Durand, 2001) at the surface of the brain. In order to obtain accurate results, the mesh along the lines and on the surface representing the brain was refined by decreasing the maximum element size.

4.3 Results

Distribution of the primary electric field

For the focal coil orientations, the main direction of the primary component of the electric field at the brain's surface is either PA (for the coil orientations depicted in Figure 4.2.2 b, c and d) or RL (Figure 4.2.2 e, f and g), consistent with the main orientation of the coil wires closest to the brain. The field along other directions is either very small (maximum of 25% of the value of the main component of the field for the circular coils) or completely negligible in the case of the figure-8 coils. This is illustrated in Figure 4.3.1. This figure also shows that the field's maximum, is always located at the region of the brain's surface closest to the coil. Regarding the magnitude of the primary field, it is highest for the figure-8 coils (maximum of 458 V/m at 75 % MSO for the figure-8 25 mm coil oriented as in Figure 4.2.2 d), and lowest for the circular coils with a perpendicular orientation (minimum value of 218 V/m at 75 %

MSO for the circular 50 mm coil oriented as in Figure 4.2.2 e). The maximum value of the primary field's magnitude is also largely independent of the PA or RL orientation of the coil wires, for a given coil type (circular and figure-8 coil) and coil orientation (circular parallel or circular perpendicular) (see Figure 4.3.1).

In the non-focal orientation, the primary component of the field is strongest in both the more posterior part of the mouse's brain and in the most anterior part of the brain (see Figure 4.3.2). In these regions, the field is aligned either with the RL or the LR direction. The field along the PA / AP direction is also strong in the lateral regions of the brain, although its magnitude along these directions is slightly smaller as compared to the magnitude of the field in the RL / LR direction. This results from the fact that the rat's brain is elongated along the PA axis, which causes the regions in the front and back of the brain to be closer to the coil wires than the lateral regions. The magnitude of the primary field is larger for the 50 mm coil than for the 70 mm coil, because the latter has its wires further away from the brain. Even with the 50 mm coil, the magnitude of the primary field in this orientation is much smaller than the magnitudes observed in the focal orientations: maximum of 118 V/m (at 75 % MSO) for the circular 50 mm non-focal coil as compared to a maximum of 458 V/m for the figure-8 25 mm PA coil. Another difference between the focal and non-focal orientations is the fact that, for the former, the primary field never reaches zero in the brain whereas, for the latter, the field is zero at the top of the brain (see Figure 4.3.2).

Distribution of the total electric field

In the focal coil orientations, the secondary component of the electric field strongly opposes the main component of the primary field: at the brain's surface, the secondary field ranges from 67 % (PA oriented figure-8 25 mm coil, Figure 4.2.2 d) to 88 % (circular 70 mm coil oriented as in Figure 4.2.2 e) of the value of the primary field, along the main direction. The magnitude of the secondary field is greater for coil's oriented perpendicularly to the head and in the RL direction. The secondary field also affects the primary field along other directions, although less than it does along the main direction. Due to the influence of the secondary component of the field, the total field has a much smaller magnitude than that of the primary component (see Figure 4.3.1): the norm of the total field ranges from a minimum of 12 % (circular 70 mm coil, oriented as in Figure 4.2.2 e) to a maximum of 36 % (PA oriented figure-8 25 mm coil, Figure 4.2.2 d) of the primary field's norm. The field's distribution is also different;

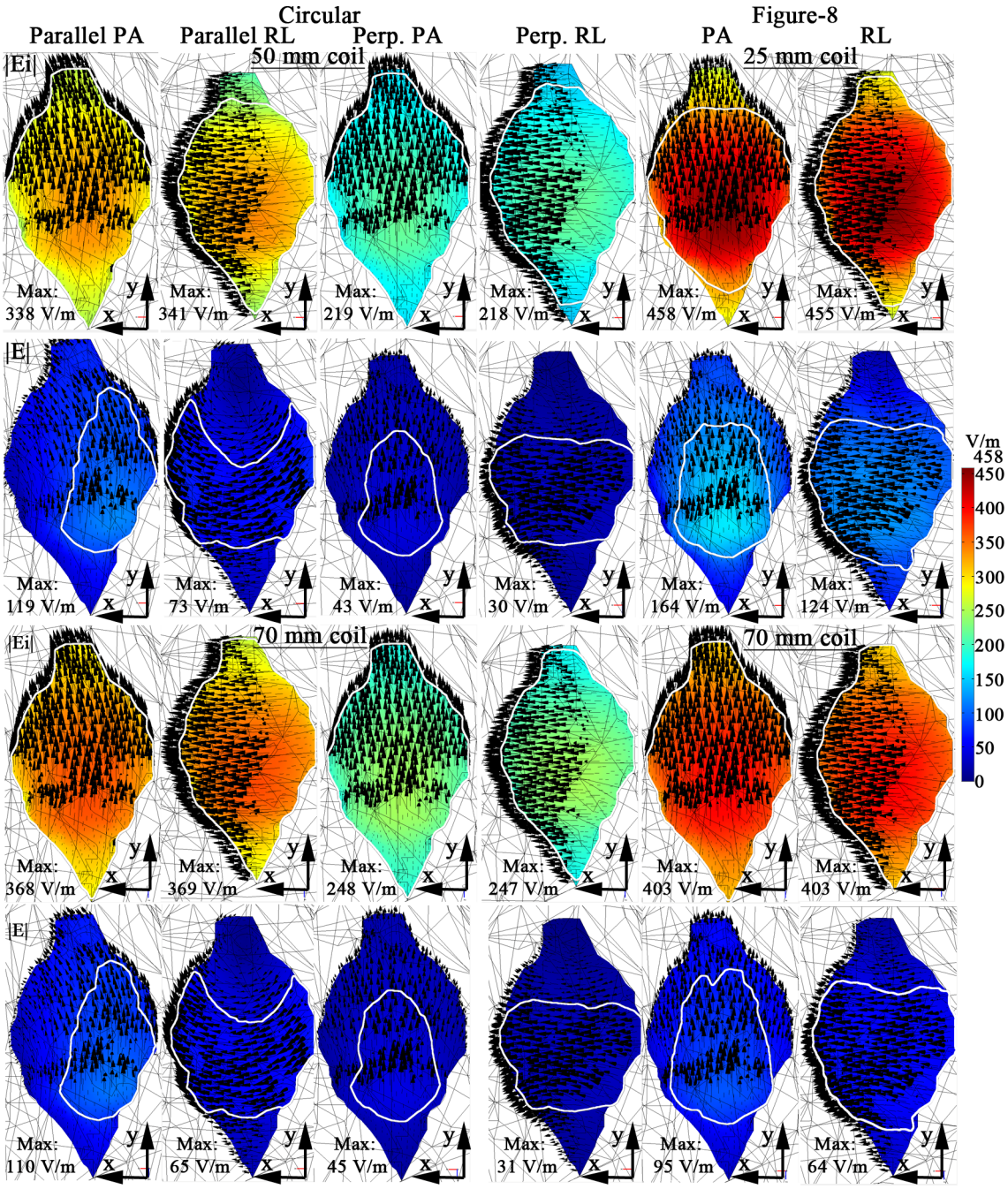

Figure 4.3.1: Magnitude of the primary component of the electric field, $|E_i|$, and of the total electric field, $|E|$, on the brain's surface for all the focal coil orientations. The first four columns (from the left) illustrate the results obtained for the circular coils, whereas the last two columns show the results obtained with the figure-8 coils. The first two sets of lines are for the 50 mm circular coil and for the 25 mm figure-8 coil and the second two sets of lines are for the 70 mm circular and figure-8 coils. For each set of two lines, the first one displays the primary electric field and the second one the total electric field. All plots use the same colourbar shown in the right of the figure. The maximum value of the field's norm is also shown in each plot. The white line encloses the HPR. All the results were obtained at 75 % MSO.

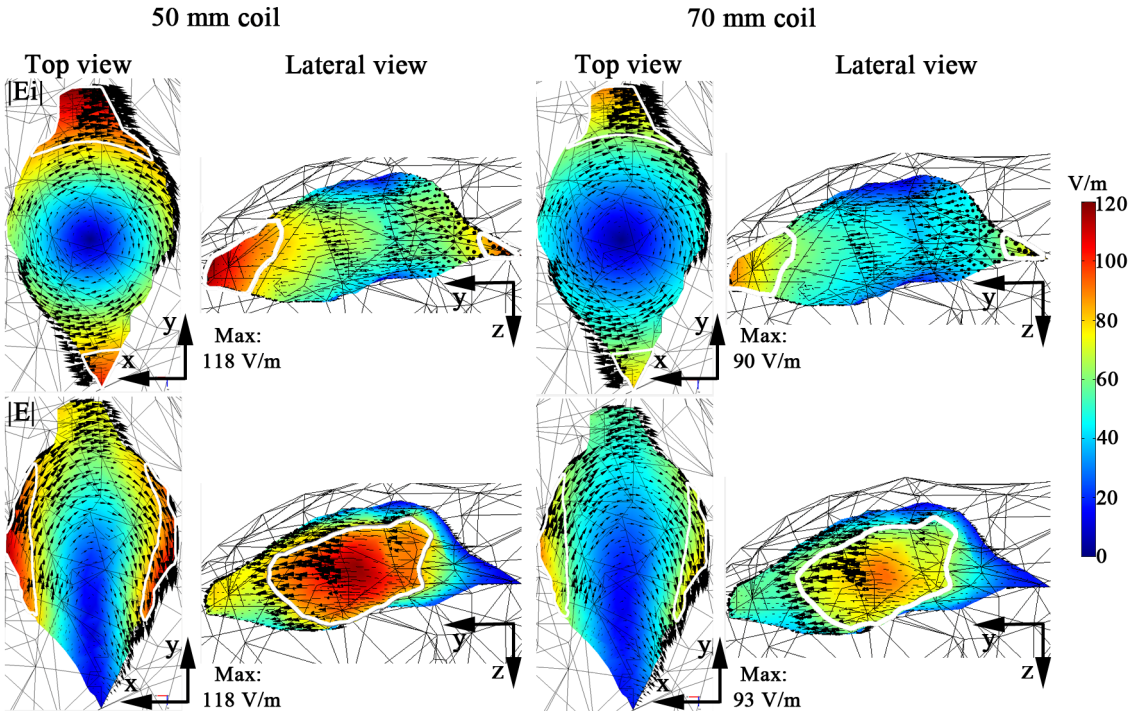

Figure 4.3.2: Magnitude of the primary component of the electric field, $|E_i|$, and of the total electric field, $|E|$, on the brain's surface for the non-focal coil orientation. The first line displays the primary electric field and the second one the total electric field. For each plot two views are shown: a top view and a lateral view from the left. All plots use the same colourbar shown in the right of the figure. The maximum value of the field's norm is also shown in each plot. The white line encloses the HPR. All the results were obtained at 75 % MSO.

however the main direction of the total electric field remains the same as that of the primary field (see Figure 4.3.1).

For the non-focal orientation the secondary field has two main effects. The first one is to decrease the field induced in the front and in the back of the brain along the LR and RL directions respectively. In the front of the brain this reduction is of about 37 % of the value of the primary electric field for the 50 mm coil and 39 % for the 70 mm coil. The second effect of the secondary field is to increase the primary field along the PA / AP directions in the lateral regions of the brain. This increase in the field can reach 75 % of the primary field for the 50 mm coil and 84 % for the 70 mm coil. The result of these two effects is that, unlike for the primary electric field, the dominant component of the total electric field along the brain's surface is in the PA / AP direction. Also, in these orientations, the maximum value of the total electric field's magnitude is very similar to the maximum value of the primary electric field's magnitude: the difference between the values is less than 3 % of the primary field's magnitude. However, the

spatial distribution of the electric field is very different: the maximum value shifts from the head's front to the lateral regions of the brain (see Figure 4.3.2).

Field's magnitude and decay along test lines

In the case of the focal coil orientations, the field due to charge accumulation resulted in a reduction of the magnitude of the total electric along the test lines (compare Figure 4.3.3 a/b with Figure 4.3.3 c/d). This result is consistent to what was observed at the surface representing the brain. The decay of the primary component of the field along the test lines, on the other hand, increased substantially (compare Figure 4.3.4 a/b with Figure 4.3.4 c/d). In the case of the circular coils, the orientation for which the total field decayed more slowly was the perpendicular RL orientation, followed by the parallel PA, perpendicular PA and parallel RL orientations (see Figure 4.3.4 c). This order was different for the decay of the primary component of the field (see Figure 4.3.4 a), which shows that the secondary field affects the field's decay differently for each orientation. For the figure-8 coils, the total field decayed more slowly in the RL orientations than in the PA orientations (see Figure 4.3.4 d). For any fixed coil orientation, the decay of the total electric field did not vary much with coil size.

Regarding the non-focal coil orientation, the secondary field affected much less the magnitude of the total electric field (compare Figure 4.3.5 a and b). Comparing the decay of the primary and total field is, however, less immediate because the test lines used for both are very different (the maximum of the primary component is located over the head's front, whereas the one of the total field is located over the left hemisphere). However, at the end of the test line, the primary electric field has decayed to less than 7 % of its maximum value along the line, whereas the total field has only decayed to about 24 % (Figure 4.3.5 c and d). As was also observed in the focal orientations, the size of the coil did not influence much the field's decay.

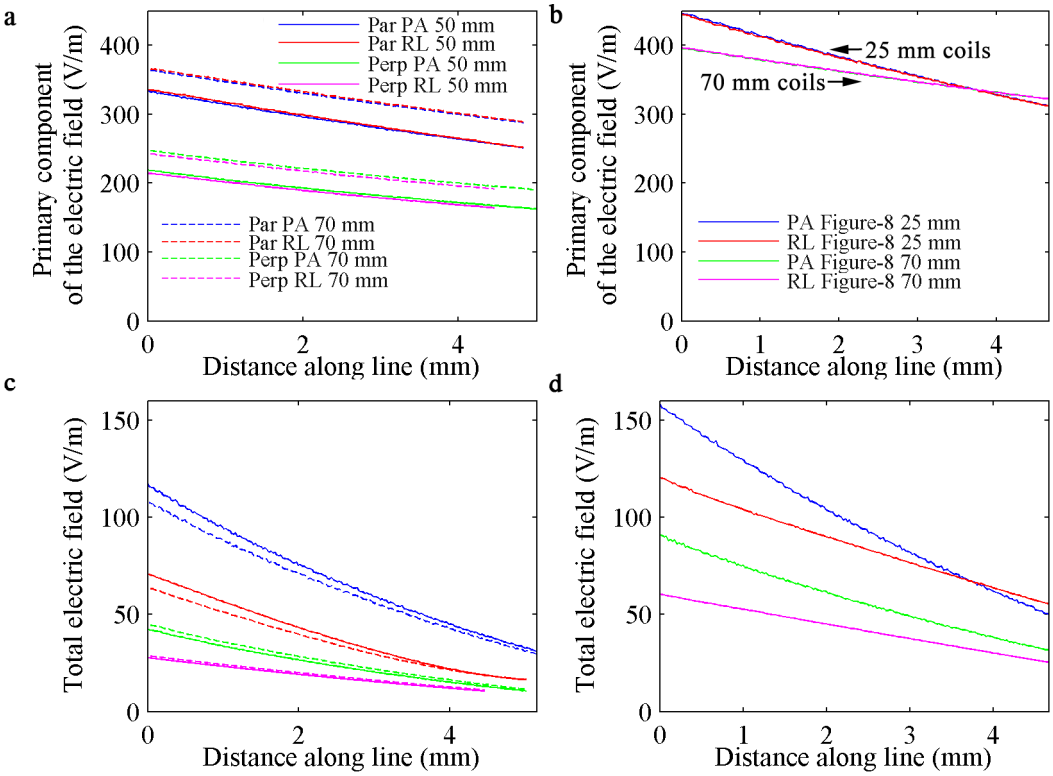

Figure 4.3.3: Magnitude of the field induced by the focal coil orientations along test lines that go from the positions of the maximum value of the field on the brain's surface to the centre of the brain. (a)/(b) Magnitude of the primary component of the electric field induced by the circular / figure-8 coils; (c)/(d) Same as (a)/(b) but now for the total electric field. All results were obtained at 75 % MSO.

In order to further assess the capability of the different coils used in this study to stimulate deeply located structures, for each case the maximum depth (MD), along the test line, at which the electric field remained larger than a reference value (RV) of 100 V/m was determined. This value is considered to be close to threshold for axon stimulation (Davey and Riehl, 2006). The results obtained at several different values of stimulator's output are summarized in Table 4.3.1. At 75 % MSO, most coil orientations failed to induce a field larger than the RV along the test lines. The only exceptions were the circular coils with a parallel PA oriented (MD of 0.7 mm for the 50 mm coil and 0.4 mm for the 70 mm coil), the circular 50 mm non-focal coil (MD of 0.6 mm), and the figure-8 25 mm coil in both orientations (MD of 2.2 mm for the PA orientations and 1.3 mm for the RL orientation). Increasing the output to 120 % MSO increased the MDs for all the latter orientations to a maximum of 4.1 mm (figure-8 25 mm coil in PA orientation). At this output, the circular coils with a parallel RL orientation, the circular 70 mm non-focal coil, and the figure-8 70 mm coil with PA orientation also induced a field greater than the RV, at MDs of 0.6 mm, 0.1 mm, 1.6 and

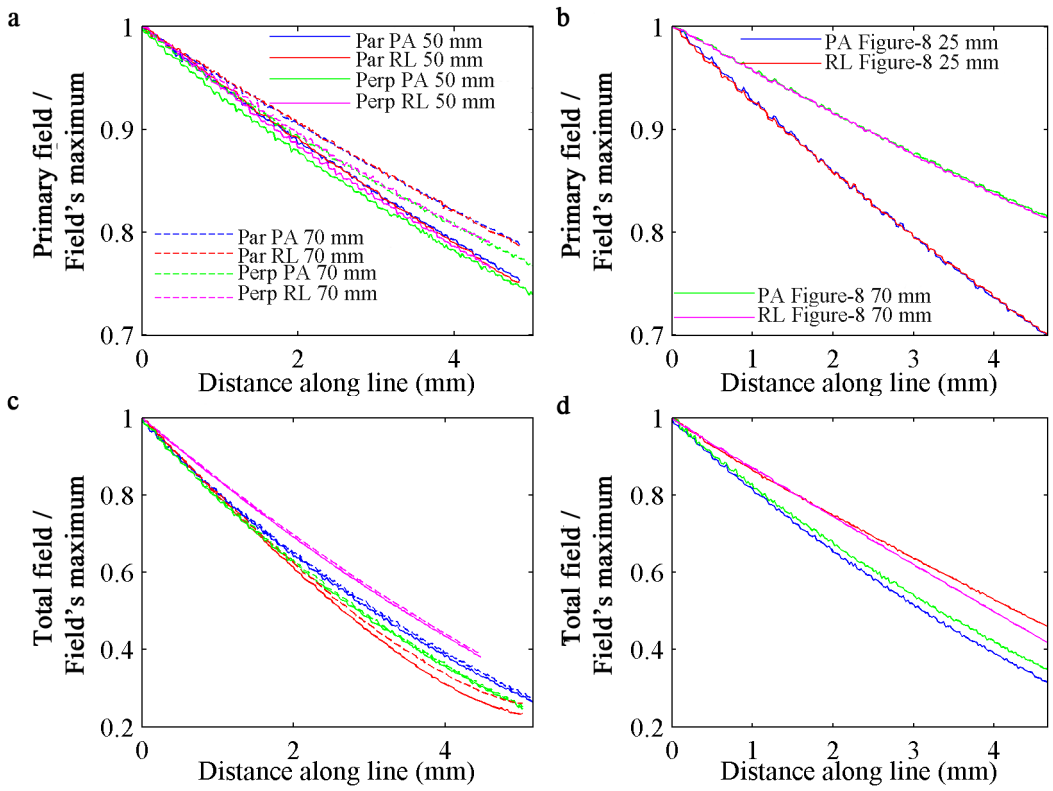

Figure 4.3.4: Decay of the field induced by the focal coil orientations along test lines that go from the positions of the maximum value of the field on the brain's surface to the centre of the brain. (a)/(b) Decay of the primary component of the electric field induced by the circular / figure-8 coils; (c)/(d) Same as (a)/(b) but now for the total electric field.

1.9 mm, respectively. With a smaller output of 50 % MSO, the only coil orientation that managed to induce a field larger than the RV was the figure-8 25 mm coil with PA orientation (MD of 0.3 mm). The circular coils with perpendicular orientations never induced a field greater than RV, regardless of the stimulation intensity used.

Field's focality

The focality of the primary component of the field is much worse than that of the total electric field for the focal coil orientations (see Table 4.3.2). This can also be observed in Figure 4.3.1. Globally, the HPR for the total electric field ranges from 15 % to 78 % of the value of the HPR for the primary field. Another difference is that the HPR of the primary field depends essentially on the size of the coils, being largest for the figure-8 70 mm coil and smallest for the figure-8 25 mm coil. The HPR for the total field, however, depends more on the orientation of the coils than on their size. This is shown by the fact that the HPR for the RL coil orientations is larger than that for PA orientations. Also, circular coils oriented perpendicularly tend to have better focality

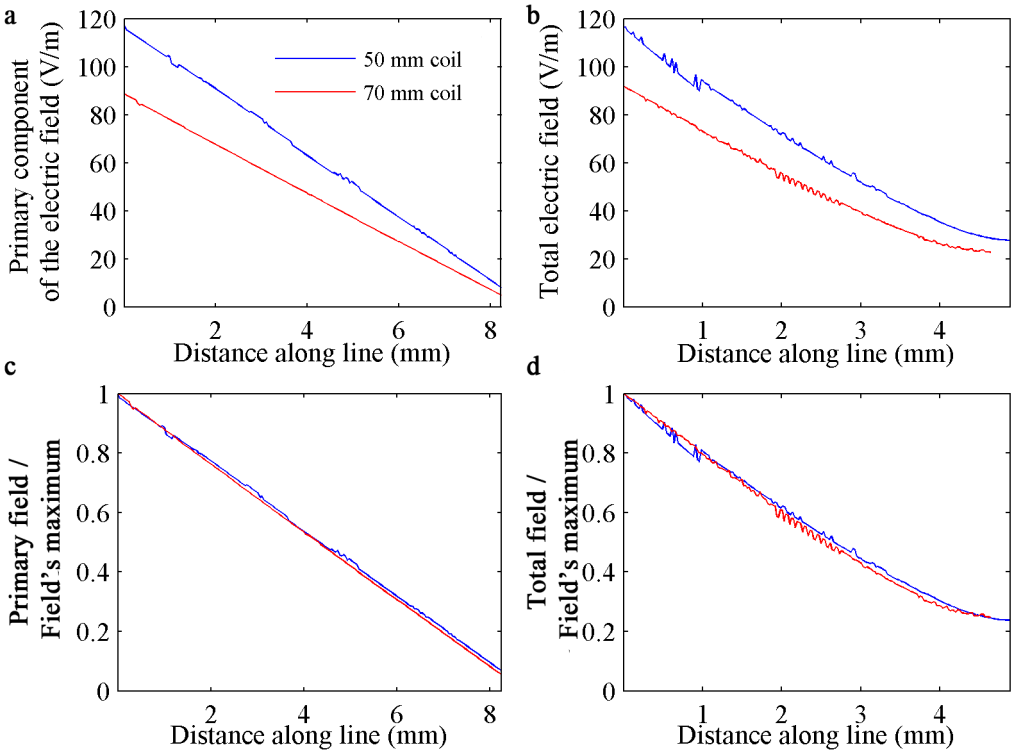

Figure 4.3.5: Magnitude and decay of the field induced by the non-focal coil orientation along test lines that go from the positions of the maximum value of the field on the brain's surface to the centre of the brain. (a)/(b) Magnitude of the primary component of the electric field / total electric field induced by the circular coils; (c)/(d) Decay of the primary component of the electric field / total electric field induced by the circular coils. The magnitude plots were obtained at 75 % MSO.

than those with a parallel orientation at the expense of a lower total field as is the case in human stimulation (Roth et al., 1991b). Of all the focal coil orientations identified in the last section as being able to induce a field greater than the RV at 75 % MSO, the one with the best focality was the circular 50 mm coil, in a parallel PA orientation, having an HPR of 0.49 cm^2. For the figure-8 25 mm coil the HPR was 0.51 cm^2 and 1.1 cm^2 for the PA and RL orientations, respectively.

The non-focal orientation induces a primary field with better focality than the total electric field (see Table 4.3.2): the HPR value for the total electric field increases about 61 % for the circular 50 mm coil and 66 % for the 70 mm coil. This is because the primary field is localized essentially in the front and back of the brain's surface whereas the total electric field is localized bilaterally in the same surface (see Figure 4.3.2).

Table 4.3.1: Maximum depth of stimulation along test lines for all the tested coil orientations. The results are shown for several stimulator outputs.

Coil orientation	Maximum depth of stimulation (mm)			
	50 % MSO	75 % MSO	100 % MSO	120 % MSO
Circular parallel 50 mm PA	-	0.7	2.0	2.8
Circular parallel 50 mm RL	-	-	-	0.6
Circular perpendicular 50 mm PA	-	-	-	-
Circular perpendicular 50 mm RL	-	-	-	-
Circular parallel 70 mm PA	-	0.4	1.8	2.6
Circular parallel 70 mm RL	-	-	-	0.1
Circular perpendicular 70 mm PA	-	-	-	-
Circular perpendicular 70 mm RL	-	-	-	-
Figure-8 25 mm PA	0.3	2.2	3.3	4.0
Figure-8 25 mm RL	-	1.3	3.1	4.1
Figure-8 70 mm PA	-	-	1.0	1.9
Figure-8 70 mm RL	-	-	-	-
Circular 50 mm non-focal	-	0.6	1.8	2.5
Circular 70 mm non-focal	-	-	0.9	1.6

Table 4.3.2 also displays the HPR as a percentage of the total area of the surface that represents the brain. From the table it can be concluded that the HPR for the primary electric field induced by the biggest coils covers almost all the surface of the brain (with the exception of the non-focal orientations for the reasons presented above). Even for the smaller figure-8 25 mm and the circular 50 mm coils, the HPR represents a minimum of 44 % and 66 % of the total area, respectively. The HPR for the total electric field, however, is much smaller: always less than 40 % of the total area, with an average value of 24 %.

Table 4.3.2: HPR for the primary component of the field and for the total electric field induced by all the coil orientations modelled in this study. The HPR is presented both in cm^2 as well as the percentage of the total area of the surface that represents the brain (2.97 cm^2).

Coil orientation	HPR (cm^2)		HPR (% of brain's area)	
	Primary field	Total field	Primary field	Total field
Circular parallel 50 mm PA	2.16	0.49	73 %	16 %
Circular parallel 50 mm RL	1.97	1.00	66 %	34 %
Circular perpendicular 50 mm PA	2.00	0.36	67 %	12 %
Circular perpendicular 50 mm RL	2.00	0.73	67 %	25 %
Circular parallel 70 mm PA	2.78	0.51	93 %	17 %
Circular parallel 70 mm RL	2.55	1.05	86 %	35 %
Circular perpendicular 70 mm PA	2.50	0.38	84 %	13 %
Circular perpendicular 70 mm RL	2.50	0.78	84 %	26 %
Figure-8 25 mm PA	1.31	0.51	44 %	17 %
Figure-8 25 mm RL	1.35	1.06	46 %	36 %
Figure-8 70 mm PA	2.97	0.59	100 %	20 %
Figure-8 70 mm RL	2.97	1.13	100 %	38 %
Circular 50 mm non-focal	0.43	0.70	15 %	23 %
Circular 70 mm non-focal	0.39	0.65	13 %	22 %

4.4 Discussion

Cause of the low induced electric field

In this work the field induced in a model of a mouse's head by several different coils with various sizes and orientations was calculated. Consistent with what was found in an earlier work (Weissman et al., 1992), many of the models studied here failed to induce a total electric field stronger than the RV in the mouse's brain, even at 120 % MSO. Based on the work of Weissman et al. (1992) the decrease of the electric field

with decreasing head's radius has been attributed to the fact that smaller heads capture a smaller fraction of the total flux of the magnetic field. The authors of that study provided a mathematical model to help prove that point. The model contained a circular coil (5 cm radius) and a spherical head located at the centre of the coil. As the radius of the sphere decreased, so did the magnitude of the electric field induced in the head. It can be shown (see (Tenforde, 1996)) that this results indeed from a decrease of the total flux of the magnetic field with decreasing head size. However, this argument is based on the use of Faraday's law, which provides information only about the non-conservative primary component of the total electric field. It could be applied to the case considered because, due to its special symmetry, no secondary component of the field was generated. Furthermore, this argument is wrong when applied to any other coil configuration relative to the sphere, even disregarding the secondary component of the electric field. As an example of this consider a spherical head model located under the central element of a figure-8 coil. As the radius of the sphere decreases, so does the flux of the magnetic field crossing the circle perpendicular to the coil's plane and located at the plane that separates both wings of the coil (see Figure 4.4.1); however the maximum value of the magnitude of the primary component of the field remains the same provided that the top of the head stays at the same distance from the coil. This stems from the fact that in TMS, the contribution of the induced currents to the total magnetic field is negligible and so the primary component of the electric field at any point inside the head is determined solely by the geometry of the stimulation coil and its position relative to the point considered, being independent of the target's size.

The dependency on the target volume is introduced exclusively via charge accumulation at the boundaries, which generates the conservative secondary component. Thus, only the specification of the boundary shape can yield the total electric field in the general (quasistatic) case. The results presented in this study show that the low total electric field results from this secondary field that tends to oppose the primary field, reducing it. For the same coil size, the secondary field increases with decreasing head's radius, which explains why the field induced in the mouse's head is low. The secondary field is also highly dependent on the geometry and orientation of the coils, which is seen by the different magnitude, decay and focality of the field induced by the different coils modelled in this study.

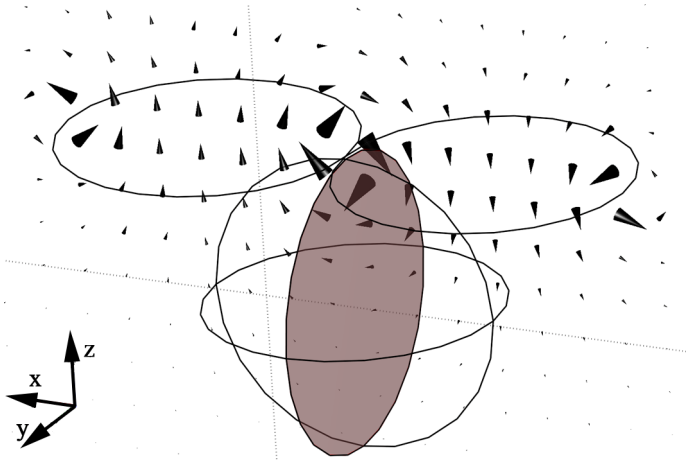

Figure 4.4.1: Vector plot of the magnetic field ($\vec{B}$) induced by a figure-8 coil. The flux across the plane highlighted in the figure increases with the radius of the sphere that represents the head.

Performance of the different coil orientations

Regarding the focal coil orientations, the smallest coils (circular 50 mm coil and figure-8 25 mm coil) proved to induce fields not only stronger than those induced by the biggest coils, but also with a smaller decay in depth. In terms of coil orientations, the only viable orientation for the circular coil was when it was placed parallel to the mouse's head inducing field in the PA direction (Figure 4.2.2 c). For the figure-8 coil, either the PA or RL orientations are capable of inducing a strong field that decays slowly.

The primary component of the field induced in the non-focal coil orientations was much lower than that induced in the focal orientations, but the total electric field was among the highest. This resulted from the fact that the secondary component of the field, in these models, decreased the magnitude of the primary component in some regions but increased it in other regions. The net result was, therefore, a total electric field with a magnitude almost equal to that of the primary field, albeit with a different spatial distribution. These orientations also proved to be able to achieve a field greater than RV at considerable depths (maximum of 2.5 mm for the 50 mm coil at 120 % MSO). However, investigators using this orientation should be aware that, unlike for the focal coil orientations, the field induced in the brain in these orientations has two main directions, one for each hemisphere: PA and AP.

Regarding the focality of the induced field, the results showed that the secondary component of the field almost always improved the focality of the primary component. The only exceptions to this were the two non-focal coil orientations, where the total

electric field had a worse focality than that of the primary field. These results oppose the generalized idea that TMS of small animals leads to whole brain stimulation because of the high coil size / head size ratio. This would be the case if only the primary field was considered, because the HPR for that component of the field is usually higher than 60 % of the total brain's surface area (except for the non-focal orientations). The HPR of the total field is, however, much lower: average of 24 % of the total area of the brain.

Still considering the focality of the field, the results show that coil size has a smaller impact than coil orientation. For the most efficient coils, the circular 50 mm coil induces a more focal field than the figure-8 25 mm coil. Other coil orientations proved to have a better focality, mainly the perpendicular PA orientation for the circular coils. However these other orientations failed to induce a strong field at the brain surface rendering them ineffective in stimulating the mouse's brain.

Model limitations and future work

The results presented here are for a homogeneous and isotropic model of a mouse. The main conclusions of this work should however hold for more realistic models, given that most charge accumulation in any model will always occur at the skin – air interface, which is correctly modelled in this work. In particular, the absence of the skull and CSF is not likely to have a significant effect on the results, given that the field induced in TMS does not have a significant radial component.

The present work highlights the importance of the field due to charge accumulation on the stimulation of mice with TMS. The results should hold qualitatively for other small animals such as rats or cats, but an accurate quantitative calculation of the field can only be obtained with numerical models. The latter are, therefore, important when designing experimental protocols and coils more suitable for small animal stimulation.

5 Conclusions

5.1 Summary of main findings

In this work numerical methods were employed to create models that enabled the calculation of the electric field induced during TMS, as well as the prediction of the response of compartmental models of neurons to this applied field. These models proved useful to study the application of TMS to deep-brain stimulation and to small animal studies. Furthermore, the models also allowed for the study of the dominant neuronal activation mechanisms in the case of TMS of the human motor cortex.

TMS of deeply located brain regions

The first application of TMS that was studied in this work concerned the stimulation of deeply located brain regions. In that study, the finite element method was used to create realistic models of coils specially designed to stimulate deep brain regions, and to study the effects of the inclusion of ferromagnetic cores on the induced field. The first part of that study focused on simple coil geometries placed over spherical head models. The results obtained in that initial study were then used to create a more detailed model, both in terms of coil geometry and complexity of the head model.

The inclusion of ferromagnetic cores in the studied coil (H1 coil) led to an increase of the magnitude of the induced field, which was greater for regions close to the core. Furthermore, the core also affected the decay of the field along certain directions. When the core was placed over the left hemisphere, the decay of the field along superior-inferior lines diminished, whereas the decay along lines going from the left hemisphere to the right one increased. In the model where the core was placed over the head's front, the field along superior-inferior lines also diminished, but the decay along lines going from anterior to posterior regions increased. Finally, the frontal core configuration also

led to an increase on the focality of the field, by making the component of the field along the left-right direction over the head's front the dominant one. The lateral core over the left hemisphere, however, slightly decreased the focality of the field.

The results that were obtained suggest that the inclusion of the ferromagnetic cores might make these coils even more useful in stimulating deep subcortical regions. However, given the different results obtained when the cores were placed over the left hemisphere and over the head's front, the choice of the optimal position of the core must be chosen in accordance with the position of the target region.

Field-single neuron interaction in TMS of the human motor cortex

The second study reported in this work involved the investigation of the dominant stimulation mechanisms of neurons in TMS of the human motor cortex. The creation of a model to study these mechanisms was done in two different steps. In the first step the finite element method was used to create an accurate model of a commercially available figure-8 coil, a model which is commonly used in these types of applications of TMS. The coil was placed over volume conductors that contained lines representing the trajectories followed by neurons. In the second step of this work, the field induced along those lines was then used to solve a compartmental version of the cable equation using numerical integration methods, such as the backward Euler's method and the Crank-Nicolson's method. As the field was given a realistic temporal waveform, with amplitudes and times courses similar to the output of commercially available monophasic and biphasic magnetic stimulators, the activation threshold of the neurons could then be calculated. The analysis also focused on the site where stimulation occurred and on which phase of the field's waveform led to activation.

The first part of this study used a volume conductor with the shape of a rectangular hexahedron. The latter was divided into two halves, modelled with the dielectric properties of GM and WM. In this study, the neuron crossed the GM-WM interface perpendicular to it. In the region where the crossing occurred, the field along the neuron had a discontinuity which was shown to be able to lead to neuronal activation within the amplitude range of the modelled monophasic stimulator.

The second part of this study used a volume conductor that modelled the central sulcus. The model also contained representations of pyramidal tract fibres (*P*), cortical interneurons oriented mainly perpendicular (*n*) and tangential (*t*) to the sulcus wall, and

pyramidal association fibres (*a*) projecting from several cortical areas into the motor cortex. The results showed that *t* neurons in the crown of the gyrus and *P* neurons located close to the coil could be stimulated at the axonal termination and fibre bend, respectively. The site of stimulation of *a* neurons varied from neuron to neuron: sometimes stimulation occurred at axonal terminations, and other times at axon bends. Contrary to what was suggested by the previous study, the sites where the axons crossed the GM-WM interface never led to stimulation. However, these sites changed the thresholds of activation at other sites, which indicates the importance of accounting for tissue heterogeneities in modelling TMS. Regarding the activation thresholds, the values obtained for stimulation of *t* neurons, in the crown of the gyrus, and *P* neurons, located close to the coil, with monophasic PA pulses were similar to those reported in the literature for the generation of *I*- and *D*-waves, respectively. This strongly suggests that stimulation of these neurons gives rise to those waves. Furthermore, *a* neurons were stimulated more easily by AP pulses than by PA pulses, which is coherent with some papers that have suggested that these neurons are implied in the mechanism of generation of late I_3-waves with monophasic AP pulses. Regarding the temporal waveform of the field, it was found that the second phase of biphasic current pulses was more efficient in stimulating neurons than the first phase of either monophasic and biphasic pulses, which can be attributed to the fact that this phase lasts twice as long as the other two phases.

TMS of small animals

The last application that was studied in this work is related to the application of TMS, more precisely rTMS, to the stimulation of small animals. The importance of this work stemmed from the appearance of several studies in which rTMS was applied to small animals, mainly rodents. In this study a realistically shaped homogeneous mouse model was created, and the field induced by several coils with different shapes (figure-8 or circular), sizes and orientations, most of which based on actual orientations used in the studies presented in the literature, was calculated by using the finite element method.

The results showed that the secondary component of the electric field, arising from charge accumulation at the air-skin interface, strongly influenced the total electric field, reducing its magnitude and increasing its decay along test lines. The focality of the field, investigated by analysing the field distribution at a surface representing the brain, was improved by the secondary component. This opposes the idea presented in many

studies that small animal stimulation leads to whole brain stimulation. In terms of the optimal orientation and geometry of the coil, it was found that the smallest figure-8 coil with a PA orientation was actually the one that induced a total electric field with the highest magnitude and with the smallest decay in depth, while maintaining a focality within the best observed in the study.

The results are also consistent with previous studies that indicated that the field induced in the head of small animals was much smaller than that induced in the human head due to a bigger ratio between the size of the coil and the size of the head. Those studies, however, attributed that effect to the fact that smaller heads capture a smaller fraction of the total magnetic field flux. In this work this hypothesis was proven to be wrong and the reported effect was, instead, attributed to the increase in the secondary component of the total electric field that occurs with smaller ratios between coil and head sizes.

5.2 Limitations of these theoretical models

In spite of all the careful implementation of the models used in this work, following the words of George Box, 'all models are wrong, (but) some are useful'. It was this work's main objective to create 'useful' models that can be employed to guide the application of TMS and help interpret the neurophysiologic basis of the results obtained in many different studies. To attain this purpose it is important to consider the importance of several parameters that served as inputs to the created models and of the effects of some of the assumed simplifications in the results obtained.

Coil geometry

The finite element method proved to be very useful in terms of designing coils, with geometries ranging from the circular and figure-8 coil to the more complex H1 coil. This is important not only in predicting the field distribution induced by actual coils in many experimental setups (e.g. the small animal TMS study), but also in predicting the performance of new coil designs created to stimulate more efficiently target regions (e.g. the H1 coil).

The approximate way the coils were modelled in this study, i.e. with lines instead of realistic representations of the wires, provides a good first order approximation to the

induced field, especially in regions not very close to the coil. This approximation might prove of great importance in the modelling of small animal TMS, as the target regions in those applications are closer to the coil as compared to applications of TMS in humans. Even so, this approximation is expected to introduce only quantitative changes in the results, nor affecting the main conclusions drawn about the importance of the field due to charge accumulation.

The construction of realistic models for coils is hindered by the fact that not much data is provided in the literature regarding the details of coil geometries. This can be overcome by doing X-ray scans on commercially available coils (see, for instance, (Thielscher and Kammer, 2002; Salinas et al., 2007)).

Volume conductor geometry

Many of the studies described throughout this work used realistic, albeit somewhat simplified, geometries for the volume conductor. In the studies about deep brain stimulation and about small animal TMS, this was crucial because the secondary component of the field arising from charge accumulation at the skin-air interface greatly affected the magnitude, decay and focality of the total electric field. In the study about neuronal activation mechanisms in TMS, charge accumulation at the skin-air interface was of less importance as compared to charge accumulation at the other boundaries between tissues represented in the model, especially the GM-WM boundary. Using more complex geometries might yield somewhat different results, but again only quantitatively. In terms of a qualitative analysis, the models considered should contain all the relevant geometric information. An exception to this is perhaps the sulcus model, for which the modelled geometry in the regions further away from the coil is significantly different from the actual geometry (see (Yousry et al., 1997)). However, this should only affect the results in a region where the field induced by the coil is already too weak to significantly affect neurons.

A way to improve these models is to use co-registered MRI and CT images and to segment those images. Using this sort of analysis, many studies have described high-resolution finite element models of heads (Chen and Mogul, 2009) and even small animals such as mice (Dogdas et al., 2007), with several different tissues present.

Dielectric properties of tissues

Creating a realistic geometry representing the head and all of the relevant tissues is only the first step in creating a realistic head model. A second important step is to attribute relevant dielectric properties to the tissues of that model. A fair amount of work has been done in this field (for a review see (Gabriel et al., 1996a)) and the results obtained for the typical frequencies attributed to TMS pulses (between 3.5 kHz and 5 kHz) are fairly consistent among the literature. However, considering fixed values for the tissues' dielectric properties is only an approximation, because it assumes that the values are constant within the entire frequency range of the stimulating pulse (from DC to about 10 kHz), which is not completely true. A more correct approach would be to include the dependency of the dielectric properties on the frequency of the pulse explicitly in the equations. This would require, however, knowledge about the values of these parameters at very low frequencies, which is still sparse. The effects of this approximation on the models considered should, however, be small.

A more serious approximation, which influences the results significantly, was to consider that the tissues are isotropic media. While this is a fair assumption for the skin, skull and GM, it is not true for the WM. This will change the field distribution in the WM significantly, which can affect some of the predictions regarding activation mechanisms. One way to take this into account is to consider information about DT-MRI into anatomically accurate head models (see (De Lucia et al., 2007)).

Electrophysiological and morphological properties of neurons

Another important limitation of the models considered stemmed from the lack of knowledge about some parameters used in the models of neurons. The importance of these parameters has already been discussed in Chapter 3, where it was argued that changes in these parameters can change the activation sites and thresholds predicted in this model. This limitation will persist until a general accepted model for each of the neurons present in the human motor cortex is described.

5.3 The future of numerical modelling in TMS

In the early days of TMS, one of the main limitations regarding numerical modelling was related to the lack of computational power. In fact, one of the first models created

(Tofts, 1990), 19 years ago, was solved on a Sun 3/260 workstation with a 'state-of-the-art' 25 MHz CPU and a staggering 32 MB of RAM memory. Nowadays it is relatively cheap to buy computers with at least two cores running at 3 GHz and more than 8 GB of RAM memory. This rapid development has eliminated one of the limitations of numerical modelling related to availability of computational power, and led to the appearance of increasingly more complex models. However, lack of availability of information regarding the inputs of the model still poses many challenges to the future of numerical modelling.

Despite these shortcomings, these kinds of models are, and will continue to be, the only available way to visualize field distributions, assess the effectiveness of different coil geometries and orientations in the stimulation of a given brain structure, and to determine the response of neurons to the applied field. The tendency shown over the last years to improve the predictions of the models and decrease computational time has a wealth of potential applications, such as real time calculation of the electric field distribution in a realistic model of a subject's head. If the model additionally includes detailed neuronal models, a prediction of the effectiveness of a given TMS session can be assessed in real time. Real-time prediction of the outcome of TMS / rTMS may, therefore, improve the effectiveness of these techniques in many therapeutic applications. These models might also prove useful in understanding the underlying physiological effects of TMS / rTMS, which is important in order to improve the effectiveness of the currently used stimulation paradigms, and also to suggest new potential applications.

Appendices

A Quasistatic approximation

In this appendix it is shown that, under the quasistatic approximation, the equations used by Comsol to determine the potentials ϕ and $\vec{A}$ reduce to the Laplace and Poisson's equation.

A.1 Formal definition of the quasistatic approximations

The quasistatic approximations have already been described in Chapter 1. However they will be presented here in a more formal manner that will prove to be more appropriate for deriving Laplace and Poisson's equation from the more general equations used in Comsol.

As was previously discussed, there are three quasistatic approximations. The first approximation (*A1*) is to consider that the wavelength of the electromagnetic stimulus is much larger than the typical dimensions of a human head, *R*. The second approximation (*A2*) is to neglect capacitive effects and to consider the cerebral tissues as essentially resistive media. The third approximation (*A3*) is to consider that currents induced in the brain by the TMS pulse are much weaker than the currents flowing in the coil. The last approximation is equivalent to considering that the skin-depth of the neuronal tissues is much larger than *R*.

From a formal point of view, approximations (*A1*) and (*A3*) can be formally expressed by the same condition (Plonsey and Heppner, 1967):

$$(A1),(A3) \Leftrightarrow kR << 1, \text{ where } k^2 = -jw\mu(\sigma + jw\varepsilon) \qquad \textbf{A.1.1}$$

To prove the last statement it is convenient to express k^2 as a function of the tissue's skin-depth, $\delta = \sqrt{2/(w\mu\sigma)}$, and of the wavelength of the electromagnetic stimulating pulse, $\lambda = 2\pi/(w\sqrt{\mu\varepsilon})$:

$$k^2 = -2/\delta^2 j + (2\pi/\lambda)^2 \qquad \textbf{A.1.2}$$

From the previous expression it can easily be seen that the approximations (*A1*) and (*A3*) and condition A.1.1 are indeed equivalent.

Regarding the second quasistatic approximation, it can be expressed formally by:

$$(A2) \Leftrightarrow \sigma + jw\varepsilon \approx \sigma \qquad \textbf{A.1.3}$$

In order for the last expression to be valid, the magnitude of the imaginary part must be smaller than the magnitude of the real part, i.e. $\omega\varepsilon/\sigma << 1$.

In what follows it will also be assumed that each media is homogeneous and isotropic and, as such, the conductivity, permeability and permittivity parameters are all scalar quantities. In the most general case, the previous parameters must be described by tensors that vary from point to point. In the latter case it is still possible to simplify the equations used by Comsol, however, the simplified equations are somewhat different from Poisson's and Laplace's equations.

A.2 General form of the equations

Comsol solves two equations in order to calculate the potentials $\vec{A}$ and ϕ. The first of these equations is obtained by substituting the constitutive relations $\vec{B} = \mu\vec{H}$, $\vec{D} = \varepsilon\vec{E}$ and expressions $\vec{B} = \vec{\nabla} \times \vec{A}$ and $\vec{E} = -\partial\vec{A}/\partial t - \vec{\nabla}\phi$ into Amperes' law, which in the case of TMS is expressed by:

$$\vec{\nabla} \times \vec{H} = \vec{J}_{coil} + \sigma\vec{E} + jw\vec{D} \qquad \textbf{A.2.1}$$

where $\vec{J}_{coil}$ is the current density in the coil. Doing this substitution the following expression is obtained:

$$\vec{\nabla} \times \vec{\nabla} \times (\mu^{-1}\vec{A}) + (jw\sigma - w^2\varepsilon)\vec{A} + (\sigma + jw\varepsilon)\vec{\nabla}\phi = \vec{J}_{coil} \qquad \textbf{A.2.2}$$

where it has been assumed that all fields have a harmonic variation with time and, therefore, derivation with respect to time can be represented by multiplication by *jw* (Cheng, 1989).

The second equation can be obtained by taking the divergence of equation A.2.2 and by noticing that the divergence of both the first term on the left and on the right of A.2.2 vanishes:

$$\vec{\nabla} \cdot \left[(jw\sigma - w^2\varepsilon)\vec{A} + (\sigma + jw\varepsilon)\vec{\nabla}\phi \right] = 0 \qquad \textbf{A.2.3}$$

It is possible to show that this equation is equivalent to the continuity equation (Jackson, 1999).

A.3 Quasistatic form of the equations

Now it is shown that equations A.2.2 and A.2.3 reduce to the Poisson equation for the vector potential and to the Laplace equation for the scalar potential, respectively. In order to do so, however, it is first necessary to define a gauge condition for the vector potential. In bioelectric phenomena, the Lorentz gauge is usually used and it is defined as (Plonsey and Heppner, 1967):

$$\vec{\nabla} \cdot \vec{A} = -(jw\varepsilon + \sigma)\mu\phi \qquad \textbf{A.3.1}$$

Beginning with equation A.2.2, the first term on the left hand side can be written as (Jackson, 1999):

$$\vec{\nabla} \times \vec{\nabla} \times (\mu^{-1}\vec{A}) = \mu^{-1}\vec{\nabla}\left(\vec{\nabla} \cdot \vec{A}\right) - \mu^{-1}\vec{\nabla}^2\vec{A} \qquad \textbf{A.3.2}$$

Substituting A.3.1 and A.3.2 into A.2.2 and collecting terms, the terms containing the scalar potential vanish and the following equation is obtained:

$$-\vec{\nabla}^2\vec{A} = \mu\vec{J}_{coil} - k^2\vec{A} \qquad \textbf{A.3.3}$$

where k^2 has been previously defined in A.1.1.

In order to estimate the relative importance of the terms in A.3.3 the coordinate variables, *(x,y,z)* can be rescaled by normalizing them by the typical dimensions associated with the human head[1]:

$$\begin{aligned} x' &= x / R \\ y' &= y / R \\ z' &= z / R \end{aligned} \qquad \textbf{A.3.4}$$

In terms of the normalized coordinate variables, A.3.3 can be rewritten as:

$$-\vec{\nabla}'^2\,\vec{A} = \mu R^2\vec{J}_{coil} - k^2R^2\vec{A} \qquad \textbf{A.3.5}$$

where the prime in the Laplacian operator means that it now contains the rescaled coordinate variables.

Under condition A.1.1, the last term of A.3.5 is negligible thus proving that the first equation used by Comsol, A.2.2, reduces under the quasistatic approximation to Poisson's equation for the vector potential:

[1] This approach is based on a similar one that has been applied to the cable equation (Basser and Roth, 1991).

$$-\vec{\nabla}^2\vec{A} = \mu\vec{J}_{coil} \qquad \textbf{A.3.6}$$

Regarding the second equation used by Comsol, A.2.3, substituting into it the Lorentz Gauge expression, A.3.1, leads to:

$$\vec{\nabla}\cdot\left[(\sigma + jw\varepsilon)\vec{\nabla}\phi\right] - (jw\sigma - w^2\varepsilon)(\sigma + jw\varepsilon)\mu\phi = 0 \qquad \textbf{A.3.7}$$

Using the second quasistatic approximation, A.1.3, the following simplified equation is obtained:

$$\vec{\nabla}\cdot\left[\vec{\nabla}\phi\right] - (jw\sigma - w^2\varepsilon)\mu\phi = 0 \qquad \textbf{A.3.8}$$

The first term of A.3.8 is just the Laplacian operator, whereas the last term can be rewritten in terms of the variable k^2. Doing so the following expression is obtained:

$$\vec{\nabla}^2\phi = k^2\phi \qquad \textbf{A.3.9}$$

The last equation can again be rescaled by using the normalized variables A.3.4. This yields that the term on the right-hand side can be neglected under the quasistatic approximation and, therefore, that the second equation used by Comsol reduces to the Laplace equation for the scalar potential:

$$\vec{\nabla}^2\phi = 0 \qquad \textbf{A.3.10}$$

B Validation of numerical calculations in Comsol

In this appendix results about Comsol validation studies are presented. The validation results show that Comsol can accurately calculate the inductance of circular and toroid cores with or without the presence of ferromagnetic cores.

B.1 Coil inductance

B.1.1 Introduction

Inductance of circular loops

In order to validate the numerical results obtained by Comsol, it was used to calculate the inductance of coil models for which theoretical expressions exist. One case that has been thoroughly studied is that of a circular loop with a circular cross-section, for which the inductance is given by the following expression (Jackson, 1999):

$$L \approx a\mu_0\left[\ln\left(\frac{8a}{s}\right) - 2 + \mathrm{Y}\right] \qquad \textbf{B.1.1.1}$$

In the previous expression, a represents the average radius of the coil, i.e. the distance between the centre of the loop and the centre of the wire, and s represents the radius of the wire. Y is a constant parameter that is set to 1/4, under the assumption that the current density in the coil is homogeneously distributed across the wire's cross section, or to 0, assuming that the current density is concentrated essentially in the surface of the wire. The choice of the parameter Y depends on the value of the skin-depth:

$$\delta = \sqrt{\frac{2}{w\sigma\mu}} \qquad \textbf{B.1.1.2}$$

Coils are made of a copper wire, a material which has a very high electrical conductivity $\sigma = 5.997\times10^7$ S/m and for which the relative magnetic permeability, μ_r, is 1. Using expression B.1.1.2 it is then possible to calculate the copper's skin-depth as a function of the frequency. For a very low frequency value of 0.1 Hz, $\delta = 205.5$ mm, a value much larger than the radius of wires used in coils and, as such, Y can be set to 1/4. For a frequency closer to the range of frequencies associated with most TMS pulses, 5 kHz, $\delta = 0.9$ mm, which is a value smaller than the radius of most wires used in TMS coils. If the wire has a very large radius, for this frequency value, then Y can be set to 0, but if the wires are thinner this approximation fails.

Inductance of toroids

In order to validate the results obtained by Comsol when ferromagnetic cores are present it was used to calculate the inductance of toroids, for which an approximate theoretical expression can easily be derived.

Toroids consist of N circular loops tightly wound around a ferromagnetic core, as shown in Figure B.1.2.1. Under certain conditions it is possible to use the following expression to calculate the inductance of the toroid:

$$L \approx \frac{\mu_0 \mu_r N^2 A}{2\pi r} \qquad \textbf{B.1.1.3}$$

where A is the cross sectional area of the toroid: $\pi(b-a)^2/4$.

Expression B.1.1.3 can be derived by applying Ampère's law and by assuming that the magnetic field inside the core is constant and therefore it can be estimated by its value at the centreline of the core. This is an approximation, given that the magnetic field varies inside the core. However, the validity of this approximation is good if the radius of the toroid is much larger than the radius of the coil. The formula also does not take into account the radius of the wire of the circular loops and frequency effects. Another approximation is that of considering that the relative magnetic permeability of the core is high enough so that most of the magnetic field flows through the core.

B.1.2 Results

Inductance of circular loops: influence of the radius of the coil

In the first set of calculations, the inductance of circular coils with different radii but with the same wire radius, s = 5 mm, was calculated. All models were solved twice,

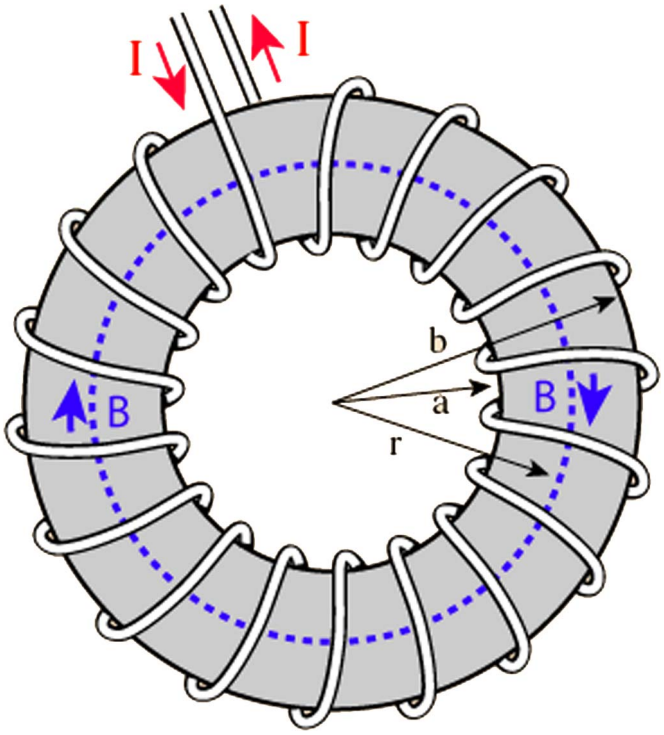

Figure B.1.2.1: Schematic drawing of a toroidal coil. The coil consists of N circular loops tightly wound around a ferromagnetic core. The parameters *a* and *b* represent the inner and outer radii of the ferromagnetic core, respectively. The parameter r represents the average radius of the toroid, i.e., the distance between the centre of the toroid and the centre of the ferromagnetic core. The blue arrows inside the core indicate the direction of the magnetic field. (Image taken from **http://hyperphysics.phy-astr.gsu.edu**).

once for a frequency of 0.1 Hz and a second time for a frequency of 5 kHz. The results obtained for a frequency of 0.1 Hz were compared with the results obtained with the theoretical expression B.1.1.1 with Y set to 1/4 (current distributed uniformly through the wire). The results obtained at a frequency of 5 kHz were compared with the same theoretical expression but now with Y set to 0 (current concentrated at the surface of the wire). These results are summarized in Table B.1.1 and Table B.1.2 respectively.

From the analysis of the results, it can be seen that there is a good general agreement between the theoretical results and the ones calculated in Comsol, with relative differences ranging from 0.07 % to 10.31 %. Despite this good agreement, the results obtained by Comsol were systematically lower than the theoretical results. There is also a systematic pattern for the relative differences: they are highest for the coils with the smallest radii and tend to decrease with increasing coil's radius until a certain value (a = 3 cm for f = 0.1 Hz and a = 5 cm for f = 5 kHz). After that, the error tends to increase with the radius of the coil.

Table B.1.1: Inductance of circular loops at low frequencies (f = 0.1 Hz) as a function of the average radius of the coil. The radius of the external sphere was set to 0.3 m and the radius of the coil's wire to 5 mm.

a (cm)	Theoretical Inductance Y=1/4 (μH)	Inductance obtained in Comsol f = 0.1 Hz (μH)	Relative difference (% of theoretical value)
1	0.0129	0.0119	7.75
2	0.0431	0.0417	3.25
3	0.0780	0.0778	0.26
4	0.1211	0.1181	2.48
5	0.1654	0.1615	2.36
6	0.2122	0.2070	2.45
7	0.2611	0.2543	2.60
8	0.3119	0.3031	2.82
9	0.3642	0.3530	3.08
10	0.4179	0.4043	3.47

Table B.1.2: Inductance of circular loops at high frequencies (f = 5 kHz) as a function of the average radius of the coil. The radius of the external sphere was set to 0.3 m and the radius of the coil's wire to 5 mm.

a (cm)	Theoretical Inductance Y=0 (μH)	Inductance obtained in Comsol f = 5 kHz (μH)	Relative difference (% of theoretical value)
1	0.0097	0.0087	10.31
2	0.0368	0.0361	1.90
3	0.0705	0.0700	0.71
4	0.1085	0.1083	0.18
5	0.1497	0.1496	0.07
6	0.1933	0.1925	0.41
7	0.2391	0.2375	0.67
8	0.2867	0.2839	0.98
9	0.3359	0.3313	1.37
10	0.3864	0.3792	1.86

The fact that the differences are highest for the coils with the smallest radii can be attributed to the fact that the theoretical expression B.1.1.1 is only an approximation. The first order corrections for that expression are proportional to *s/a* (Jackson, 1999) and, therefore, they tend to increase for the coils with smaller radii. The fact that the relative difference tends to increase for the coils with higher radius is probably related to the way the model was built in Comsol. In order to calculate the scalar and vector potentials in models with coils it is necessary that the latter are surrounded by an external medium representing air. In the outer surfaces of this medium approximate boundary conditions must be set: $\phi = 0$ and $\vec{n} \times \vec{A} = 0$. The latter are valid only if the surfaces are far away from the coil. In these models, the external medium was represented by a sphere with a radius of 30 cm. As the coils became bigger, the imposed boundary conditions led to errors, which resulted in the increased relative error. To test this hypothesis, the same models were solved but now using a bigger external sphere with a radius of 1 m. The results of this study are presented in Table B.1.3, for f = 0.1 Hz and Table B.1.4, for f = 5 kHz. Analysing the tables it can be seen that the increased sphere's radius led to a decrease of the relative difference for the inductance of the coil with highest radius. The relative error for the inductance of the coil with a radius of 5 cm was less affected by the radius increase, and the inductance of the coil with the smallest radius wasn't affected at all by the radius of the outer sphere. These results support the hypothesis that the error increase observed for bigger coils is related to the radius of the outer sphere.

Table B.1.3: Inductance of circular loops at low frequencies (f= 0.1 Hz) as a function of the average radius of the coil. The radius of the external sphere was set to 1 m and the radius of the coil's wire to 5 mm.

a (cm)	Theoretical Inductance Y=1/4 (μH)	Inductance obtained in Comsol f = 0.1 Hz (μH)	Relative difference (% of theoretical value)
1	0.0129	0.0119	7.75
5	0.1654	0.1617	2.24
10	0.4179	0.4100	1.89

Table B.1.4: Inductance of circular loops at high frequencies (f=5 kHz) as a function of the average radius of the coil. The radius of the external sphere was set to 1 m and the radius of the coil's wire to 5 mm.

a (cm)	Theoretical Inductance Y=0 (μH)	Inductance obtained in Comsol f = 5 kHz (μH)	Relative difference (% of theoretical value)
1	0.0097	0.0087	10.31
5	0.1497	0.1495	0.13
10	0.3864	0.3856	0.21

Inductance of circular loops: influence of the radius of the wire

In the second study, the inductance of a coil with an average radius of 5 cm but with wire radius ranging from 1 mm to 5 mm was calculated. The results of this study are presented in Table B.1.5, for low frequencies, and Table B.1.6, for high frequencies.

The results again show a good agreement between Comsol and the theoretical expression, with relative differences ranging between 0.07 % and 3.23 % of the theoretical value. For low frequencies, f = 0.1 Hz, the relative differences show a slight trend to increase with decreasing wire radius, which may be linked to the fact that the finite element's mesh inside the wires contains less elements for the smallest wire radius. For high frequencies, f = 5 kHz, the trend for the error to increase for the smaller radius is much more pronounced. This is related to the fact that the approximation that the current is concentrated at the surface of the coil's wire starts to fail for the smaller radius. At this frequency the skin-depth is of 0.9 mm, a value that is no longer small compared to the smallest wire radius. As a direct consequence of that, the values calculated by Comsol at low and high frequencies grow closer with decreasing radius of the wires.

Inductance of toroids

In order to test how accurately Comsol calculated the inductance of a toroidal core model a model was built with the following parameters: a= 11 cm, b= 22 cm and r= 16.5 cm (see Figure B.1.2.1). The model contained 4 circular loops (wire radius of 2 mm) wound around the ferromagnetic core, which was modelled with a relative magnetic permeability of 10^4. With these parameters, the theoretical expression B.1.1.3 yields a value of 1843.1 μH for the toroid's inductance.

Table B.1.5: Inductance of circular loops at low frequencies (f = 0.1 Hz) as a function of the radius of the wire of the coil. The radius of the external sphere was set to 0.3 m and the average radius of the coil to 5 cm.

s (mm)	Theoretical Inductance Y=1/4 (μH)	Inductance obtained in Comsol f = 0.1 Hz (μH)	Relative difference (% of theoretical value)
1	0.2665	0.2592	2.74
2	0.2229	0.2175	2.42
3	0.1975	0.1928	2.38
4	0.1794	0.1750	2.45
5	0.1654	0.1615	2.36

Table B.1.6: Inductance of circular loops at high frequencies (f = 5 kHz) as a function of the radius of the wire of the coil. The radius of the external sphere was set to 0.3 m and the average radius of the coil to 5 cm.

s (mm)	Theoretical Inductance Y=0 (μH)	Inductance obtained in Comsol f = 5 kHz (μH)	Relative difference (% of theoretical value)
1	0.2508	0.2589	3.23
2	0.2072	0.2143	3.43
3	0.1818	0.1854	1.98
4	0.1637	0.1647	0.61
5	0.1497	0.1496	0.07

In Comsol, the circular loops could not be in direct contact with the ferromagnetic core, because that would lead to problems related to the construction of the mesh. Hence, in the models there is a gap between the outer surface of the core and the inner surface of the coil. The results obtained for the inductance of the toroid as a function of the gap are shown in Table B.1.7. The inductance values obtained in Comsol are in good agreement with those predicted by the theoretical expression. Even so, it can be seen that Comsol's values are always slightly higher than those given by the theoretical expression, especially for the smaller gaps.

As a final study the impact that the relative magnetic permeability had on the results was also analysed. The data, presented in Table B.1.8, show that for low values of μ_r

there is a big difference between the theoretical expression and the value given by Comsol. This is related to the fact that, when μ_r is small, a non-negligible portion of all the magnetic field lines passes outside the core and, as such, the theoretical expression does not apply. For high values of μ_r the agreement again becomes good.

Table B.1.7: Inductance of toroidal cores (f = 1 Hz) as a function of the gap between the circular loops and the ferromagnetic cores and for a core with μ_r=10^4. The radius of the external sphere was set to 0.3 m in this model.

Gap (mm)	Theoretical Inductance (μH)	Inductance obtained in Comsol (μH)	Relative difference (% of theoretical value)
0.25	1843.07	1902.54	3.23
0.5	1843.07	1883.78	2.21
1	1843.07	1850.63	0.41

Table B.1.8: Inductance of toroidal cores (f = 1 Hz) as a function of the relative magnetic permeability value (μ_r) and for a fixed gap of 1 mm between the circular loops and the ferromagnetic cores. The radius of the external sphere was set to 0.3 m in this model.

μ_r	Theoretical Inductance (μH)	Inductance obtained in Comsol (μH)	Relative difference (% of theoretical value)
1	0.18	0.98	444.44
10	1.84	3.27	77.72
100	18.43	20.08	8.95
1000	184.31	186.72	1.31
10000	1843.07	1850.63	0.41

B.1.3 Conclusions

The presented results show that Comsol can calculate very accurately the inductance of the coils and the influence of ferromagnetic cores on the inductance. The differences between Comsol results and those of the theoretical expressions can always be explained by failures of the assumptions under which the theoretical expressions were derived.

C Electrophysiological and morphological properties of the modelled neurons

In this appendix a full description of the electrophysiological and morphological properties of the neurons modelled in this work is presented.

C.1 Discretized cable equation

The models of neurons used throughout this work all assume a division of the neuron into several cylindrical compartments. For each compartment, the electrophysiological properties of the neuron's membrane, the axial conductance of the intracellular medium and the diameter of the compartment must be specified. These parameters are crucial in order to solve the discretized version of the cable equation:

$$C_m \frac{dV(x)}{dt} + I_{ionic}(x) = G_a(V(x-\Delta x) - 2V(x) + V(x+\Delta x)) - G_a\left(\int_x^{x+\Delta x} E_x(s)ds - \int_{x-\Delta x}^{x} E_x(s)ds\right) \quad \text{C.1.1}$$

In this work two different types of neuron models were used, the main properties of which will be presented in this appendix.

C.2 Axon model used in tissue heterogeneity study

The first model used in this work contained only a representation of a myelinated axon. Each Ranvier node of the modelled axon was attributed non-linear membrane dynamics, as described by Sweeney at al (Sweeney et al., 1987). These membrane properties are based on experimental data obtained from voltage clamp experiments

performed on rabbit myelinated nerve fibres (Chiu et al., 1979). Sweeney et al. adjusted Chiu's data from 14 ºC to 37 ºC (body temperature). According to those studies, the ionic current term in C.1.1 can be written as:

$$I_{ionic,n} = \pi d_i \delta [g_{Na} m^2 h (V(x) - E_{Na}) + g_L (V(x) - E_L)] \quad \textbf{C.2.1}$$

where d_i is the diameter of the Ranvier node, δ is its length and the remaining parameters are described in Table C.2.1. The most notable feature of this expression is the absence of a potassium current, as opposed to neurons from other species that contain voltage-gated potassium channels. In these membranes, repolarisation of the membrane's potential during an AcPt is, however, assured because the membrane has a higher leakage conductance than membrane's that contain active potassium channels.

The functions m and h describe the behaviour of the sodium voltage-gated channels and they are obtained by solving a set of ordinary differential equations similar to that described in the model partially described in Chapter 1 (see page 53):

$$\begin{aligned} \frac{dm}{dt} &= \alpha_m (1-m) - \beta_m m \\ \frac{dh}{dt} &= \alpha_h (1-h) - \beta_h h \end{aligned} \quad \textbf{C.2.2}$$

In the previous expression, the functions α_m, β_m, α_h and β_h all depend on the transmembrane potential according to (Basser and Roth, 1991):

$$\begin{aligned} \alpha_m(V) &= \frac{126 + 0.363V}{1 + \exp\left(-\frac{49+V}{5.3}\right)} \\ \beta_m(V) &= \alpha_m(V) \exp\left(-\frac{V+56.2}{4.17}\right) \\ \alpha_h(V) &= \beta_h(V) \exp\left(-\frac{V+74.5}{5}\right) \\ \beta_h(V) &= \frac{15.6}{1 + \exp\left(-\frac{56+V}{10}\right)} \end{aligned} \quad \textbf{C.2.3}$$

where, V in the last expressions is the transmembrane potential, in mV, and $[\alpha]=[\beta]=\text{ms}^{-1}$.

Regarding the membrane's capacitance at the Ranvier nodes, it is given by:

$$C_m = \pi d_i \delta c_n \quad \textbf{C.2.4}$$

where c_n is the membrane's capacitance per unit area of the membrane (see Table C.2.1).

Table C.2.1: Electrophysiological and morphological properties of the axon model used in the studies about the importance of tissue heterogeneities in stimulation mechanisms in TMS.

Neuron's section	Membrane's electrical parameters		Morphological parameters
Ranvier Node (Basser and Roth, 1991)	Nodal capacitance per unit area (c_n)	2.5 μF/cm^2	Length (δ): 1.5 μm Diameter (d_i): $d_i = 0.6\ d_o$
	Resistivity of axoplasm (ρ_a)	54.7 Ω cm	
	Leakage conductance (g_L)	0.128 S/cm^2	
	Sodium maximum conductance (g_{Na})	1.445 S/cm^2	
	Leakage Nernst potential (V_L)	-80.01 mV	
	Sodium Nernst potential (V_{Na})	35.35 mV	
Myelinated internodes (Tasaki, 1955; Basser and Roth, 1991)	Myelin capacitance per unit area (c_{mye})	0.005 μF/cm^2	Length (L): L=100 d_o Diameter: d_o
	Resistivity of axoplasm (ρ_a)	54.7 Ω cm	
	Myelin conductance per unit area (g_{Lmye})	10^{-5} S/cm^2	
	Membrane's resting potential (V_r)	-80 mV	

The myelinated internodes in this axon mode were modelled as passive RC circuits with properties based on experimental data from the frog nerve fibre (Tasaki, 1955). In this model, the ionic current term is given by:

$$I_{ionic,n} = \pi d_i \Delta x g_{Lmye} (V(x) - V_r) \qquad \textbf{C.2.5}$$

where Δx is the length of the spatial step used in the interneuron's discretization, and the parameters g_{Lmye} and V_r are described in Table C.2.1. The capacitance of the myelinated sections is given by an expression similar to C.2.4 but with c_n substituted by c_{mye}, the capacitance per unit area of the myelinated internode (see Table C.2.1).

Regarding the axial conductance, it is related to the resistivity of the axoplasm, ρ_a, and the inner diameter of the axon according to the following expression (Basser, 1993):

$$G_a = \frac{\pi d_i{}^2}{4\rho_a \Delta x} \qquad \textbf{C.2.6}$$

where the value used for ρ_a is presented in Table C.2.1.

Finally, regarding the morphological properties of the axon, the inner diameter of the axon and the length of the myelinated internodes - L - are all related to the outer diameter of the membrane (the diameter of the axon including the myelinated sheath) - d_o - according a set of expressions known as Rushton's scaling laws (Rushton, 1951):

$$\begin{aligned} L / d_o &= 100 \\ d_i / d_o &= 0.6 \end{aligned} \qquad \textbf{C.2.7}$$

For the value used for d_o, 10 μm, the inner diameter and the length of the myelinated internodes yield, respectively, 6 μm and 10^3 μm.

C.3 Neuron models used in motor cortex study

The neuron model that was used in the studies about the motor cortex is considerably more complex than the one that was described previously. This is because this model contains sections representing not only the Ranvier nodes and myelinated internodes, but also the initial segment, the axon's hillock, the soma and the apical dendrite.

Regarding the Ranvier nodes, the initial segment and the axon's hillock, they were all modelled with active membrane properties, based on the data from human myelinated nerve fibres (Wesselink et al., 1999). An introductory description of this model has already been presented in Chapter 1 (see page 53). As was then mentioned, the ionic current term is given, in this model, by the following expression:

$$\begin{aligned} I_{ionic}(x) = \pi d_i \Delta x [& g_{Na} m^3 h (V(x) - E_{Na}) + g_K n^4 (V(x) - E_K) \\ & + g_L (V(x) - E_L)] \end{aligned} \qquad \textbf{C.3.1}$$

where the values for the parameters that appear in the expression are presented in Table C.3.1. The dimensionless variables m, h and n are obtained by solving a set of ordinary differential equations of the form of C.2.2, where the functions α and β associated with each of the dimensionless variables are given by the following expressions (see (Wesselink et al., 1999)):

Table C.3.1: Electrophysiological properties of the neuron model used in the studies about TMS of the motor cortex.

Neuron's section	Electrophysiological parameters	
Ranvier Node (Wesselink et al., 1999)	Nodal capacitance per unit area (c_n)	2.8 μF/cm^2
	Resistivity of axoplasm (ρ_a)	33 Ω cm
	Leakage conductance (g_L)	0.06 S/cm^2
	Sodium maximum conductance (g_{Na})	3 S/cm^2
	Potassium maximum conductance (g_K)	0.03 S/cm^2
	Leakage Nernst potential (V_L)	-84.14 mV
	Sodium Nernst potential (V_{Na})	43.7 mV
	Potassium Nernst potential (V_K)	-84 mV
Initial Segment	Same properties as Ranvier Node	
Axon hillock	Same properties as Ranvier Node	
Myelinated internodes (Tasaki, 1955)	Myelin capacitance per unit area (c_{mye})	0.005 μF/cm^2
	Resistivity of axoplasm (ρ_a)	33 Ω cm
	Myelin conductance per unit area (g_{Lmye})	10^{-5} S/cm^2
	Membrane's resting potential (V_r)	-84 mV
Soma (Mainen et al., 1995; Manola et al., 2007)	Soma capacitance per unit area (c_{soma})	2.8 μF/cm^2
	Resistivity of axoplasm (ρ_a)	33 Ω cm
	Soma conductance per unit area (g_{Lsoma})	2.73×10^{-4} S/cm^2
	Membrane's resting potential (V_r)	-84 mV
Apical dendrite	Same properties as soma	

$$\alpha_m(V) = 4.6\frac{18.4+V}{1-\exp\left(-\frac{18.4+V}{10.3}\right)}$$
$$\beta_m(V) = 0.33\frac{-22.7-V}{1-\exp\left(\frac{V+22.7}{9.16}\right)}$$
$$\alpha_h(V) = 0.21\frac{-111-V}{1-\exp\left(\frac{V+111}{11}\right)}$$
$$\beta_h(V) = \frac{14.1}{1+\exp\left(-\frac{28.8+V}{13.4}\right)}$$
$$\alpha_n(V) = 0.0517\frac{93.2+V}{1-\exp\left(-\frac{93.2+V}{1.1}\right)}$$
$$\beta_n(V) = 0.092\frac{-76-V}{1-\exp\left(\frac{V+76}{10.5}\right)} \qquad \textbf{C.3.2}$$

In the last expressions, *[V]* = mV and $[\alpha]=[\beta]=ms^{-1}$.

All other sections of the neuron (myelinated internodes, soma and dendrite) were modelled with passive membrane properties and, therefore, the ionic current term in those sections was modelled with an expression similar to C.2.5. Table C.3.1 contains the values of the conductance and capacitance per unit area used for each of the passive sections on the model. The passive membrane properties of myelinated internodes were the same as those used in the previous model (Tasaki, 1955), whereas those used to model the soma and dendrite were based on properties described in (Mainen et al., 1995) and in (Manola et al., 2007).

Morphologically, this model is also different from the previous model, given that it uses a different set of scaling relations (Wesselink et al., 1999):

$$L = C_L \ln(d_o / D_L)$$
$$d_i = C_d d_o - D_d \qquad \textbf{C.3.3}$$

where C_L = 787 μm, D_L = 3.44 μm, C_d = 0.76 and D_d = 1.81 μm. Another difference between this model and the previous one is that many of the sections on this neuron have variable diameters along the section.

This model was used to describe pyramidal tract neurons, pyramidal association fibres and cortical interneurons. The details of the model remained the same when applied to

any of these types of neurons. However some specific parameters changed, mostly the diameters and tapering factors of the various sections comprising the neuron. Table C.3.2 summarizes the main differences between the various sections of the neurons.

Table C.3.2: Morphological properties of the neuron model used in the studies about TMS of the motor cortex. d_o and d_i represent the outer and inner diameter of the axon, respetively, L represents the length of each section and d_{init}, d_{end} represent, respectively, the initial and final diameter of the section.

Neuron	Axon (μm)		Soma (μm)			Dendrite (μm)			Initial Segment (μm)			Axon Hillock (μm)		
	d_o	d_i	L	d_{init}	d_{end}	L	d_{init}	d_{end}	L	d_{init}	d_{end}	L	d_{init}	d_{end}
P1-P4 (Manola et al., 2007)	6-20	2.8-13.4	80	60	8	1000 (*P2*) 1760	8	8	20	d_i	d_i	10	d_i	2 d_i
a1-a2 (Yamashita and Arikuni, 2001)			32-20	22-15	8	984-401	8	8						
n1-n4 t1-t4 (Wang et al., 2002)	3.5-6	0.9-2.8	20	10	10	50	2	2						

D Validation of numerical methods used to solve the discretized cable equation

The discretized version of the cable equation, for the neuron models used in the motor cortex study, was solved using a Crank-Nicolson's algorithm with a staggered grid approach. In this appendix some details about the implementation of this algorithm in MatLab are discussed. Furthermore the studies performed to validate the algorithm are also presented.

D.1 Implementation of the algorithm in MatLab

The implementation of the Crank-Nicolson's method used to solve the discretized cable equation was performed in MatLab 7.1 (R14) SP3 (www.mathworks.com). The algorithm has already been explained in detail in Chapter 1 (see page 55). The program created in MatLab also includes a graphical user interface (GUI) that allows for specification of many of the parameters of the model. The general organization of the GUI is depicted in Figure D.1.1. Solving a given problem using the designed program follows a series of steps. The first step involves the specification of the neuron's electrophysiological and morphological parameters, as well as the spatial discretization of the neuron, i.e. the number of compartments a given section of the neuron is divided into. This is performed, in the designed GUI, in the 'Neuron model' menu (see Figure D.1.1 c). The next step is the specification of the stimulation parameters. This is done in the menu 'Stimulation' (Figure D.1.1 d). The program permits the modelling of either TMS of the neuron or its electrical stimulation with an intracellular electrode. The latter form of stimulation was implemented only for validation purposes, as will be discussed below in more detail. If TMS mode is selected, the program allows the user to specify

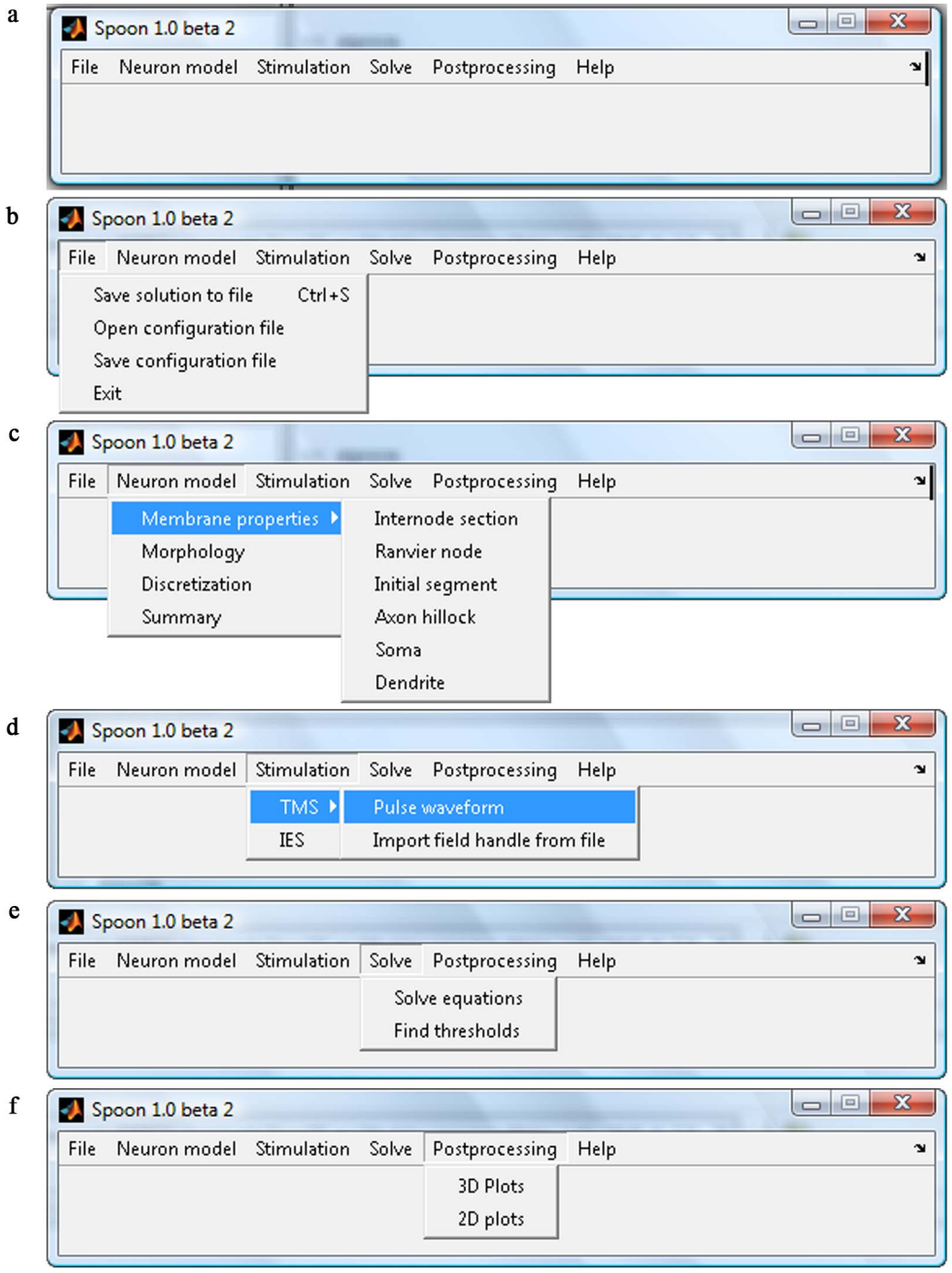

Figure D.1.1: Organization of the GUI created in MatLab to solve the discretized cable equation. (a) Initial interface; (b) File menu; (c) Neuron model menu; (d) Stimulation menu; (e) Solve menu; (f) Postprocessing menu.

the field's waveform (see Figure D.1.2). It also allows the field along the neuron, previously calculated using Comsol and MatLab, to be imported. After the stimulation parameters are specified, the 'Solve' menu (Figure D.1.1 e) allows the solution to be calculated. This menu includes the option to solve a given problem, given a predetermined intensity of stimulation (capacitor's charging voltage in TMS or intensity

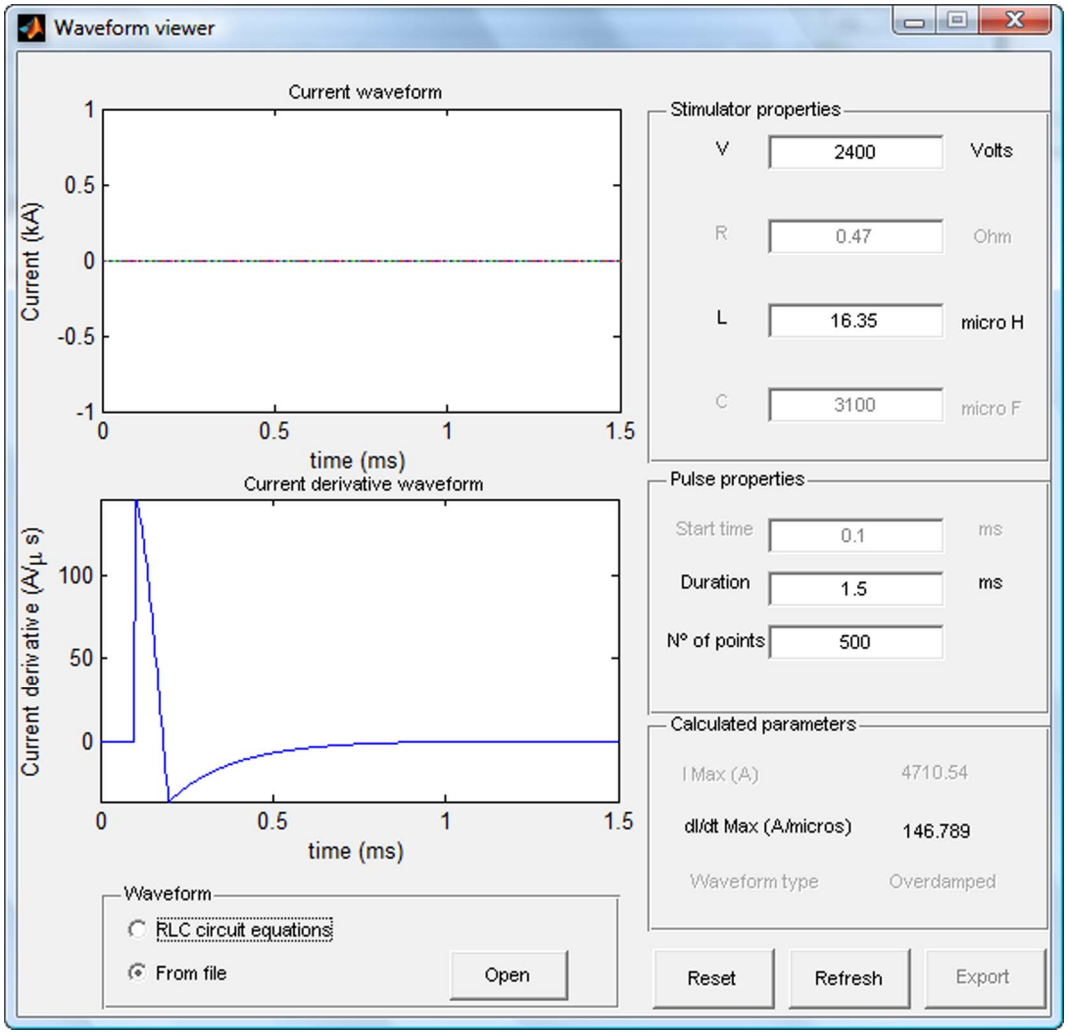

Figure D.1.2: GUI created in MatLab that allows the specification of the field's temporal waveform in TMS. The interface allows the input of some of the properties of the magnetic stimulation (capacitor's charging voltage, *V*, and coil's inductance, *L*), as well as some of the parameters of stimulation, such as the duration of the stimulating pulse and the number of points in the temporal discretization. The waveform of the field can also be imported from a text file. In the latter case, the current waveform is not displayed. In the example above, the waveform of the monophasic Magstim 200 stimulator is shown.

of injected current in electrical stimulation). Additionally it also includes the option to find the threshold of stimulation within a given tolerance parameter. Finally, the GUI also includes several tools for the visualization of the solution ('Postprocessing' menu, Figure D.1.1 f). The program allows the following parameters to be visualized: the transmembrane potential, the dimensionless variables *m*, *h* and *h*, the electric field along the neuron (only in TMS), and the electric field's first spatial derivative. These parameters can be visualized using space-time plots in 3D, or simple 2D plots at a fixed point in time (2D space plot) or space (2D time plot). The GUI also includes a 'File'

menu (Figure D.1.1 b) that allows solutions and configurations (neuron model properties and stimulation parameters) to be saved or loaded.

D.2 Validation of the method implemented in MatLab

D.2.1 Introduction

Comparison with NEURON

In order to validate the results obtained with the program created in MatLab, these were compared with the results obtained with another program that is commonly used in the scientific literature for the calculation of the neuron's response: NEURON (http://www.neuron.yale.edu/neuron/). The latter includes tools that allow the calculation of the neuron's response if the extracellular potential is specified. As the field induced in TMS cannot be specified solely in terms of an extracellular potential, another type of stimulation was modelled: electrical stimulation. The field induced during this form of stimulation can be expressed in terms of an extracellular potential and, thus, it can be modelled in NEURON. This form of stimulation is appropriate to validate the algorithms implemented in MatLab, even though the main objective of the latter is to calculate the response of the neuron to the field applied in TMS. This is because, the algorithms implemented in MatLab for TMS and electrical stimulation differ only in what concerns the specification of the activation function.

D.2.2 Methods

Specification of the model

The model used for the validation studies includes a neuron that is assumed to lie in a purely resistive homogeneous and isotropic medium (Warman et al., 1992; McIntyre and Grill, 1999). Stimulation is delivered through a point source electrode placed close to the neuron (see Figure D.2.2.1). In this model, the extracellular potential, V_e, induced by the electrode is given by (see (Rattay, 1986; Warman et al., 1992)):

$$V_e = \frac{\rho_e I_{ext}}{4\pi\sqrt{\Delta z^2 + (x - x_c)^2}} \qquad \textbf{D.2.2.1}$$

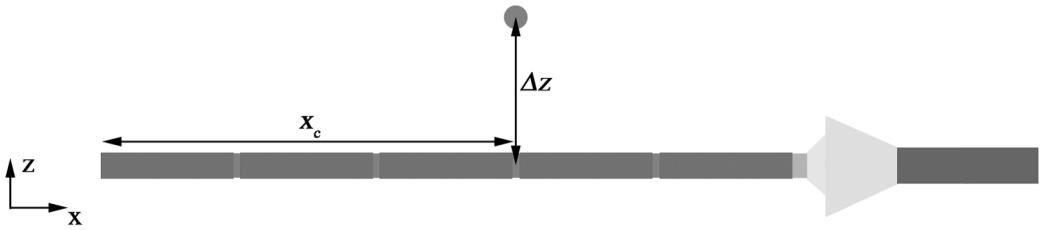

Figure D.2.2.1: Model used to validate the algorithms in MatLab. The model contains a point source electrode (indicated by the grey circle) placed above the neuron model. Distance along the neuron is measured from left (axon termination) to right (apical dendrite termination).

where ρ_e is the resistivity of the extracellular medium (300 Ω cm according to (Rattay, 1986; Warman et al., 1992)), I_{ext} is the current injected through the electrode, Δz is the vertical distance between the neuron and the electrode, x measures distance along the axis of the neuron and x_c is the position of the electrode along this axis (see Figure D.2.2.1).

The activation function for electrical stimulation is, as was the case for TMS, proportional to the first spatial derivative of the electric field along the neuron. As the electric field in electrical stimulation is proportional to the gradient of the external potential, it is possible to write the activation function as:

$$S = -\lambda^2 \frac{\partial E_x}{\partial x} = \lambda^2 \frac{\partial^2 V_e}{\partial x^2} \qquad \textbf{D.2.2.2}$$

In this particular case, the activation function is given by the following expression:

$$S = \lambda^2 \frac{\rho_e I_{ext}}{4\pi} \left[\Delta z^2 + (x - x_c)^2\right]^{-5/2} \left[2(x - x_c)^2 - \Delta z^2\right] \qquad \textbf{D.2.2.3}$$

The spatial waveform of the activation function is shown in Figure D.2.2.2. Depending on the sign of the injected current, two forms of stimulation can be identified: cathodal stimulation ($I_{ext} < 0$) and anodal stimulation ($I_{ext} > 0$). The typical shape of the activation function contains three lobes: a central one, with the highest magnitude, and two side-lobes with a magnitude smaller than that of the central lobe. In cathodal stimulation, the central lobe induces a depolarization, whereas in anodal stimulation depolarization is induced by the side-lobes. Due to the magnitude difference between the central and side-lobes, cathodal stimulation can be attained at a lower threshold than anodal stimulation.

Regarding the temporal waveform of the current stimulus, it is usually a square-shaped wave with a duration τ_{dur} and intensity $I_{ext\,max}$.

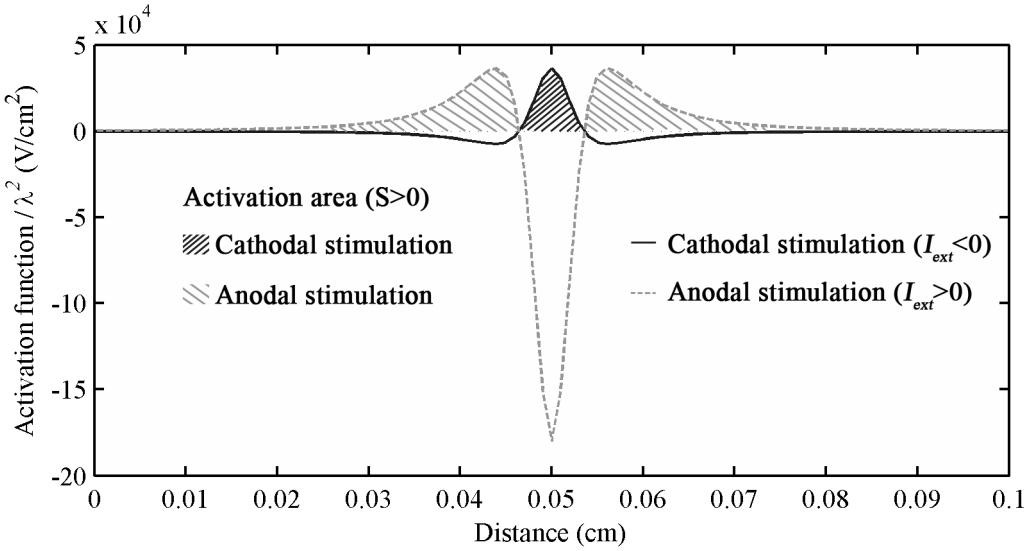

Figure D.2.2.2: Activation function (divided by λ^2) in electrical stimulation with a point source electrode. In this particular case, the electrode is placed at Δz = 50 μm and x_c = 0.05 cm. The intensity of the injected current has been adjusted so that the amplitude of the central lobe in cathodal stimulation is the same as the amplitude of the side-lobes in anodal stimulation: $I_{ext\ max\ cathodal}$ = -0.19 mA and $I_{ext\ max\ anodal}$ = 0.94 mA.

Implementation of the model in MatLab

The model parameters were controlled using the same GUI implemented in MatLab and described earlier. The panel responsible for the input of the parameters can be accessed in the menu 'Stimulation: IES' (see Figure D.1.1 d) and is shown in Figure D.2.2.3. This panel allows the specification of all the parameters that appear in D.2.2.3, except the space constant. It also allows the specification of the details related to the temporal waveform of the current stimulus, specifically the duration, start time and maximum amplitude. Finally the GUI allows the specification of the number of points in the temporal discretization as well as the total simulation time.

The neuron model used in the simulations is the same as the one used for modelling of pyramidal neurons, which was described in Appendix C. The algorithm used to solve the resultant discretized cable equation was the same as the one used to solve the cable equation in the case of TMS.

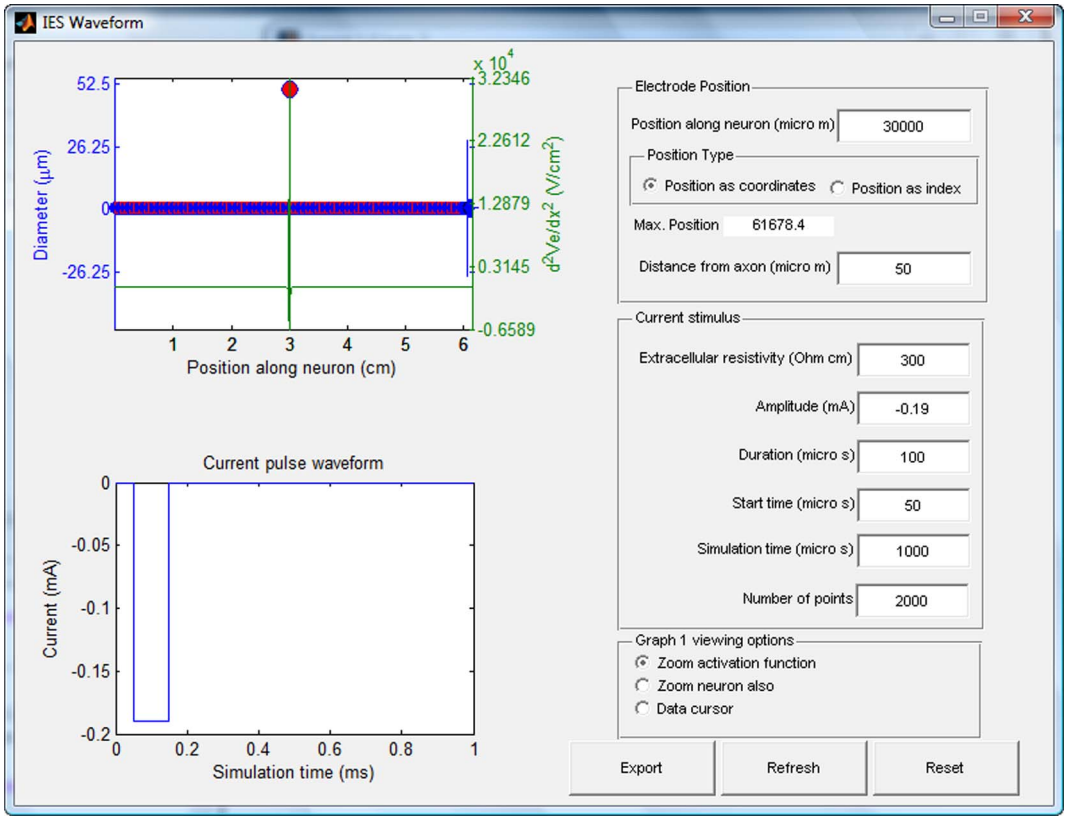

Figure D.2.2.3: GUI created in MatLab for the specification of stimulation parameters in electrical stimulation. The GUI is divided into two columns: the left column contains the spatial and temporal waveforms of the stimulating pulse, whereas the right column allows the specification of several parameters. The right column is divided essentially into two panels, named Electrode Position and Current stimulus. This menu allows the specification of all the relevant parameters in the model. It also allows the specification of the parameters that relate to the temporal discretization.

Implementation of the model in NEURON

The implementation of the model in NEURON (version 6.0) followed the same steps as it did in MatLab. The first step was the creation of the neuron model. As NEURON does not include, by default, the type of active membrane dynamics that was used in this model (see Appendix C), several scripts were written in order to implement these dynamics in NEURON (see (Hines and Carnevale, 2000) for more details on how to implement membrane dynamics in NEURON). After the properties of the neuron model were completely specified, the second step of the implementation was the modelling of electrical stimulation. This was done using a set of tools available at the NEURON discussion forum (http://www.neuron.yale.edu/phpBB/index.php) that allow the solution of the cable equation to be found from the specification of the extracellular potential: *xtra* mechanism. These last set of tools led to the creation of a GUI in

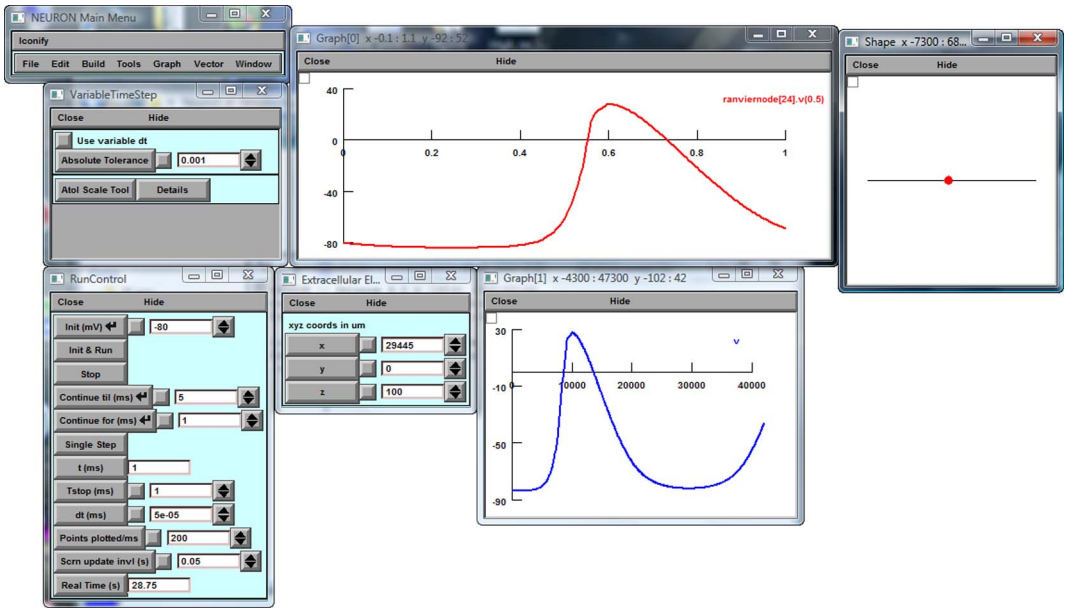

Figure D.2.2.4: GUI of the program created in NEURON to model electrical stimulation of the neuron modelled in this work. The GUI allows the input of the same parameters as the one that was created in MatLab. It also allows the visualization of the solution with different types of 2D plots.

NEURON for the input of all stimulation parameters (see Figure D.2.2.4). This GUI also allowed for the values of the transmembrane potential, at each point in space and time, to be exported as a text file. This text file could then be imported by MatLab so that the solutions of the two methods could be compared.

The method used by NEURON to solve the resultant set of equations is the implicit backward Euler method. Although NEURON also includes the Crank-Nicolson method, the latter is not stable when used to solve problems that include the *xtra* mechanism (see (Canervale and Hines, 2004)).

D.2.3 Results

Comparison of stimulation thresholds

The first validation study that was performed was the comparison between stimulation thresholds obtained in MatLab and NEURON for several different positions of the stimulating electrode. The results are summarized in Table D.2.1 and Table D.2.2, for the case of cathodal and anodal stimulation respectively. The results indicate that there is a good general agreement between stimulation thresholds obtained in MatLab and NEURON. As expected, the differences between the two programs tend to be higher for the larger time step (Δt = 5 μs) than for the smaller one. The only exception occurs for

Table D.2.1: Threshold values obtained in MatLab and NEURON for the case of cathodal stimulation with the electrode placed at a distance Δz = 50 μm above the neuron and centred at various positions along it. The duration of the stimulating pulse was of 100 μs and total stimulation time was of 1 ms. The variable Δt indicates the time step used in the simulation.

Position of cathode	Thresholds obtained in MatLab (mA)		Thresholds obtained in NEURON (mA)		Relative error between the results (% of NEURON value)	
	Δt = 5 μs	Δt = 0.5 μs	Δt = 5 μs	Δt = 0.5 μs	Δt = 5 μs	Δt = 0.5 μs
Middle of myelinated internode	-0.106	-0.110	-0.114	-0.110	7.0 %	0.0 %
End of myelinated internode	-0.012	-0.012	-0.013	-0.012	7.7 %	0.0 %
Ranvier node	-0.009	-0.009	-0.010	-0.009	10.0 %	0.0 %
Middle of initial segment	-0.022	-0.022	-0.023	-0.023	4.3 %	4.3 %
Middle of axon hillock	-0.028	-0.028	-0.029	-0.029	3.4 %	3.4 %
Middle of soma	-0.054	-0.059	-0.062	-0.061	12.9 %	3.3 %
Beginning of dendritic tree	-0.125	-0.129	-0.133	-0.130	6.0 %	2.3 %

Table D.2.2: Threshold values obtained in MatLab and NEURON for the case of anodal stimulation with the electrode placed at a distance Δz = 50 μm above the neuron and centred at various positions along it. The duration of the stimulating pulse was of 100 μs and total stimulation time was of 1 ms. The variable *Δt* indicates the time step used in the simulation.

Position of anode	Thresholds obtained in MatLab (mA)		Thresholds obtained in NEURON (mA)		Relative error between the results (% of NEURON value)	
	Δt = 5 μs	Δt = 0.5 μs	Δt = 5 μs	Δt = 0.5 μs	Δt = 5 μs	Δt = 0.5 μs
Middle of myelinated internode	0.273	0.285	0.299	0.287	8.7 %	0.7 %
End of myelinated internode	0.077	0.078	0.080	0.078	3.8 %	0.0 %
Ranvier node	0.058	0.059	0.061	0.059	4.9 %	0.0 %
Middle of initial segment	0.021	0.021	0.021	0.021	0.0 %	0.0 %
Middle of axon hillock	0.019	0.019	0.019	0.019	0.0 %	0.0 %
Middle of soma	0.018	0.018	0.018	0.017	0.0 %	5.9 %
Beginning of dendritic tree	0.028	0.028	0.029	0.028	3.4 %	0.0 %

anodal stimulation with the electrode placed over the middle of the soma, where the two solutions diverge slightly when the smaller time step is used. The results also show that the relative difference between the two sets of threshold values is slightly higher for cathodal stimulation than for anodal stimulation.

Comparison of the response of the transmembrane potential

Another way to compare the solutions obtained from MatLab and NEURON was to analyse the spatial and temporal evolution of the transmembrane potential. This is shown in Figure D.2.3.1 for the case where the stimulating electrode is placed over one of the neuron's Ranvier nodes. The 3D space-time plots show a good general agreement between the two solutions. A more detailed analysis can be seen by comparing 2D temporal plots of the transmembrane potential at the two Ranvier nodes closest to the stimulating electrodes (see Figure D.2.3.2). These plots show a very good agreement between the solutions in the case of cathodal stimulation. The solutions are also very similar in the case of anodal stimulation, although in that case there is a slight temporal lag between the two solutions, the solution from NEURON being slightly more delayed

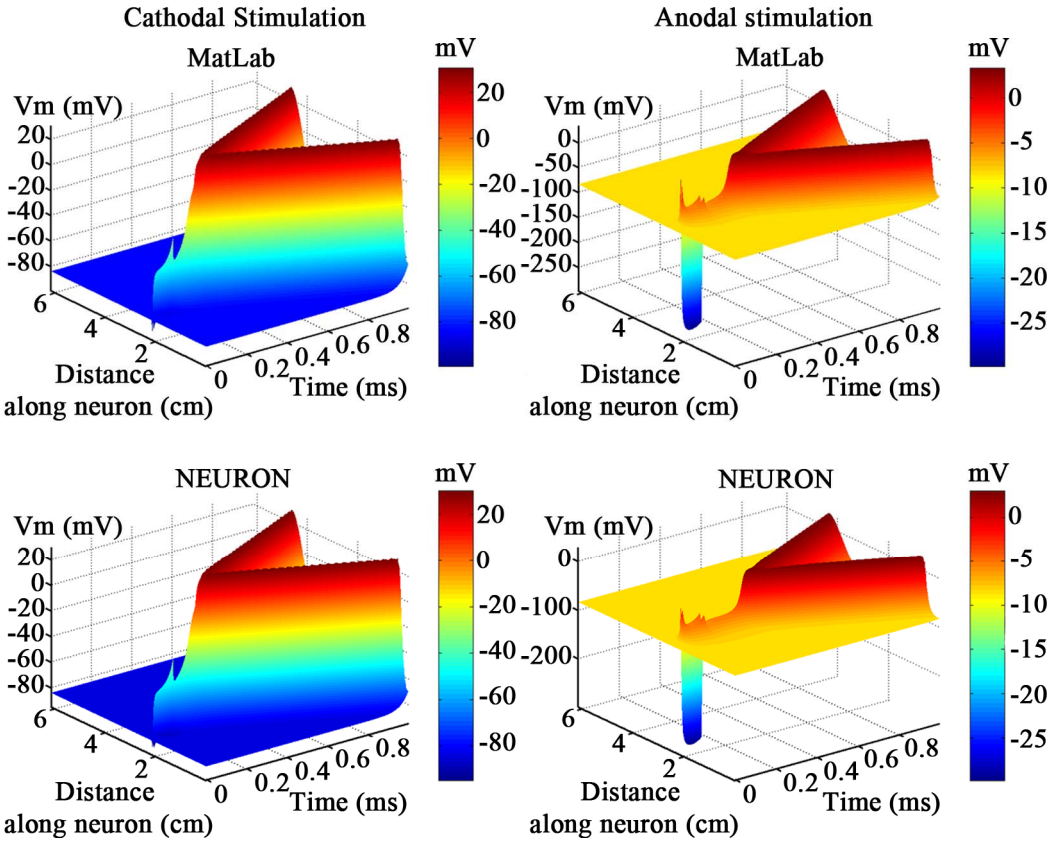

Figure D.2.3.1: 3D space-time plots of the evolution of the transmembrane potential. The left column shows the results for cathodal stimulation at threshold (I_{ext} = -0.009 mA), when the electrode is placed directly above one of the Ranvier nodes. The left column shows the results for anodal stimulation at threshold (I_{ext} = 0.059 mA), for the electrode placed over the same Ranvier node. The top line is the solution obtained from MatLab, whereas the bottom line is the solution obtained from NEURON. In both simulations a time step of 0.5 μs, and the duration of the stimulating current pulse was of 100 μs.

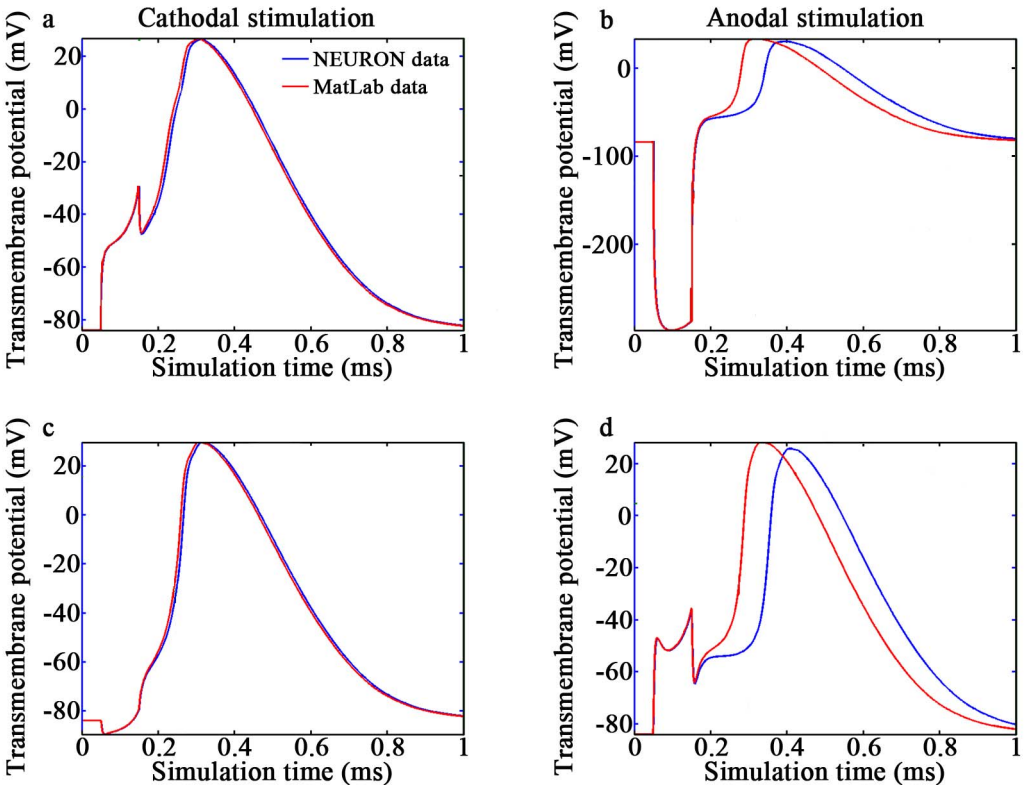

Figure D.2.3.2: 2D time plots of the evolution of the transmembrane potential. The left column shows the results for cathodal stimulation at threshold (I_{ext} = -0.009 mA), when the electrode is placed directly above one of the Ranvier nodes. The left column shows the results for anodal stimulation at threshold (I_{ext} = 0.059 mA), for the electrode placed over the same Ranvier node. The top line of each column is the solution at the Ranvier node directly under the electrode, whereas the bottom line is the solution at the Ranvier node immediately next to the one under the electrode. In both simulations a time step of 0.5 μs, and the duration of the stimulating current pulse was of 100 μs.

than the solution from MatLab (the difference between the action potential peaks is of about 73 μs).

Apart from the good agreement between the solutions obtained from both implementations, the general behaviour of the solution is also close to what was expected from the theoretical considerations discussed above. In cathodal stimulation, stimulation occurs in the Ranvier node directly under the electrode because, in this form of stimulation, the central peak of the stimulating pulse, occurring under the electrode, is depolarizing (see Figure D.2.3.2 a). At the neighbour Ranvier nodes, this form of stimulation induces hyperpolarization (see Figure D.2.3.2 b), due to the negative side-lobes of the activation function (see Figure D.2.2.2). In anodal stimulation the opposite happens: directly under the electrode there is a strong hyperpolarization (Figure D.2.3.2

b) and, as such, the action potential is originated in the neighbouring Ranvier nodes that are depolarized by the stimulating current pulse (Figure D.2.3.2 d).

Convergence rates

The last set of calculations that was performed compared the evolution of the thresholds predicted in MatLab and in NEURON with the step of the temporal discretization. The convergence rates depended on the point of the neuron the electrode was placed over. For points over Ranvier nodes, for instance, convergence was very fast. For points over myelinated internodes, convergence was slower. This was observed both in MatLab and in NEURON. The convergence in this the latter case, is illustrated in Figure D.2.3.3 for both anodal and cathodal stimulation. The figure shows that MatLab and NEURON both tend to the same threshold value as the number of points in the temporal discretization increases (see Figure D.2.3.3 a and b). However, MatLab initially tends to underestimate the thresholds (their absolute value), whereas NEURON has the opposite behaviour.

In order to determine the speed of convergence, a relative convergence (RC) value was determined according to:

$$RC_{\text{N points}} = \left| \frac{I_{threshold}\big|_{\text{N points}} - I_{threshold}\big|_{\text{2000 points}}}{I_{threshold}\big|_{\text{2000 points}}} \right| \times 100 \qquad \textbf{D.2.3.1}$$

where $I_{threshold}|_{\text{N points}}$ is the threshold current value using N points in the temporal discretization. The curves built using this expression can be seen in Figure D.2.3.3 c and d for cathodal and anodal stimulation, respectively. The curves were then fit to power functions, which are indicated in the plots as well. From the curves and the expressions used to fit the data it can be concluded that the algorithms implemented in MatLab tend to converge faster with number of points in the temporal discretization, than those implemented in NEURON. This is expected because NEURON used an implicit Backward Euler method. The latter converges more slowly than the Crank-Nicolson method with a staggered grid that is implemented in MatLab.

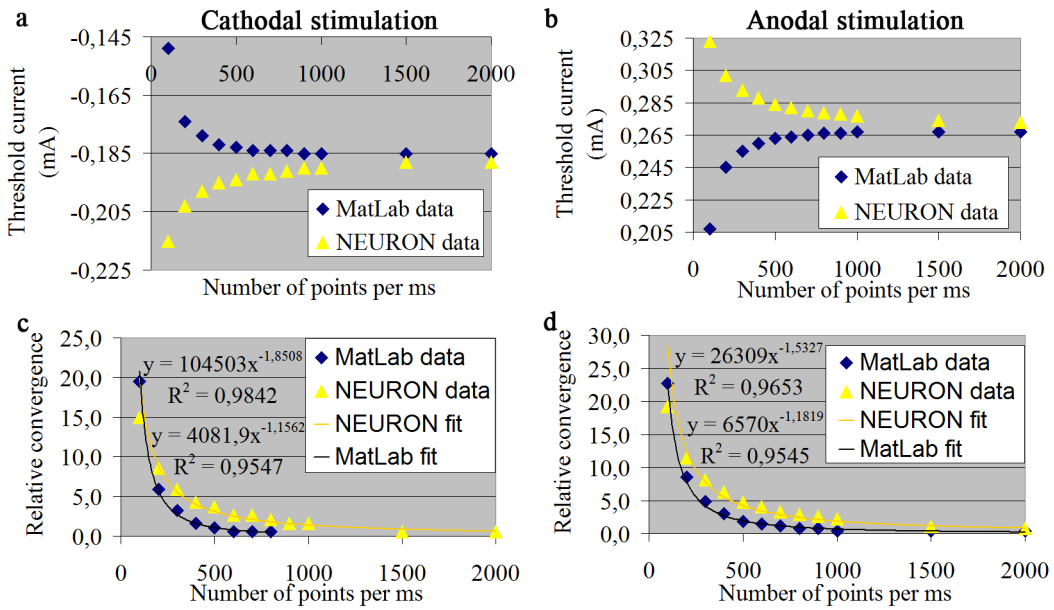

Figure D.2.3.3: Convergence of threshold values obtained in MatLab and NEURON with the number of points in the temporal discretization. The plots in the top line, *a* and *b*, indicate the threshold values for cathodal and anodal stimulation, respectively. The plots in the bottom line, *c* and *d*, show the relative convergence of the threshold values obtained in cathodal and anodal stimulation, respectively. Also shown in the plots in the bottom is the power function used to fit the data. The top expression in the plots is the fit to the data from MatLab, whereas the bottom expression is the fit to the data from NEURON. All of these values were obtained with the electrode placed over the first point in the first myelinated internode. The duration of stimulation was of 100 µs and Δz = 50 µm.

D.2.4 Conclusion

The results obtained with the algorithms implemented in MatLab are in good agreement with the results obtained using NEURON. This is shown by the very small difference between the thresholds predicted from both programs (differences of always less than 6 % of the value predicted by NEURON for a time step of 0.5 µs). The spatial and temporal dependency of the transmembrane potential calculated by both programs is also very similar. The small differences between the two solutions, like for instance the temporal lag shown in the previous section, can be attributed to the fact that both programs use different algorithms to solve the cable equation, each algorithm converging at a different rate with the temporal time step.

Therefore, the algorithms in MatLab yield a solution that is qualitatively and quantitatively close to what is expected.

References

Abou-Khalil B An update on determination of language dominance in screening for epilepsy surgery: The Wada test and newer noninvasive alternatives. Epilepsia 2007;48:442-455.

Ahmed Z, Wieraszko A Modulation of learning and hippocampal, neuronal plasticity by repetitive transcranial magnetic stimulation (rTMS). Bioelectromagnetics 2006;27:288-94.

Amassian VE, Eberle L, Maccabee PJ, Cracco RQ Modelling magnetic coil excitation of human cerebral cortex with a peripheral nerve immersed in a brain-shaped volume conductor: the significance of fiber bending in excitation. Electroencephalogr Clin Neurophysiol 1992;85:291-301.

Barker AT, Jalinous R Non-Invasive Magnetic Stimulation of Human Motor Cortex. Lancet 1985;1:1106-1107.

Barrett R, Berry M, Chan TF, Demmel J, Donato JM, Dongarra J, et al. Templates for the Solution of Linear Systems: Building Blocks for Iterative Methods, 2nd ed.: Society for Industrial and Applied Mathematics, 1993.

Basser PJ Cable Equation for a Myelinated Axon Derived from Its Microstructure. Medical & Biological Engineering & Computing 1993;31:S87-S92.

Basser PJ Scaling laws for myelinated axons derived from an electrotonic core-conductor model. J Integr Neurosci 2004;3:227-44.

Basser PJ, Roth BJ Stimulation of a Myelinated Nerve Axon by Electromagnetic Induction. Medical & Biological Engineering & Computing 1991;29:261-268.

Baumann SB, Wozny DR, Kelly SK, Meno FM The electrical conductivity of human cerebrospinal fluid at body temperature. Ieee Transactions on Biomedical Engineering 1997;44:220-223.

Benzi M Preconditioning techniques for large linear systems: A survey. Journal of Computational Physics 2002;182:418-477.

Bohning DE, Shastri A, Nahas Z, Lorberbaum JP, Andersen SW, Dannels WR, et al. Echoplanar BOLD fMRI of brain activation induced by concurrent transcranial magnetic stimulation. Invest Radiol 1998;33:336-40.

Brodal P The Central Nervous System: Structure and Function, 2nd ed.: Oxford University Press Inc, 1998.

Burke D, Hicks R, Gandevia SC, Stephen J, Woodforth I, Crawford M Direct comparison of corticospinal volleys in human subjects to transcranial magnetic and electrical stimulation. J Physiol 1993;470:383-93.

Canervale NT, Hines M The Neuron book. Cambridge, 2004.

Cantello R Applications of transcranial magnetic stimulation in movement disorders. Journal of Clinical Neurophysiology 2002;19:272-293.

Carbunaru R, Durand DM Toroidal coil models for transcutaneous magnetic stimulation of nerves. Ieee Transactions on Biomedical Engineering 2001;48:434-441.

Chen M, Mogul DJ A structurally detailed finite element human head model for simulation of transcranial magnetic stimulation. Journal of Neuroscience Methods 2009;179:111-120.

Cheng DK Field and Wave Electromagnetics, 2nd ed.: Addison-Wesley Publishing Company, 1989.

Chiu SY, Ritchie JM, Rogart RB, Stagg D Quantitative Description of Membrane Currents in Rabbit Myelinated Nerve. Journal of Physiology-London 1979;292:149-166.

Cohen D, Cuffin BN Developing a More Focal Magnetic Stimulator .1. Some Basic Principles. Journal of Clinical Neurophysiology 1991;8:102-111.

Comsol Comsol Multiphysics version 3.5 Reference guide. Comsol, 2008.

Cooley JW, Dodge FA, Jr. Digital computer solutions for excitation and propagation of the nerve impulse. Biophys J 1966;6:583-99.

Davey K, Epstein CM Magnetic stimulation coil and circuit design. Ieee Transactions on Biomedical Engineering 2000;47:1493-1499.

Davey KR, Riehl M Suppressing the surface field during transcranial magnetic stimulation. Ieee Transactions on Biomedical Engineering 2006;53:190-194.

Day BL, Dressler D, Denoordhout AM, Marsden CD, Nakashima K, Rothwell JC, et al. Electric and Magnetic Stimulation of Human Motor Cortex - Surface Emg and Single Motor Unit Responses. Journal of Physiology-London 1989;412:449-473.

De Lucia M, Parker GJ, Embleton K, Newton JM, Walsh V Diffusion tensor MRI-based estimation of the influence of brain tissue anisotropy on the effects of transcranial magnetic stimulation. Neuroimage 2007;36:1159-70.

Di Lazzaro V, Oliviero A, Mazzone P, Insola A, Pilato F, Saturno E, et al. Comparison of descending volleys evoked by monophasic and biphasic magnetic stimulation of the motor cortex in conscious humans. Experimental Brain Research 2001;141:121-127.

Di Lazzaro V, Oliviero A, Pilato F, Saturno E, Dileone M, Mazzone P, et al. The physiological basis of transcranial motor cortex stimulation in conscious humans. Clinical Neurophysiology 2004a;115:255-266.

Di Lazzaro V, Oliviero A, Pilato F, Saturno E, Dileone M, Meglio M, et al. Comparison of descending volleys evoked by transcranial and epidural motor cortex stimulation in a conscious patient with bulbar pain. Clinical Neurophysiology 2004b;115:834-838.

Di Lazzaro V, Oliviero A, Pilato F, Saturno E, Insola A, Mazzone P, et al. Descending volleys evoked by transcranial magnetic stimulation of the brain in conscious humans: effects of coil shape. Clin Neurophysiol 2002;113:114-9.

Di Lazzaro V, Oliviero A, Profice P, Saturno E, Pilato F, Insola A, et al. Comparison of descending volleys evoked by transcranial magnetic and electric stimulation in conscious humans. Electromyography and Motor Control-Electroencephalography and Clinical Neurophysiology 1998;109:397-401.

Di Lazzaro V, Ziemann U, Lemon RN State of the art: Physiology of transcranial motor cortex stimulation. Brain Stimulation 2008;1:345-362.

Dogdas B, Stout D, Chatziioannou AF, Leahy RM Digimouse: a 3D whole body mouse atlas from CT and cryosection data. Physics in Medicine and Biology 2007;52:577-587.

Eaton H Electric field induced in a spherical volume conductor from arbitrary coils: application to magnetic stimulation and MEG. Med Biol Eng Comput 1992;30:433-40.

Epstein CM, Davey KR Iron-core coils for transcranial magnetic stimulation. Journal of Clinical Neurophysiology 2002;19:376-381.

Esselle KP, Stuchly MA Quasi-Static Electric-Field in a Cylindrical Volume Conductor Induced by External Coils. Ieee Transactions on Biomedical Engineering 1994;41:151-158.

Esser SK, Hill SL, Tononi G Modeling the effects of transcranial magnetic stimulation on cortical circuits. J Neurophysiol 2005;94:622-39.

Fox PT, Narayana S, Tandon N, Sandoval H, Fox SP, Kochunov P, et al. Column-based model of electric field excitation of cerebral cortex. Hum Brain Mapp 2004;22:1-14.

Frankenhaeuser B, Huxley AF Action Potential in Myelinated Nerve Fibre of Xenopus Laevis as Computed on Basis of Voltage Clamp Data. Journal of Physiology-London 1964;171:302-&.

Gabriel C, Gabriel S, Corthout E The dielectric properties of biological tissues: I. Literature survey. Phys Med Biol 1996a;41:2231-49.

Gabriel S, Lau RW, Gabriel C The dielectric properties of biological tissues .2. Measurements in the frequency range 10 Hz to 20 GHz. Physics in Medicine and Biology 1996b;41:2251-2269.

Goncalves S, de Munck JC, Verbunt JPA, Heethaar RM, da Silva FHL In vivo measurement of the brain and skull resistivities using an EIT-based method and the combined analysis of SEF/SEP data. Ieee Transactions on Biomedical Engineering 2003;50:1124-1128.

Grandori F, Ravazzani P Magnetic Stimulation of the Motor Cortex - Theoretical Considerations. Ieee Transactions on Biomedical Engineering 1991;38:180-191.

Hallett M Transcranial magnetic stimulation: a primer. Neuron 2007;55:187-99.

Han BH, Lee SY, Kim JH, Yi JH Some technical aspects of magnetic stimulation coil design with the ferromagnetic effect. Medical & Biological Engineering & Computing 2003;41:516-518.

Haueisen J, Ramon C, Eiselt M, Brauer H, Nowak H Influence of tissue resistivities on neuromagnetic fields and electric potentials studied with a finite element model of the head. IEEE Trans Biomed Eng 1997;44:727-35.

Heller L, van Hulsteyn DB Brain stimulation using electromagnetic sources: theoretical aspects. Biophys J 1992;63:129-38.

Hille B Ionic channels of excitable membranes, 2nd ed. Sunderland: Sinauer Associates Inc., 1992.

Hines M Efficient computation of branched nerve equations. Int J Biomed Comput 1984;15:69-76.

Hines ML, Carnevale NT The NEURON simulation environment. Neural Computation 1997;9:1179-1209.

Hines ML, Carnevale NT Expanding NEURON's repertoire of mechanisms with NMODL. Neural Computation 2000;12:995-1007.

Hodgkin AL, Huxley AF, Katz B Measurement of Current-Voltage Relations in the Membrane of the Giant Axon of Loligo. Journal of Physiology-London 1952;116:424-448.

Hsu KH, Durand DM A 3-D differential coil design for localized magnetic stimulation. Ieee Transactions on Biomedical Engineering 2001;48:1162-1168.

Hughes TJR The finite element method. Linear static and dynamic finite element analysis. New York: Dover, 2000.

Jackson JD Classical Electrodynamics, 3rd ed. New York: John Wiley & Sons, 1999.

Jacobsson P. Nedelec elements for computational electromagnetics, 2007.

Jalinous R. Guide to magnetic stimulation: The Magstim Company, 1998:1-59.

Kammer T, Beck S, Thielscher A, Laubis-Herrmann U, Topka H Motor thresholds in humans: a transcranial magnetic stimulation study comparing different pulse waveforms, current directions and stimulator types. Clinical Neurophysiology 2001;112:250-258.

Kammer T, Vorwerg M, Herrnberger B Anisotropy in the visual cortex investigated by neuronavigated transcranial magnetic stimulation. Neuroimage 2007;36:313-21.

Kaneko K, Kawai S, Fuchigami Y, Shiraishi G, Ito T Effect of stimulus intensity and voluntary contraction on corticospinal potentials following transcranial magnetic stimulation. Journal of the Neurological Sciences 1996;139:131-136.

Kim DH, Georghiou GE, Won C Improved field localization in transcranial magnetic stimulation of the brain with the utilization of a conductive shield plate in the stimulator. Ieee Transactions on Biomedical Engineering 2006a;53:720-725.

Kim EJ, Kim WR, Chi SE, Lee KH, Park EH, Chae JH, et al. Repetitive transcranial magnetic stimulation protects hippocampal plasticity in an animal model of depression. Neurosci Lett 2006b;405:79-83.

Kobayashi M, Ueno S, Kurokawa T Importance of soft tissue inhomogeneity in magnetic peripheral nerve stimulation. Electromyography and Motor Control-Electroencephalography and Clinical Neurophysiology 1997;105:406-413.

Lassek AM The human pyramidal tract II A numerical investigation of the Betz cells of the motor area. Archives of Neurology and Psychiatry 1940;44:718-724.

Lassek AM The human pyramidal tract. IV. A study of the mature, myelinated fibers of the pyramid. The Journal of Comparative Neurology 1942;76:217-225.

Levkovitz Y, Roth Y, Harel EV, Braw Y, Sheer A, Zangen A A randomized controlled feasibility and safety study of deep transcranial magnetic stimulation. Clinical Neurophysiology 2007;118:2730-2744.

Liebetanz D, Fauser S, Michaelis T, Czeh B, Watanabe T, Paulus W, et al. Safety aspects of chronic low-frequency transcranial magnetic stimulation based on localized proton magnetic resonance spectroscopy and histology of the rat brain. Journal of Psychiatric Research 2003;37:277-286.

Lisanby SH, Belmaker RH Animal models of the mechanisms of action of repetitive transcranial magnetic stimulation (rTMS): Comparisons with electroconvulsive shock (ECS). Depression and Anxiety 2000;12:178-187.

Liu R, Ueno S Calculating the activating function of nerve excitation in inhomogeneous volume conductor during magnetic stimulation using the finite element method. Ieee Transactions on Magnetics 2000;36:1796-1799.

Maccabee PJ, Amassian VE, Eberle LP, Cracco RQ Magnetic coil stimulation of straight and bent amphibian and mammalian peripheral nerve in vitro: locus of excitation. J Physiol 1993;460:201-19.

Maccabee PJ, Amassian VE, Eberle LP, Rudell AP, Cracco RQ, Lai KS, et al. Measurement of the Electric-Field Induced into Inhomogeneous Volume Conductors by Magnetic Coils - Application to Human Spinal Neurogeometry. Electroencephalography and Clinical Neurophysiology 1991;81:224-237.

Maccabee PJ, Nagarajan SS, Amassian VE, Durand DM, Szabo AZ, Ahad AB, et al. Influence of pulse sequence, polarity and amplitude on magnetic stimulation of

human and porcine peripheral nerve. Journal of Physiology-London 1998;513:571-585.
Magstim C. Magstim® Coils & Accessories Operating Manual 1623-23-06. In: Magstim C editor, 2005.
Magstim C. Magstim Rapid P/N 3576-23-08 Operating manual: Magstim, Company, 2006:61.
Mainen ZF, Joerges J, Huguenard JR, Sejnowski TJ A model of spike initiation in neocortical pyramidal neurons. Neuron 1995;15:1427-1439.
Malmivuo J, Plonsey R Bioelectromagnetism: Principles and applications of bioelectric and biomagnetic field, 1st ed.: Oxford University Press, 1995.
Manola L, Holsheimer J, Veltink P, Buitenweg JR Anodal vs cathodal stimulation of motor cortex: a modeling study. Clin Neurophysiol 2007;118:464-74.
Manola L, Roelofsen BH, Holsheimer J, Marani E, Geelen J Modelling motor cortex stimulation for chronic pain control: electrical potential field, activating functions and responses of simple nerve fibre models. Med Biol Eng Comput 2005;43:335-43.
Martin JH Neuroanatomy. Text and Atlas, 2nd ed. Stamford: Appleton & Lange, 1996.
Mascagni MV. Numerical Methods for Neuronal Modeling. In: Koch C, Segev I, editors. Methods in neuronal modeling: from ions to networks, 2 ed. Cambridge: MA: MIT press, 1998.
McComas AJ, Wilson P An investigation of pyramidal tract cells in the somatosensory cortex of the rat. J Physiol 1968;194:271-88.
McIntyre CC, Grill WM Excitation of central nervous system neurons by nonuniform electric fields. Biophysical Journal 1999;76:878-888.
Meyer G Forms and Spatial Arrangement of Neurons in the Primary Motor Cortex of Man. Journal of Comparative Neurology 1987;262:402-428.
Mills KR The basics of electromyography. Journal of Neurology Neurosurgery and Psychiatry 2005;76:32-35.
Miranda PC, Hallett M, Basser PJ The electric field induced in the brain by magnetic stimulation: A 3-D finite-element analysis of the effect of tissue heterogeneity and anisotropy. Ieee Transactions on Biomedical Engineering 2003;50:1074-1085.
Mountcastle VB The columnar organization of the neocortex. Brain 1997;120:701-722.
Nagarajan SS, Durand DM, Warman EN Effects of Induced Electric-Fields on Finite Neuronal Structures - a Simulation Study. Ieee Transactions on Biomedical Engineering 1993;40:1175-1188.
Nakamura H, Kitagawa H, Kawaguchi Y, Tsuji H Direct and indirect activation of human corticospinal neurons by transcranial magnetic and electrical stimulation. Neurosci Lett 1996;210:45-8.
Nilsson J, Panizza M, Roth BJ, Basser PJ, Cohen LG, Caruso G, et al. Determining the Site of Stimulation during Magnetic Stimulation of a Peripheral-Nerve. Electroencephalography and Clinical Neurophysiology 1992;85:253-264.
Ogiue-Ikeda M, Kawato S, Ueno S The effect of repetitive transcranial magnetic stimulation on long-term potentiation in rat hippocampus depends on stimulus intensity. Brain Res 2003;993:222-6.
Pascual-Leone A, Houser CM, Reese K, Shotland LI, Grafman J, Sato S, et al. Safety of Rapid-Rate Transcranial Magnetic Stimulation in Normal Volunteers. Electroencephalography and Clinical Neurophysiology 1993;89:120-130.

Pascual-Leone A, Walsh V, Rothwell J Transcranial magnetic stimulation in cognitive neuroscience - virtual lesion, chronometry, and functional connectivity. Current Opinion in Neurobiology 2000;10:232-237.

Patton HD, Amassian VE Single-Unit and Multiple-Unit Analysis of Cortical Stage of Pyramidal Tract Activation. Journal of Neurophysiology 1954;17:345-363.

Paus T, Jech R, Thompson CJ, Comeau R, Peters T, Evans AC Transcranial magnetic stimulation during positron emission tomography: A new method for studying connectivity of the human cerebral cortex. Journal of Neuroscience 1997;17:3178-3184.

Peterchev AV, Jalinous R, Lisanby SH A transcranial magnetic stimulator inducing near-rectangular pulses with controllable pulse width (cTMS). IEEE Trans Biomed Eng 2008;55:257-66.

Plonsey R, Barr RC Bioelectricity: a quantitative approach. New York: Kluwer Academic, 2000.

Plonsey R, Heppner DB Considerations of Quasi-Stationarity in Electrophysiological Systems. Bulletin of Mathematical Biophysics 1967;29:657-&.

Rattay F Analysis of models for external stimulation of axons. IEEE Trans Biomed Eng 1986;33:974-7.

Reilly JP Peripheral-Nerve Stimulation by Induced Electric Currents - Exposure to Time-Varying Magnetic-Fields. Medical & Biological Engineering & Computing 1989;27:101-110.

Ren CY, Tarjan PP, Popovic DB A Novel Electric Design for Electromagnetic Stimulation - the Slinky Coil. Ieee Transactions on Biomedical Engineering 1995;42:918-925.

Robillard PN, Poussart Y Specific-impedance measurements of brain tissues. Med Biol Eng Comput 1977;15:438-45.

Roth BJ Mechanisms for Electrical-Stimulation of Excitable Tissue. Critical Reviews in Biomedical Engineering 1994;22:253-305.

Roth BJ, Basser PJ A model of the stimulation of a nerve fiber by electromagnetic induction. IEEE Trans Biomed Eng 1990;37:588-97.

Roth BJ, Cohen LG, Hallett M The electric field induced during magnetic stimulation. Electroencephalogr Clin Neurophysiol Suppl 1991a;43:268-78.

Roth BJ, Saypol JM, Hallett M, Cohen LG A Theoretical Calculation of the Electric-Field Induced in the Cortex during Magnetic Stimulation. Electroencephalography and Clinical Neurophysiology 1991b;81:47-56.

Roth Y, Amir A, Levkovitz Y, Zangen A Three-dimensional distribution of the electric field induced in the brain by transcranial magnetic stimulation using figure-8 and deep H-coils. Journal of Clinical Neurophysiology 2007;24:31-38.

Roth Y, Zangen A, Hallett M A coil design for transcranial magnetic stimulation of deep brain regions. Journal of Clinical Neurophysiology 2002;19:361-370.

Rothwell JC Techniques and mechanisms of action of transcranial stimulation of the human motor cortex. Journal of Neuroscience Methods 1997;74:113-122.

Ruohonen J. Transcranial magnetic stimulation: modelling and new techniques. Biomag Laboratory. Espoo: Helsinki University of Technology, 1998:52.

Ruohonen J, Virtanen J, Ilmoniemi RJ Coil optimization for magnetic brain stimulation. Ann Biomed Eng 1997;25:840-9.

Rush S, Driscoll DA Current distribution in the brain from surface electrodes. Anesth Analg 1968;47:717-23.

Rushton WA A theory of the effects of fibre size in medullated nerve. J Physiol 1951;115:101-22.

Sack AT Transcranial magnetic stimulation, causal structure-function mapping and networks of functional relevance. Current Opinion in Neurobiology 2006;16:593-599.

Sakai K, Ugawa Y, Terao Y, Hanajima R, Furubayashi T, Kanazawa I Preferential activation of different I waves by transcranial magnetic stimulation with a figure-of-eight-shaped coil. Exp Brain Res 1997;113:24-32.

Salinas FS, Lancaster JL, Fox PT Detailed 3D models of the induced electric field of transcranial magnetic stimulation coils. Phys Med Biol 2007;52:2879-92.

Shaldivin A, Kaptsan A, Belmaker RH, Einat H, Grisaru N Transcranial magnetic stimulation in an amphetamine hyperactivity model of mania. Bipolar Disord 2001;3:30-4.

Silva S, Basser PJ, Miranda PC Elucidating the mechanisms and loci of neuronal excitation by transcranial magnetic stimulation using a finite element model of a cortical sulcus. Clin Neurophysiol 2008;119:2405-2413.

Silva VC, Meunier G, Foggia A A 3-D Finite-Element Computation of Eddy Currents and Losses in Laminated Iron Cores Allowing for Electric and Magnetic-Anisotropy. Ieee Transactions on Magnetics 1995;31:2139-2141.

Silvester PP, Ferrari RL Finite elements for electrical engineers, 3 ed. Cambridge: Cambridge University Press, 1996.

Standring S Gray's Anatomy: The Anatomical Basis of Clinical Practice, 39 ed.: Elsevier Churchill Livingstone, 2004.

Starzynski J, Sawicki B, Wincenciak S, Krawczyk A, Zyss T Simulation of magnetic stimulation of the brain. Ieee Transactions on Magnetics 2002;38:1237-1240.

Sweeney JD, Mortimer JT, Durand D. Modeling of mammalian myelinated nerve for functional neuromuscular stimulation. Ninth Annual Conference of the Engineering in Medicine and Biology Society. Boston, MA, 1987:1577-1578.

Tasaki I New measurements of the capacity and the resistance of the myelin sheath and the nodal membrane of the isolated frog nerve fiber. Am J Physiol 1955;181:639-50.

Tenforde TS. Interaction of ELF Magnetic Fields with Living Systems. In: Polk C, Postow E, editors. Handbook of Biological Effects of Electromagnetic Fields, 2nd ed: CRC Press, 1996:185-230.

Thielscher A, Kammer T Linking physics with physiology in TMS: A sphere field model to determine the cortical stimulation site in TMS. Neuroimage 2002;17:1117-1130.

Thielscher A, Kammer T Electric field properties of two commercial figure-8 coils in TMS: calculation of focality and efficiency. Clinical Neurophysiology 2004;115:1697-1708.

Tofts PS The Distribution of Induced Currents in Magnetic Stimulation of the Nervous-System. Physics in Medicine and Biology 1990;35:1119-1128.

Tsugorka T, Dovgan' O, Stepanyuk A, Cherkas V Variety of types of cortical interneurons. Neurophysiology 2007;39:227-236.

Ueno S, Tashiro T, Harada K Localized Stimulation of Neural Tissues in the Brain by Means of a Paired Configuration of Time-Varying Magnetic-Fields. Journal of Applied Physics 1988;64:5862-5864.

Virtanen J, Ruohonen J, Naatanen R, Ilmoniemi RJ Instrumentation for the measurement of electric brain responses to transcranial magnetic stimulation. Medical & Biological Engineering & Computing 1999;37:322-326.

Wagner TA, Zahn M, Grodzinsky AJ, Pascual-Leone A Three-dimensional head model simulation of transcranial magnetic stimulation. Ieee Transactions on Biomedical Engineering 2004;51:1586-1594.

Wang Y, Gupta A, Toledo-Rodriguez M, Wu CZ, Markram H Anatomical, physiological, molecular and circuit properties of nest basket cells in the developing somatosensory cortex. Cereb Cortex 2002;12:395-410.

Warman EN, Grill WM, Durand D Modeling the effects of electric fields on nerve fibers: determination of excitation thresholds. IEEE Trans Biomed Eng 1992;39:1244-54.

Wassermann EM Risk and safety of repetitive transcranial magnetic stimulation: report and suggested guidelines from the International Workshop on the Safety of Repetitive Transcranial Magnetic Stimulation, June 5-7, 1996. Electroencephalogr Clin Neurophysiol 1998;108:1-16.

Wassermann EM, Lisanby SH Therapeutic application of repetitive transcranial magnetic stimulation: a review. Clinical Neurophysiology 2001;112:1367-1377.

Weissman JD, Epstein CM, Davey KR Magnetic Brain-Stimulation and Brain Size - Relevance to Animal Studies. Electroencephalography and Clinical Neurophysiology 1992;85:215-219.

Werhahn KJ, Fong JKY, Meyer BU, Priori A, Rothwell JC, Day BL, et al. The Effect of Magnetic Coil Orientation on the Latency of Surface Emg and Single Motor Unit Responses in the First Dorsal Interosseous Muscle. Electroencephalography and Clinical Neurophysiology 1994;93:138-146.

Wesselink WA, Holsheimer J, Boom HBK A model of the electrical behaviour of myelinated sensory nerve fibres based on human data. Medical & Biological Engineering & Computing 1999;37:228-235.

Yamashita A, Arikuni T Axon trajectories in local circuits of the primary motor cortex in the macaque monkey (Macaca fuscata). Neuroscience Research 2001;39:233-245.

Yousry TA, Schmid UD, Alkadhi H, Schmidt D, Peraud A, Buettner A, et al. Localization of the motor hand area to a knob on the precentral gyrus - A new landmark. Brain 1997;120:141-157.

Zangen A, Roth Y, Voller B, Hallett M Transcranial magnetic stimulation of deep brain regions: evidence for efficacy of the H-coil. Clinical Neurophysiology 2005;116:775-779.

Zheng J, Li L, Huo X. Analysis of electric field in real rat head model during transcranial magnetic stimulation. 27th Annual Conference of the IEEE Engineering in Medicine and Biology Society. Shangai, 2005:1529-1532.

Zienkiewicz OC, Taylor RL The Finite Element Method. Volume 1: The Basis, 5th ed. Oxford: Butterworth-Heinemann, 2000.

Zimmermann KP, Simpson RK "Slinky" coils for neuromagnetic stimulation. Electromyography and Motor Control-Electroencephalography and Clinical Neurophysiology 1996;101:145-152.

Zyss T, Mamczarz J, Vetulani J The influence of rapid-rate transcranial magnetic stimulation (rTMS) parameters on rTMS effects in Porsolt's forced swimming test. International Journal of Neuropsychopharmacology 1999;2:31-34.